GENERATION AND PROPAGATION OF AFRICAN SQUALL LINES

by

David Bolton

Atmospheric Physics Group,

Imperial College of Science and Technology

A thesis submitted for the degree of

Doctor of Philosophy in the University of London

and for the

Diploma of Membership of the Imperial College

April 1981

GENERATION AND PROPAGATION OF AFRICAN SQUALL LINES

by

David Bolton

ABSTRACT

Observational studies of severe local storms are summarised, indicating the particular case of the travelling squall line as a line of thunderstorms with an arc-shaped leading edge which normally travels faster than the wind at any level; appropriate synoptic conditions in West Africa are reviewed. Squall lines affecting Minna (Nigeria) during 1974-1976 are identified using mainly surface data, and composite vertical profiles at Minna are obtained. Results suggest that a strong jet around 650 mb is essential for squall line development, whilst strong upper level winds have an inhibiting effect; also, as for other severe local storms, a warm moist surface layer, with dry air aloft is needed, indicating latent heat transfer as an essential driving mechanism.

In a review of squall line models, two-dimensional steady state models are found to represent quite well a mature squall line. No model, however, explains how such a two-dimensional disturbance, moving transverse to the mean flow and faster than the wind at any level, can be generated from a localised initial perturbation. In particular, study of individual linear modes of a stratified sheared flow reveals that the fastest growing buoyancy-driven mode is almost invariably longitudinal, while all amplifying modes have their phase speeds less than the maximum flow speed. However, fastest growing modes with group speeds greater than the maximum flow speed are found for profiles with a mid-level velocity maximum, though not for monotonic profiles. Furthermore, constructive interference of modes excited by a localised initial cell results in formation of a transverse line of cells, which for flows with a mid-level velocity maximum is preceded by a nearly two-dimensional arc front, advancing faster than the flow at any level. Application to actual soundings with jets gives realistic initial development of squall lines.

CONTENTS

LIST OF ABBREVIATIONS 6

LIST OF PRINCIPAL SYMBOLS 6

1. INTRODUCTION 10

2. A REVIEW OF SQUALL LINE OBSERVATIONS

2.1 SEVERE LOCAL STORMS AND SQUALL LINES

2.1.1 General properties of severe local storms 13

2.1.2 Geographical distribution of severe local storms 15

2.1.3 Cellular structure of severe local storms 19

2.2 TRAVELLING SQUALL LINES

2.2.1 Surface observations 22

2.2.2 Satellite observations 24

2.2.3 Recent intensive observations 27

2.2.4 Summary of squall line structure 37

2.3 SQUALL LINES IN WEST AFRICA

2.3.1 Climatological conditions 37

2.3.2 Synoptic perturbations 41

2.3.3 Some statistics of West African squall lines 45

3. SQUALL LINES AT MINNA, NIGERIA

3.1 IDENTIFICATION AND MEAN PROPERTIES OF SQUALL LINES

3.1.1 Squall line of 12 September 1977 51

3.1.2 Identification of squall lines 54

3.1.3 Some squall line statistics 65

3.2 MEAN ATMOSPHERIC CONDITIONS AT MINNA DURING THE SQUALL LINE SEASON

3.2.1 Time-height sections 71

3.2.2 GATE mean midday and midnight soundings 74

3.3 ATMOSPHERIC CHANGES ASSOCIATED WITH SQUALL LINES AT MINNA

3.3.1 Mean 24 hour changes 78

3.3.2 Mean 12 hour changes 82

3.3.3 Vertical section 85

4. A REVIEW OF SQUALL LINE MODELS

4.1 UNSTABLE GRAVITY WAVE MODEL

4.1.1 Basic equations 92

4.1.2 Linear modes 95

4.1.3 Growth of an initially localised perturbation 100

4.2 OTHER GRAVITY WAVE MODELS
4.2.1 Stable gravity wave model 105
4.2.2 Forced gravity wave (wave-CISK) model 106

4.3 TWO-DIMENSIONAL MODELS
4.3.1 Basic equations 112
4.3.2 Overturning models 115
4.3.3 Density current models 119
4.3.4 Use of an assumed flow 123

4.4 NUMERICAL MODELS
4.4.1 Zero and one-dimensional models 124
4.4.2 Two-dimensional models 124
4.4.3 Three-dimensional models 125

4.5 OTHER DYNAMICAL MODELS
4.5.1 Mixing models 130
4.5.2 Rigid cylinder models 130
4.5.3 Sinking jet model 132

5. LINEAR MODES OF AN UNSTABLY STRATIFIED SHEARED FLOW

5.1 INTRODUCTION
5.1.1 Basic equations 133
5.1.2 Hyperbolic tangent profiles 136
5.1.3 Numerical methods 138

5.2 NUMERICAL RESULTS FOR MONOTONIC PROFILES
5.2.1 Introduction 144
5.2.2 Plane Couette flow: $\mu = 0$ 145
5.2.3 Hyperbolic tangent profile: $\mu = 2$ 151
5.2.4 Shear layer: $\mu = \infty$ 154

5.3 ORIENTATION OF THE FASTEST GROWING MODE
5.3.1 Free and forced convection 156
5.3.2 Mean flow forcing 163

5.4 LARGE RICHARDSON NUMBER EXPANSIONS
5.4.1 Long wave expansion, $-R_\theta \gg k^2$ 168
5.4.2 Short wave expansions 170
5.4.3 General remarks 177

5.5 NUMERICAL RESULTS FOR JET PROFILES
5.5.1 Introduction 178
5.5.2 Plane Poiseuille flow: $\mu = 0$ 181
5.5.3 Th^2 jet profile: $\mu = 5$ 184

5.6 GROUP VELOCITIES
5.6.1 Two dimensions 192
5.6.2 Three dimensions 195

6. GROWTH OF AN INITIALLY LOCALISED PERTURBATION

6.1 INTRODUCTION
6.1.1 Mathematical analysis 198
6.1.2 Numerical method 202

6.2 CASE STUDIES WITH PLANE POISEUILLE FLOW
6.2.1 Introduction 206
6.2.2 Two-dimensional study 207
6.2.3 Three-dimensional study 207
6.2.4 Effect of changing various parameters 209

6.3 CASE STUDIES WITH OTHER VELOCITY PROFILES
6.3.1 Unsheared flow 217
6.3.2 Statically neutral hyperbolic tangent profiles 217
6.3.3 Unstably stratified plane Couette flow 221
6.3.4 Mixed Poiseuille and Couette flow 225

6.4 CASE STUDIES WITH ATMOSPHERIC DATA
6.4.1 Analysis of data 230
6.4.2 Squall lines at Minna 231
6.4.3 VIMHEX squall line 237
6.4.4 Comparison with other models 237

6.5 CONCLUDING REMARKS 241

REFERENCES 243

APPENDIX A: ESTIMATION OF STORM VELOCITIES FROM SURFACE REPORTS OF SQUALLS 252

APPENDIX B: THREE-DIMENSIONAL LAGRANGIAN VORTICITY EQUATIONS 254

APPENDIX C: THE COMPUTATION OF EQUIVALENT POTENTIAL TEMPERATURE 257

ACKNOWLEDGEMENTS 265

LIST OF ABBREVIATIONS.

AEJ: African Easterly Jet
AKE: Available Kinetic Energy
APE: Available Potential Energy
ASECNA: Agence pour la Securite de la Navigation Aerienne
GATE: Global Atmospheric Research Project's Atlantic Tropical Experiment
ITCZ: Inter-Tropical Convergence Zone
KE: Kinetic Energy
PE: Potential Energy
SLS: Severe Local Storm
SQL: Squall Line
TEJ: Tropical Easterly Jet

LIST OF PRINCIPAL SYMBOLS.

(a) Dimensional.

B_0 = static stability in (4.3)
B = characteristic static stability (5.5)
c = storm speed relative to inflow in section 4.3.2
c' = characteristic speed (4.97)
c_Δ = speed of propagation of density current head in (4.96), (4.98)
e = standard error of difference of means (3.6), (3.8)
$\tilde{f}$ = Fourier transform of initial perturbation in (4.37)ff, (6.1)ff
g = accelaration due to gravity
H = flow boundary in section 4.3.2
H_0 = density scale height, given by (4.15)
h = $-\delta\phi/B_0$ as in (4.12)ff
$\tilde{h}$ = Fourier transform of $\rho_0^{\frac{1}{2}} h$
K = common value of eddy momentum and heat diffusion coefficients
l = $\rho_0^{-\frac{1}{2}} h$ in (4.22)ff in (4.5)ff
$\tilde{l}$ = Fourier transform of $\rho_0^{\frac{1}{2}} l$
N = $(-gB)^{\frac{1}{2}}$ in (5.10)
p = pressure
δp = perturbation pressure in (4.1)ff
Q = heat source in (4.56)
$\tilde{Q}$ = Fourier transform of $\rho_0^{\frac{1}{2}} Q$
$\tilde{q}$ = $-ik\delta\tilde{h}$ in (5.44)
S = characteristic shear (5.4)
t = time
(U, V) = velocity of a point in asymptotic theory in section 4.1.3

$\underline{U}_0$ = (U_0, V_0) = mean flow in (4.5)ff

(U_0, V_0, W_0) = inflow velocity in (4.69)ff, (B.9)ff

$\underline{u}$ = (u, v, w) = fluid velocity in (4.1)ff

$(\delta u, \delta v)$ = perturbation horizontal velocity in (4.5)ff

$(\tilde{\delta u}, \tilde{\delta v}, \tilde{w})$ = Fourier transform of $\rho_0^{\frac{1}{2}}(\delta u, \delta v, w)$

(u_r, v_r) = relative velocity components in (3.2) and in section 3.3.2

(x, y, z) = coordinates of fluid element

(x_0, y_0, z_0) = initial coordinates of fluid element

z_1, z_2 = inflow and outflow levels in (3.1)ff; = flow boundaries in (4.4)

z_* = steering level in (4.79)ff

$\underline{\alpha}$ = (α, β) = propagation vector (4.9)

(α_0, β_0) = saddle point in asymptotic theory (4.40)ff

α = wavenumber (4.10)

θ = potential temperature

$\lambda_0, \lambda_1, \lambda_2$ = terms in expansion of c_θ in (5.110)

$\underline{\xi}$ = (ξ, η, ζ) = vorticity in (4.26), (4.71)ff, (B.14)ff

$\underline{\xi}_0$ = (ξ_0, η_0, ζ_0) = inflow vorticity in (4.75)ff, (B.14)ff

ρ = density

ρ_0 = steady state density in (4.1)ff; = inflow density in (4.67)ff, (B.1)ff

σ = $\sigma_r + i\sigma_i$ = time dependence in (4.16)ff

σ_i = growth rate

σ' = modified time dependence (4.20)

σ_0 = first approximation to growth rate in (6.4)

ϕ = log potential temperature in sections 4.1.1, 4.3.1, etc

ϕ_0 = steady state log potential temperature in sections 4.1.1,...

$\delta\phi$ = perturbation log potential temperature in (4.1)ff

$\delta\phi_p$ = parcel excess log potential temperature (3.3)

(b) Non-Dimensional.

Ai, Bi = Airy functions

c = $c_r + ic_i$ = non-dimensional form (5.16) of σ

c_r = phase speed (5.17)

c_0 = first approximation to phase speed in (6.5)

$\underline{c}_g$ = group velocity (5.159)

c_g = group speed in (5.155), (6.22)

c_θ = $c_{\theta r} + ic_{\theta i}$ = form of c for particular direction of propagation θ

F_A, F_N = Froude numbers (4.94), (4.100)

G_1 = KE gained by mean flow through buoyancy term in (5.105)

G_2 = KE gained by mean flow through shear term in (5.105)

G_3 = total KE gained by perturbation in (5.106)

$H_\nu^{(1)}, H_\nu^{(2)}$ = Hankel functions

J { = local Richardson number (4.55) and (5.7)
{ = local Richardson number at the boundary (5.122)

J_ν = Bessel function

k = wavenumber (4.31), (5.3)

k_0 { = first approximation to saddle point in (6.19)
{ = parameter for initial updraught (6.42)

k_c = cut off wavenumber (4.34)

k_m = wavenumber of maximum amplification (4.35)

k_s = critical wavenumber in (5.33), (5.37) etc

L = lapse rate (5.8)

Q = component (5.15) of mean flow perpendicular to propagation vector

q = exponent (6.12) in asymptotic theory

R = mean Richardson number (5.6)

R_θ = modified Richardson number (5.23)

R_a = Rayleigh number (4.32) and (5.9)

Ri = observational Richardson number

T = time in (5.12), (6.25)

U = speed (6.9) of point in asymptotic theory

$\underset{\sim}{U}$ = (U, V) = mean flow (5.13)

U_m = $\max(U)$ in (6.25)

W = component (5.14) of mean flow in direction of propagation

(X, Y, Z) = coordinates

Y, Y_1, Y_2 = parabolic cylinder functions

Y_ν = Bessel function

Z_+, Z_- = turning points of (5.120)

Z_* = pole in (5.61), (5.120)

Z_0 = velocity maximum in (5.77), (5.139)

Z_s = inflexion point in (5.30)ff

$\mathcal{Z}$ = iZ in (5.53)

θ = direction of propagation (4.11)

λ = ic_θ in (5.53)

μ = parameter for hyperbolic tangent profiles (5.27), (5.34)

ν = parameter given by (4.54), (5.69), (5.82)

τ = time in (5.11)

ϕ = direction of motion of point in asymptotic theory in (6.7)f

But God made the earth by his power;
he founded the world by his wisdom
and stretched out the heavens by his understanding
When he thunders, the waters in the heavens roar;
he makes the clouds rise from the ends of the earth.
He sends lightning with the rain
and brings out the wind from his storehouses.

Jeremiah 10: 12 and 13
(New International Version).

CHAPTER 1. INTRODUCTION.

Severe local storms in the United States are notorious for the immense damage and loss of life associated particularly with hail and tornadoes. Such destruction from a West African squall line is however unusual, damage being normally limited to lightning strikes, strong winds and occasional flooding. Why then study West African squall lines? Basically their economic importance is seen not negatively in their destruction, but positively in that, particularly in the Sahel, they bring most of the annual rainfall, as shown by Eldridge (1957) in one of the few pre-1970 studies, following the earlier definitive study of Hamilton and Archbold (1945).

Hamilton and Archbold's study was notable in that it not only gave a summary of observations of squall lines, but also suggested a dynamical model for their structure. This thesis correspondingly falls into two parts, observational (chapters 2 and 3) and theoretical (chapters 4 - 6), each part consisting of a review of published work followed by original material.

The observational review, chapter 2, opens with a consideration of the squall line as a member of the more general class of severe local storms, identifying those features which it shares in common with other severs local storms, and those in which it differs. Restricting attention now to squall lines, a review is made of both older observations and more recent studies which make use of satellites and intensive upper air data. These are summarised in a schematic squall line structure due to Betts (1978) before turning to squall lines in West Africa in particular, where suitable climatological conditions are identified, and statistics are presented.

Apart from structural differences between West African squall lines and severe local storms elsewhere, one other difference may be noted - the relative scarcity of observations, Nigeria for instance having in 1976 only three radiosonde stations to cover an area nearly four times that of the United Kingdom. It is therefore appropriate that the observational study of squall lines in chapter 3 should be based on data from a single upper air station, Minna in Nigeria, supplemented by reports from surrounding surface stations, and, where available, satellite images. After opening with a description of one of these squall lines at Minna, the chapter moves into the listing of properties which could be used in their identification, and some

statistics are presented for the squall lines thus identified. Time - height sections for the GATE period agree with the conclusions of chapter 2 that the conditions necessary for the occurrence of squall lines are a strong jet around 650 mb, lighter upper level winds, and a warm moist surface layer with dry air aloft. Mean soundings on non - squall and squall days provide further confirmation of these conditions, while 'before and after' soundings hint at the changes brought about by passage of a squall line, particularly a lowering of the jet, and the replacement of warm moist low level air by dry air brought down in cool convective scale and warm mesoscale downdraughts. Finally, striking confirmation of these changes is provided by a composite vertical section.

Turning now in chapter 4 to a review of squall line models, there are, apart from some ad hoc models considered briefly at the end of the chapter, two main classes of model: mathematical and numerical, and these are reviewed in turn. In mathematical models, drastic simplifications have to be made, particularly in the thermodynamics, in order to obtain a tractable set of equations; as a result, clearer understanding of some features may be gained at the expense of misrepresenting others. Numerical models on the other hand are limited only by the capacity of the computer (and the programmer's time!), so can, at least theoretically, go into great detail and produce realistic simulations; because of their complexity however, it can be difficult to gain as clear an understanding of cause and effect as is possible with the simpler mathematical models.

Within the class of mathematical models, there are two main divisions: the simple linear gravity wave models which are mainly appropriate to initial development, and the sophistieated non linear steady state models of Moncrieff and collaborators which are applicable to the mature stage. These are reviewed in turn in chapter 4, commencing with the unstable gravity wave model which forms the subject of the last two chapters, two aspects of tropical squall lines being mentioned which have particular relevance to the linear model, namely their orientation transverse to the mean flow, and their motion faster than the environmental wind at any level. After dealing with the other mathematical models, the review then turns to numerical studies, taking them in order of increasing complexity, and culminating in the full three dimensional simulation of Moncrieff and Miller (1976). No one model emerges as leading to a comprehensive understanding of the

squall line; rather each, in spite of its particular weaknesses sheds light on some aspect of the squall line, and with this expectation, the study of the unstable gravity wave model is now taken up.

Considering first normal modes in chapter 5, the account opens with an introduction to the profiles studied and numerical methods used, then proceeds in much the same way as did the original investigation. Examination of antisymmetric profiles proves generally unhelpful in modelling tropical squall lines, but throws light on the relation between free and forced convection, and emphasises the importance of the longitudinal roll rather than any transverse mode as being the fastest growing when there is appreciable buoyancy. Since the longitudinal roll corresponds to the limit: modified Richardson number $\rightarrow -\infty$, large Richardson number expansions are examined, and suggest the importance of jet profiles in giving rise to both rapidly growing, and rapidly moving transverse modes. Results with symmetric jet profiles show that the rapidly growing transverse mode is a very special case, and not likely to be of help in modelling squall lines; a consideration of group velocities however shows that in the rapidly moving short transverse modes there is the possibility of formation of a patch of convection the forward edge of which moves, as required, faster than the mean flow at any level, and an approximation gives the observational rule of Fernandez (1980) that the velocity of a squall line will be close to the maximum mid level environmental wind.

Turning finally to the initial value problem in chapter 6, both mathematical and numerical results confirm the constructive interference of short wave modes for a jet profile to form an amplifying patch of convection with a transverse arc front moving faster than the mean flow at any level, and this is suggested as a model for the tropical squall line. Correspondingly, results with monotonic and mixed profiles throw light on middle latitude squall lines, and storm splitting. Finally, case studies with atmospheric profiles are presented, and the model is discussed.

CHAPTER 2. A REVIEW OF SQUALL LINE OBSERVATIONS.

2.1 SEVERE LOCAL STORMS AND SQUALL LINES.

2.1.1 General Properties of Severe Local Storms.

A severe local storm (SLS) is, according to Huschke (1959) 'a destructive storm of mesometeorological scale'. Such storms will be thunderstorms, accompanied by very strong surface winds or large hailstones, and sometimes tornadoes (Winston 1956); the word local is used to distinguish these storms from cyclones. In this study, it will be convenient before directing attention to squall lines to identify those features which hold for all SLS's, following the description proposed by Ludlam and collaborators, and summarised in Ludlam's (1963) review. Other models, notably that of Newton (1963) have been proposed, but a summary of these is deferred until the end of chapter 4.

The SLS may, according to Ludlam (1963) be regarded as a device which exchanges the upper and lower troposphere, and in which mixing is unimportant. It derives its energy primarily from release of latent heat of condensation of water vapour contained in warm moist air which rises in one or more updraughts, and will normally move to maintain a constant supply of such air. Favourable thermodynamic conditions for occurrence of SLS's are thus a warm moist layer of air at the surface (i.e. high equivalent potential temperature θ_E - see Bolton 1980a), with relatively cool air aloft (i.e. low potential temperature θ); attempts to quantify these conditions, reviewed for instance by Gokhale (1975), have not however produced any entirely satisfactory measure. Fulks (1951) noted that in the United States there is normally also an inversion around 850 mb, which disappears with passage of the storm; generally it is true that a stable layer around this height will favour severe storms by providing a lid under which temperature and moisture content may increase until, with the removal of the stable layer, explosive development may take place (Newton 1963; Carlson and Ludlam 1968).

Associated with the updraught will be a downdraught in which drag and evaporative cooling due to rain falling from the updraught into clear relatively dry middle level air to the side causes the middle level air to be brought down to the surface* (Byers and Braham 1949;

* An additional, mesoscale downdraught may be brought about by dynamical forcing: see section 2.2.3b.

Ludlam 1963). A further aspect of favourable thermodynamic soundings should therefore be dry (and hence low θ_e) middle level air. On reaching the ground, the downdraught air spreads out from the precipation area(s) as a cold pool; most is left behind, but some flows out ahead, and where this meets the environmental air, there is frequently a sharp temperature contrast referred to as the pseudo - cold front, or, more recently, the squall front. Warm air ahead of the storm is lifted over the front (Newton 1963) and condensation in this air will usually cause a roll cloud, or arcus, of great length to be formed overhead, spanning the squall front (Ludlam 1980).

Besides a suitable thermodynamic sounding, there is strong observational evidence that a suitable wind profile is necessary. Byers and Battan (1949) have shown that strong vertical shears of order $10^{-3}s^{-1}$ tend to disrupt growth of local thunderstorms. However, many papers, reviewed for example in Marwitz (1972) establish the need for even larger wind shears, at least 2.5×10^{-3} s^{-1} over the depth of the troposphere for occurrence of SLS's in middle latitudes. For example Porter et al (1955) stated that squall lines in the Central United States only form if winds at 500 mb are 20 m/s or higher, and tend to dissipate if they move into areas of lighter winds. In the tropics, Ludlam (1963) talked of the need for strong shear at low levels, but otherwise little has been published on suitable wind profiles, though Dugdale (personal communication) stated as an empirical rule used by forecasters in Nigeria that squall lines only form if there is a strong jet, at least 15 m/s, around 700 mb, a result which will be seen to be borne out by the study in chapter 3.

Ludlam (1980) suggested that the role of the strong shear is to tilt the updraught so that precipation is able to fall into the clear dry air to the side. He used the Richardson number, Ri, as a measure of the relative magnitude of the shear as available to organise the flow as opposed to the buoyancy to disrupt it. Defining the Richardson number as the ratio of available potential energy (positive area in simple parcel theory) to the kinetic energy corresponding to the difference in wind velocities at the inflow and outflow levels of the updraught, Ludlam suggested that in middle latitudes, SLS's will occur for values of -Ri less than about 5, while cumulus and ordinary cumulonimbus will be preferred for -Ri greater than about 25 (quoted in Moncrieff and Green 1972). In the tropics, Grover (1974), with a modified definition of Richardson number, found that the nine squall

lines which he identified in Venezuela corresponded roughly to $1 < -Ri < 3$; below the lower cut - off value of 1, storm systems tended to be weaker and less organised, possibly because of insufficient buoyancy. In general it seems reasonable to conclude that SLS's are restricted to a fairly small range of Richardson numbers, say $1 < -Ri < 5$.

Summarising conditions for occurrence of SLS's, it is necessary to have a warm moist surface layer building up under an inversion, with relatively cool, dry air aloft, and a strongly sheared wind profile. In addition, a mechanism is needed which will trigger off the SLS by removal of the low level inversion, which according to Newton (1963) could be an extended period of intense solar heating, or forced ascent; the ascent may be forced by orography, or by a large scale motion system such as a cold front, waves in a jet stream, or, as will be considered in section 2.3.2, an easterly wave (these large scale motion systems will incidentally have strong shears associated with them, which provides another reason for the association between strong shears and SLS's, as noted for example in Beebe and Bates 1955). Once the storm has been initiated, ascent over the squall front will in general be sufficient to sustain further growth.

Having studied SLS's in general, it is now time to examine how they vary from one another. Two divisions will be considered: geographical location, and cellular structure.

2.1.2 Geographical Distribution of Severe Local Storms.

Fig 2.1, taken from Ludlam (1963) shows the areas subject to SLS's, as identified by accompanying squalls and roll clouds, or by occurrence of large hailstones.

The middle latitude storms occur in the hatched areas: Central and Southern Europe, Mid - West United States, in a belt across Northern India to Southern China, and in the Southern Hemisphere in Argentina, South Africa, and South East Australia. They are closely related to the mean position of the strongest winds in the middle troposphere during the SLS season (indicated by broad arrows). These middle latitude storms normally move with a speed near to the mean tropospheric wind speed, but their paths are, in the Northern Hemisphere, often to the right, or sometimes to the left, of the mean wind. They usually produce large hailstones, and sometimes tornadoes.

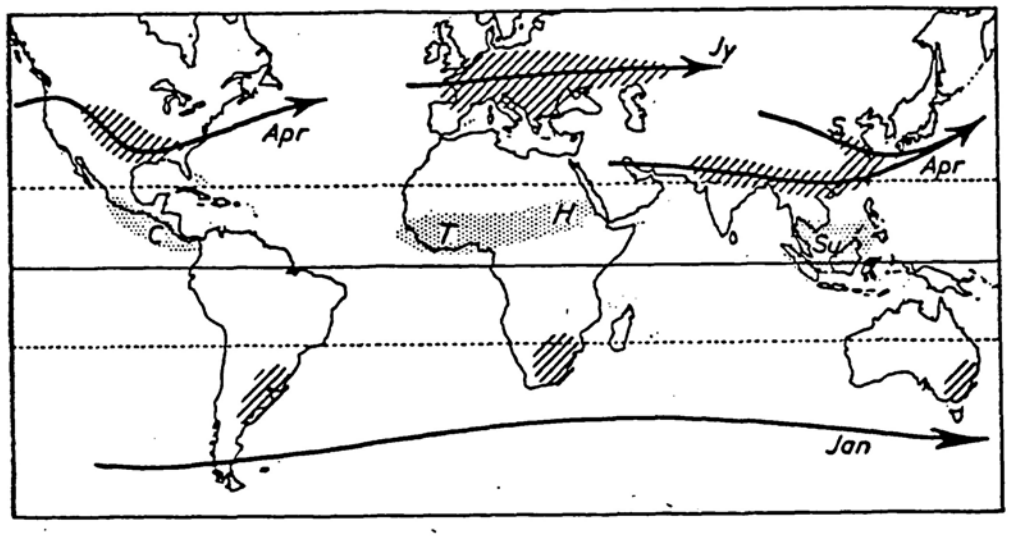


Fig 2.1. Distribution of Severe Local Storms (from Ludlam 1963).

In middle latitudes (hatched regions), the storms usually produce large hailstones and sometimes tornadoes. They are closely related to the mean position of the strongest winds in the middle troposphere during the severe local storm season (broad arrows)

In low latitudes (dotted regions), the storms only very exceptionally produce large hailstones. They mostly occur where the inter - tropical convergence zone becomes sharply defined and accompanied by a considerable lower level wind shear. The storms are known locally as chubascos (C), disturbance lines, line - squalls or tornadoes (T), haboobs (H), and sumatras (Su).

The tropical SLS's occur in the regions shown dotted: Malaysia (where they are known as sumatras, denoted Su); West Coast of Central America (where they are known as chubascos, C); Sudan (where they take the form of haboobs or dust storms, H); and West Africa (where they are variously called disturbance lines, line - squalls or tornadoes, T). This list is not however exhaustive, as they have also been studied recently in the Central Pacific (Line Islands) and near the north coast of South America (Barbados and Venezuela), references for which will be given in section 2.2.3. These tropical storms mostly occur where the inter - tropical convergence zone becomes sharply defined and accompanied by a strong middle level jet (next section). They move at a speed around or slightly greater than the maximum middle tropospheric wind speed, and hardly ever produce hail or tornadoes (in spite of the use of this name for them in West Africa).

The difference in properties of SLS's between middle latitudes and the tropics may be related to the different wind profiles which, according to Ludlam (1963), result in different storm structures, illustrated crudely in fig 2.2. In middle latitudes (fig 2.2a), SLS's occur in situations where wind speeds increase more or less steadily with height. The greater wind speed aloft means that updraught air originating at low levels ahead of the storm will flow out at upper levels also ahead of the storm giving rise to a cirrus anvil which points forward; the downdraught air will similarly remain behind the storm, with the storm itself moving at a speed very near to that of the mean wind. In the tropics however (fig 2.2b), there is a low - level jet rather than strong upper level winds. Updraught and downdraught will, in this case, both originate ahead of the storm and both flow out behind, with the result that the anvil trails behind; a storm speed near to, or greater than the strongest tropospheric wind speed is now possible.

The differing structures could also account for the difference in production of large hail. In middle latitudes, embryo hail originating in the updraught could fall back into the updraught and be recycled, whereas in the tropics it would fall into the downdraught and be swept out. Browning (1977) however stated that recycling can only occur in supercells (next section), and it is the absence of these in the tropics which accounts for the difference, whilst Sulakvelidze et al (1970) and Gokhale (1975) discounted the recycling mechanism altogether, preferring one dimensional models in which growth takes place under favourable

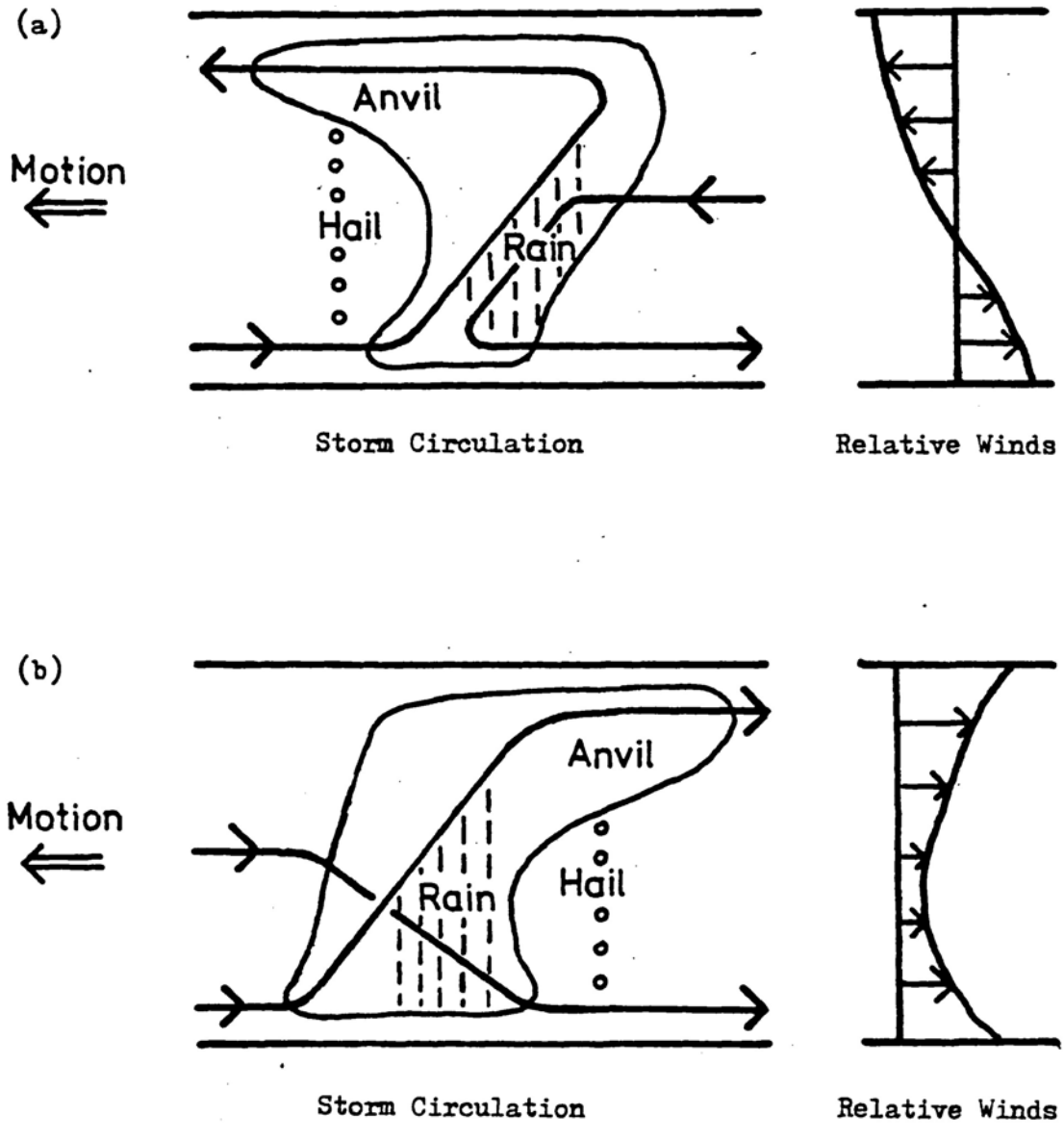


Fig. 2.2. Storm - relative circulation in severe local storms, after Ludlam (1963; simplified).

(a) Middle latitude case: storm moves at middle level environmental wind speed, anvil projects forward.

(b) Tropical case: storm moves faster than environmental wind at any level, anvil trails behind.

thermodynamic conditions. In any case, it should be noted that the two-dimensional structure is an over-simplification: in the tropics, three-dimensionality is required for crossing over of airstreams, while in middle latitudes, account has not been taken of rotation of environmental wind with height, or of motion to the right or left of the mean wind, which again dictate a three-dimensional structure (Browning 1964).

2.1.3 Cellular Structure of Severe Local Storms.

A cell is, according to Browning (1977) 'a dynamical entity characterised by a compact region of relatively strong vertical air motion which can be identified by radar from its associated volume of relatively intense precipitation'. Browning, modifying a classification of Marwitz (1972), suggested that hailstorms, which include most middle latitude SLS's, fall into three categories: unicellular storms, multicell storms, and squall lines, as follows.

(a) A unicellular SLS consists of a single cell of long duration - the supercell. This has a single updraught/downdraught circulation which persists for several hours in a quasi-steady state. In the Northern Hemisphere, supercells normally rotate and move to the right, sometimes to the left, of the mean wind; sometimes a pair of right and left moving supercells, with the right cell the stronger is formed by splitting of a single supercell. Browning (1977) suggested that much of the large hail and tornadoes in the United States is due to supercells.

(b) A multicell storm consists of a number of cells, with successive cells usually forming on the right flank of the storm and dissipating on the left, so that the storm as a whole propagates to the right in a discrete way. Individual cells are usually ordinary cells as described by Byers and Braham (1949) which, in less than an hour go through a sequence of cumulus stage (updraught only), mature stage (updraught and downdraught) and dissipating stage (downdraught only); according to Browning (1977) they may instead be supercells. Supercell storms usually begin and end life as evolving multicell storms, as for example the Wokingham storm (Browning 1962).

(c) A squall line is defined in Huschke (1959) as 'any non-frontal line or narrow band of active thunderstorms (with or without

squalls*)'. According to Browning's classification, the squall line differs from the multicell storm in that the line elements are laterally aligned, and tend not to interfere disruptively with one another by competing for the same moist air.

In the tropics, the first two categories of SLS appear to be absent. Squall lines do however occur, and may take the form of stationary lines of cumulonimbus, not accompanied by squalls, as reported over the GATE area by Mansfield (personal communication), or of lines which propagate at a speed near to, or slightly greater than the maximum tropospheric wind speed, and are almost always accompanied by squalls. Only these latter travelling squall lines which are accompanied by squalls qualify as true SLS's, and it is with them that this study will be primarily concerned (the special case of the haboob will not be considered).

What determines which type of SLS will occur? Since thermodynamic profiles are apparently the same in all cases, the answer presumably lies in the wind profiles. Considering first middle latitudes, both supercell and multicell SLS's form in regions of strong shear throughout the troposphere; they differ however in that whilst the mean subcloud wind for supercells is greater than 10 m/s and is backed by more than 60^{o} from the tropospheric mean wind, the mean subcloud wind for multicells is less than 5 m/s and is in much the same direction as the tropospheric mean (Marwitz 1972). Idealised wind hodographs due to Chisholm and Renick (1972) are shown in figs 2.3a,b. According to Browning (1977), profile 2.3a, with its low-level directional shear, favours the supercell since it permits a greater low-level storm-relative inflow kinetic energy, which helps to maintain a steady updraught.

An idealised hodograph for a tropical squall line is shown in fig 2.3c. This is based on a mean pre-squall sounding at Minna in Nigeria (fig 3.12), but terminated at 10 km owing to the large differences between West African and South American soundings above this level. It shows a clear middle level jet, and very little turning

* A squall, according to Huschke is 'a strong wind characterised by a sudden onset, a duration of the order of minutes, and a rather sudden decrease in speed. In U.S. observational practice, a squall is reported only if a wind speed of 8 m/s or higher is sustained for at least two minutes (thereby distinguishing it from a gust)'

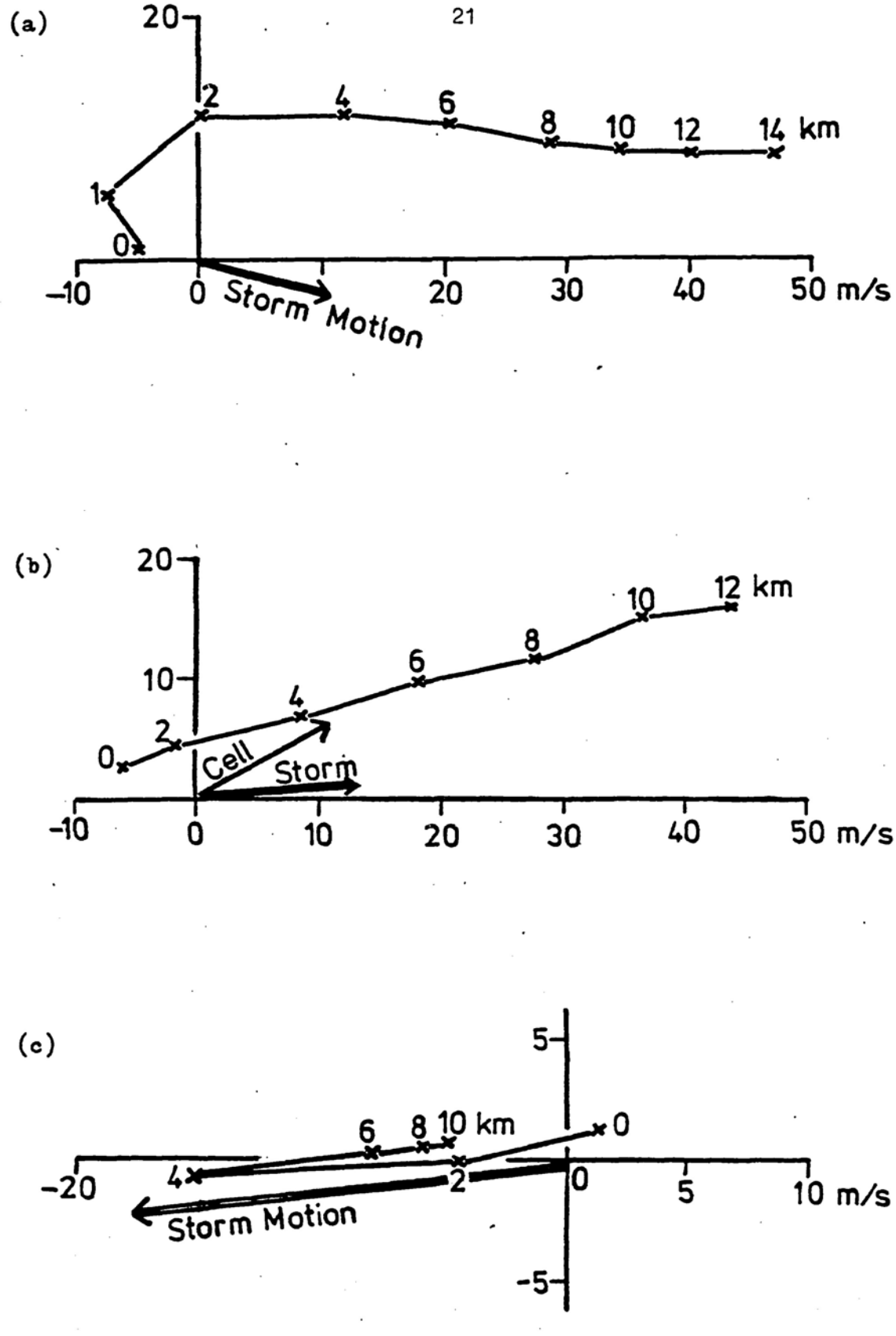


Fig. 2.3. Typical wind hodographs for (a) Supercell storm (b) Multicell storm (after Chisholm and Renick 1972) (c) Squall line (based on mean sounding at Minna, Nigeria)

Storm motion is denoted by a double arrow. Note that (c) is terminated at 10 km, and is on a different scale from (a) and (b).

with height, propagation being at roughly the jet speed. Zipser (1977) pointed out that this situation is also true of some middle latitude squall lines, a fact which is not always evident in published work; for example, Moncrieff and Green (1972), in using an Indian 'Nor'wester' squall line as a study of a case with unidirectional shear, failed to point out that there is a wind maximum at 600 mb, and that the squall line moved at this maximum speed. It could therefore be speculated that all travelling squall lines are associated with a strong middle level wind maximum, and move at a speed near to or slightly greater than the maximum speed; further investigation of this point is however required.

2.2 TRAVELLING SQUALL LINES.

The term squall line (SQL) will henceforth be assumed to refer only to travelling squall lines, i.e. those squall lines (other than haboobs) occurring in the tropics and sometimes in middle latitudes which are associated with a middle level jet, and move at roughly the jet speed. Various observations of these SQL's will now be presented.

2.2.1 Surface Observations.

Hamilton and Archbold (1945) described the appearance to a surface observer of the West African 'disturbance line', a term which they used to cover anything from banks of heavy cloud to belts of thunderstorms. Their description, which forms the basis of the following account is broadly applicable to SQL's everywhere.

The first indication of approach of a SQL is a dark heavy bank of cumulonimbus, with tops often reaching 9 km, or even higher, accompanied by lightning and thunder. At the forward edge of the cloud base there is a well-marked roll of low cloud extending from roughly 200 m to 1 km.

Just before arrival of the roll cloud, the wind, previously south westerly, falls calm, and as the roll cloud passes overhead, there is a sudden squall from between S.E. and N.E., commonly gusting 15 - 20 m/s at Lagos, though gusts in excess of 25 m/s occasionally occur in Northern Nigeria. Two or three minutes later, a heavy downpour of rain sets in. At the same time the cloud base becomes ragged and very low, say 100 - 200 m high over land, but the base may well be so indefinable that it can be considered to be at the surface; this is frequently the case at sea.

The rate of rainfall at first is often about 1 mm per minute, a fall of 20 mm in the first 15 minutes, followed by 10 mm in the next 15 minutes being quite common. The wind is squally when the rain is heavy, and moderates with the rain. The zone of squally winds, heavy rain and low cloud has a thickness of about 50 km.

Behind this zone, the low cloud lifts and gaves way to strato-cumulus at 300 - 600 m, which may soon clear. Above is a complete cover of altostratus with base usually as high as 3 km, often 4 km, from which light rain falls. About 2 or 3 hours after the beginning of the storm, the rain ceases entirely, and the surface wind falls calm, or even begins once more to blow lightly from S.E. to S.W. After another hour, the medium cloud lifts further and begins to break.

The forward edge of the SQL is usually taken to be the point of the first wind gust. Its arrival is accompanied by a temperature drop, the magnitude of which depends on the location and time of day - inland in the afternoon there may be a fall of 10°C, but there will be little change in the morning. With the temperature drop, relative humidity will approach 100%, though mixing ratio will fall, often attaining its lowest value after several hours, by which time the temperature is beginning to recover (Zipser 1977). With the onset of the rain a few minutes after the first gust, there is a pressure jump which may be as high as 3 mb inland, though 1 mb is more usual; later, pressure falls below its pre-squall level (allowing for diurnal variation).

A single observer would have difficulty in telling the difference between a SQL and an isolated thunderstorm, which may have practically all the characteristics just described. What distinguishes the SQL is its greater extent, which is only apparent when reports from a network of stations are analysed. Then the forward edge, as identified by the first gusts, will normally be seen to form a convex arc, which also marks the position of the squall front (pseudo-cold front); behind this is a mesohigh, followed by a mesolow, associated with the pressure changes which were noted.

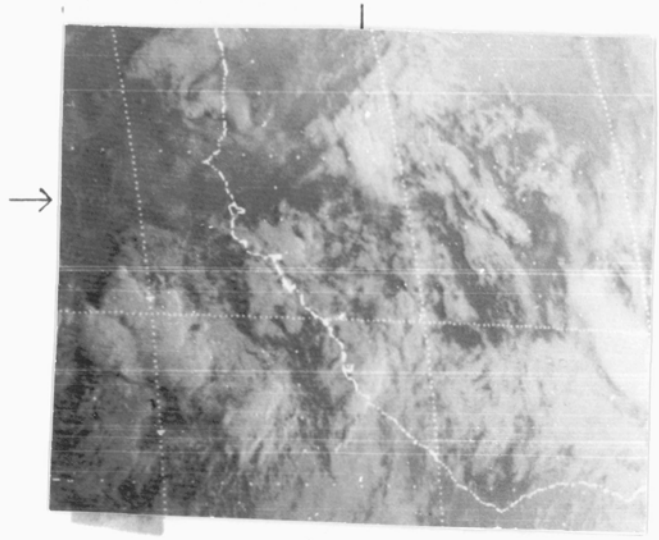
Different workers disagree as to where the boundary lies between the isolated thunderstorm and the SQL. Hamilton and Archbold (1945), whilst believing that the difference is just one of north - south extent, regarded only the largest disturbances as true SQL's, and talked of intermediate cases, such as those over Nigeria which strike

Bida, Minna and Kaduna at about the same time in the evening, then reach Yelwa subsequently at a time consistent with the usual speed of SQL's. Eldridge (1957) on the other hand made no such distinction, and regarded as a SQL any phenomenon of the thunderstorm or squall type which appears on the synoptic charts to move across the area with a degree of regularity. Some of the statistics which they obtained are presented in section 2.3.3.

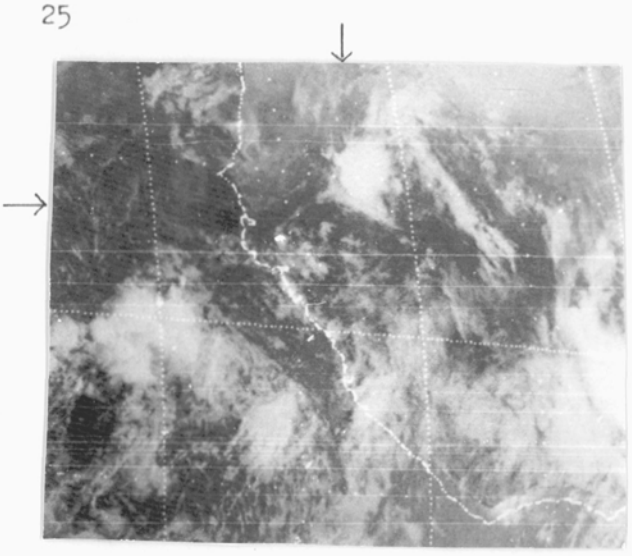
2.2.2 Satellite Observations.

Satellite images are a valuable supplement to surface reports in establishing the motion and mesoscale structure of SQL's. SQL's may be identified in both infra-red and visible images as distinct cloud masses characterised by explosive growth, high brightness, and a generally convex leading edge. Payne and McGarry (1977) only included those cloud masses which achieved areas of at least 1° square, and had lifetimes of at least six hours. Along the leading edge, according to Fortune (1977), the roll cloud can sometimes be seen, detached from the main cloud mass, as a low level feature on the visible image only; behind, the main cloud mass sometimes has points of brilliance visible, while its rear edge is generally rather indistinct and fibrous. These features are clearly evident in the sequence of visible images on 5 September 1974 (fig 2.4) of the principal SQL of a family (fig 2.5) which occurred over West Africa during a 48 hour period and were studied by Fortune (1977, 1980).

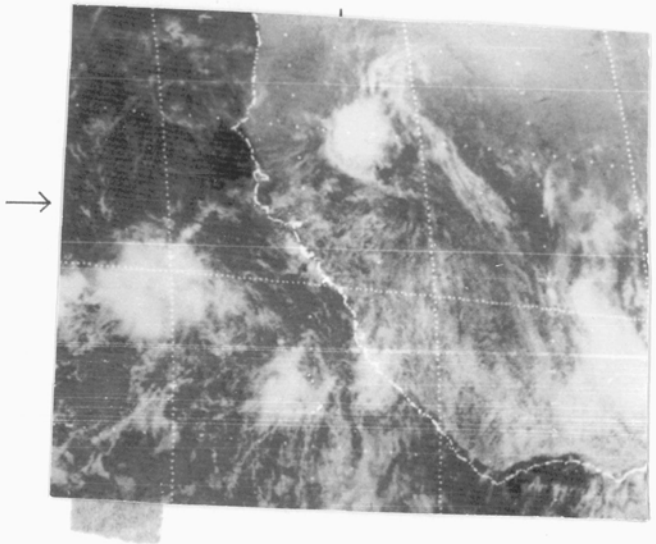
Latrasse (1972) classified SQL images into two types depending on whether there is a single or double arc. Gurka (1976) however, using both visible and enhanced infra-red images identified four types (fig 2.6) depending on the relation of the arc front to the main cloud mass. Type 1, with the arc-shaped forward edge to the main cloud mass corresponds most closely to Fortune's description above; the image in type 2 has a comma shape, with the roll cloud detached from the main cloud mass; in type 3, convective cells are actively growing along the arc front, whilst in type 4, applicable mainly to decaying systems, the arc front contains only older clouds with uniform tops. Gurka also found that the speed of the squall front is very nearly equal to the maximum surface gust. Though Gurka's categories were deduced from study of thunderstorms in the United States, Fortune (1977) stated that all the types have been observed in images of West African SQL's; fig 2.4 exhibits a progression from type 2 to type 4.



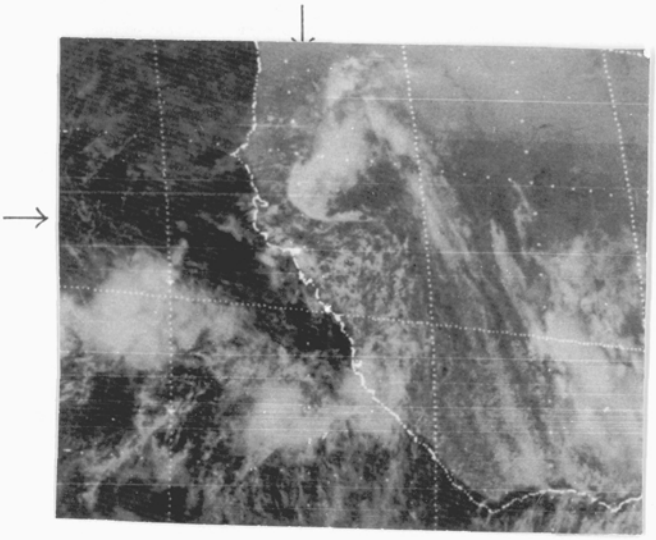
(a) 0800



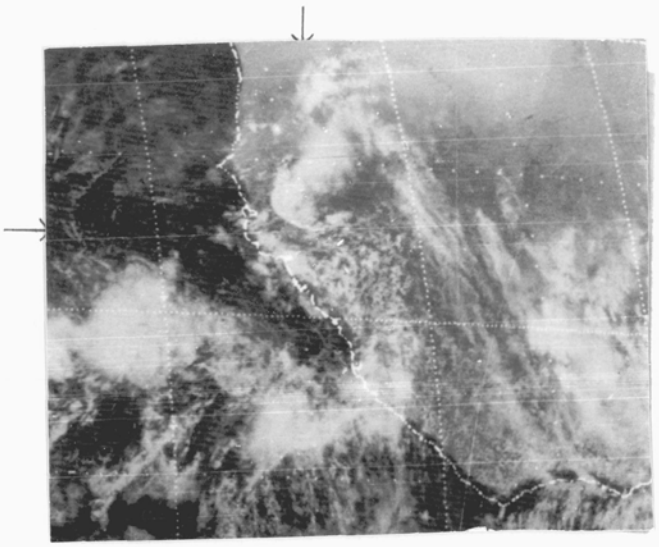
(b) 0930



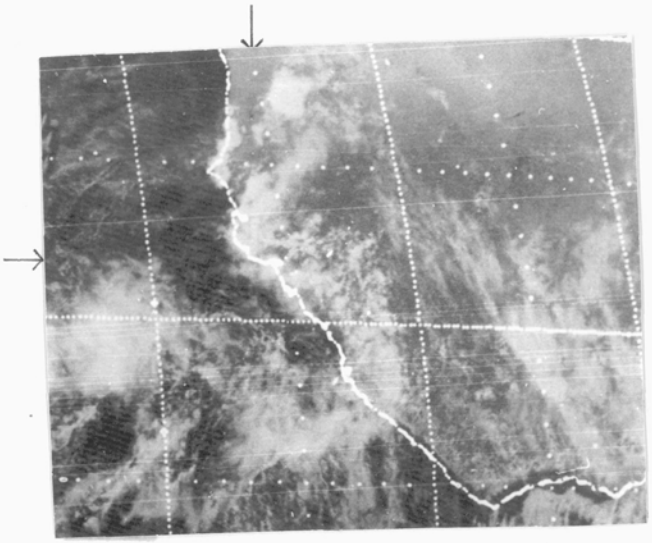
(c) 1100



(d) 1230



(e) 1400



(f) 1530

Fig 2.4. The 'Fortune' squall line of 5 September 1974. Visible Synchronous Meteorological Satellite images over West Africa at 1½ hour intervals. Arrows indicate position of squall line.

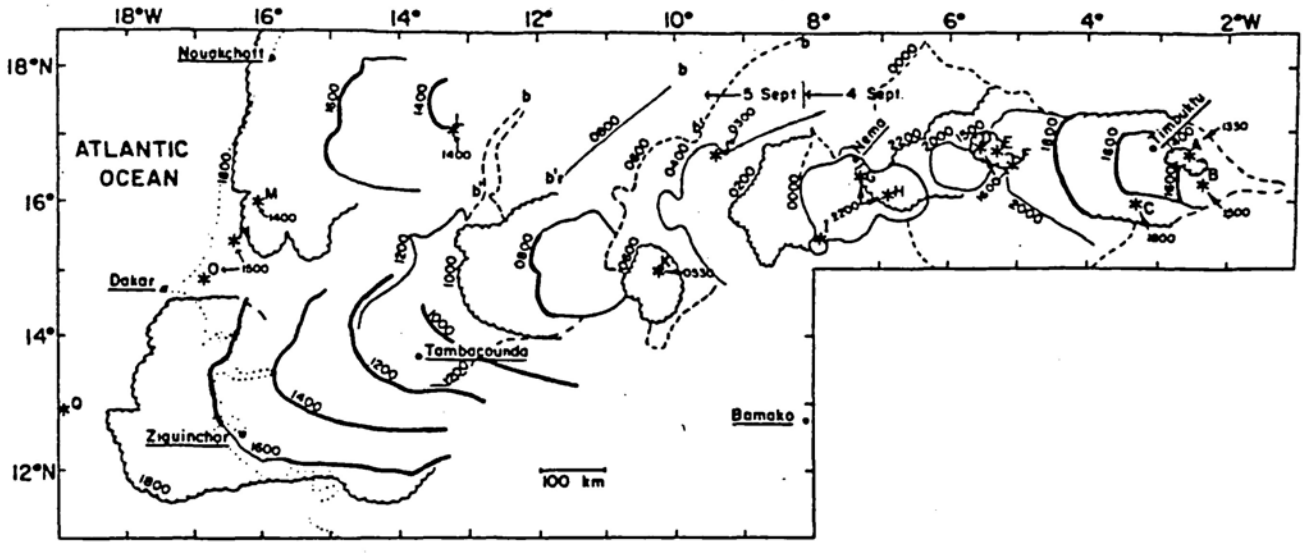


Fig 2.5. The 'Fortune' family of squall lines, 4 - 5 September 1974 (from Fortune 1980). Asterisks mark the point of origin of the squall line elements A - Q, with the hour of origin indicated. Alternating scalloped and thin lines are the leading edge of the anvil cloud at 2 hour intervals. Thick solid curves mark the position of the arc front on the visible pictures. Dashed lines outline the anvil every 6 hours. The arcs to the west of point K are the principal squall line, shown in fig 2.4. Line b-b' is a long-lived but dormant arc of middle cloud.

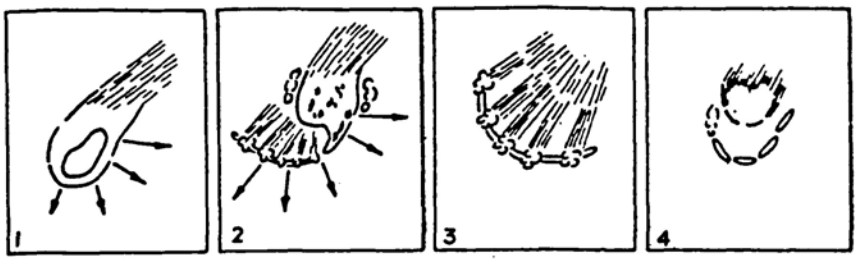


Fig 2.6. Classification of squall lines in satellite imagery into four types according to Gurka (1976).

A final category may also be noted in which the cloud mass extends forward of the squall front, so that there is no longer a clear leading edge. This, according to ASCENA (1974) is an indication that the storm is weakening.

2.2.3 Recent Intensive Observations

Recently a number of intensive studies of SQL's have been made in which surface observations have been supplemented by use of radar, radiosonde ascents, aircraft traverses and/or satellite data. Several of these studies will be listed, and some of their findings presented, paying particular attention to atmospheric soundings in order to set the scene for the Nigerian results obtained in chapter 3. The results which are presented will be mainly those which throw light on features common to all SQL's; for a detailed comparison of SQL's in different locations, the reader is referred to Fernandez (1981).

(a) Line Islands Experiment, February - April 1967. Zipser (1969) studied a SQL which crossed the region on 1 April 1967; his time-height section for Palmyra is shown in fig 2.7. The SQL moved at about the maximum wind speed, and the wind section shows an increase in low level shear on arrival of the SQL, with return to previous conditions in roughly six hours. Behind the squall front, air between 900 and 800 mb has very low values for θ_E which, Zipser concluded, indicates that it originated in the middle troposphere (600 - 400 mb), and descended in unsaturated mesoscale downdraughts.

(b) Barbados Experiment, 1968. Here one SQL was observed, and it was analysed by Zipser (1977). This SQL moved faster than the wind at any level, though opposite ends of the arc front were nearly at right angles, and moving at noticeably different speeds. Zipser gave post-squall soundings of temperature T and dew-point T_d in this and several other cases (fig 2.8); they show a characteristic 'onion' shape. At the surface is a layer of cool saturated air, typically 150 - 400 m deep, which must have descended in intense rain-cooled saturated convective-scale downdraughts (these would be 10 - 12 km wide with vertical velocities of order 1 - 10 m/s); this saturated layer is deepest near the squall front, which is consistent with the observed greatest pressure there. Above this surface layer, the bulge of the 'onion' is associated with a large dew-point depression around 900 mb, indicating warm air with a relative humidity which may be as low as 50% - a clear indication of descent in a gentler mesoscale downdraught

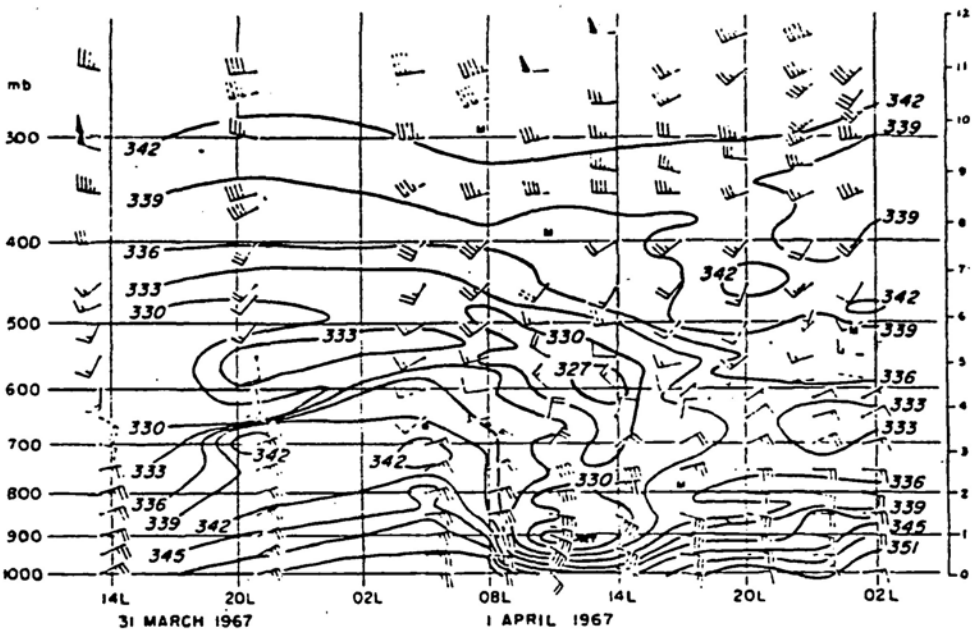


Fig 2.7. Time-height section at Palmyra during Line Islands Experiment showing arrival at 0800 on 1 April 1967 of squall line moving from 120° at 15 m/s (from Zipser 1969).

Rawinsonde winds are plotted in the conventional manner, with each full barb representing 5 m/s; dashed wind arrows represent reduced confidence in that observation. The contours are of equivalent potential temperature θ_E K.

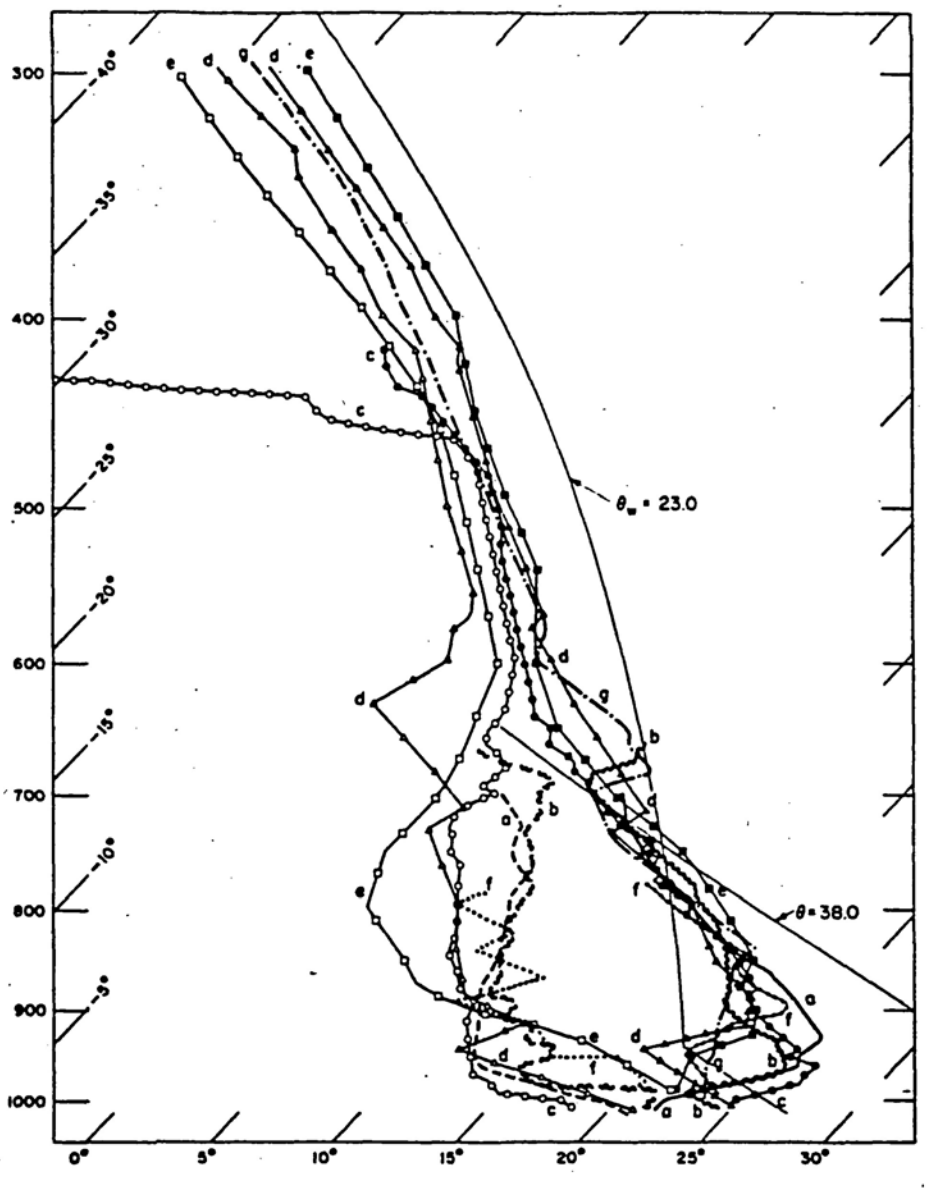


Fig 2.8. Tephigram showing T, T_d for various post-squall soundings (from Zipser 1977).

(a) GATE Queen Air sounding, mostly in rain, 5 September 1974.

(b),(c),(d) Various GATE oceanic soundings, 12 September 1974.

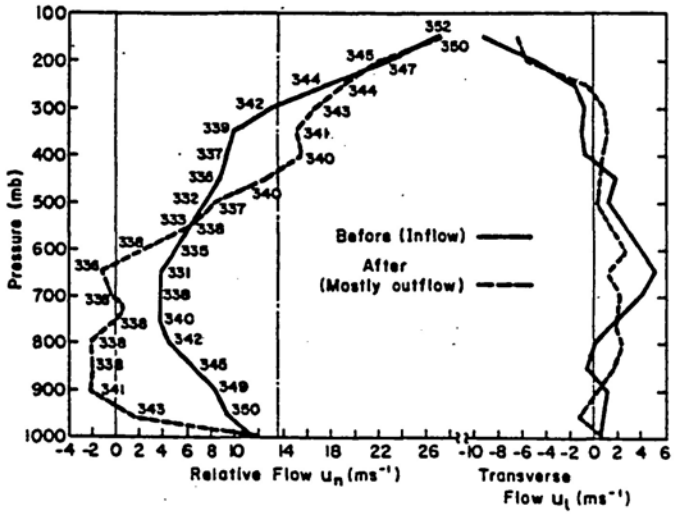
(e),(f) Venezuelan soundings, 28 August 1969.

(g) Barbados sounding (no T_d available), 18 August 1968.

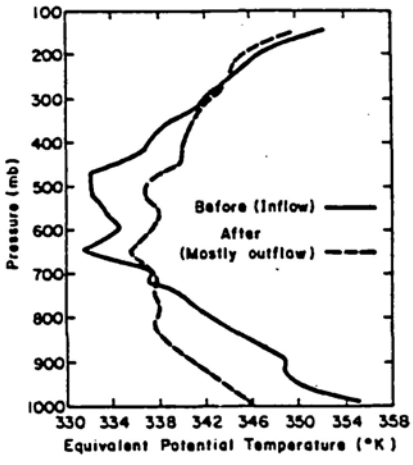
(of width 100 - 500 km, with vertical velocities typically 10 cm/s); the mesoscale descent is dynamically forced (Miller and Betts 1977), though evaporation of rain falling from the anvil may also play a part (Zipser 1969) (see section 4.4.3). Finally, around 600 mb, the dew-point depression is again small, indicating the probable location of the base of a deep cloud layer - the anvil.

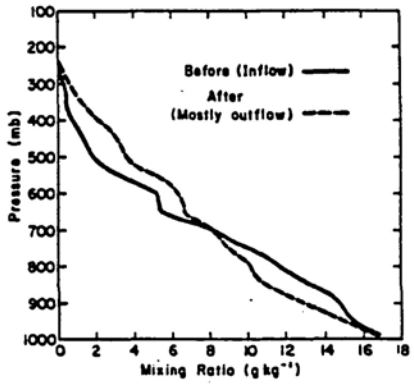
(c) VIMHEX: Venezuelan International Meteorological and Hydrological Experiment, June - September 1972. Betts, Grover and Moncrieff (1976) identified seven SQL's over Venezuela, and fig 2.9 shows the mean modification to the environment by four of them. Here and in the studies which follow, the speed of the SQL was greater than that of any pre-squall wind, so that winds relative to the storm show inflow at all levels beforehand; all the studies also show increase of relative flow at low levels, indicating up-gradient momentum transfer (Moncrieff and Miller 1976), and weak transverse flow, which nevertheless shows a change, indicating that three-dimensional structure is important. Venezuelan features which are not shared by the other studies are a single reversal of the shear at 700 mb in the pre-squall sounding, and some inflow behind the SQL (950 - 650 mb), the origin of this inflow air being unclear. Before the SQL, according to Miller and Betts (1977), the lowest 150 mb (the subcloud layer) is moist and well-mixed; afterwards this layer is cooled and stabilised, and mixing ratio is decreased up to 700 mb, the associated decrease in θ_e indicating descent. Above 700 mb the air is moistened, indicating ascent in updraughts; the moistening almost balances the lower-level drying, suggesting that the convergence of moisture into the system almost equalled the rainfall.

(d) Compositing of Nigerian Observations. Before dealing with other West African studies, mention should be made of the use of compositing, a technique which can be applied to data from routine observations in sparsely covered regions, where SQL's will typically pass only one station at which a sounding is made. The distance of this single sounding ahead of or behind the squall front is computed from the speed of the SQL and the time at which it reached the station, and thus the sounding may be plotted on a vertical section at an appropriate distance from the squall front. Soundings for other SQL's may be similarly entered, and, assuming the variation between different SQL's is not too great, a representative section perpendicular to the squall front will be obtained. Such a study was made at Lagos, Nigeria in 1962 by Obasi (1976), who emphasised the importance of SQL's by



(a) (b)





(c) (d)

Fig 2.9. Mean modification to the environment for four squall lines during VIMHEX (from Betts, Grover and Moncrieff 1976).

(a), (b) Storm-relative flow (a) along and (b) transverse to motion of squall line (mean motion from 080° at 13.6 m/s, represented by dash-dot line).

(c) Equivalent potential temperature θ_e.

(d) Mixing ratio r,

estimating that in West Africa they provide 40% of the annual rainfall, and that their mean annual latent heat release amounts to 25% of insolation. Obasi's temperature and humidity sections (not shown) indicate a cool moist surface layer, surmounted by a warm dry layer after passage of the SQL, as inferred by Zipser (1977). The wind fields (fig 2.10) show post-squall increases in easterly and northerly momentum at low levels, though they do suffer from considerable scatter, and from there being only four pre-squall soundings available.

(e) ASECNA: Agence pour la Securité de la Navigation Aerienne conducted two experiments, the later of which, Operation Pre-GATE ASECNA, 1 - 10 August 1973 was the more successful. Four disturbances were intensively studied making use of data from the existing station network in the Sahel; the results are published in ASECNA (1974, 1975). They plotted the paths of the disturbances and found instances of splitting and coalescence; the rainfall pattern was non-uniform, distributed in cores along the disturbance paths. Only two of the disturbances were regarded by ASECNA as genuine SQL's, but this distinction is questionable, being based on a detailed data study rather than on any obvious objective criterion. Riehl et al (1974), including all four disturbances as SQL's, presented some further data analyses. Their mean wind profile (fig 2.11a) does not, as in other studies, show a significant jet, though the SQL's did travel faster than the wind at any level. Two-dimensional relative wind fields at various levels were plotted for each SQL, those for 3 August 1973 (figs 2.11 b,c) being typical. Below 500 mb, flow was found to be cyclonic, as illustrated by the 850 mb field; in contrast the 200 mb field shows anticyclonic flow. Below 600 mb there was net convergence, of order 2×10^{-5} s^{-1} at the surface; above was divergence. The mean vertical velocity as found from this total divergence shows ascent everywhere (fig 2.11d); if however the zonal wind component alone is used (fig 2.11e), the resulting vertical motion is much smaller, and there is descent outside the main convective area. The majority of the convergence is hence in the north-south direction.

(f) GATE: Global Atmospheric Research Programme's Atlantic Tropical Experiment, June - September 1974. Mention has already been made in section 2.2.2 of the use of satellite data by Fortune (1977, 1980) to study a West African SQL over the land. Supplementing the satellite data with GATE radiosonde and aircraft data, Fortune (1980) was able to infer wind fields similar to those of Riehl et al (1974), and mass

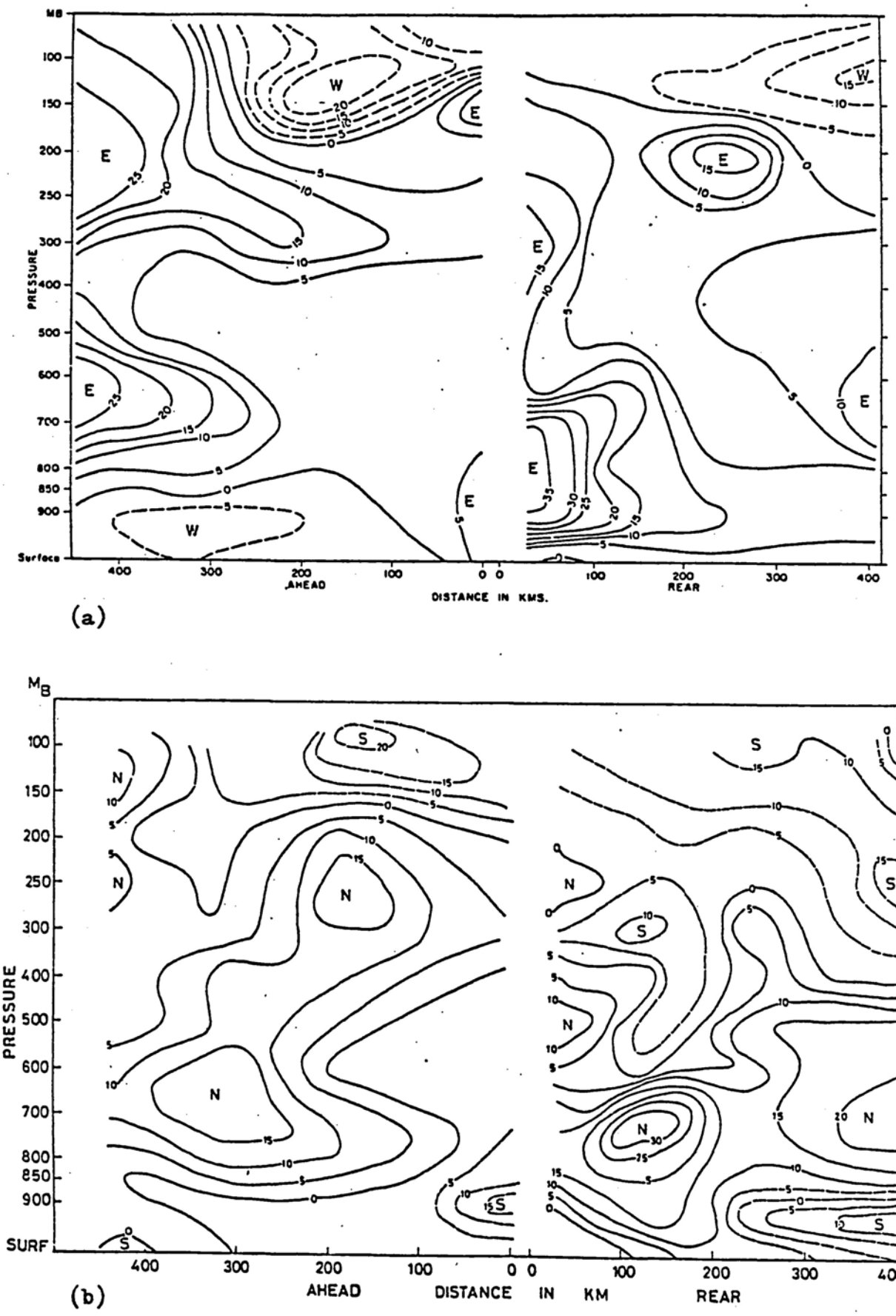
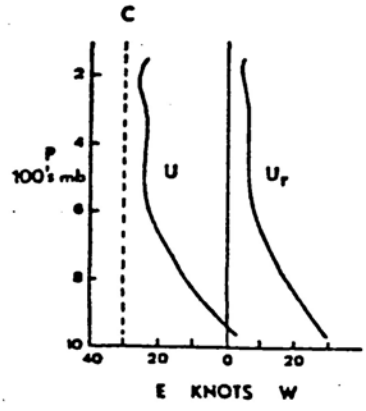
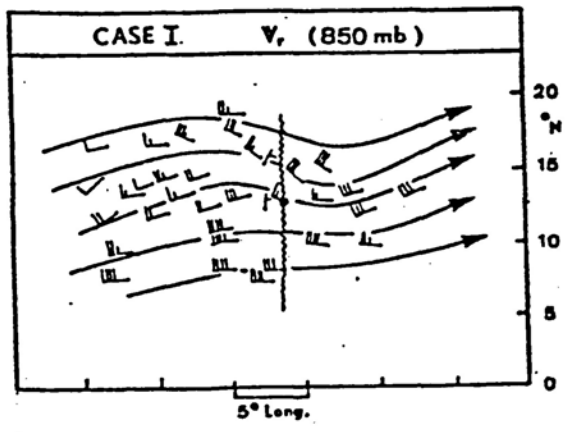


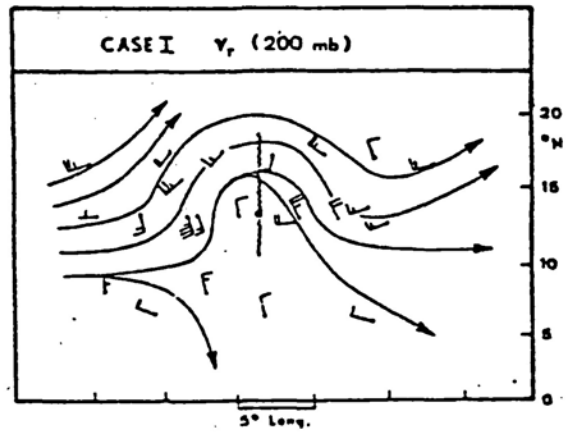
Fig 2.10. Composite vertical sections of (a) 'zonal' (b) 'meridional' wind component for squall lines at Lagos, Nigeria during 1962 (from Obasi 1976). 'Zonal' and 'meridional' refer to the components along and perpendicular to the storm motion; units are in knots.



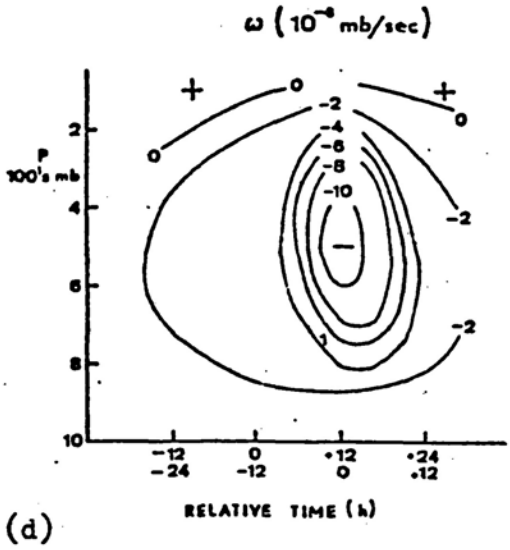
(a)



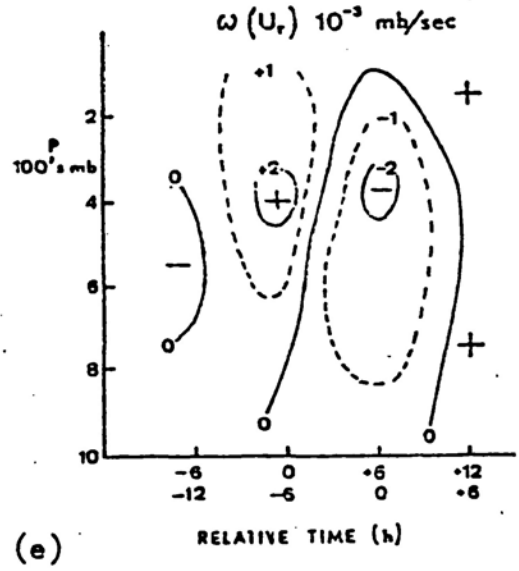
(b)



(c)



(d)



(e)

Fig 2.11. Some ASECNA results (from Riehl et al 1974).

(a) Relation between propagation speeds and actual and relative wind profiles (mean of 4 squall lines).

(b), (c) Relative winds at (b) 850 (c) 200 mb (3 Aug 1973 SQL only).

(d), (e) Vertical cross section of ω computed from (a) total (b) zonal horizontal divergences (mean of 4 squall lines).

fluxes. The latter indicate an upward transfer into the anvil of around 2×10^{10} kg/s, while both mesoscale and convective scale downdraughts have transfers from 1/10 to 1/5 as large; these mass fluxes exceed those in a tropical cloud cluster (see (ii) below), though cloud clusters affect a greater area.

Primarily however, GATE was concerned with study of convection over the sea, making use of ship and aircraft-based observations. Several studies of SQL's have made use of GATE data, including the following.

(i) Mansfield (1977) examined four SQL's which moved from NE at roughly 1 m/s faster than the maximum wind speed. His time-height sections for westerly and southerly wind components (fig 2.12) show a strong association between the occurrence of a SQL and of a strong 650 mb north-easterly jet. A second easterly jet is also present around 150 mb, though absent in Venezeula (fig 2.9).

(ii) The time development of a similar set of SQL's was considered by Frank (1978). He found that SQL's form in conditions of strong northerly wind component and vorticity at 700 mb, with weak convergence at low levels, divergence around 600 mb; as they mature, low level convergence increases, and development of deep upward motion causes the divergence peak to shift to 250 mb. Initially, temperatures are warm at the surface, cool at upper levels, while humidities are low around 600 mb; as the system develops, there is moistening at low levels, with some surface cooling, and rapid upper level heating, which Frank attributed to both latent heat release and absorption of solar radiation by cirrus (but see sections 2.3.1 and 3.3.1). Frank compared SQL's with cloud clusters, which are more loosely organised convective areas. Their divergence and thermodynamic fields are similar, but the wind profiles differ in that SQL's are associated with much stronger wind shear, especially at low levels (fig 2.13).

(iii) Houze (1977) carried out a detailed study of one of the SQL's, that of 4 September 1974. He gave time-height sections similar to those of Zipser (1969), accompanied by surface traces which show clearly the sudden onset of the squall front, and a recovery time of order 6 hours before pre-squall conditions are resumed, this recovery time being interpreted as the time taken for the anvil to clear. Houze made a detailed radar study of the SQL elements; he found that new line elements were generated ahead of the SQL, while

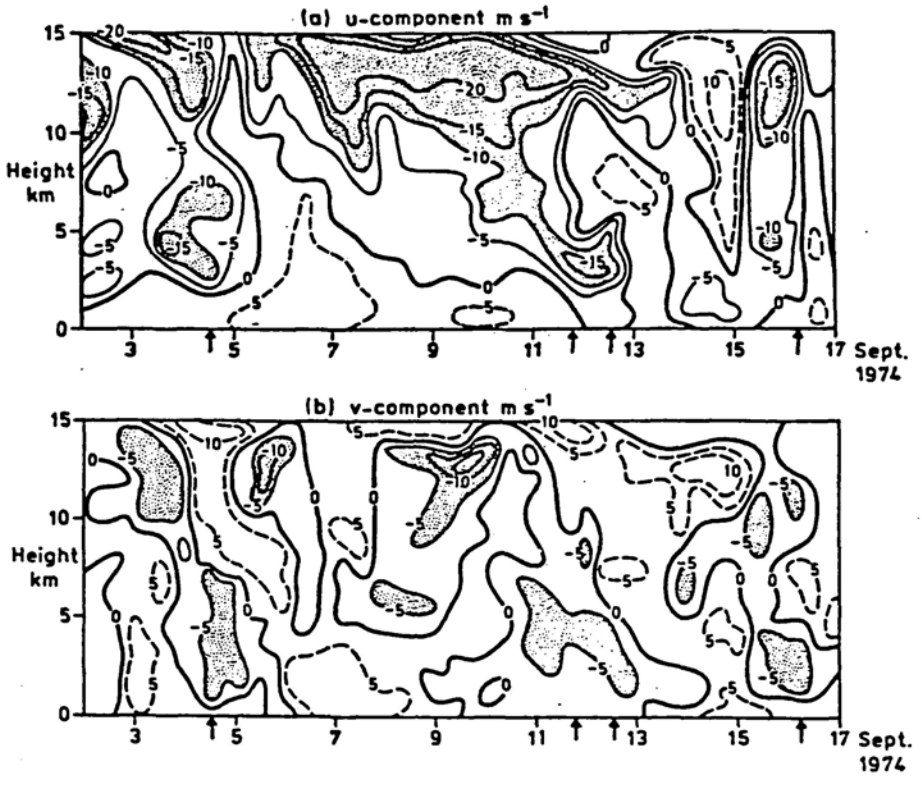


Fig 2.12. GATE time-height sections from Oceanographer of (a) westerly (b) southerly wind component. Arrows denote times of arrival of squall lines (from Mansfield 1977).

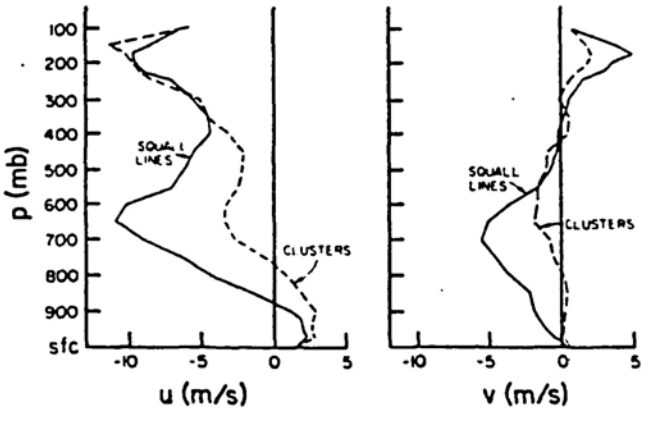


Fig 2.13. Mean GATE zonal winds u and meridional winds v for squall lines (solid line) and cloud clusters (dashed line) (from Frank 1978).

old ones dissipated to the rear and joined the anvil, leaving large quantities of moisture aloft to feed the anvil precipitation. The fact that 40% of the precipitation fell from the anvil suggested that it was sustained by organised ascent in the upper half troposphere.

2.2.4 Summary of Squall Line Structure.

Houze (1977) summarised his observations in a conceptual picture of the SQL, shown in fig 2.14. Betts (1978) used this picture to illustrate his review of present understanding of SQL structure, which is quoted below.

> 'Squall lines have relative inflow from the front as they propagate through the air. They move by discrete growth of new line elements ahead of old ones (Houze 1977). The growth of new cells is organised along the spreading gust front, itself fed by downdraughts from decaying cells (Moncrieff and Miller 1976). The high level outflow streams off to the rear, and precipitation from the anvil forms a large region of nearly stratiform rain behind the leading edge. There is some evidence of mesoscale ascent in the middle-upper troposphere, helping maintain the anvil, and good evidence of lower troposphere mesoscale descent under the anvil. It is not clear whether this mesoscale downdraught is primarily dynamically driven (Miller and Betts 1977) or driven by evaporation of falling precipitation (Zipser 1969, 1977). This mesoscale downdraught, which often is warm and dry by the time it reaches 900 - 950 mb, is undercut by cooler relatively moister downdraught air which probably descended in cloud-scale downdraughts in the squall line... The low-level mixed layer of high θ_E is swept up into the cloud and probably ascends with a little dilution to the upper troposphere. It is replaced by lower θ_E air, with a more complex structure resulting from cloud- and meso-scale downdraughts: a cool, moist layer underlying a warmer, much dryer layer. The inversion between the two layers caps the lower layer, which becomes well mixed over the warm ocean and grows into the sinking dry stable layer above by entrainment processes. The mixing down of drier air from the layer above means that the minimum 10 m dewpoint is reached some time after the passage of the squall front.'

2.3 SQUALL LINES IN WEST AFRICA

Attention will now be restricted to West African SQL's. The principal features of the large-scale flow will be outlined, bringing out aspects favourable to the occurrence of SQL's, and some studies will be presented.

2.3.1 Climatological Conditions.

Fig 2.15a shows the mean July surface streamline pattern over the African region, adapted from Riehl (1954). Two airstreams affect West Africa: from the S. Atlantic ocean comes the warm moist S.E.

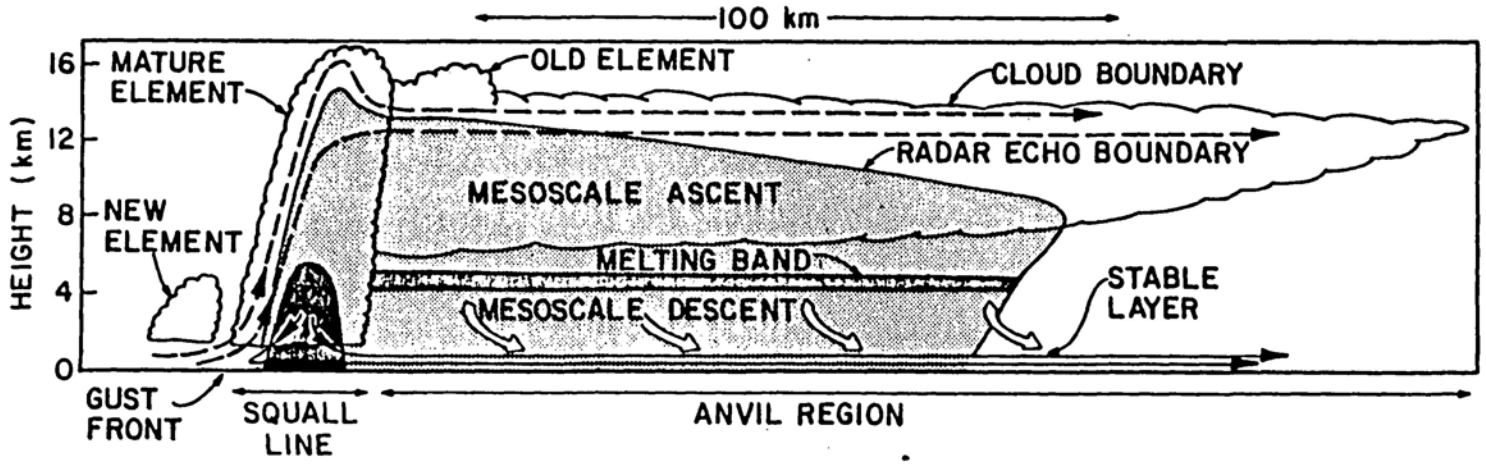


Fig 2.14. Schematic cross-section through squall-line system. Streamlines show flow relative to the squall-line. Dashed streamlines show updraft circulation, thin solid streamlines show convective-scale downdraft circulation associated with mature squall-line element, and wide arrows show mesoscale downdraft below the base of the anvil cloud. Dark shading shows strong radar echo in the melting band and in the heavy precipitation zone of the mature squall-line element. Light shading shows weaker radar echoes. Scalloped line indicates visible cloud boundaries (from Houze 1977).

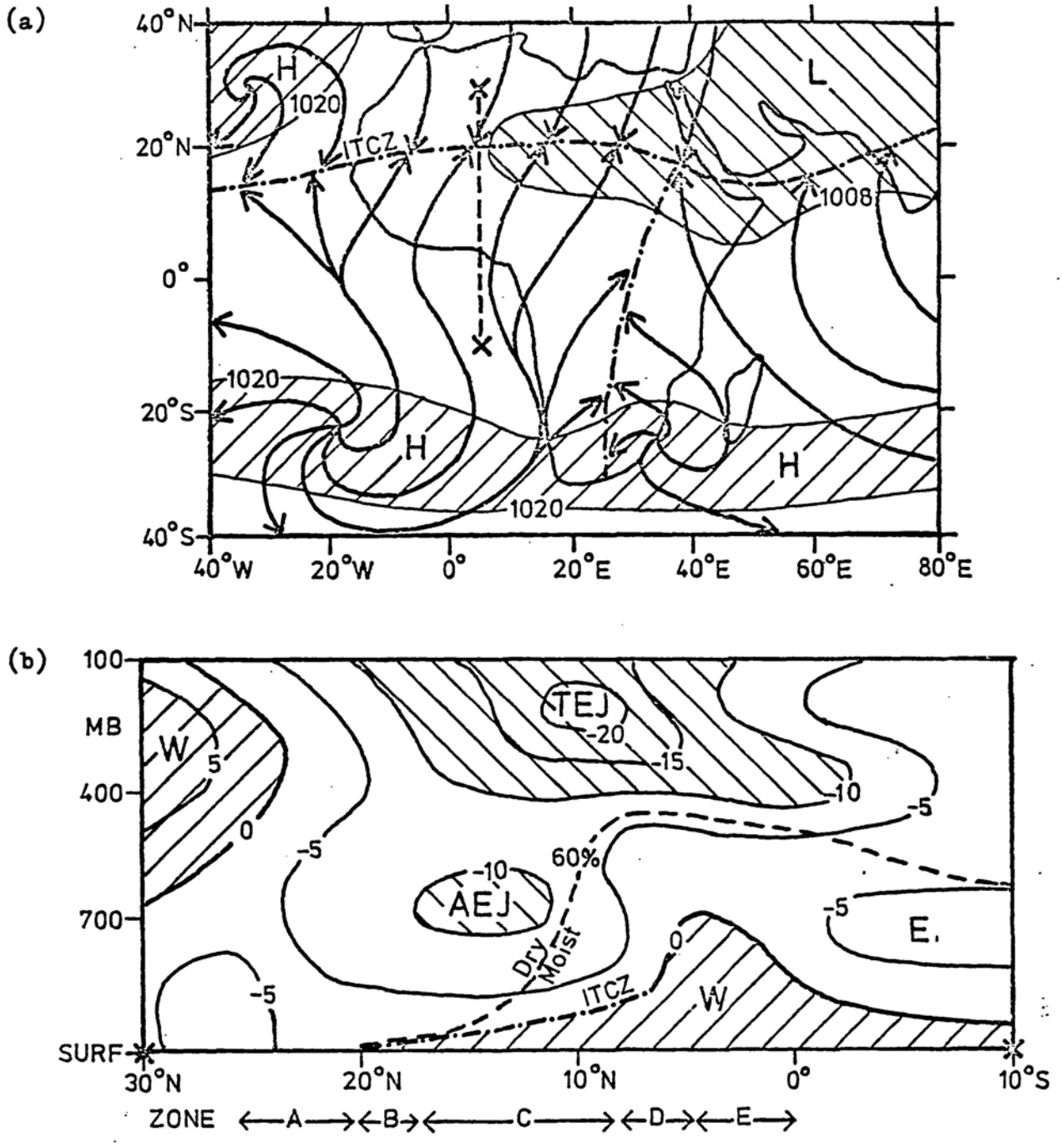


Fig 2.15. (a) Mean July surface pressure pattern and associated streamlines over Africa (adapted from Riehl 1954). Pressure is given in mb, dash-dot lines are confluence lines.

(b) Suggested vertical cross-section of zonal wind along line XX in (a) (adapted from August profile in Burpee 1972). Wind speeds are in m/s, with hatcing for all westerlies, and for easterlies over 10 m/s; boundary of dry air is located by 60% relative humidity contour.

monsoon current, which has become south westerly by the time it reaches the coast, while over the Sahara comes the hot dry north easterly 'Harmattan' air. The boundary between these two airstreams is variously known as the inter-tropical convergence zone (ITCZ), inter-tropical front or inter-tropical discontinuity; any of these terms may also refer to the intersection of this boundary with the surface, or the terms Equatorial trough or monsoon trough may be applied; here, ITCZ will be used throughout, context making the meaning clear. The ITCZ reaches its maximum northerly latitude in July or August, around 20°N as shown.

A north-south vertical cross section for West Africa at 5°E (along line XX in fig 2.15a) is given in fig 2.15b; this was adapted from the August section in Burpee (1972), and is broadly applicable for any longitude between 10°W and 35°E. In it, the sloping of the ITCZ indicates that the Harmattan air has risen over the cooler monsoon air, though south of 5°N the winds become light, and the transition ceases to be well defined. Near 20°N, the boundary of the airstreams is also the boundary between moist and dry air, as delineated by the 60% relative humidity contour (inferred from Reed et al 1977); further south however, low level moisture is mixed upwards by convection, with the result that the humidity boundary lies well into the easterly air.

Above the ITCZ are two easterly jets, the African easterly jet (AEJ) around 650 mb, and the tropical easterly jet (TEJ) around 150 mb. The AEJ is attributed by Carlson (1969a) to thermal wind balance: a temperature increase from 25°C over the S. Atlantic to 45°C over the Sahara produces strong easterly shear at low levels, whilst at middle levels, the shear reverses in response to a reversal of the temperature gradient. (The validity of the thermal wind balance so near the Equator is confirmed by several workers, for example Schove 1946, who found that for latitudes 5° - 15° N, wind shear is backed from the isotherms by about 20°.) The TEJ could be the result of a second reversal of the temperature gradient associated with upper level warming over the Sahara in the descending part of the Hadley circulation, coupled (Omotosho 1976) with cooling further south due to the greater infra-red emissivity of cloud tops as compared with clear air (though this cooling would be offset by the increased solar absorption during the day: see sections 2.2.3f and 3.2.2); conservation of angular momentum of air transferred south round the upper level Saharan anticyclone is another possible mechanism (Reiter 1963).

At other times of the year, the airflow pattern will move south,

with the ITCZ lagging about 1½ months behind the sun; the jets do however become much weaker. As the airflow pattern moves, the surface weather changes, and Hamilton and Archbold (1945) divided the weather into various zones, depending on position with respect to the ITCZ; these are shown at the bottom of fig 2.15b, as modified by Adejokun (1964). Zones A and B correspond to 'dry season' weather with convection limited to some high cloud, with small cumulus in zone B. Around 300 km south of the ITCZ, there is a change to 'rainy season' weather in zones C and D. Convection here takes the form of isolated thunderstorms and SQL's in zone C, steady monsoonal rain in zone D. Finally, at locations near the coast, the rainy season is interrupted by a 'little dry season', zone E, where convection is limited to small middle level cloud. This account is however rather idealised, the motion of the ITCZ in practice being distinctly irregular.

The restriction of SQL's to zone C can be explained by reference to the conditions needed for the occurrence of SLS's (section 2.1.1). Here alone the monsoon air forms a fairly shallow moist surface layer, with a stable layer above at the boundary of the hot dry middle and upper level Harmattan air. In addition there is considerable wind shear, with the middle level AEJ maximum favouring SQL's rather than other types of SLS. The role of the TEJ is less obvious, though it has been suggested that strong upper easterlies inhibit occurrence of SQL's by causing anvil outflow to the front at upper levels; this would cut off further solar heating and disorganise the storm by raining into the inflow (Dhonneur 1974). The data of section 3.3.1 support this inhibiting role of the TEJ.

2.3.2 Synoptic Perturbations.

Mention has already been made of the findings of Riehl et al (1974) that the SQL has cyclonic inflow at low and middle levels, anticyclonic outflow at upper levels. These results are confirmed by other studies including those of Schove (1946) and Okulaja (1970), whose emphasis however is on the associated trough. Whilst such synoptic features can arise from a variety of causes, one synoptic perturbation is of particular importance during the SQL season: the easterly wave.

Easterly waves over West Africa have been studied in detail by Carlson (1969 a,b), Burpee (1972, 1974, 1975), and by Reed et al (1977) and Norquist et al (1977). The waves here were found to originate around 20 - 30° E; their properties depended somewhat on the method of analysis used, but typical were: wavelength 2500 - 4000 km; period

3 - 5 days; speed 8 - 10 m/s. Their structure is perhaps most clearly revealed in the results which Reed et al (1977) obtained from combined GATE land and sea data, by compositing relative to the 700 mb vorticity maximum. Streamlines thus obtained for the total wind field are shown in fig 2.16. At the surface, two lines of confluence can be seen; the north-south line is associated with a maximum of low-level convergence, and above it at 850 mb is a clear cyclonic circulation; at 700 mb and 200 mb there is strong easterly flow with strong diffluence, and in fact divergence at 200 mb.

Fig 2.17 shows various perturbation vertical cross-sections along the central latitude, which suggest two energy sources for the waves. Barotropic conversion (of mean flow kinetic energy to eddy kinetic energy) is indicated by the strong correlation between westerly wind deviation from mean (fig 2.17a) and southerly wind deviation (not shown), which, since it occurs south of the AEJ maximum implies down-gradient momentum transfer; the correlation of upward motion (fig 2.17b) with positive temperature deviation (fig 2.17c) on the other hand indicates baroclinic conversion (of eddy available potential energy to eddy kinetic energy). Rennick (1976) and Simmons (1977) in recent numerical models found that the barotropic conversion was the more important. Norquist et al (1977) confirmed this observationally over the ocean, but over the land they found that baroclinic conversion predominates; the necessary eddy available potential energy was then only partly supplied from zonal available potential energy generated by the strong Saharan heating, the remainder, they suggest being due to latent heat release. SQL's would make an important contribution to this release, especially further north, and it is significant that the mean latitude of the 700 mb vorticity maximum for the easterly wave, and the mean latitude of SQL generation are both around 12^{o}N.

An association between SQL's and easterly waves is thus suggested, and has indeed long been recognised, though the connection is not altogether clear (that they are distinct entities is evidenced by the fact that SQL's move roughly twice as fast as easterly waves). According to Okulaja (1970), each easterly wave has a SQL associated with its zone of convergence and vice-versa. Fortune (1977) suggested that the SQL which he studied originated in a region of synoptic-scale forcing, but that it eventually grew to dominate the synoptic environment, at which point it was located at an easterly wave trough.

Perhaps the clearest indication of the relationship between SQL's

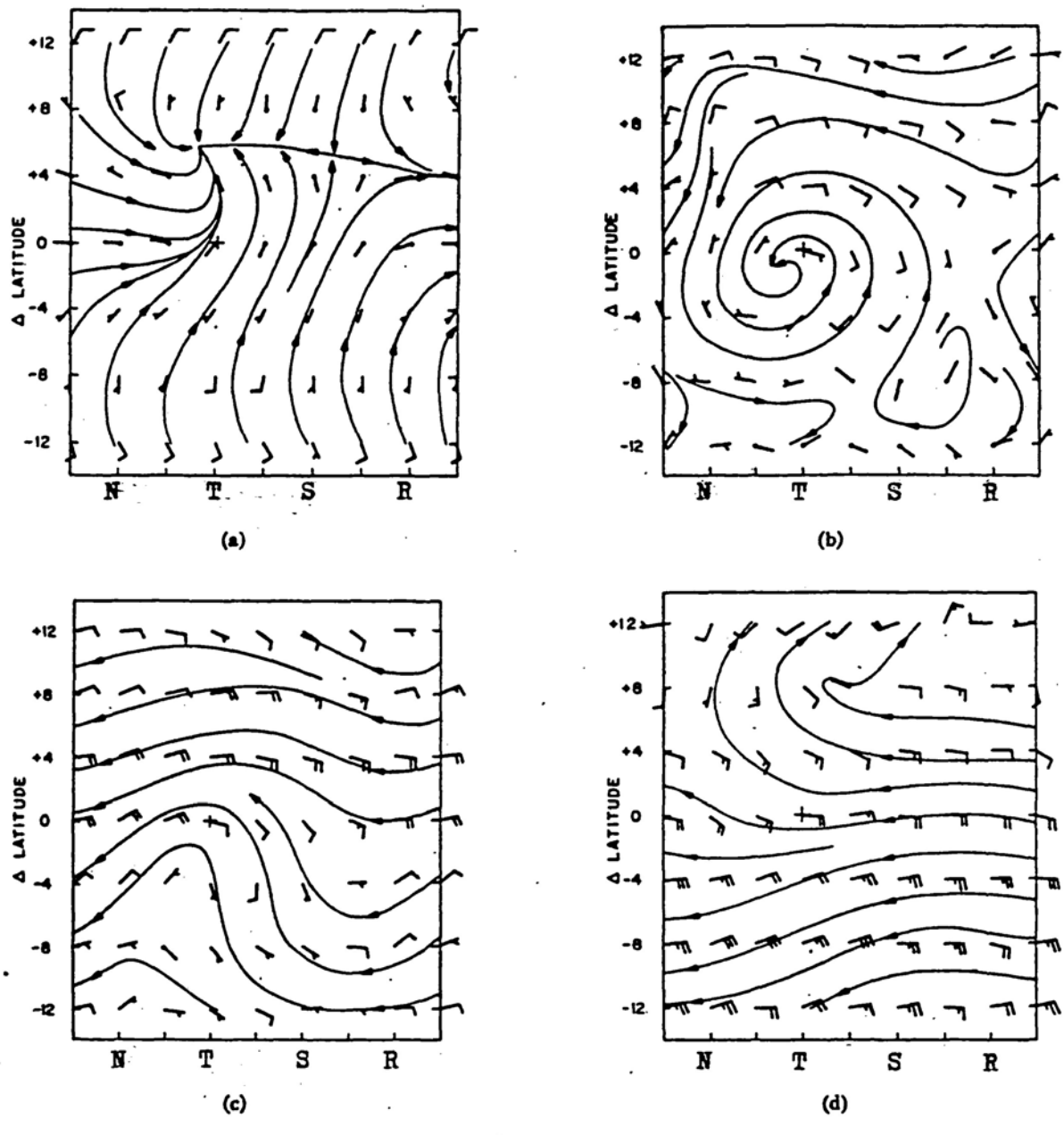


Fig 2.16. Streamlines for the total wind field (from Reed, Norquist and Recker 1977): (a) surface (b) 850 mb (c) 700 mb (d) 200 mb.

A cross denotes the disturbance centre at 700 mb, and N, T, S, R refer to the north wind, trough, south wind and ridge sectors of the wave respectively, the separation between these being approximately 6° longitude. One full barb corresponds to 5 m/s, one half barb to 2.5 m/s, and no barb to 1 m/s.

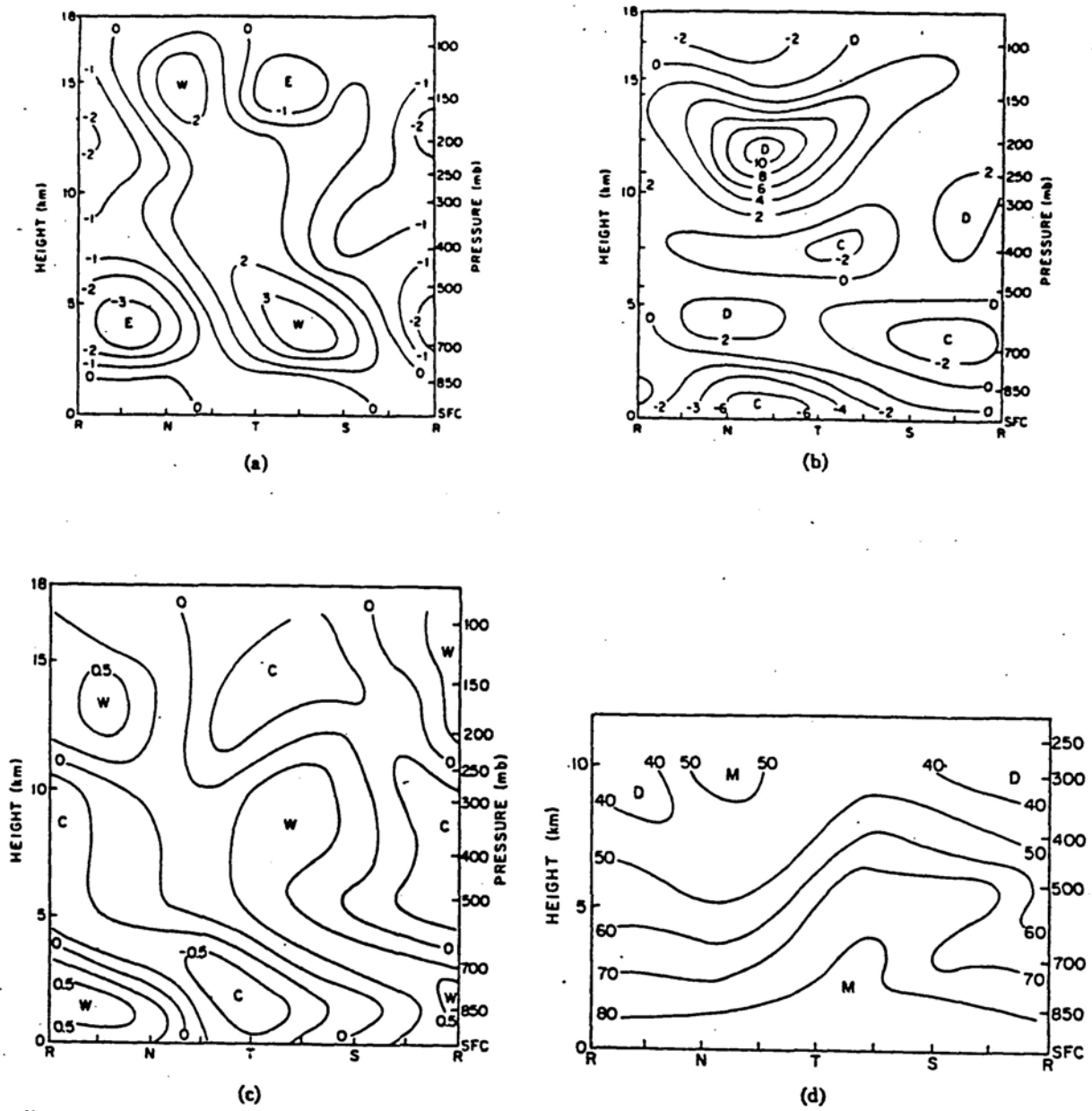


Fig 2.17. Vertical cross-sections along the reference latitude (from Reed, Norquist and Recker 1977).

(a) Westerly wind deviation from mean at each level (m/s)
(b) Divergence (10^{-6} s^{-1})
(c) Temperature deviation from mean at each level (^{o}C)
(d) Relative humidity (%).

R, N, T, S refer to ridge, north wind, trough and south wind sectors of the wave respectively.

and easterly waves is given by Payne and McGarry (1977) who, identifying SQL's from satellite images according to criteria listed in section 2.2.2, classified the points of origin and decay of those in GATE phase III (September 1974) according to easterly wave phase (fig 2.18). Their results show preferred locations for development east of the northerly wind maximum 'N' (ahead of the trough), and for termination east of the ridge 'R'. These results can be related to the conditions necessary for occurrence of SLS's (section 2.1.1). East of the northerly wind maximum there is a shallow layer of warm moist south westerly inflow at low levels, with dry air aloft (figs 2.16 a; 2.17 c,d), providing ideal thermodynamic conditions; also the AEJ is at its strongest here (large easterly anomaly at 4 km in fig 2.17a), thus providing the necessary shear, whilst also apparent is the weakening of the TEJ (large westerly anomaly at 15 km) which was noted in section 2.3.1 as a possible additional factor (though arguably this and the SQL could be totally unrelated consequences of the easterly wave); finally, triggering is provided by the low level convergence, high level divergence which occurs here (fig 2.17b). Conversely, east of the ridge, although the low level air is still warm, and the AEJ still strong, the TEJ has strengthened (zonal anomaly at 15 km now easterly), and the divergence pattern is no longer favourable. To what extent however this is a case of the SQL being initiated by a favourable environment, and to what extent the environment is moulded by the SQL is not clear; a SQL located ahead of the trough could be expected to force the synoptic scale motion as a result of its own vertical motion, and it may be this forcing, which has not been included in the numerical models of easterly waves which accounts for the discrepancy between model and observed energetics over the land, where most SQL's occur.

2.3.3 Some Statistics of West African Squall Lines.

As already indicated, there is some ambiguity as to what is regarded as a SQL by different workers, and statistics which they obtain must inevitably reflect to some extent the definition chosen. Furthermore the four studies which will be presented do not refer to exactly the same geographical areas. Nevertheless, there is broad general agreement between them, so that, although a few results will be quoted from each, a satisfactory overall impression does emerge.

(a) Hamilton and Archbold (1945), as previously mentioned (section 2.2.1), regarded only the longest lived disturbances as genuine SQL's, but their statistics relate to all disturbances which produced squalls over 15 m/s at five Nigerian stations during the period 1939 - 1941

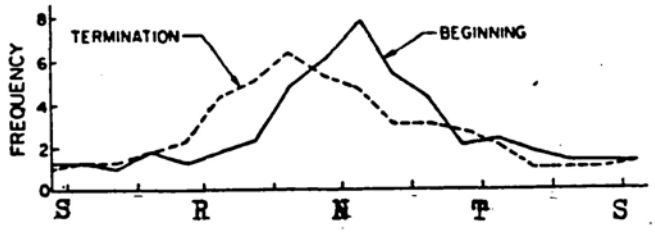


Fig 2.18. Frequency distribution of the location of the leading edge of squall lines at times of generation and decay versus wave phase for 46 squall lines in GATE phase III (from Payne and McGarry 1977).

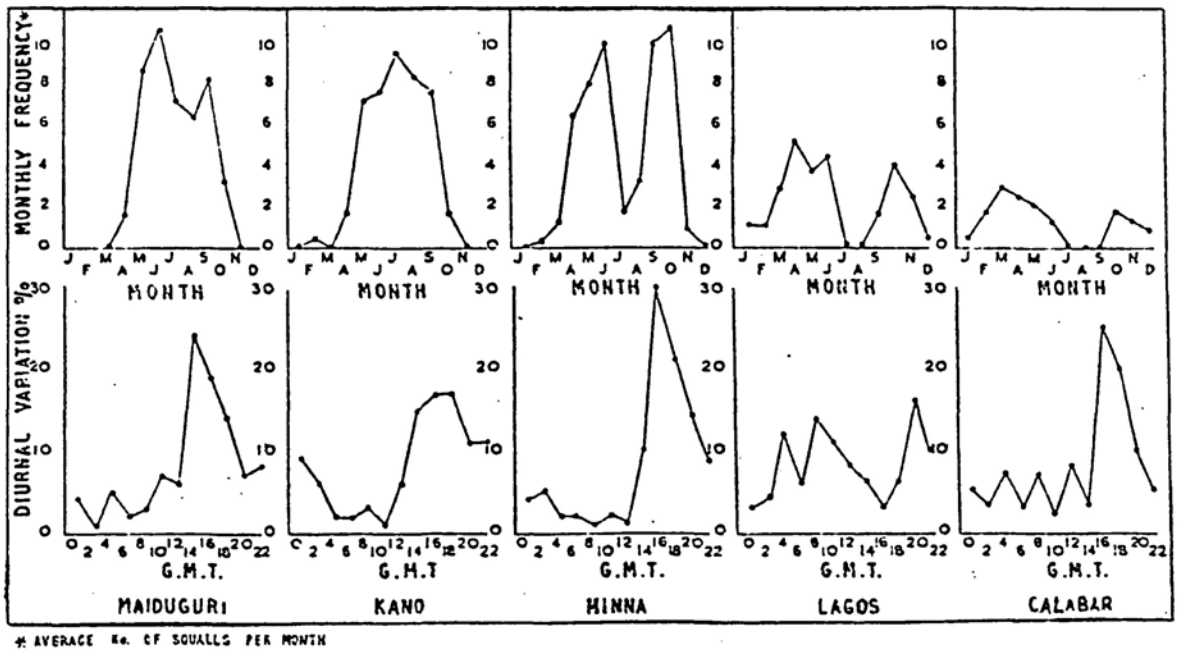


Fig 2.19. Monthly frequency and diurnal variation of squalls over 15 m/s at various Nigerian stations (from Hamilton and Archbold 1945).

(fig 2.19). Their monthly distribution can be related to the north-south section of mean zonal wind (fig 2.15b): when the ITCZ is at its northernmost limit, Kano and Maiduguri at 12°N are in zone C, so only experience a single SQL season; Lagos and Calabar at 7°N and 5°N respectively are well into zone D, so that their SQL season is interrupted by a period of steady monsoonal rain or even a little dry season; Minna at 10°N is intermediate. The important role of solar heating as a triggering mechanism is suggested by the early afternoon peak in diurnal distribution at all locations except Lagos, which lies on the coast (Calabar, though coastal, has a peak due to generation in the Cameroon mountains to the east: fig 3.2).

(b) Eldridge (1957) identified 283 West African SQL's in 1955 from synoptic charts, with lifetimes ranging from 6 to 60 hours. They moved at speeds ranging from 8 to 22 m/s, from directions lying between N and SE, the average being approximately 14 m/s from ENE. Eldridge noted a tendency for the south end of the line to trail, with the result that sometimes the line is oriented NW to SE, yet moving from roughly due E. Table 2.1 gives the distribution by month of the length and distance travelled. The fact that SQL's at the beginning and end of the year tend to be shorter and to travel less far is again consistent with the movement of the ITCZ, only small areas near the coast lying in zone C at this time of year.

Table 2.1. Summary of lengths of, and distances travelled by, West African Squall Lines in 1955 (from Eldridge 1957).

Month	Length (km)					Distance travelled (km)				Total
	<80	80 -240	240 -400	400 -560	>560	<800	800 -1600	1600 -2400	2400 -3600	
Jan	2	3	1			6				6
Feb	1	3	2	1		7				7
Mar	1	14	4	6	1	20	5	1		26
Apr	2	17	6	7	1	27	5	1		33
May	1	2	8	5	3	11	5	2	1	19
Jun		4	11	12	2	14	11	3	1	29
Jul		5	9	12		14	6	3	3	26
Aug		3	15	10	3	16	13	2		31
Sep		4	12	18	4	19	9	7	3	38
Oct		17	13	9	5	38	5		1	44
Nov	1	10	2	3	1	17				17
Dec	1	2	2	2		6	1			7
Total	9	84	85	85	20	195	60	19	9	283

(c) Obasi (1976) made a study for 1962 similar to that of Eldridge, but considered only SQL's over 80 km in length. He obtained similar results, except that he only identified 127 SQL's; the reason for the reduction

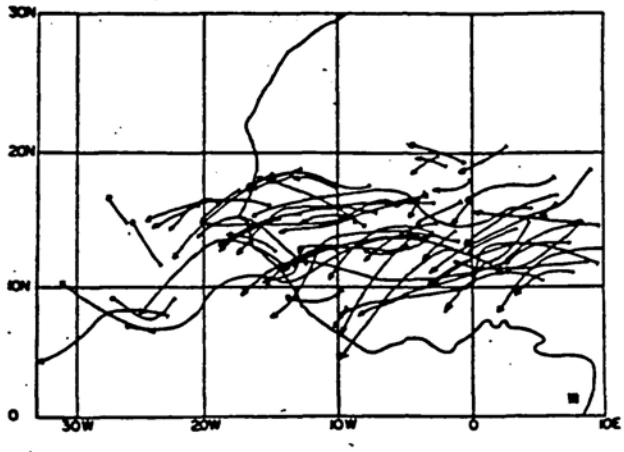
from Eldridge's total of 283 is not clear, as the restriction on length accounted for only a small part of the difference. Table 2.2 gives Obasi's classification of direction of motion and maximum gust against speed of motion; greater propagation speeds do tend to be associated with stronger gusts, though there is certainly not the almost one-to-one correspondence between the two as found by Gurka (1976) - see section 2.2.2.

Table 2.2. Summary of speeds, directions and maximum gust speeds of West African squall lines in 1962 (from Obasi 1976).

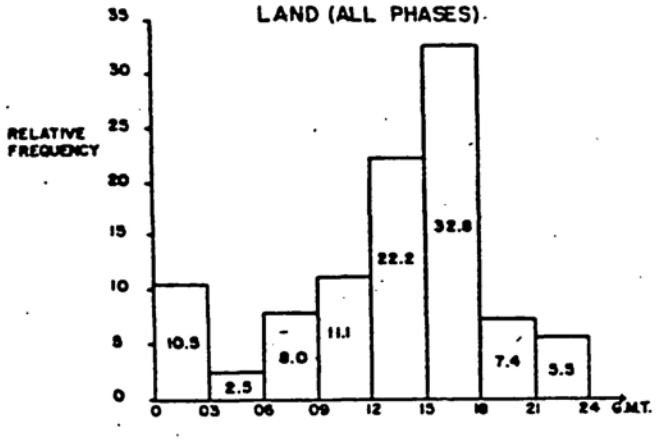
Speed	Direction: from				Gust (m/s)								Total
(m/s)	NE	ENE	E	ESE	< 12.5	12.5 -15	15- 17.5	17.5 -20	20- 22.5	22.5 -25	25- 27.5	≥ 27.5	
< 12.5	1	1	2	0		1	1	1	1				4
12.5-15	8	5	14	0	6	1	11	2	5		1	1	27
15-17.5	21	11	30	1	9	11	22	13	6	2			63
17.5-20	5	5	6	0	1	2	4	4	4	1			16
20-22.5	3	0	7	0		1	1	2	6				10
22.5-25	1	0	0	0					1				1
25-27.5	0	2	4	0			4					2	6
Total	39	24	63	1	16	16	43	22	23	3	1	3	127

(d) Aroliden et al (1976) identified 176 SQL's in 1974 during GATE, from infra-red satellite images, according to criteria similar to those of section 2.2.2. Fig 2.20a shows the actual tracks of those which occurred during GATE phase III; almost all the SQL's generated and decayed between 7° and 17° N, which is again related to the position of the ITCZ. 90% of the SQL's were generated over the land, and a number of these dissipated at or near the coast, indicating again the important role of solar heating over land. This is also evident in fig 2.20b, in which it can be seen that over half the SQL's over the land were generated between 1200 and 1800 GMT. Fig 2.20c shows preferred areas of generation over the land. Two particular areas within the 10° - 20° N latitude band may be noted: 5° - 0° W, which contains the swampy area in Mali at the northernmost limit of the River Niger often referred to as the 'Niger bend', and 5° - 10° E, which contains the Jos Plateau and Air Massif in Nigeria and Niger respectively. Other workers such as Obasi (1976) also quote these upland areas as preferred regions of generation, together with the Fouta Djalon Mountains (Guinea), Atakora Hills (Benin), Oshogbo Hills and Adamawa Highlands (Nigeria), Cameroon Highlands (Cameroon), and Marra Mountains (Sudan), which indicates clearly the role of orographic forcing as a trigger mechanism. The significance of the Niger bend,

(a)



(b)



(c)

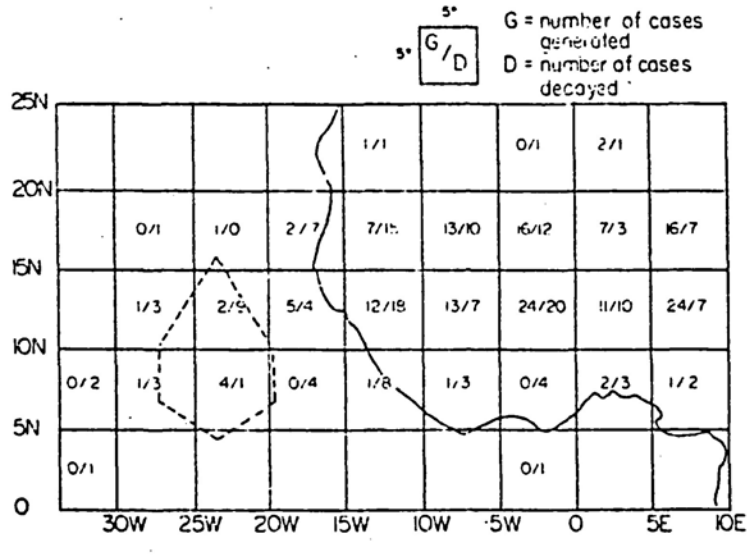


Fig 2.20. Squall lines in GATE (from Aspliden, Tourre and Sabine 1976).

(a) Tracks of all squall lines in phase III.

(b) Generation relative frequency (%) with respect to time for squall lines over the land in all three phases.

(c) Number of squall lines which generated and decayed in each 5^{o} square for all three phases.

and Lake Chad, also quoted by Obasi, is less clear; a possible explanation is moistening of warm dry surface air from surrounding regions, but it may instead be some semi-permanent convergence in the large-scale flow pattern.

Three trigger mechanisms for West African SQL's have thus emerged: synoptic convergence, particularly ahead of an easterly wave trough, solar heating and orography. Often these will occur together, though the fact that SQL's are generated over the sea indicates that the latter two are not essential.

CHAPTER 3. SQUALL LINES AT MINNA, NIGERIA.

3.1 IDENTIFICATION AND MEAN PROPERTIES OF SQUALL LINES.

In this chapter, a study of SQL's is made using routine upper air data from a single station, Minna in Nigeria, over a period of slightly more than two years, starting in June 1974, the month in which regular upper air soundings commenced.

3.1.1 Squall Line of 12 September 1977.

On 12 September 1977, I was fortunate to be positioned on a hill some 5 km west of Minna when a SQL arrived from the east. The first indication was a long dark line of cumulonimbus on the horizon, shown in fig 3.1a at 1555 GMT (4.55 pm local time). At 1611, the forward edge of the cloud mass arrived in the form of a long roll cloud (fig 3.1b). Two minutes later came a squall as the cumulonimbus belt itself arrived, seen to the SSE in fig 3.1c as a typical oppressive arch, accompanied by heavy rain. Though the front of the SQL had a nearly two-dimensional appearance, the cumulonimbus belt was clearly divided into distinct cells, so that I remained dry, though heavy rain fell to the north and south. By 1640, when the cumulonimbus belt had passed over, the individual cells could be clearly seen to the west (fig 3.1d), whilst to the east, a rainbow showed clearly against a background of altostratus. The arrival of the altostratus belt at 1656 was accompanied by the onset of a steady drizzle, which persisted for half an hour, before moderating. Soon after, darkness prevented further observation.

A visit to the meteorological station at Minna established that the SQL had arrived there at 1605 with a gust of 20 m/s from 180° and the simultaneous onset of rain, followed shortly after by thunder. The squall cleared by 1627, whilst the rain became moderate, rainfall in the first two hours being 7·6 mm. The hourly log recorded a temperature drop from 29·7 to 21·4°C, and a rise in relative humidity from 65% to 93% between 1600 and 1700, whilst the pressure rose from 980.7 to 981·4 mb, about 0·5 mb of this change being attributable to the SQL (the remainder being normal diurnal variation).

The next three hours showed a very slight recovery of pre-squall conditions, with temperature rising to 21·7°C, and relative humidity falling to 89% by 2000; the rise in pressure is entirely attributable to the diurnal variation.



(a)



(b)

Fig 3.1. Squall line at Minna on 12 September 1977

(a) View to E at 1555 GMT (4.55 pm local time) showing advancing line of cumulonimbus.

(b) View to NE at 1611 GMT showing roll cloud.



(c)



(d)

Fig 3.1. Minna squall line continued.

(c) View to SSE at 1613 GMT showing front of cumulonimbus belt and edge of rain area.

(d) View to W at 1648 GMT showing individual cumulonimbus.

These surface observations correspond to a fairly typical SQL according to section 2.2.1. It would however have been very difficult to distinguish the SQL from an isolated thunderstorm, but for observation of the nearly two-dimensional roll cloud and front of the cumulonimbus belt, and these features are not normally recorded in routine surface observations. Identification of SQL's at Minna therefore required that the Minna data be supplemented by surface observations at surrounding stations, and by satellite images when available. The locations of meteorological stations in Nigeria can be seen in fig 3.2.

3.1.2 Identification of Squall Lines.

In identifying possible SQL's, all reports of thunderstorms at Minna ($9^{\circ}37'N$, $6^{\circ}34'E$) were noted, and those which exhibited at least some of the following features were picked out.

(i) Maximum squall speed at least 12 m/s.
(ii) Rainfall at least 5 mm.
(iii) Storm duration at least 3 hours.
(iv) Pressure jump at least 0.5 mb (pressure jumps were estimated to the nearest 0.5 mb by making use of hourly records, and subtracting off diurnal variation).

Records at stations within a radius of approximately 300 km of Minna were examined for reports of features (i), (ii) and (iii) at times consistent with sensible propagation velocities, and seven stations were found to have regular records which corresponded fairly well with those at Minna: Jos ($9^{\circ}55'N$, $8^{\circ}54'E$), Kano ($12^{\circ}00'N$, $8^{\circ}30'E$), Kaduna ($10^{\circ}32'N$, $7^{\circ}26'E$), Lokoja ($7^{\circ}48'N$, $6^{\circ}43'E$), Bida ($9^{\circ}04'N$, $5^{\circ}59'E$), Yelwa ($10^{\circ}53'N$, $4^{\circ}45'E$) and Ilorin ($8^{\circ}30'N$, $4^{\circ}32'E$). Noting that a typical SQL length in table 2.1 is 300 km, it is not surprising that hardly any SQL's affected all the stations, whilst several affected only Minna and one other station. Also, even if a station was affected by a thunderstorm which clearly was related to a SQL, there was not necessarily a squall reported, whilst rainfall could be be very small if no cumulonimbus cell passed directly over the station, and storm duration could be as little as an hour, particularly at the beginning and end of the SQL season (when the moist south westerly surface layer was relatively shallow).

With these considerations in mind, SQL's were identified as thunderstorms which exhibited features (i) - (iv) at Minna, and (i) -

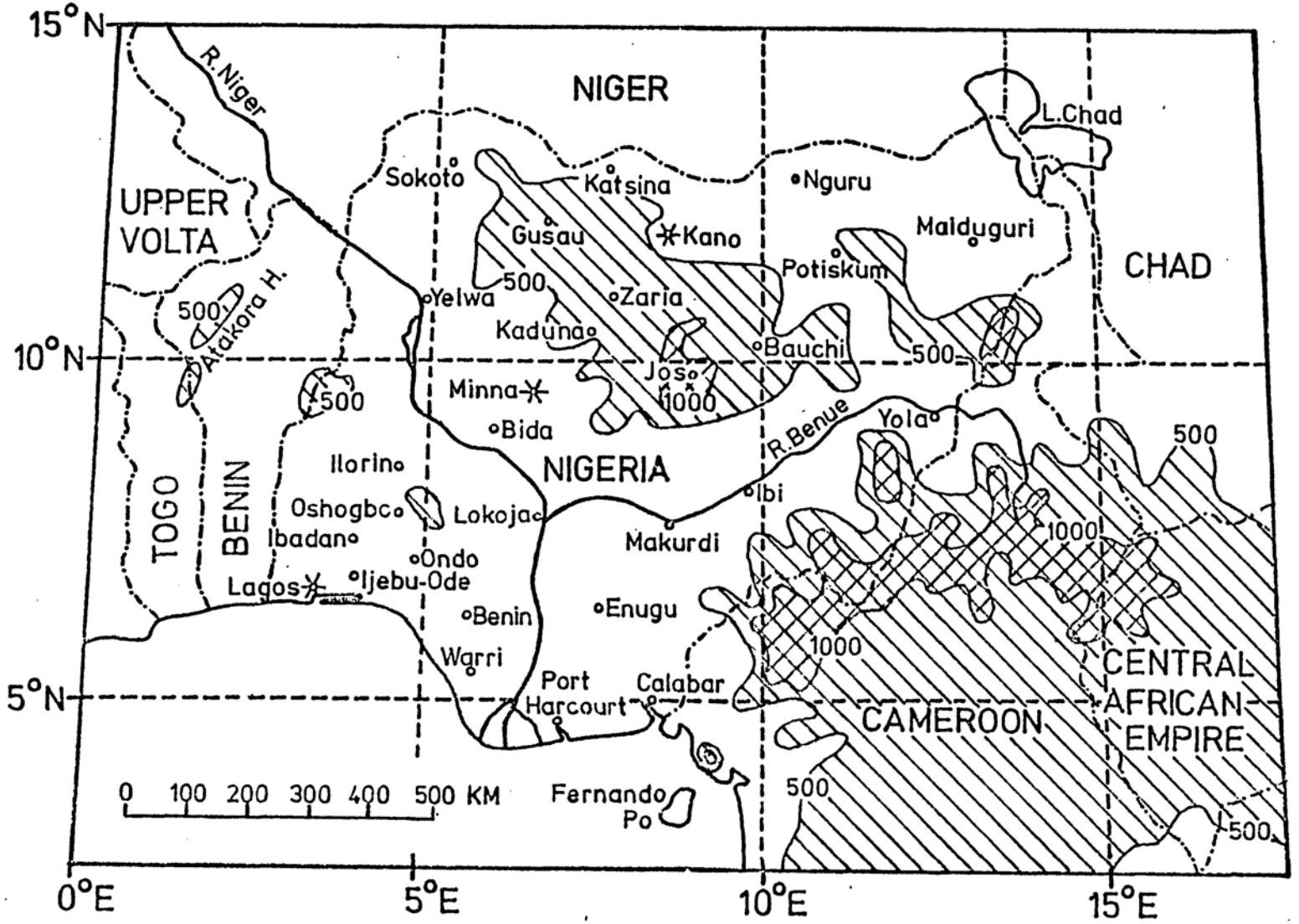


Fig 3.2. Map showing location of meteorogical stations in Nigeria. Contour heights are given in metres, national boundaries are denoted by dash-dot lines.

(iii) in at least one other station, though the conditions, particularly at Minna, were somewhat relaxed in cases where there were a number of clear reports at other stations. Porter et al (1955), in a study of SQL's in the United States adopted a similar, but slightly more stringent set of criteria. Eighty SQL's, listed in table 3.1, were thus identified during the period June 1974 - August 1976, while in another nineteen cases of possible SQL's (not listed) the data were judged to be inconclusive.

In the table, the time recorded at a station is taken to be the time of the first reported squall; in cases where there was a thunderstorm but no reported squall, an estimated time, enclosed in square brackets [ ] is given as five minutes before the onset of the rain. Round brackets ( ) are used to denote cases where rainfall and storm duration were significantly less than the required values. The entries under 'Minna soundings' are given to indicate which SQL's were included in the analyses which follow; in general, regular soundings were available at 1200 GMT, with 0000 soundings available during GATE, and occasionally afterwards.

The storm velocities in the table were estimated by making use of the reported times of squalls at the various stations. The SQL was assumed to have a parabolic shaped front, and to move with constant velocity along the axis of the parabola. Some or all of the parameters storm velocity, distance of Minna from centre line of storm path, and radius of curvature of centre of parabolic front were then chosen so as to minimise the sum of squares of the differences between reported and estimated times of squalls at the stations (see Appendix A). This method is able to cope with cases such as that mentioned in section 2.3.3b, where the south end of the SQL trails, but was nevertheless found to be not entirely satisfactory: it could only be applied when squalls were reported at several stations not on a straight line, and even then results had to be interpreted with caution.

During GATE, it was possible to supplement the surface data with half-hourly visible and infra-red images from Synchronous Meteorological Satellite SMS-1. Though Minna was located near the edge of these pictures, and though none of the cloud masses was as regular as the sequence in fig 2.4, they were still sufficiently clear to permit verification of the conclusions reached using surface data, particularly with regard to storm velocities. Three typical cases will be presented, showing visible images, and maps indicating reported squalls, and tracks of

Table 3.1. Squall Lines affecting Minna, June - December 1974.

Key. Overbar: indicates occurrence of squall on preceding day, e.g. $\overline{0838}$ = 1638 on previous day
- : station not affected by squall line
[] : estimated time (no reported squall)
/ : complete sounding available
WX : winds not available
Blank: data insufficient for adequate determination
( ) : weak storm (rainfall < 5 mm, duration < 3 hours)
o : no sounding available
WO : only winds available

Date	Times of reported squalls									Storm vel.	Minna squall vel.	Press. jump	Rainfall	Soundings	
	Minna	Jos	Kano	Kaduna	Lokoja	Bida	Yelwa	Ilorin	Other	deg,m/s	deg,m/s	mb	mm	Before mdy. Midnight	After mdy.
1. 6.74	1827	-	$\overline{1616}$	[1722]	-	-	2015	-	Zaria $\overline{1642}$	080,29	090,29	2.5	5.5	o o	o
3. 6.74	0000	$\overline{0716}$	$\overline{0838}$	-	-	0045	-	-	Zaria $\overline{0707}$		030,14	1.0	9.6	o o	o
9. 6.74	1826	1406	1740	1640	2022	1915	1957	2152	Zaria 1514, Ibadan 2430, Ikeja	075,21	100,22	2.5	21.3	o /	o
15. 6.74	1940	1445	-	-	-	2048	1958	2342	Sokoto 2014 $\lfloor\overline{2642}$		090,18	1.5	13.1	/ /	/
16. 6.74	1736	1544	1824	-	1736	1827	-	2116	Yola $\overline{1145}$	080,25	150,15	1.0	13.2	/ /	/
22. 6.74	0810	[0143]	-	0625	-	0902	-	1130	Yola $\overline{0515}$, Ibadan 1435	070,20	140,15	2.5	20.2	WX /	/
25. 6.74	0853	[0410]		(0635)	[0939]	[1015]	-	-	Ibadan $\overline{1625}$	075,15	110,15	2.0	8.2	/WX	/
27. 6.74	0133	-	$\overline{0149}$	0002	0040	[0245]	0515	[0605]	Yola $\overline{1156}$, Zaria 0000, Ibadan 0705,	090,16	110,14	0.5	24.5	/ /	o
9. 8.74	1114	0724	-	[1009]	[1320]	1224	-	1504	Makurdi [1105] $\lfloor$Ikeja 0915	080,19	080,22	1.0	10.5	o /	/
23. 8.74	1635	-	-	1545	-	1830	-	-		070,18	110,15	0.5	0.0	/ /	/
25. 8.74	1915	1509	1340	[1718]	-	[1927]	-	[2145]		075,18	110,12	1.0	8.6	/ /	/
26. 8.74	1835	[1211]	1400	1634	-	-	2210	-		080,17	090,15	1.5	9.6	/WX	WX
28. 8.74	2110	[$\overline{1246}$]	$\overline{1632}$	$\overline{1748}$	-	-	2343	-	Zaria $\overline{1731}$, Sokoto $\overline{2507}$ $\lceil\overline{1020}$	090,17	040,10	0.5	7.4	/WX	WX
2. 9.74	0005	[$\overline{0815}$]	$\overline{0655}$	$\overline{0328}$	-	[0125]	[0225]	0405	Maid'i $\overline{1545}$, Pot'm $\overline{1015}$, Bauchi	080,18	100,15	0.0	30.5	/ /	/
4. 9.74	1438	-	1310	1305	-	[1540]	1815	-	Maid'i 0304, Zaria 1316, Sokoto	090,16	090,11	1.0	2.9	/ /	WX
9. 9.74	1950	-	-	[1719]	-	-	2250	-	$\lfloor$1900	100,17	090,13	1.5	13.3	/WX	/
10. 9.74	1930	[1551]		[1534]	-	[(2153)]	2012	[(2207)]	Nguru 0748, Gusau 1542	075,16		1.0	14.5	/WX	/
18. 9.74	1715	1435	-						Gusau 1945	090,20	090,15		17.3	/ /	/
19. 9.74	1620	-	-	1448	[1441]		[1910]	[2235]	Zaria 1407	095,19	090,18	0.5	4.7	/ /	/
22. 9.74	1545	-		-	-	1720	[2015]	-	Gusau 1403	090,13	090,19	2.0	16.2	/ /	o
17.10.74	1730	-	-	-	-	1852	-	-			090,13	1.5	7.9	/ o	/
22.10.74	1628	-	-	-	-	-	2018	-			080,20	1.0	12.5	/ /	/
23.10.74	1556	-	-	-	-	1620	-	-			080,13	0.5	20.4	/ o	/

Table 3.1 continued. Squall Lines affecting Minna, 1975.

Date	Times of reported squalls								Other	St.vel. deg,m/s	Sq.vel. deg,m/s	Pr. mb	Ra. mm	Sndgs. B	M	A
	Minna	Jos	Kano	Kaduna	Lokoja	Bida	Yelwa	Ilorin								
7. 2.75	1713	-	-	-	1850	-	-	-			030,13	3.0	18.6	WX	WX	/
16. 3.75	1716	-	-	[1535]	-	1832	-	[1902]			090,15	4.0	16.9	WX	o	/
6. 4.75	1812	-	-	-	-	(1930)	-	-			050,15	1.0	15.7	/	o	/
14. 4.75	0130	-	-	-	-	(0302)	-	-			090,12	2.0	34.4	/	o	/
23. 4.75	2005	[1137]	1730	1717	-	2135	-	-	Makurdi 1020, Ondo 1620, Ibadan	080,10	100,19	1.5	1.2	o	o	o
24. 4.75	1615		-	1620	1322	1538	[2125]	-	1804, Gusau (1815), Ikeja 1900		090,17	2.5	29.2	o	o	/
25. 4.75	1920		1655	1705	-	(2058)	-	-	Gusau (2053)	085,16	090,14	3.0	14.2	/	o	o
30. 4.75	1850	[1415]	-	1735	[1942]	1953	-	[2350]		080,17	120,20	3.5	7.8	WX	o	o
2. 5.75	2103	-	1503	1857	-	2245	-	-	Gusau (1840)	060,14	080,22	0.5	33.1	o	o	o
14. 5.75	2002	1610	-	1915	-	2118	2510	[2505]		100,14	130,13	2.0	12.1	/	o	/
17. 5.75	1640	1252	-	1537	1646	1715	1953	[2025]	Gusau (1858)	095,18	100,18	1.5	11.6	/	o	/
19. 5.75	0405	-	-	0038	-	0533	-	-	Gusau (0200)	070,15	050,18	0.0	34.6	/	o	/
26. 5.75	2150	[1753]	-	1920	-	2330	2708	[2619]		095,15	030,15	1.5	9.4	/	o	/
1. 6.75	2207	[1605]	-	2030	-	2335	2210	2632			080,20	0.0	19.6	o	o	/
5. 6.75	2125	1720	-	2025	-	2305	-	2620	Ibadan 2950, Ikeja 2935	075,17	050,21	2.0	10.7	/	o	/
12. 6.75	1924	[1710]	-		-	2036	-	[2447]			090,23	3.0	20.0	/	o	/
21. 6.75	0520	-	0241	0155	-	-	-	-	Zaria 0100	070,13	050,14	0.0		/	/	/
21. 6.75	[1602]	1348	-	1415	-	1748	-	-	Potiskum 0524, Makurdi 1345			3.0	37.3	/	o	/
29. 6.75	1626		1607	1632	[1720]	[1715]	[1813]		Makurdi [1705]		090,15	1.0	17.9	/	o	/
28. 7.75	1745	-		1445	-	[1910]	[1957]	-		060,14	160,15	1.5	6.7	/	o	/
5. 8.75	[1545]	-	1100	1345	[1835]	-	[1823]	-	Gusau 1433	070,15			6.6	/	/	/
6. 9.75	0635	-	0205	0403	-	-	-	[1239]		070,16	150,15	2.0	17.6	/	/	/
18. 9.75	0450	[0135]	-	[0105]	-	0635	-	-		065,18	070,18	1.0	6.4	o	o	/
21. 9.75	(1646)	-	-	-	-	(1835)	-	-			100,18	2.5	5.5	o	o	o
22. 9.75	[1645]	-	-	[1418]	-	1915	1820	-				1.0	57.8	o	o	o
27. 9.75	1750	-	-	-	-	1906	-	2225			090,20	2.0	24.1	o	o	o
29. 9.75	1805	-	-	1502	[2017]	-	1708	-			090,15	1.0	19.2	o	o	o
7.10.75	1510	-	1037	-	[1535]	-	1710	-			150,16	0.0	11.2	WX	o	/
8.10.75	1638	-	-	-	-	1820	1721	-			080,15	2.0	15.6	/	o	o
18.10.75	1005	-	-	1410	-	1010	[1433]	-	Zaria 1300		140,18	1.0	14.8	/	o	/
27.10.75	1503	-	-	-	-	1647	-	[1900]			050,14	1.0	13.2	/	o	WO

Table 3.1 continued. Squall Lines affecting Minna, January - August 1976

Date	Times of reported squalls								Other	Storm vel. deg,m/s	Minna squall vel. deg,m/s	Press. jump mb	Rainfall mm	Sound'gs Before mdy.	Sound'gs Midnight	Sound'gs After mdy.
	Minna	Jos	Kano	Kaduna	Lokoja	Bida	Yelwa	Ilorin								
14. 2.76	1355	-		-	1620	1645	-	-			080,12		2.7	o	o	o
23. 3.76	1735	-		-	1912	1905	-	-	Ibadan 2521, Lagos 2713	070,15	090,14	1.0	0.0	WX	o	o
23. 4.76	1620	[1046]	1752	1508	1943	1710	-	[1540]			160,25		1.2	/	o	/
3. 5.76	[2101]	1426	1825	1919	-	-	-	-				1.0	1.2	/	o	WX
5. 5.76	1550	1006	-	1505	-	1612	-	[1920]	Oshogbo 1518	100,14	120,22	2.0	0.7	/	o	WX
14. 5.76	1740	[1352]	-	[(1658)]	-	1820	2115	-		100,18	110,12	1.0	4.8	/	o	WX
19. 5.76	1755	-	-	(1555)	-	1907	-	2230		080,15	080,20	1.0	11.3	/	o	/
21. 5.76	1950	[1402]	-	1805	-	[2135]	-	-		080,15	080,11	2.0	1.5	/	o	/
22. 5.76	1705	-	1935	-	-	1910	[1815]	[2232]	Gusau (1348)	065,13	090,20	2.0	15.2	/	o	/
27. 5.76	1743	-	1340	(1649)	-	-	2015	[(2150)]	Gusau 1552	070,19	090,14	2.0	4.9	/	o	/
28. 5.76	1759	-	-	[1730]	-	1945	-	-	Zaria 1713		090,18	1.0	9.0	/	o	/
31. 5.76	1634	[(1256)]	-	1501	[1352]	1802	1825	[1758]	Gusau 1420		100,18	2.0	22.5	/	o	/
2. 6.76	1945	1820	-	2027	2322	1940	2310	-	Zaria 2027		090,23		22.4	/	o	/
5. 6.76	1549	[1128]	1120	1303	-	[1702]	-	[2240]		075,14	080,13		27.2	/	o	/
7. 6.76	[1950]	1748	2028	2045	-	2046	2441	-	Oshogbo 2510				13.4	/	o	/
9. 6.76	0739	[0158]	0222	0505	-	0902	-	[1150]		075,14	090,14		7.8	/	o	/
11. 6.76	1528	-	1020	1210	[1434]	1632	1724	-	Potiskum 0604	075,16	,09		13.6	/	o	/
17. 6.76	[1415]	-	-	[1548]	1320	1445	-	1720	Pot'm 0510, Gusau 1620, Sokoto 2050	070,18	050,15		7.0	/	o	/
20. 6.76	2045	-	1640	1809	2348	2230	2229	-	Zaria 1750				9.2	WX	o	WX
22. 6.76	[(1740)]	-	1715	1630	-	1825	2137	-					10.2	/	o	/
28. 6.76	[0306]	0106	0530	0052	[0458]		-	[0723]	Zaria 0347, Lagos 0920	070,17			1.0	/	o	/
6. 7.76	(1408)	[0900]	-	-	1406	1513		[(1815)]	Sokoto 1948	085,14	,14			/	o	/
31. 7.76	1840	[1037]	-	1540	-	[2110]		-	Zaria 1552		,12	1.0	20.2	/	o	/
14. 8.76	1952	[1458]	-	2010	1903	2105		2330			130,15	0.5	2.4	/	o	/
25. 8.76	1435	[0913]	-	-	1545	1513		[1757]		080,15	160,13	0.0	0.0	/	o	/
26. 8.76	[1927]	[1249]	-	1701	-	2108		-	Maiduguri 1608			1.5	13.0	/	o	/

squall fronts as sketched from infra-red images.

On 22 September 1974 (fig 3.3), a number of SQL's occurred, all corresponding to type 1 in Gurka's (1976) classification in section 2.2.2; three of them are indicated by arrows. No. 1 persisted throughout the day but did not affect Minna; at 1100 it shows a detached roll cloud (this feature was not present in any of the SQL's affecting Minna during the period). SQL no. 2, which did affect Minna, and no. 3, 200 km to the north both appear at 1400, and by 1530 they have moved about 80 km west and grown significantly; the infra-red tracks (fig 3.4) show that they were both generated on the Jos plateau, and that subsequently they merged and slowed down. These latter two SQL's reveal one obvious flaw in the method of identification using surface data alone: though initially distinct, they both affected stations within a 300 km radius of Minna and so could not have been distinguished.

The SQL which affected Minna on 23 August 1974 (fig 3.5) corresponded more closely to Gurka's type 3, very little anvil outflow being evident at any stage in its life. It was oriented NW - SE, but moved from 070°, a situation similar to that which Eldridge (1957) noted (section 2.3.3b); this illustrates the danger of assuming the motion to be at right angles to the squall front. Like no. 2 of fig 3.3, it was generated near the highest point of the Jos plateau.

Finally, fig 3.6 shows the SQL of 4 September 1974; this is typical of those in which strong winds at upper levels blow part of the anvil outflow ahead of the squall front. The cloud mass does not correspond to any of Gurka's categories, having a diffuse leading edge, so that tracking the progress of the squall front is rendered difficult. Indeed, such cases are omitted by some workers who identify SQL's solely from satellite images, for example Mansfield (personal communication). The large number of surface reports, indicating a realistic propagation speed of 15 m/s, taken together with the pressure jump of 1 mb and duration of 7 hours at Minna do however firmly identify this disturbance as a SQL. It is possible that there was a sharp leading edge at an earlier stage of development, but this cannot be checked as no satellite images are available before 1400. For the same reason, the place of generated cannot be located, though the reported squall at Kano makes it unlikely to have been the Jos plateau.

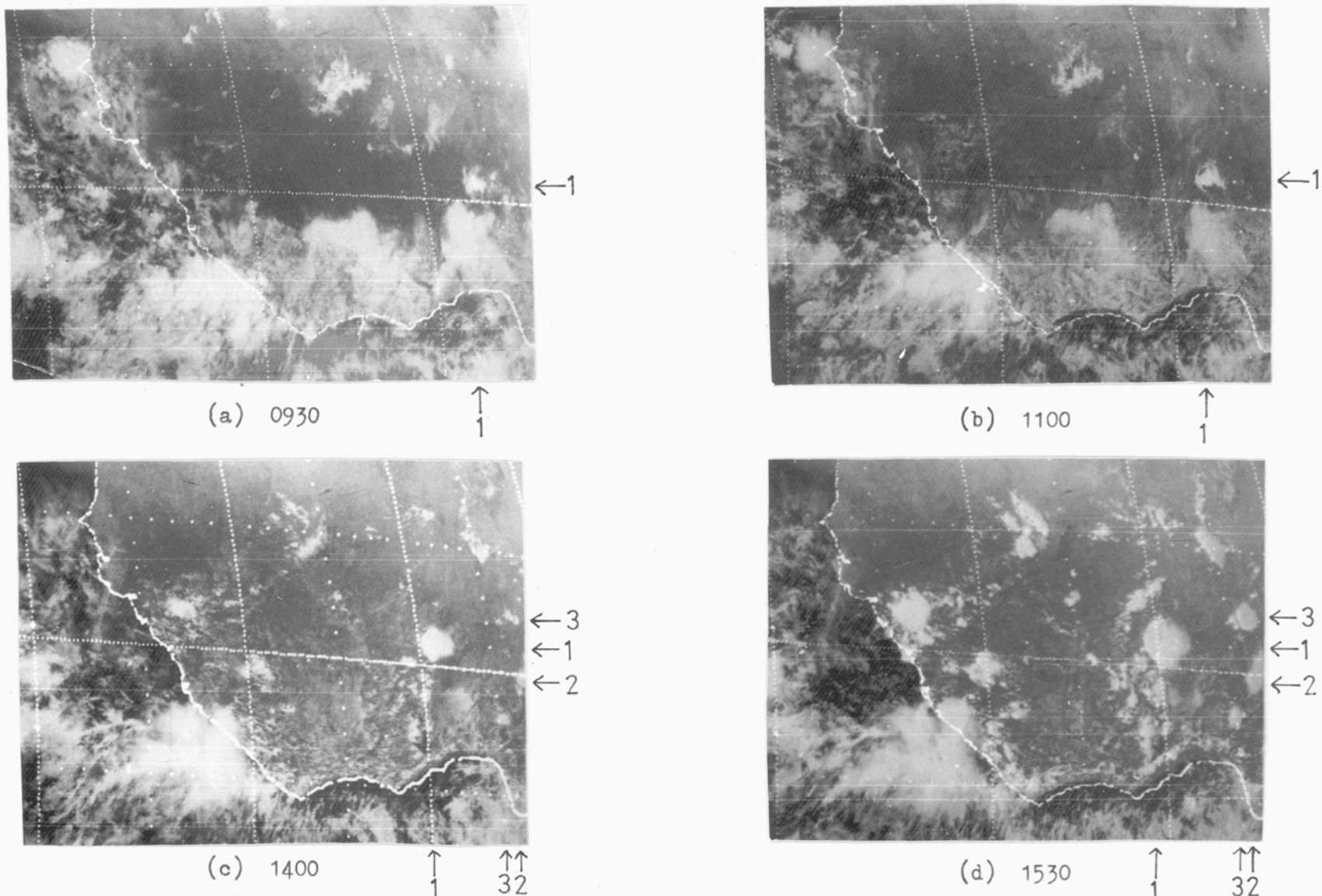


Fig 3.3. Visible SMS-1 images on 22 September 1974 at 1½ hour intervals (image at 1230 was not available). Arrows indicate positions of three squall lines, of which no. 2 affected Minna.

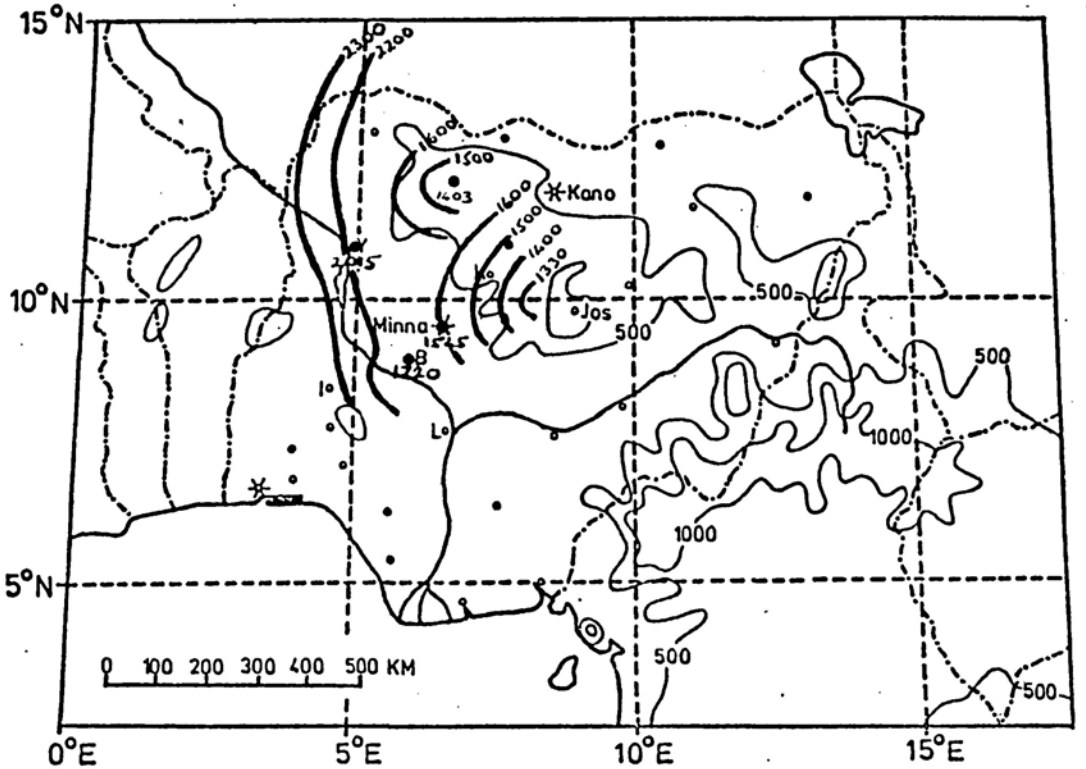
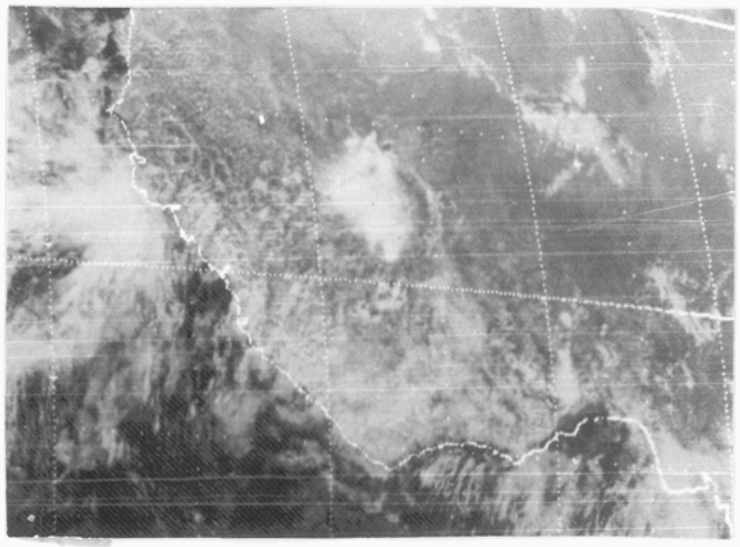
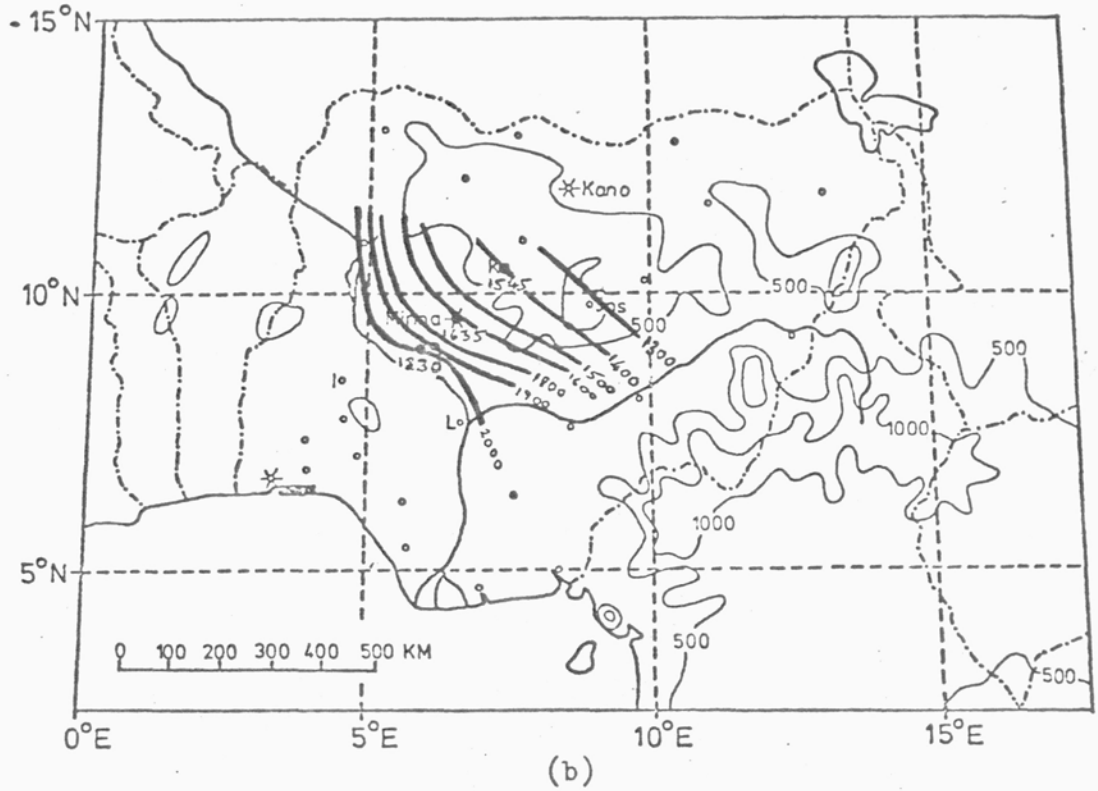


Fig 3.4. Map of reported squall occurrences, and leading edges of SMS-1 infra-red images of squall lines no's 2 and 3 of fig 3.3 (images from 1630 to 2130 were not available).



(a)

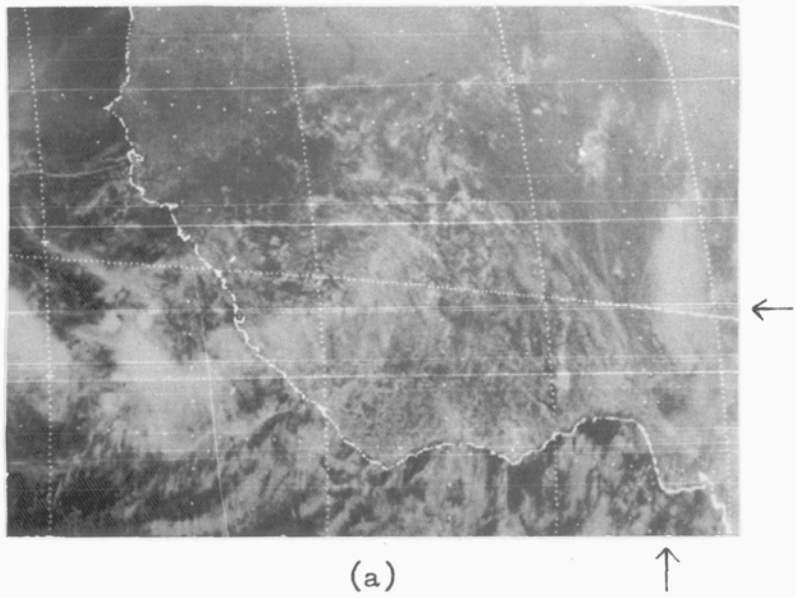


(b)

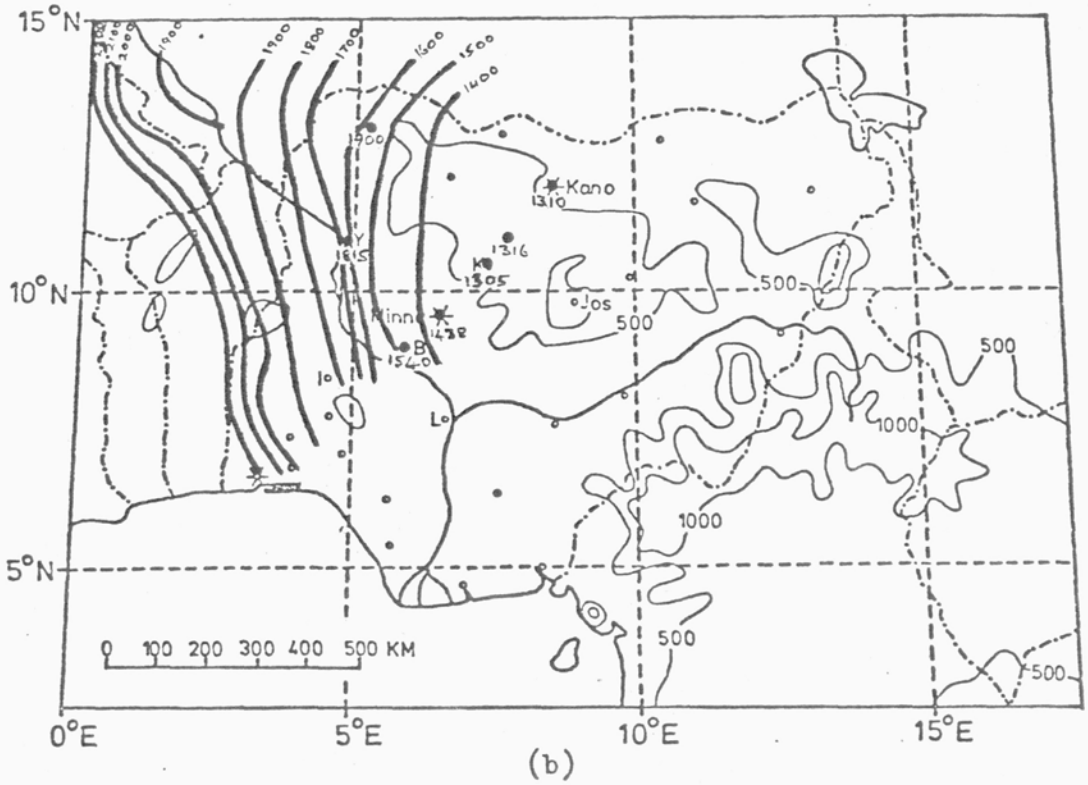
Fig 3.5. Squall line of 23 August 1974.

(a) Visible SMS-1 image at 1400 GMT; arrows indicate location of squall line.

(b) Map of reported squall occurrences, and progress of leading edge of infra-red image of squall line.



(a)



(b)

Fig 3.6. Squall line of 4 September 1974.

(a) Visible SMS-1 image at 1400 GMT; arrows indicate location of squall line.

(b) Map of reported squall occurrences, and progress of leading edge of infra-red image of squall line (images before 1400 were not available).

3.1.3 Some Squall Line Statistics.

Table 3.2 gives a summary by month of the times of occurrence at Minna of, and number of stations affected by the SQL's identified in table 3.1, but considering only the first two years, June 1974 - May 1976 of the full 27 month period in order to eliminate bias (the number of stations affected is based on reports from Minna, Jos, Kano etc., plus those listed under 'other').

Table 3.2. Summary by month of times of, and number of stations affected by Squall Lines at Minna, June 1974 - May 1976.

Month	Time of day								No. of stns. affected					Total
	0-3	3-6	6-9	9-12	12-15	15-18	18-21	21-24	≤3	4-5	6-7	8-9	≥10	
Jan														
Feb					1	1			2					2
Mar						2				2				2
Apr	1					2	4		2	2	2		1	7
May		1				8	2	3		7	5	2		14
Jun	2	1	2			3	4	2		4	8		2	14
Jul						1				1				1
Aug				1		2	2	1	1	1	4			6
Sep	1	1	1		1	6	3		4	5	1	2	1	13
Oct				1	1	5			5	2				7
Nov														
Dec														
Total	4	3	3	2	3	30	15	6	14	24	20	4	4	66

The distribution by time of day shows that SQL's occur at all times, but that there is a sharp peak in the afternoon, with over half the SQL's occurring between 1500 and 2100. Now, the results of Aspliden et al (1976) in fig 2.20b show that over half the SQL's over the land during GATE were generated between between 1200 and 1800, i.e. three hours earlier; so, allowing propagation from the east at about 15 m/s, this suggests a peak location of generation some 150 km east of Minna, that is on the Jos plateau. Some confirmation is provided by the reported squall times, which in many cases suggest a disturbance spreading out from an initial location on the Jos plateau. Thus the two trigger mechanisms of solar heating and orography combine in the generation of many of these SQL's.

At the beginning and end of the rainy season (February-April and October), when the depth of moist air is small, the number of stations affected is relatively small, presumably because SQL's do not travel far before running into a region with insufficient moisture supply.

These short-lived SQL's affect only stations in the immediate neighbourhood of Minna, so would fall into Hamilton and Archbold's (1945) intermediate category (see section 2.2.1), but here they will be regarded as true SQL's. In the middle of the rainy season, SQL's often affect more stations, and there is a tendency for a significant number to occur later in the day than the peak time of 1500 - 1800, suggesting that a number of these longer-lived SQL's are generated in the early afternoon well to the east of the Jos plateau, possibly in the region of Lake Chad, or over the high ground on the Cameroon border. The greater number of stations affected in the middle of the rainy season is consistent with the greater lengths and distances travelled in Eldridge's (1957) results (table 2.1). The Minna results do however show a pronounced drop in the number of SQL's in July and early August, presumably because the SQL belt has moved to the north; such a drop would not occur in Eldridge's results since he is considering the whole of West Africa, not just a single station.

Fig 3.7 shows frequency diagrams at Minna of pressure jump, rainfall and Richardson number. Here and in subsequent statistics, the full 27 month period to August 1976 in table 3.1 is considered, but owing to the absence of the relevant data, not all 80 SQL's are included in any particular study. The pressure jump and rainfall show considerable scatter, with relatively small means of 1·4 mb and 13·6 mm respectively; this provides some justification for the low cut-off values (0·5 mb and 5 mm) adopted in the identification of SQL's, and for the fact that a significant number have been included in which even these cut-off values are not attained.

In the tropics, Ludlam's (1980) definition of Richardson number (see section 2.1.1) breaks down, as wind velocities at the inflow and outflow levels are often nearly equal. Grover (1974) instead defined the Richardson number to be

$$Ri = APE \;/\; AKE$$

where Available Potential Energy, $APE = \int_{z_1}^{z_2} g\,\delta\phi_p\, dz$ (3.1)

and Available Kinetic Energy, $AKE = \frac{1}{2}\left\{ \int_{z_1}^{z_2} \left| \frac{\partial u_r}{\partial z} \right| dz \right\}^2$ (3.2)

are calculated from the pre-squall sounding, with

z_1 = level of inflow (taken to be 0.5 km)

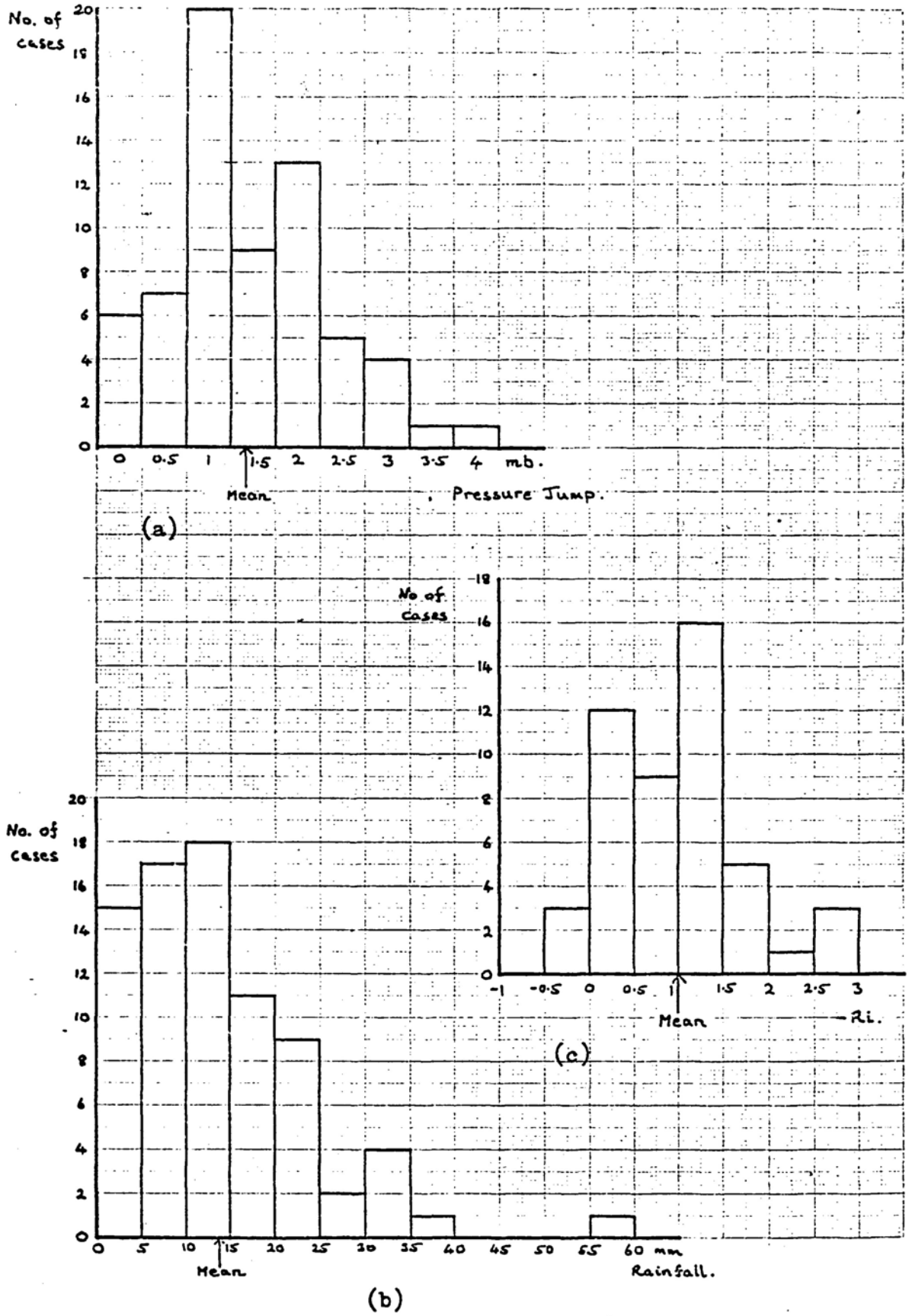


Fig 3.7. Frequency diagrams for squall lines affecting Minna June 1974 - August 1976 of

(a) Pressure jump, to nearest 0.5 mb;

(b) Rainfall, mm; (c) Minus Richardson number.

$\delta\phi_p$ = excess log potential temperature above its environment of a parcel rising from the inflow level z,

i.e. $$\delta\phi_p = \ln\left(\theta_{\text{parcel}} / \theta_{\text{environment}}\right) \qquad (3.3)$$

z_1 = equilibrium level of parcel (level where $\delta\phi_p = 0$)

and u_r = storm-relative velocity component in direction of motion.

It was with this definition that Grover found the nine Venezuelan SQL's which he studied to satisfy approximately $1 \leq -Ri \leq 3$, the mean being $\overline{-Ri} = 1{\cdot}7$.

For the Minna SQL's, a slightly different definition of available kinetic energy was adopted:

$$AKE = \frac{1}{2}\left\{\int_{z_1}^{z_2} \left|\frac{\partial \underline{u}}{\partial z}\right| dz\right\}^2 \qquad (3.4)$$

the vector shear being used instead of the storm-relative shear as the storm velocity was in many cases unknown; the error thus introduced is quite small for the almost unidirectional profiles considered. Also, inflow height was taken to be the height of the 950 mb surface; $\delta\phi_p$ was thus the excess log potential temperature of a parcel taken from this level dry adiabatically to its lifting condensation level (found using eqn. (22) of Bolton 1980a), then moist adiabatically above (θ_{parcel} being found here by inverting eqn. (43) of Bolton 1980a). Results are shown in fig 3.7c. As in Grover's results, the need for strong shear is indicated by the upper limit 2·7 on -Ri. Results differ from Grover's however in the values of -Ri significantly less than 1 occur, negative values even appearing in three cases, corresponding to no net positive area on a tephigram, which is quite unrealistic. The likely reason for the inadequate buoyancy in these cases is that many SQL's occurred in the late afternoon, so that solar heating would have appreciably increased -Ri from the value which has been inferred from the midday sounding. Grover's soundings, being closer to the actual SQL would have largely avoided this difficulty, so there is no reason to reject his lower bound $-Ri \geq 1$.

Various workers have suggested methods for estimation of storm speeds from other parameters, for example:

(i) As mentioned in section 2.2.2, Gurka (1976) noted that the storm speed is nearly equal to the maximum squall speed.

(ii) Moncrieff and Miller (1976) gave a formula (see section 4.3.2b) modified by Fernandez and Thorpe (1979) to

$$\text{storm speed} \quad c = \bar{U} + 0.32\,(\text{APE})^{\frac{1}{2}} \qquad (3.5)$$

where $\bar{U}$ is the component of the mean tropospheric wind in the direction of propagation, and APE is defined by (3.1).

(iii) It will be shown later (section 5.6.2) that the storm velocity should be expected to be close to the maximum mid-level environmental wind velocity, a result confirmed observationally by Fernandez (1981).

When these methods are used to estimate the speed of Minna SQL's, errors are typically several m/s, similar to those found by Fernandez and Thorpe (1979) and Fernandez (1981) for SQL's over Venezuela, the East Atlantic and West Africa. But what is really required is to know direction as well. This is not actually considered by Gurka in (i), while Moncrieff and Miller's study (ii) is essentially a two-dimensional one, which presupposes knowledge of the direction of propagation. Plausibly however, the respective directions of the squall and mean wind may be assumed in these two cases, so that the three estimates of the storm velocity are:

(i) the squall velocity
(ii) the Moncrieff - Miller velocity, i.e. the mean wind velocity, with speed increased by an amount $0{\cdot}32\,(\text{APE})^{\frac{1}{2}}$.
(iii) the maximum wind velocity.

These are tested against the data in fig 3.8. Various mean velocities are shown in fig 3.8a, these being: storm: from 079° at 16·4 m/s; squall: 093°, 14·5 m/s; mean: 099°, 6·9 m/s; maximum: 089°, 15·5 m/s. On average, the storm moves faster than any of these latter three, and from a more northerly direction. In fig 3.8b, u and v are the westerly and southerly components of the storm velocity, each 5 m/s x 5 m/s square giving the number of times values of u and v occur in the relevant range. Figs 3.8 c, d and e are similar, with u and v replaced by relative velocity components u_r and v_r along and perpendicular to the (i) squall, (ii) Moncrieff - Miller, and (iii) maximum velocities respectively. In these latter three cases, the magnitude of the relative velocity, $|\underline{v}_r| = (u_r^2 + v_r^2)^{\frac{1}{2}}$ gives a measure of the error of the estimate; in each case, values of $|\underline{v}_r|$ as great as the actual storm speed are not uncommon. In particular, for the squall and Moncrieff - Miller velocities, $|\underline{v}_r|$ exceeds the storm speed in 20% of all cases, while the magnitude of the vector mean value of $\underline{v}_r$ is at least 5 m/s, indicating an unacceptably large systematic error, in

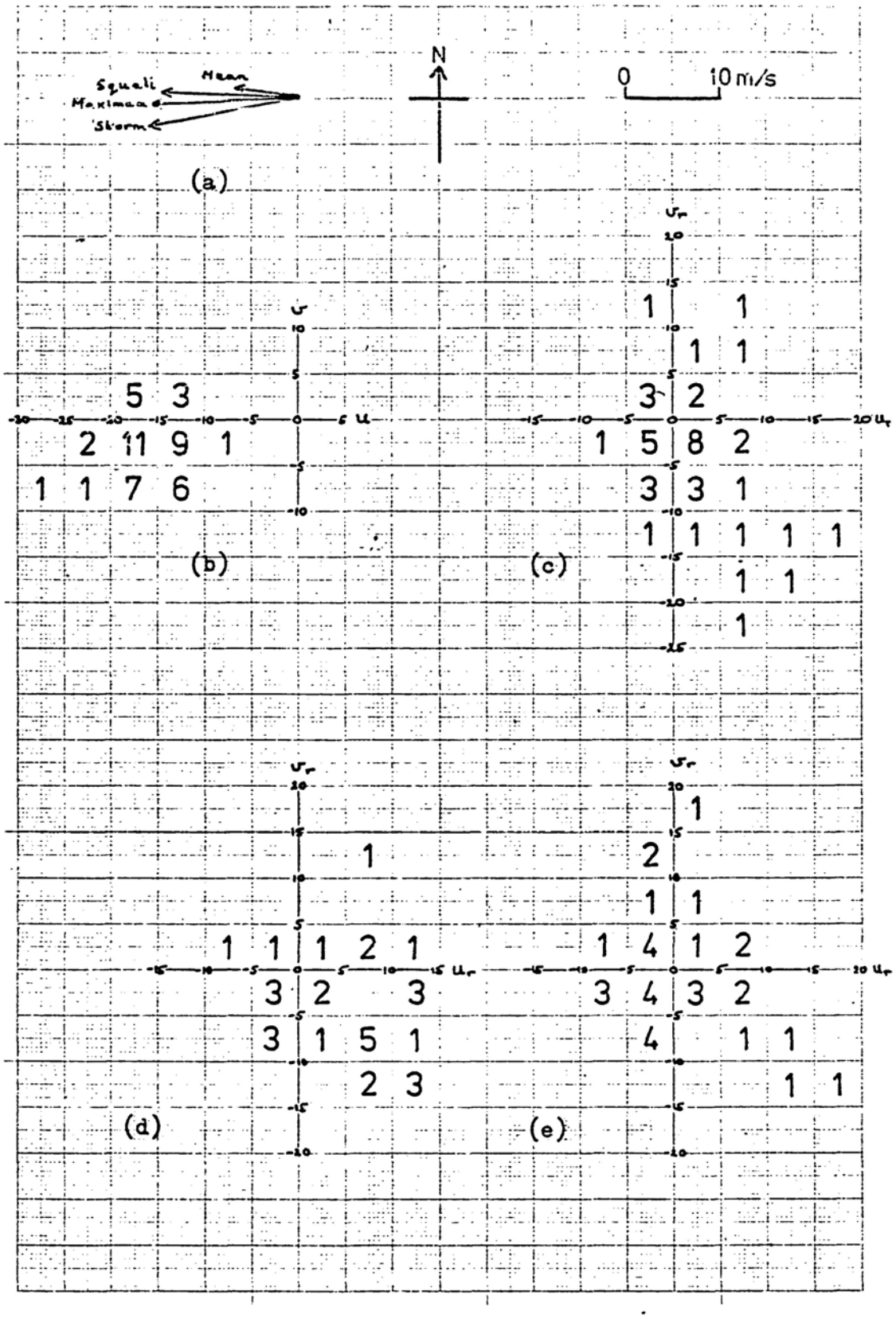


Fig 3.8. Velocity statistics for squall lines affecting Minna in the period: June 1974 - August 1976.

(a) Means of storm velocity, squall velocity, maximum mid-tropospheric wind velocity and mean tropospheric wind velocity.

(b) - (e) Scatter diagrams of storm velocity (m/s) relative to:

(b) the ground (c) squall velocity (d) 'Moncrieff-Miller' velocity

(e) maximum mid-tropospheric wind velocity.

addition to the enormous scatter. The systematic error and scatter are somewhat less for the maximum velocity, which is thus suggested as the most satisfactory general estimate of SQL velocity, thus confirming the results of Fernandez (1980). However, even this is subject to substantial errors, and, in the particular situation at Minna, the mean storm velocity 079°, 16·4 m/s is an even better estimate, as indicated by the smaller scatter in fig 3.8b than in any of the other diagrams.

3.2 MEAN ATMOSPHERIC CONDITIONS AT MINNA DURING THE SQUALL LINE SEASON.

3.2.1 Time - Height Sections.

Figs 3.9 and 3.10 show time-height sections (slightly simplified) at Minna for the periods 10 July - 1 August and 1 - 23 September 1974, based on midday and midnight soundings. Times of occurrence of SQL's at Minna are denoted ▽ ; the dashed arrow on 20 August indicates uncertainty in the identification of this storm as a SQL. Dashed contours indicate absence of two or more consecutive soundings.

The velocity components u and v are taken along and perpendicular to the mean SQL velocity during the GATE period: from 083° at 17·5 m/s. This mean differs slightly from the 079°, 16·4 m/s obtained over the 27 month period in section 3.1.3. Henceforth however, the GATE mean will be adopted as the reference mean, partly for consistency, and partly because of the greater confidence in the value brought about by the use of satellite images. Since the GATE mean direction, 083°, differs only slightly from due east, u and v will for convenience be referred to as 'westerly' and 'southerly' components.

In the wind profiles 3.9a and 3.10a, all 'westerlies' ($u > 0$) are hatched, but 'easterlies' are only hatched if in excess of 8 m/s. Near the surface are 'westerlies', whilst aloft are 'easterlies' with a fluctuating AEJ at 650 mb, and a stronger, but also fluctuating TEJ at upper levels. As in Mansfield (1977) (fig 2.12), all SQL's occur when there is a strong AEJ maximum, here at least 8 m/s and normally more than 12 m/s, confirming Dugdale's forecasting rule quoted in section 2.1.1; correspondingly the TEJ is, on the whole, relatively weak. The lack of SQL's in July could be explained by lack of these conditions. The transverse wind components, figs 3.9b and 3.10b, are generally weaker, with 'southerly' (positive v) and 'northerly' alternating in lower levels, consistent with the passage of easterly waves, though the reversal aloft found by Reed et al (1977) is not evident. There is no

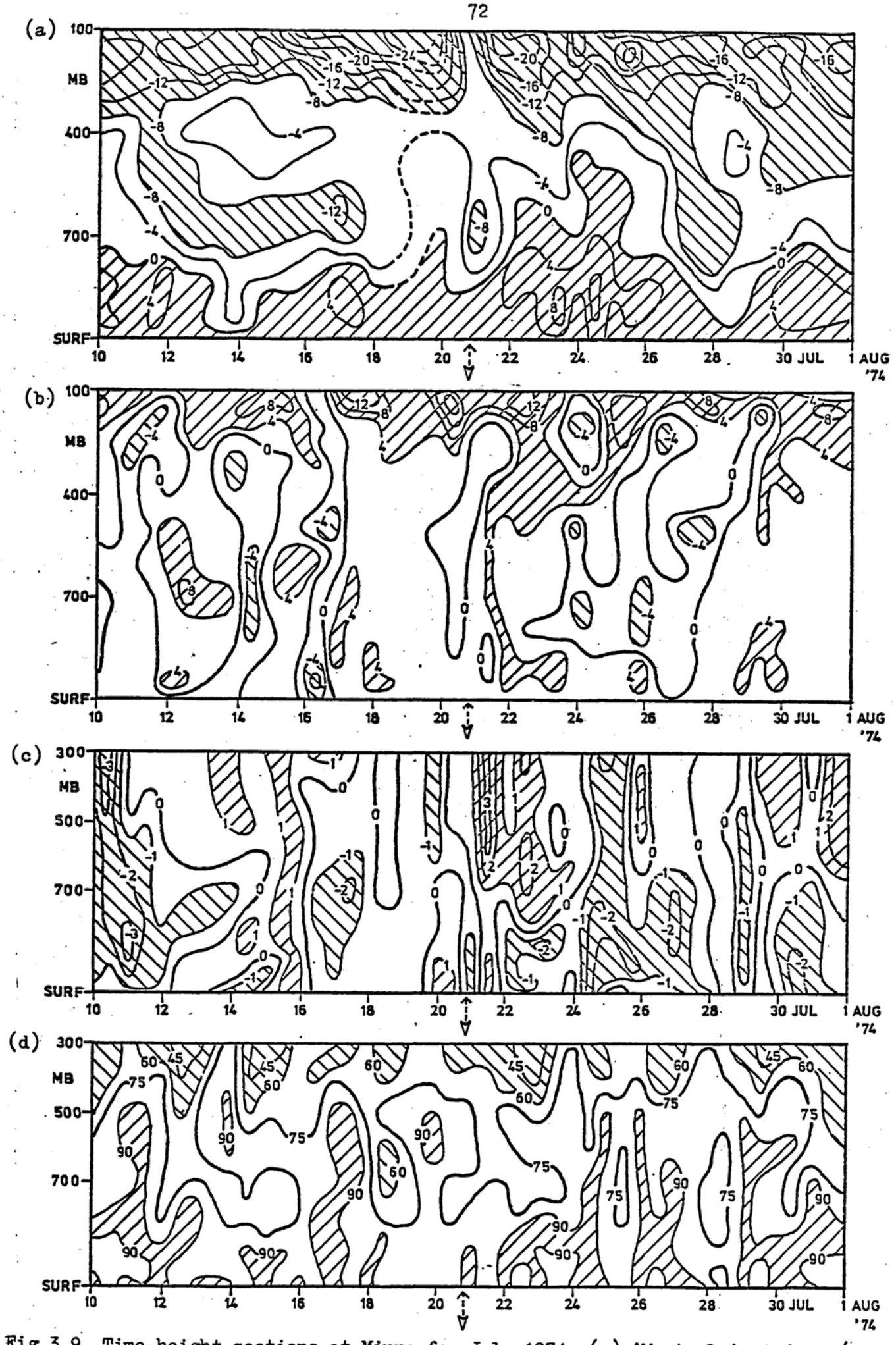


Fig 3.9. Time-height sections at Minna for July 1974 (a) 'Westerly' wind u m/s (b) 'Southerly' wind v m/s (c) Temp. deviation $\delta T^{o}C$ (d) Rel. humidity U% .

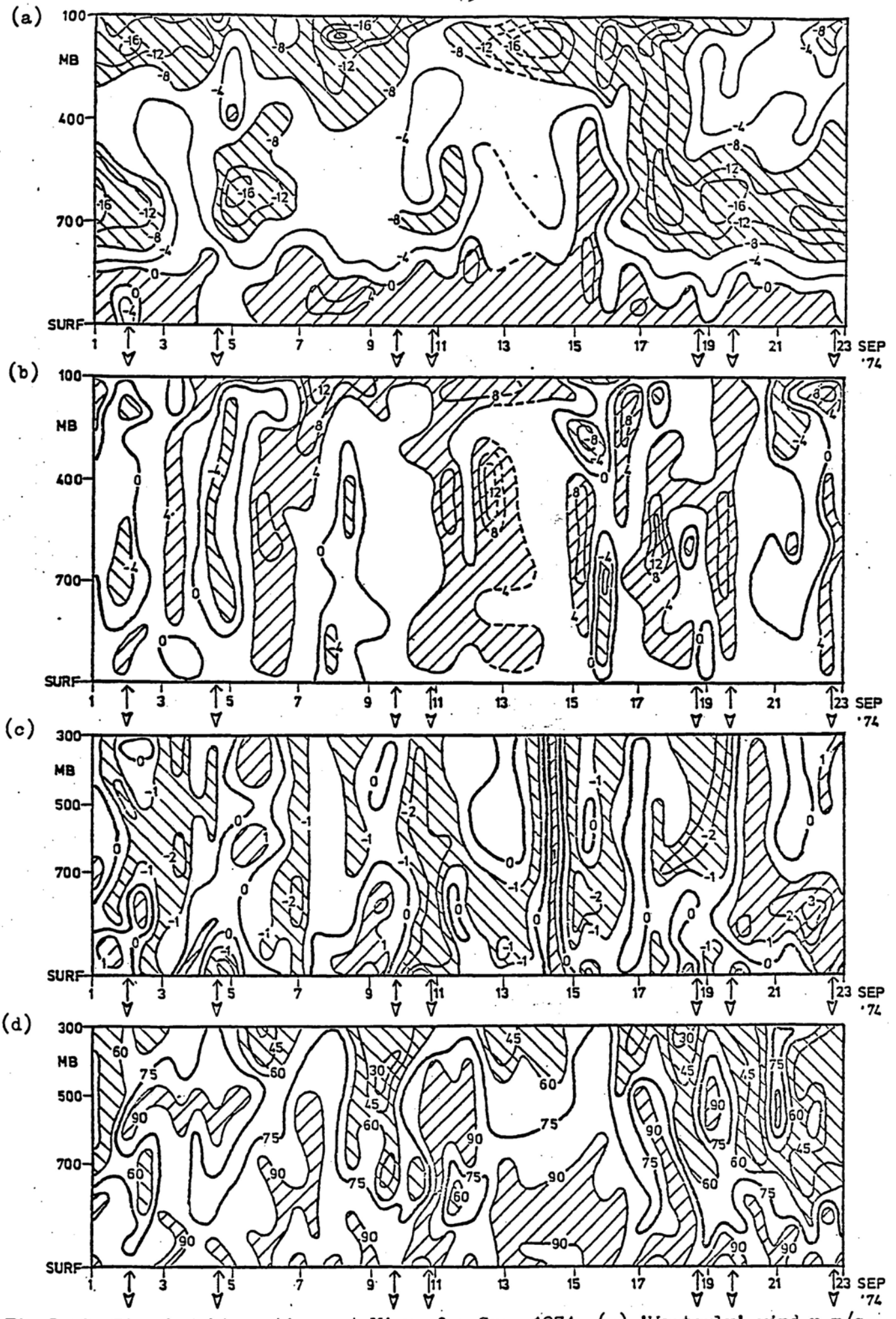


Fig 3.10. Time-height sections at Minna for Sep. 1974 (a) 'Westerly' wind u m/s (b) 'Southerly' wind v m/s (c) Temp. deviation $\delta T^{\circ}C$ (d) Rel. humidity U% .

clear connection between this wind component and the occurrence of SQL's.

The temperature deviation δT in figs 3.9c and 3.10c is computed as the difference between the actual temperature and the appropriate GATE mean for the level and the time of day. Passage of easterly waves is again suggested by the alternation of warm and cold anomalies at low levels, and there is some evidence of a reversal aloft as expected from Reed et al's (1977) section, fig 2.17c. The easterly wave correlation of cold anomalies with southerly winds is not particularly obvious however. Reports of SQL's tend to coincide with warm anomalies at the surface, though the relationship is not as clear as with the 'easterly' jet.

The sections for percentage relative humidity U, figs 3.9d and 3.10d, show alternatively dry and moist conditions, there being some correlation between moist conditions and southerly winds. Squall lines tend to occur in conditions where there is moist air near the surface ($U \geq 90\%$), but dry air ($U \leq 60\%$) reaching down to 700 mb or lower. These conditions are quite common in September, but rare in July, when movement of the ITCZ to the north gives a generally greater depth of moist air (section 2.3.1), and hence very few SQL's.

In conclusion, the time-height sections broadly confirm the conditions appropriate for SQL occurrence as a low level jet, with a shallow warm moist surface layer surmounted by a dry layer. Fluctuations in the variables suggest passage of easterly waves, but they are not sufficiently regular to permit correlation of SQL occurrence with wave phase.

3.2.2 GATE Mean Midday and Midnight Soundings.

For the period 10 June - 22 September 1974, mean soundings at 1200 and 0000 GMT were computed at Minna for days on which SQL's did not occur, and their differences were examined, standard errors being computed in order to obtain a measure of significance. If for the variables X_{12} and X_{00}, numbers of observations available over the period are N_{12} and N_{00}, and the standard deviations are σ_{12} and σ_{00}, the standard error of the difference of the means is

$$e = \left(\frac{\sigma_{12}^2}{N_{12}} + \frac{\sigma_{00}^2}{N_{00}} \right)^{\frac{1}{2}} \qquad (3.6)$$

The means $\bar{X}_{12}$ and $\bar{X}_{00}$ may then be regarded as significantly different at the 95% confidence level if

$$\left| \bar{X}_{12} - \bar{X}_{00} \right| > 2\,e \qquad (3.7)$$

(see for instance Spiegel 1972). Results are shown in fig 3.11, error bars of length e being drawn.

As in the time-height sections, winds are taken along and perpendicular to the GATE mean direction of SQL motion (083°); these are shown in fig 3.11 a and b, the mean SQL speed (17·5 m/s) being indicated by a dash-dot line. Both 1200 and 0000 means show a strong TEJ at 150 mb, that at 0000 being slightly stronger, though the difference is not really significant; the AEJ maximum at 650 mb is, in both cases much weaker. A similar wind profile was obtained for cloud clusters by Frank (1978). The most significant difference between the 1200 and 0000 mean winds is an increased 'southerly' component in the middle troposphere during the day, possibly the adjustment flow generated by temperature differences due to the greater energy absorption during the day, and emission at night of the cloud tops as compared to the clear air to the north (McBride and Gray 1980); the greater nocturnal emission was earlier noted in section 2.3.1 in connection with maintenance of the TEJ. The other significant difference between the 1200 and 0000 means is the surface wind is nearly calm at night.

The potential temperature and temperature profiles (fig 3.11 c, e) show little diurnal variation except near the surface, where there is significant solar warming at 1200. In contrast, θ_e shows an increase in upper levels at night, and this is rendered significant by its occurrence at all levels from 850 to 300 mb. This increase may be traced to increases at night in upper level moisture, as indicated by the profiles of mixing ratio and relative humidity (fig 3.11 g, h), lower levels showing a corresponding decrease. Such a change is presumably the after-effect of mixing upwards of low level moisture by afternoon convection.

In considering SQL conditions, one further variable is helpful: parcel log potential temperature excess $\delta\phi_p$, defined by (3.3), the initial level being taken at 950 mb. The 0000 profile (fig 3.11f) shows less buoyancy at all levels than at 1200, and this is particularly significant below 800 mb, where there is a strong negative buoyancy at 0000, but very little negative buoyancy at 1200. Thus in the afternoons on non-SQL days, there is very little hindrance to small convection, and consequently little opportunity for formation of the warm moist surface layer necessary for SQL development.

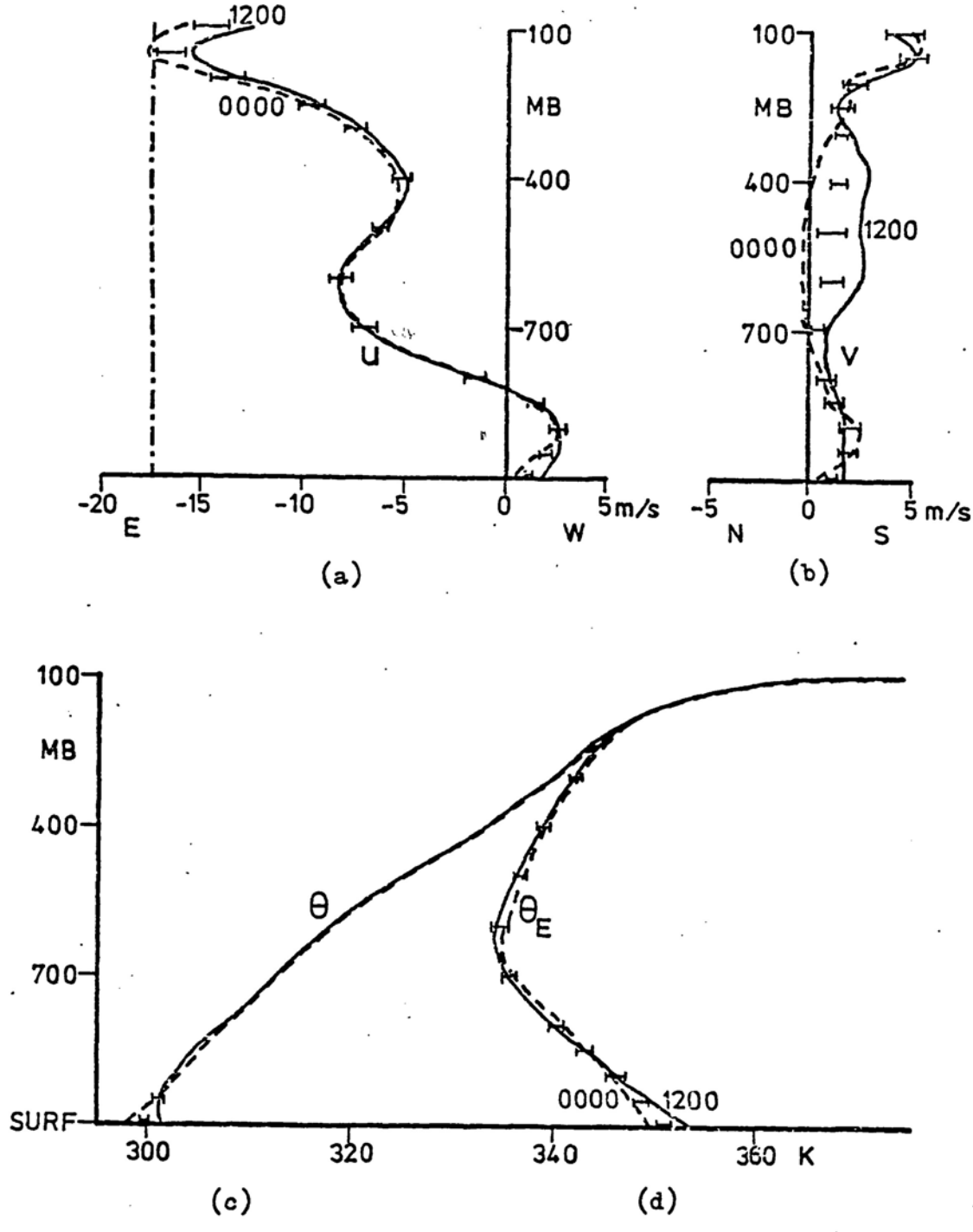


Fig 3.11. Minna means for July - September 1974 on non-squall line days.

(a) 'Westerly' wind component u m/s (b) 'Southerly' wind component v m/s

(c) Potential temperature θ K (d) Equivalent potential temperature θ_E K

Full line: 1200 mean Dashed line: 0000 mean

Dash-dot line: mean speed of squall line

Bars denote one standard error for difference of means.

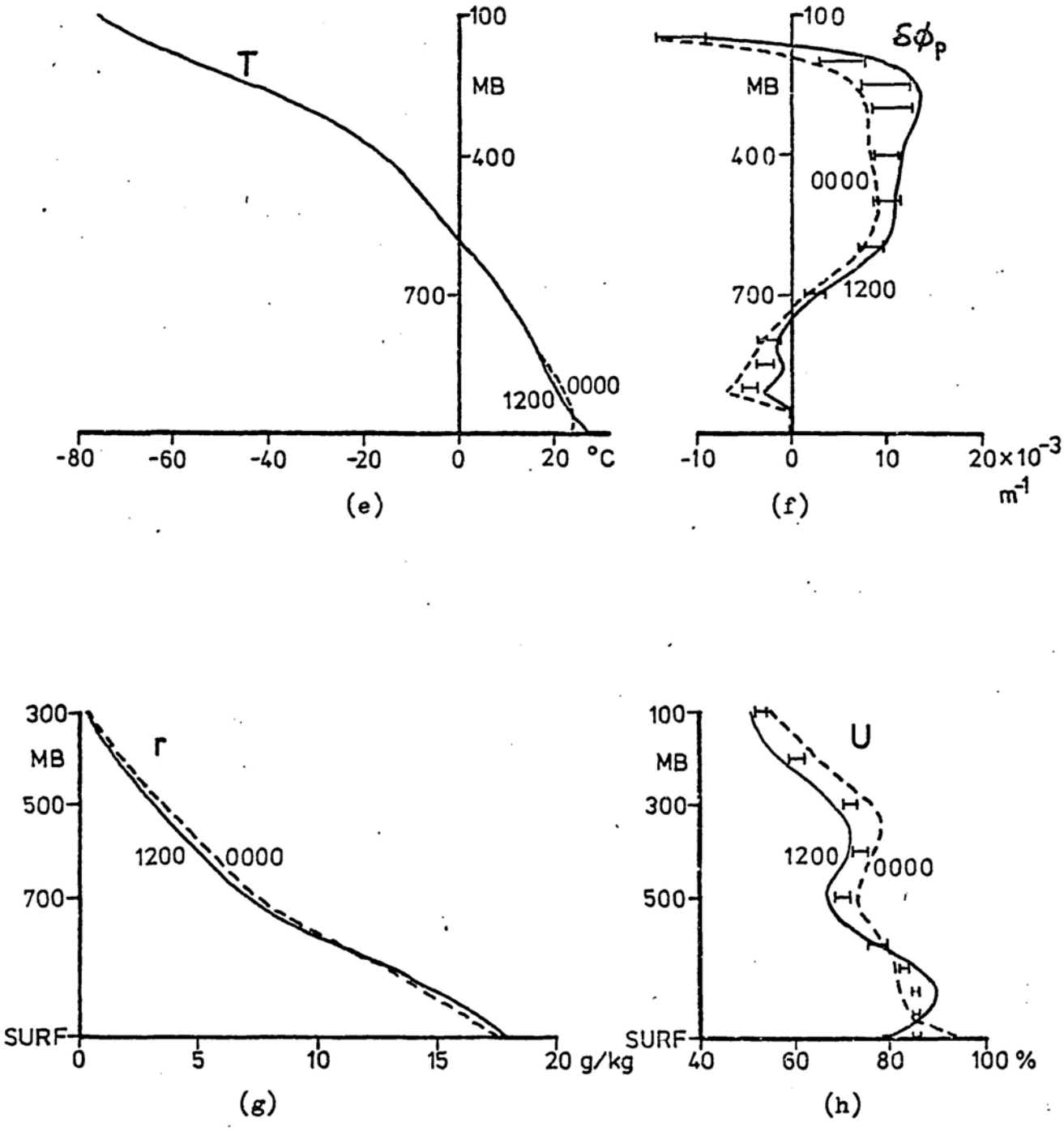


Fig 3.11. Minna non-squall day means continued.

(e) Temperature T°C (f) Parcel excess log potential temperature $\delta\phi_p$

(g) Mixing ratio r g/kg (h) Relative humidity U %

Full line: 1200 mean Dashed line: 0000 mean.

3.3 ATMOSPHERIC CHANGES ASSOCIATED WITH SQUALL LINES AT MINNA.

3.3.1 Mean 24 Hour Changes.

The relatively large number of midday soundings available at Minna, compared with midnight soundings meant that an obvious way of studying the change associated with passage of a SQL was to compare means of midday soundings before and after passage, including only those cases where both soundings were available. For some variables, very little change was detectable, the 24 hour time span being considerably greater than the time taken to revert to pre-squall conditions; other variables did however show a significant change. In this case, since soundings are available both before and after passage of each SQL which was included, it is possible to find the standard deviation σ of the difference between the two soundings, and evaluate the standard error as

$$e = \frac{\sigma}{N^{\frac{1}{2}}} \qquad (3.8)$$

(where N is the number of SQL's included). This is a more satisfactory measure than the standard error as computed from the separate standard deviations σ_{before} and σ_{after} of the soundings before and after a SQL, the two being related by

$$\frac{\sigma}{N^{\frac{1}{2}}} \leq \left(\frac{\sigma_{before}^2 + \sigma_{after}^2}{N} \right)^{\frac{1}{2}} \qquad (3.9)$$

Results are shown in figs 3.12, based on a total of 60 SQL's during the whole 27 month period June 1974 - August 1976.

The wind profiles are still taken along and perpendicular to the GATE mean direction of propagation, 083°, with the dash-dot line giving the mean SQL speed of 17·5 m/s. The 'westerly' means (fig 3.12a) differ from those on non-SQL days in that the upper level TEJ is much weaker, while the AEJ has a much stronger maximum at 650 mb, a situation similar to that found in Frank's (1978) comparison of cloud clusters with SQL's. The AEJ is actually stronger than the TEJ both in the means and in most of the individual soundings, which supports the conclusion of section 2.3.1 that a necessary condition for occurrence of a SQL is a strong middle level wind maximum, preferably stronger than any upper level wind. The 'southerly' means in contrast show very little shear.

After passage of the SQL, the 'westerly' mean shows very little change except for an increase from 400 to 200 mb. The lack of low

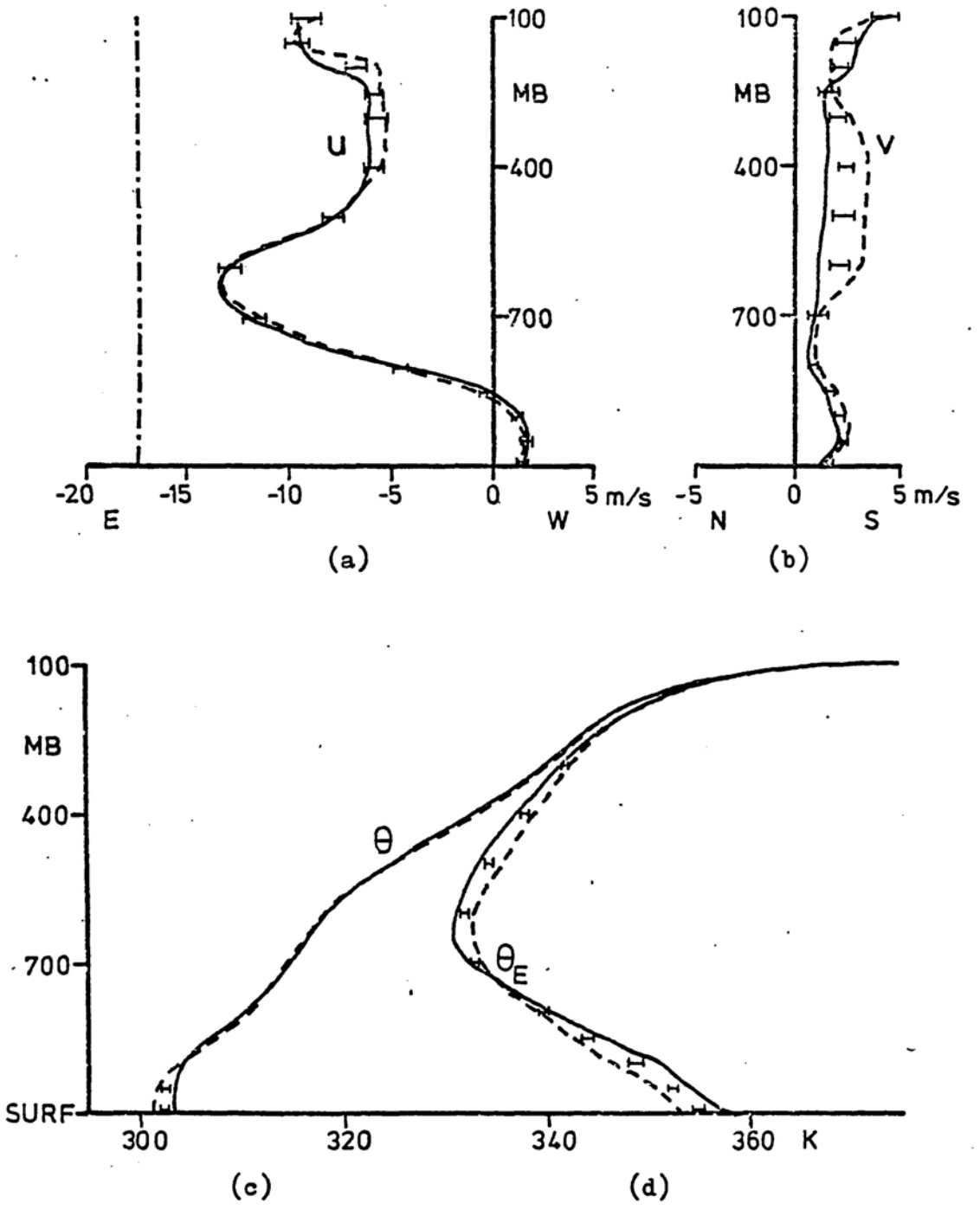


Fig 3.12. Minna means before and after squall line for 24 hour interval.

(a) 'Westerly' wind component u m/s (b) 'Southerly' wind component v m/s
(c) Potential temperature θ K (d) Equivalent potential temperature θ_E K

Full line: before Dashed line: after
Dash-dot line: mean speed of squall line
Bars denote one standard error for difference of means.

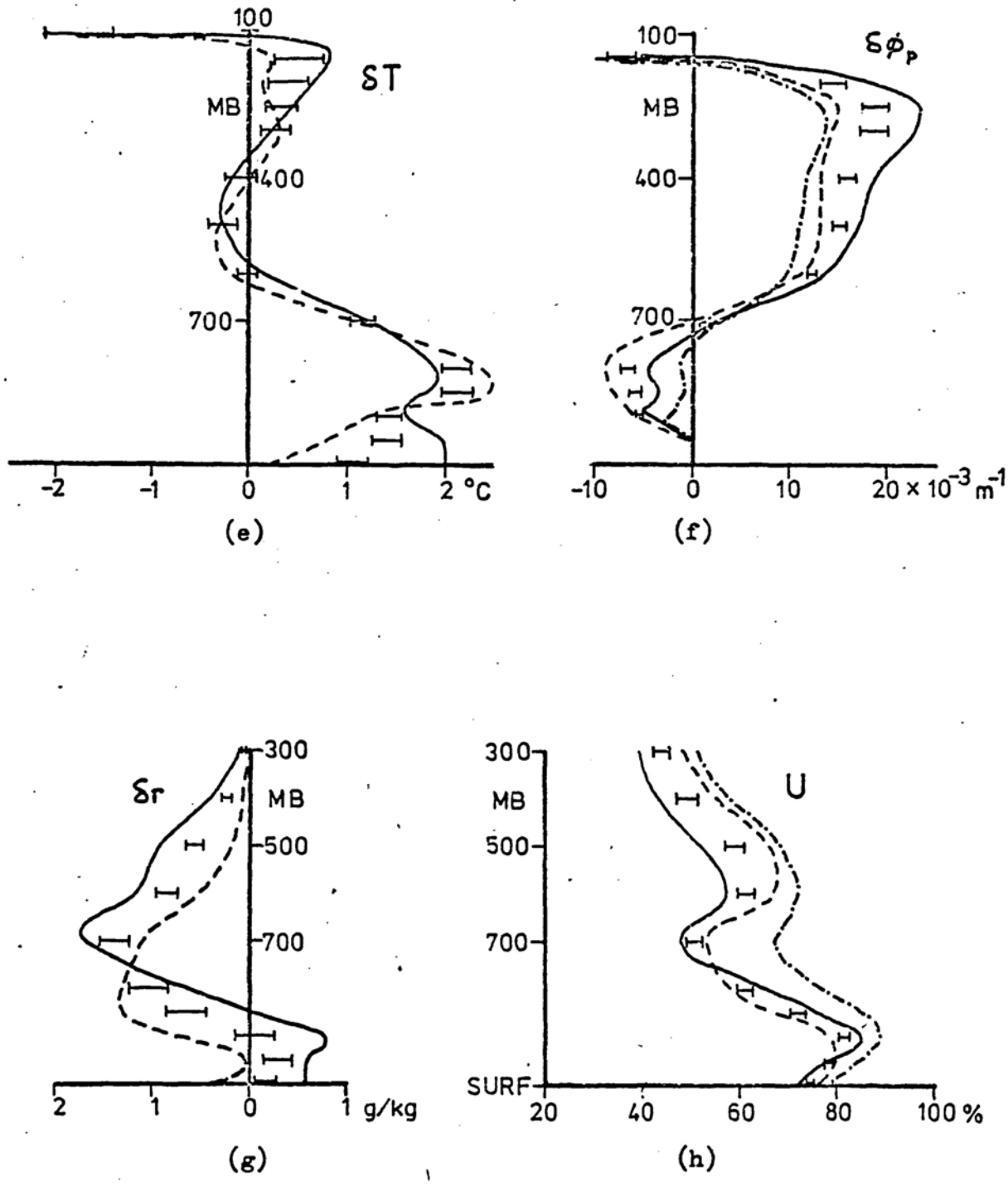


Fig 3.12. Minna 24 hour 'before and after' means continued.

(e) Temperature deviation $\delta T^{\circ}C$ (f) Parcel log potential temp. excess $\delta\phi_p$

(g) Mixing ratio deviation δr g/kg (h) Relative humidity U %

Full line: before Dashed line: after

Dash-dot line: non-squall mean.

level change is in sharp contrast to the increase in low level shear observed in Vimhex (fig 2.9a) and other studies, suggesting that the wind profile returns to pre-squall conditions in substantially less than 24 hours. Surprisingly however, there is a significant increase in the 'southerly' mean between 600 and 300 mb. Retention of southerly momentum of low level air rising in updraughts is a possible, though unlikely explanation; more plausibly, the change is due to movement of easterly wave troughs past Minna, bearing in mind the preferred generation of SQL's ahead of the troughs (section 2.3.2).

The potential temperature profile (fig 3.12c) shows significant cooling at low levels, consistent with convective scale downdraught outflow (section 2.2.3b). The temperature changes are however more clearly seen on the δT profile (fig 3.12e), where excess temperature above the GATE mean non-SQL 1200 sounding (fig 3.11e) is plotted. Now, apart from the low level cooling, a significant warming is evident from 850 to 750 mb, associated with mesoscale downdraught outflow (section 2.2.3b), whilst above 300 mb there is cooling, which agrees with the finding of Fernandez (1980), but is in contrast to the heating found by Frank (1978) (section 2.2.3f), and suggests increased emission rather than absorption by the cloud tops. The mean pre-squall sounding shows a temperature 2°C above the non-SQL mean at levels up to 800 mb, indicating the need for a warm surface layer. The large anomalies at upper levels are probably spurious, arising from the fact that the GATE mean on which they are based is not a good approximation at upper levels to the mean for the whole 27 month period.

The θ_E profile (fig 3.12d) shows a significant post-squall decrease below 750 mb and increase above; as the values are means over a considerable length of time relative to the SQL, no conclusion can be drawn about origin of the various layers. Except near the surface, the changes in θ_E are due to changes in mixing ratio, seen in fig 3.12g, where the excess δr above the GATE non-SQL 1200 mean (fig 3.11g) is plotted. The near balance of the low level drying and upper level moistening is similar to the VIMHEX result (fig 2.9d). The pre-squall conditions are slightly moister than the non-SQL mean at low levels, but very much drier above 850 mb, so much so that even after the moistening brought about by the updraught ascent, the post-squall sounding remains significantly drier than the non-SQL mean. This importance of the dry air aloft is again evident in the relative humidity profile (fig 3.12h). Here, both pre and post-squall soundings have a smaller relative humidity at all levels than the non-SQL mean (dash-dot line),

though the post-squall surface relative humidity approaches the non-SQL mean, as surface cooling more than compensates for the drying.

The pre-squall $\delta\phi_p$ profile (fig 3.12f) shows a much greater negative buoyancy below 700 mb than for the non-SQL mean, but significantly greater positive buoyancy above, so that conditions are ideal for accumulation of potential energy in a surface layer through solar heating. The post-squall sounding shows even greater negative buoyancy below 700 mb, so it is not surprising that convection is suppressed after passage of a SQL. There is however an overall net positive area, which, taken with the restoration of pre-squall wind conditions means that occurrence of a second SQL within a relatively short space of time is not unlikely; examination of table 3.1, for instance, furnishes nine occasions on which SQL's occurred within 24 hours of each other.

3.3.2 Mean 12 Hour Changes.

When considering 12 hour changes, relatively few pairs of 'before and after' soundings were available (only 21), so that it was necessary to include together cases where the pre-squall sounding was at 1200 with those where it was at 0000. Since these cases did not occur in equal numbers, the following technique was adopted to eliminate diurnal effects. The difference of each sounding from the relevant GATE non-SQL mean, 1200 or 0000 as appropriate (fig 3.11), was found, and with the exception of δT and δr, this was now added to the overall mean non-SQL sounding (1200 and 0000 combined), to give the adjusted sounding which was used.

Since most cases where 12 hour 'before and after' soundings were available fell during GATE, SQL velocities were usually available, and it was possible to find storm-relative mean winds (fig 3.13 a,b). The component u_r along the direction of propagation shows inflow at all levels; the dash-dot line indicates the mean storm-relative speed of the ground. A change in the low-level winds can now be seen after passage of the SQL, with decreased relative flow below 800 mb; above, relative flow is increased up to 600 mb, and above 500 mb. These changes in the relative flow are more complicated than those observed in VIMHEX (fig 2.9a) and other studies, with the result that evaluation of momentum transfer is difficult; a possible alternative approach would be consideration of divergence associated with mesoscale vertical motions, and this is examined in the next section.

The changes in the other variables are very similar to those obtained in the 24 hour 'before and after' study; less confidence can

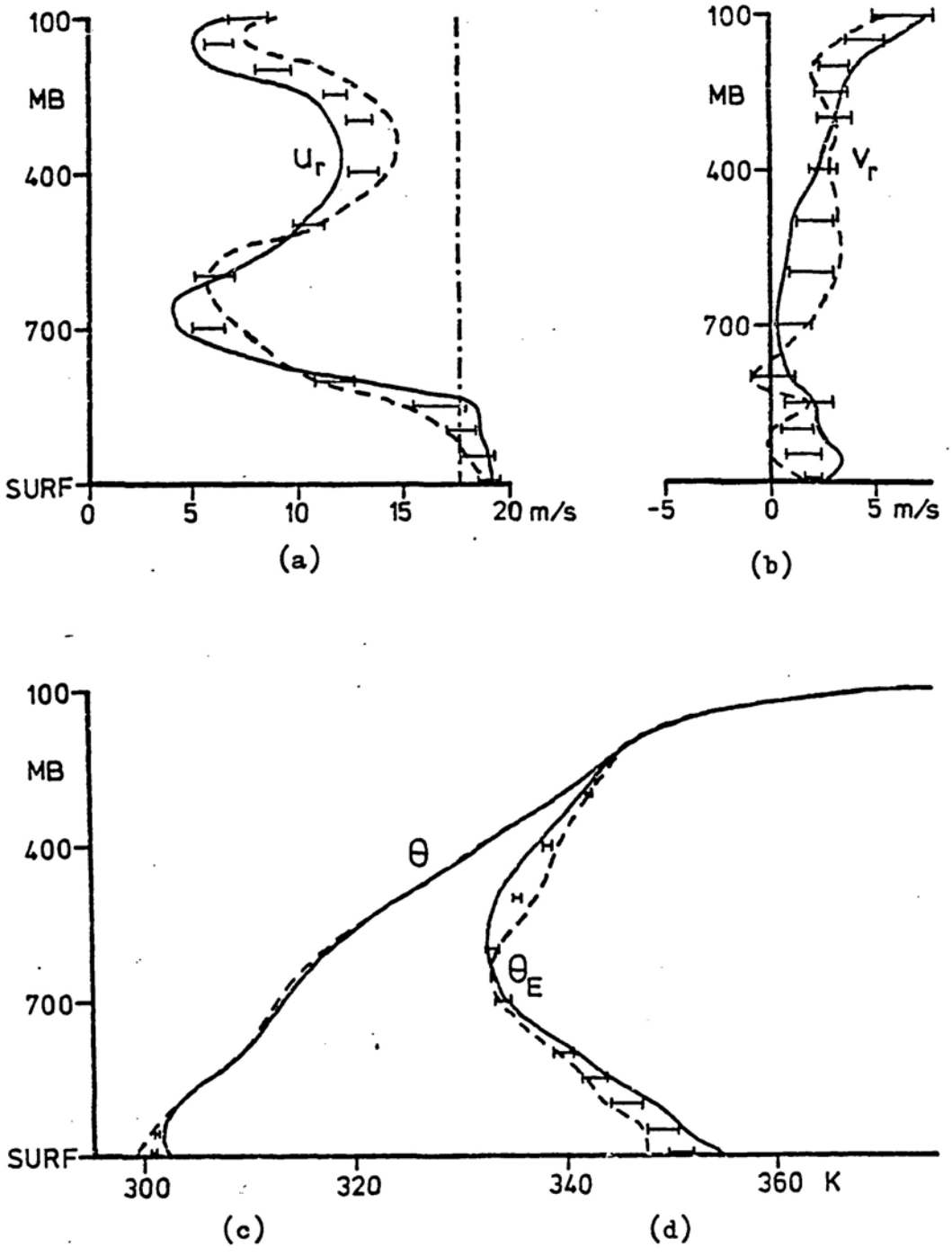


Fig 3.13. Minna means before and after squall line for 12 hour interval

(a),(b) Storm-relative flow u_r,v_r m/s along and transverse to motion of SQL.
(c) Potential temperature θ K (d) Equivalent potential temperature θ_e K

Full line: before Dashed line: after
Dash-dot line: mean speed of squall line.

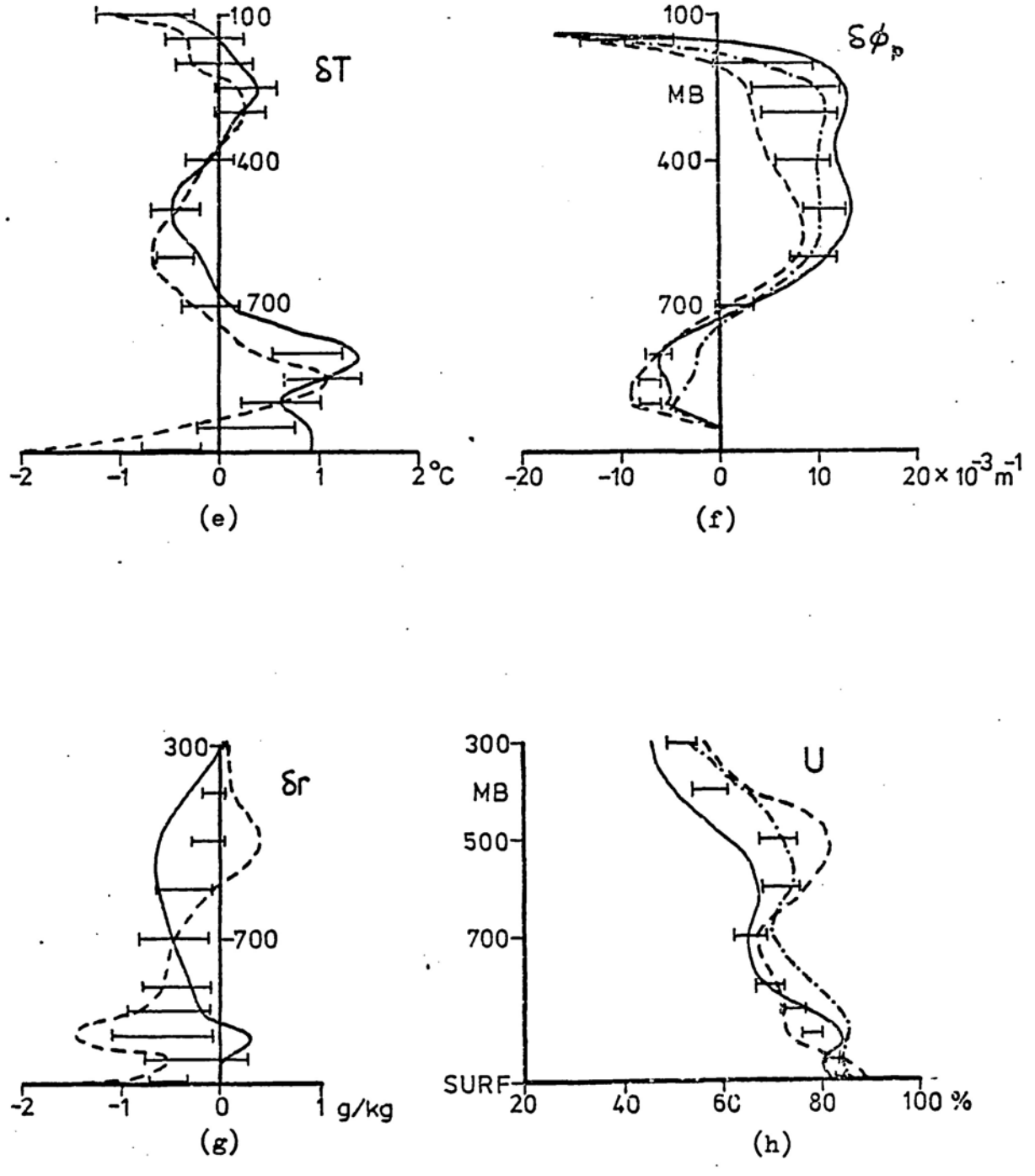


Fig 3.13. Minna 12 hour 'before and after' means continued.

(e) Temperature deviation δT°C (f) Parcel excess log potential temp. $\delta\phi_p$

(g) Mixing ratio deviation δr g/kg (h) Relative humidity U %

Full line: before Dashed line: after

Dash-dot line: non-squall mean.

however be placed in the significance of the changes owing to the relatively small number of SQL's included.

A tephigram showing temperature T and dew point T_d for the mean 12 hour 'before and after' soundings, and for the non-SQL mean is given in fig 3.14. The warm moist surface layer with dry air aloft can be seen in the 'before' sounding, while there is some evidence of the 'onion' shape described by Zipser (1977) (section 2.2.3b), though this is not as apparent as in Zipser's soundings (fig 2.8), which were taken much closer to the squall front.

3.3.3 Vertical Section.

In producing vertical sections, it was found that differences from one SQL to another resulted in far too much scatter when compositing was carried out as in section 2.2.3d. To reduce this, storms were grouped together in 150 km blocks according to the distance from the sounding, and each 150 km block was averaged (this technique also reduces fluctuations due to cellular structure of an individual SQL such as give rise to much of the scatter for example in fig 2.7). Considerable smoothing was thus achieved, and satisfactory values obtained, except unfortunately in the 150 km either side of the squall front, where very few soundings were available (as few SQL's occurred close to midday or midnight). Since midday and midnight soundings were grouped together, the technique employed in the 12 hour 'before and after' study was used to eliminate diurnal effects. Results are shown in fig 3.15.

Wind components were again taken relative to the SQL motion. The component u_r in the direction of propagation (fig 3.15a) shows inflow everywhere ahead, outflow everywhere behind, except for three small regions shown dotted; the scarcity of soundings means that no significance should be attached to these. Other contours have been drawn to correspond to those in the time-height sections (figs 3.9a, 3.10a), assuming a mean SQL velocity of 17·5 m/s from 083°. The 17.5 m/s contour then represents air at rest relative to the ground; flow would be 'westerly' in the three small hatched regions near the surface ($u_r > 17{\cdot}5$ m/s), 'easterly' everywhere else, with 'easterly' velocities in excess of 8 m/s being shown hatched. Arrival of the squall front can be seen to be accompanied by a lowering of the 650 mb 'easterly' jet, with decreased relative flow below 650 mb, increased relative flow above. The fact that there is normally an easterly squall at the surface associated with arrival of the SQL presumably means that if

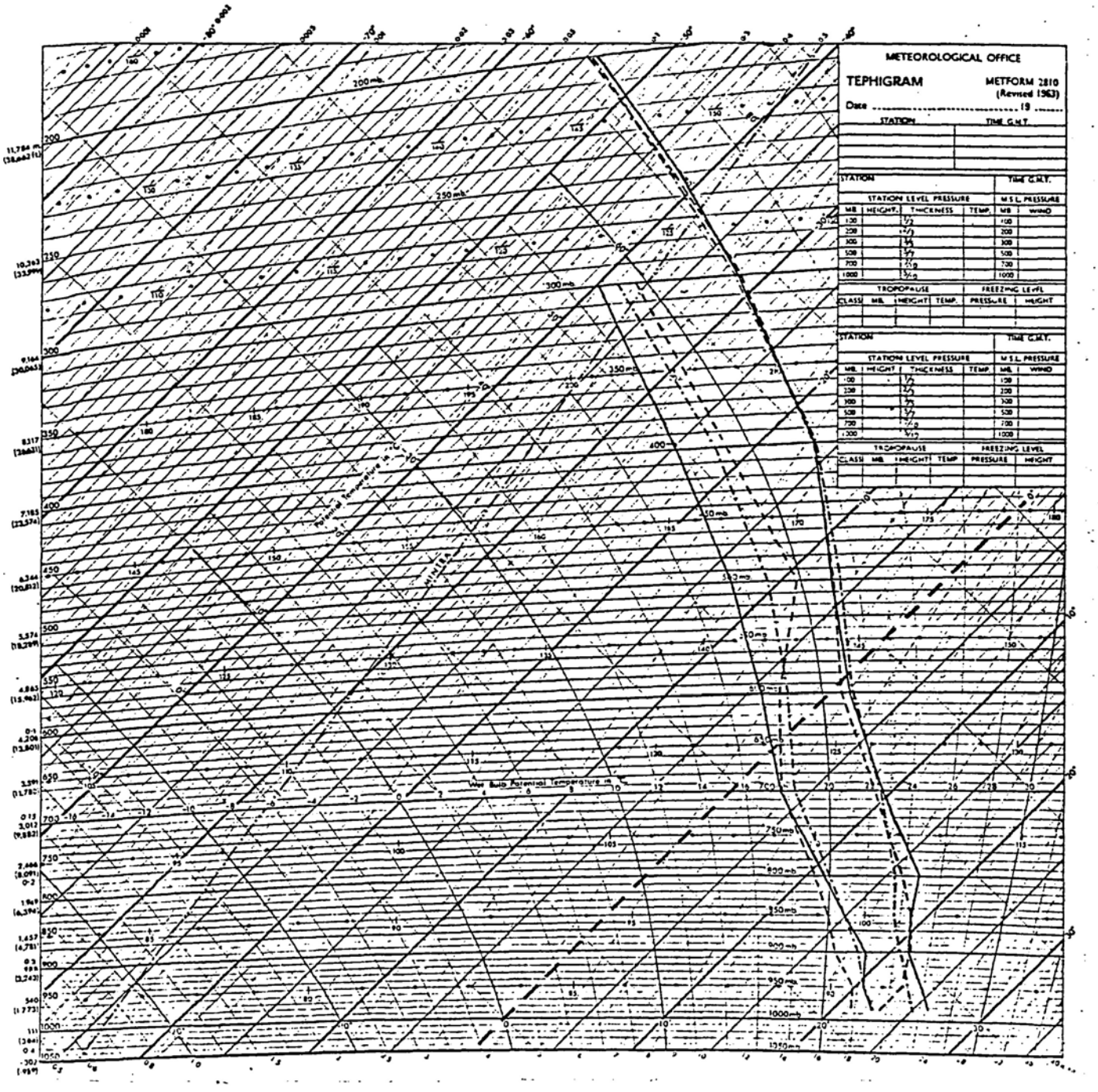


Fig 3.14. Minna mean soundings for temperature T and dew point T_d.
Full and dashed lines are 12 hour 'before and after' means;
dash-dot line is non-squall line mean.

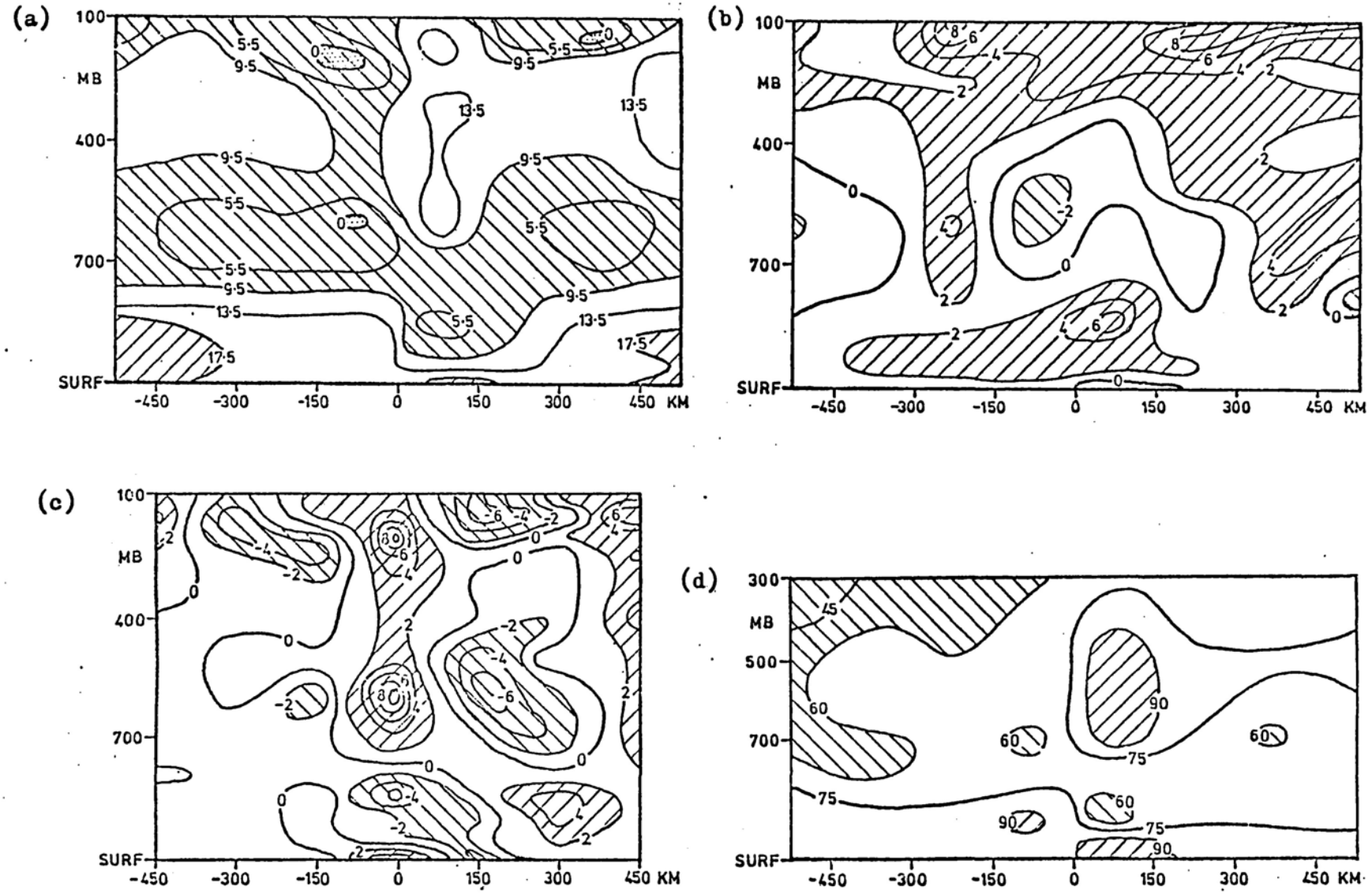


Fig 3.15. Composite vertical section through squall line.
(a) Storm-relative wind component in direction of propagation, u_r m/s (b) Storm-relative transverse wind component, v_r m/s
(c) Gradient of storm-relative wind, $\partial u_r/\partial x\ 10^{-5} s^{-1}$ (d) Relative humidity, U %

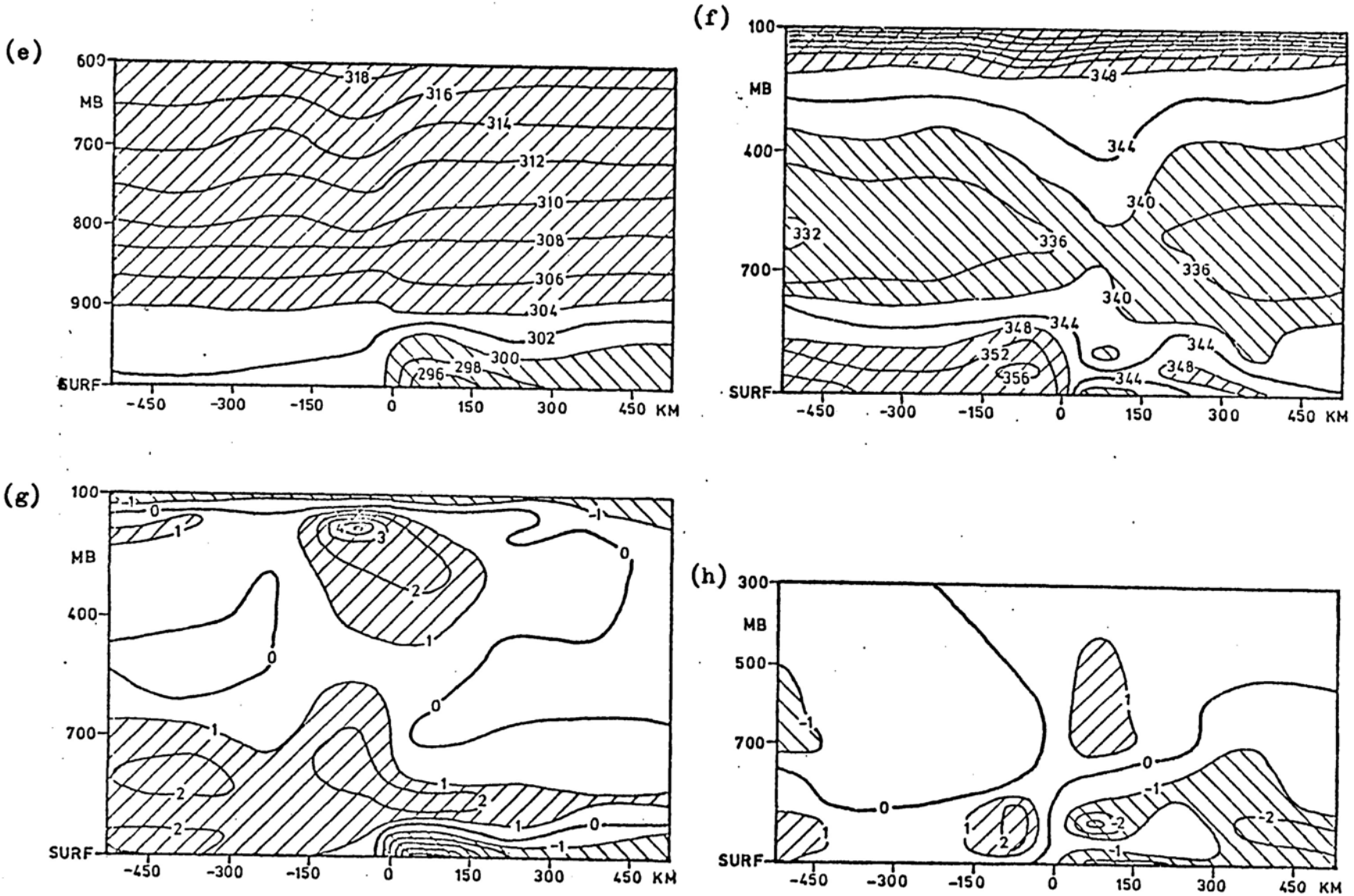


Fig 3.15. Composite vertical section through squall line continued.
(e) Potential temperature θ K (note different vertical scale)
(f) Equivalent potential temperature θ_E K
(g) Temperature deviation δT °C
(h) Mixing ratio deviation δr g/kg.

data of sufficient resolution were available, the 'easterly' jet would actually be seen to reach the surface. However, results here show instead onset of 'westerly' flow at the surface, but as this was observed in only one of the two soundings which fall an this 150 km block, it is assumed to be spurious. The lowering of the jet agrees with the results of Zipser (fig 2.7) and Obasi (fig 2.10a), while the changes in the relative flow are similar to those of VIMHEX (fig 2.9). The fact that the jet has recovered its pre-squall height after 300 km, or, equivalently 6 hours, would explain the absence of any clear indication of these effects in the 24 and 12 hour 'before and after' soundings. The transverse velocity component v_r is shown in fig 3.15b. Before arrival of the SQL, middle level winds have a small 'northerly' component, while at the surface there is 'southerly' flow. Afterwards, the middle level winds become increasingly 'southerly', consistent with the 'before and after' soundings, whilst at low levels, the 'southerlies' at first become stronger before weakening.

Fig 3.15c shows the gradient of the relative wind, $\partial u_r/\partial x$ computed from fig 3.15a. To find the total divergence, $\partial v_r/\partial y$ would also be required, and this is not available for single station data. However, if one assumes no net divergence in the transverse direction (which would hold in the case of a truly two-dimensional system), the $\partial u_r/\partial x$ values would be actual divergences, so that mesoscale vertical velocities could be computed from

$$w = -\int_{surface}^{z} \frac{\partial u_r}{\partial x}\, dz \qquad (3.10)$$

With this assumption, ignoring the surface divergence which is probably spurious, the lower level convergence, upper level divergence on arrival of the SQL suggests strong upward motion (of order 20 cm/s), whilst behind, the middle level convergence, low level divergence is consistent with a slightly weaker mesoscale downdraught, as inferred thermodynamically by Zipser (1969) (section 2.2.3a). Thus it may be helpful to interpret the changes in the wind component in the direction of motion as the response to the buoyancy-induced vertical motion needed to satisfy continuity; this has the advantage over the concept of momentum transfer of being applicable even in more complicated cases, such as the 12 hour 'before and after' sounding (fig 3.13a) where, although there is a significant change in the relative flow, evaluation of momentum transfer is difficult. However, the results should be interpreted with extreme caution, since w at 100 mb as inferred from (3.10) is substantially different from zero in most places; furthermore, the

ASECNA results in fig 2.11 show a similar profile for vertical motion when only zonal divergence is considered, whereas the total divergence field only indicates upward motion.

The potential temperature section, fig 3.15e, shows a cooling of about 6 K at the surface on arrival of the SQL, whilst from 900 to 850 mb there is a warming of 1 K, with cooling again at upper levels. These changes are again evident from the temperature deviation (fig 3.15g), which also shows that pre-squall temperatures are 1° or 2°C above average; the large temperature excess at 150 mb immediately before the squall front is probably spurious, being a mean of only three soundings. Behind the squall front temperatures revert, initially rapidly, then more slowly to their pre-squall values; even after 500 km, or equivalently 10 hours, surface temperature is still 3°C below its pre-squall value so that, in contrast to the velocities, temperatures show a significant change in the 24 hour 'before and after' sounding (fig 3.12). In the θ_E field, fig 3.15f, averaging is now over a sufficiently short time scale relative to the SQL (in contrast to the 'before and after' soundings) to permit tracking of air parcels using conservation of θ_E. Thus the surface value 337 K immediately behind the squall front suggests an origin for the downdraught air around 600 mb, consistent with Zipser's conclusion (section 2.2.3a), while the 950 mb pre-squall value of 356 K indicates an outflow level of 150 mb.

The relative humidity section, fig 3.15d, shows pre-squall conditions to be moist below 850 mb, dry above. Arrival of the SQL results in the surface layer becoming nearly saturated, while there is considerable drying between 900 and 850 mb, and moistening above. Fig 3.15h however shows that mixing ratio is reduced at the surface, so the near-saturation must be achieved solely by the fall in temperature; at higher levels however, relative humidity changes can be attributed to corresponding changes in mixing ratio. As with the temperature sections, return to pre-squall conditions is at first rapid, then more gradual. Immediately behind the squall front, the cold nearly saturated surface layer, surmounted by warm dry air, then in turn by more nearly saturated air, would result in a plot on a tephigram very similar to Zipser's 'onion' soundings in fig 2.8; later however, the contrasts become less marked, which explains why fig 3.14 does not correspond exactly with Zipser's 'onion'.

In conclusion, the use of 'before and after' soundings, and the method of compositing adopted have both made it possible with routine

single station soundings to deduce most of the aspects of the SQL section which have been inferred from the use of much higher resolution measurements of a single SQL. In particular, the need is confirmed beforehand of a strong jet around 650 mb, lighter upper level winds and a warm moist surface layer with dry air aloft, while passage of the SQL is shown to lower the jet, and replace warm moist low-level air by drier air brought down in cool convective-scale and warm mesoscale downdraughts. Continuation of this study over a longer period of time would, hopefully, remove some of the uncertainties in the results, especially near the squall front, but substantial progress can only now come through resolution of the structure and evolution of individual cells, which necessitates an intensive study with several aircraft traverses of a single SQL.

CHAPTER 4. A REVIEW OF SQUALL LINE MODELS.

Having inferred the principal observational features of SQL's, it is now time to turn to modelling them. Apart from ad hoc models which will be considered briefly at the end of this chapter, models fall into two principal classes, mathematical and numerical, and the mathematical models in turn may be divided into gravity wave and two-dimensional models. Since it is a gravity wave model which will be subsequently developed, this will be considered first.

4.1 UNSTABLE GRAVITY WAVE MODEL.

Gravity wave models have been widely studied in connection with convection because they generate regions of low-level convergence which can trigger and sustain growth of convective elements. Most familiar are the stable gravity waves in which gravity acts solely as a restoring force. In moist convection however, latent heat release acts as a driving mechanism, and for a model to be at all realistic, this must be included in the equations of motion. Use of a forcing term is one possibility, but this will be shown to have its drawbacks, so that instead the preferred method will be to modify the static stability, so that the flow becomes convectively unstable.

In order for the equations to be tractable, the gravity wave models in general omit non-linear effects, and so are only applicable to the initial growth stage. Their linearity permits separation of variables and use of transforms, so making possible the normal mode and initial value problem analyses which form the subjects of chapters 5 and 6. To set the scene for these chapters, the basic equations will first be derived, then the two methods of analysis introduced.

4.1.1 Basic Equations.

Though SQL's may eventually grow to dominate their synoptic-scale environment, initially at least, Coriolis accelerations are very much smaller than convective accelerations and may be neglected. Also, pressure p, density ρ and log potential temperature $\phi = \ln T\,(1000/p)^{R/c_p}$ will only deviate by small amounts δp, $\delta\rho$, $\delta\phi$ from steady state values $p_o(z)$, $\rho_o(z)$, $\phi_o(z)$, and elastic compressibility may be neglected, so that the equations of motion and continuity may be written

$$\frac{D\underline{u}}{Dt} + \nabla\left(\frac{\delta p}{\rho_o}\right) - g\delta\phi\,\underline{k} = K_M \nabla^2 \underline{u} \qquad (4.1)$$

$$\nabla.(\rho_o \underline{u}) = 0 \,. \qquad (4.2)$$

Assuming that there is negligible heat generation from dissipation of mechanical energy, and that log potential temperature mixing obeys a simple diffusion law, the thermodynamic equation for dry convection may be taken as

$$\frac{D}{Dt}\delta\phi + B_o w = K_H \nabla^2 \delta\phi , \qquad (4.3)$$

where the static stability $B_o = d\phi_o/dz$ is positive except near the surface. For moist convection, the effect of latent heat release may be parameterised by the method of Moncrieff and Miller (1976), outlined in section 4.3.1, which is equivalent to use of a modified value for B_o, which will then be negative over a substantial layer, thus providing the necessary energy source.

Finally, the only boundary conditions required will be

$$w = \delta\phi = 0 \qquad \text{at} \qquad z = z_1 , z_2 \qquad (4.4)$$

corresponding to fixed rigid boundaries, which is a reasonable approximation in view of the large reduction in amplitude of convective motions above the tropopause.

Apart from the diffusion terms, this system of equations is the Boussinesq (1903) system. Though molecular viscosity is negligible, eddy viscosity is important and needs consideration. For simplicity, the Prandtl number will be taken to be 1, so that $K_M = K_H = K$, say. In the absence of diffusion, fastest growing linear modes will in general be tall infinitely thin towers; such rapid horizontal variation is however prevented by the diffusion terms $K(\partial^2/\partial x^2 + \partial^2/\partial y^2)$, so these must be included. The scale of vertical variation on the other hand is of the order of the depth of the whole convective layer, so the vertical diffusion terms $K\partial^2/\partial z^2$ can plausibly be omitted. Omission of these terms does not necessarily lead to greater errors at the boundaries than would any of the obvious extra boundary conditions needed for their inclusion: near the ground the diffusion coefficients fall off linearly with height, while there is no physical upper boundary, so that nowhere is the classical 'no-slip' condition of bounded incompressible flow a satisfactory approximation. Furthermore, though omission of the $K\partial^2/\partial z^2$ terms could lead to spurious generation of vorticity, this is likely to be negligible in comparison with the generation of vorticity through buoyancy.

For the linear gravity wave model, it is now assumed that all variables are given by small deviations from steady state values. Such an approximation is an obvious limitation for instance in updraught

cores, where vertical velocities commonly exceed any mean flow horizontal velocity. However, it is reasonable to expect that the fringes of a disturbance will be well represented, as found for instance by Simmons and Hoskins (1979) (see section 4.1.3). Also the linear approximation would be the first term in any nonlinear expansion. So, assuming that w, $\delta\phi$, $\delta p/\rho_o$ are small, and that u, v are given by small perturbations δu, δv from mean states $U_o(z)$, $V_o(z)$, where the mean flow velocity $\underline{U}_o = (U_o, V_o)$ is not necessarily constant in direction, (4.1) - (4.3) become

$$\left(\frac{\partial}{\partial t} + \underline{U}_o.\nabla_H - K\nabla_H^2\right)(\delta u, \delta v) + w\frac{d\underline{U}_o}{dz} + \nabla_H\frac{\delta p}{\rho_o} = 0 \qquad (4.5)$$

$$\left(\frac{\partial}{\partial t} + \underline{U}_o.\nabla_H - K\nabla_H^2\right)w - g\delta\phi + \frac{\partial}{\partial z}\frac{\delta p}{\rho_o} = 0 \qquad (4.6)$$

$$\frac{\partial}{\partial x}\delta u + \frac{\partial}{\partial y}\delta v + \frac{1}{\rho_o}\frac{\partial}{\partial z}(\rho_o w) = 0 \qquad (4.7)$$

$$\left(\frac{\partial}{\partial t} + \underline{U}_o.\nabla_H - K\nabla_H^2\right)\delta\phi + B_o w = 0 \qquad (4.8)$$

where $$\nabla_H \equiv \left(\frac{\partial}{\partial x}, \frac{\partial}{\partial y}\right)$$

Now carry out a double Fourier transform in the x and y directions, and consider a single Fourier component with spatial dependence $\exp\{i(\alpha x + \beta y)\}$. This will correspond to a wave travelling in the direction of propagation vector

$$\underline{\gamma} = (\alpha, \beta, 0) \qquad (4.9)$$

Defining the wavenumber

$$\gamma = (\alpha^2 + \beta^2)^{1/2} \qquad (4.10)$$

then the inclination of the direction of propagation to the x-axis is

$$\theta = \cos^{-1}(\alpha/\gamma). \qquad (4.11)$$

Eliminating $\delta u, \delta v$ and $\delta p/\rho_o$ from (4.5) - (4.8) then gives

$$\left\{\left(\frac{\partial}{\partial t} + i\underline{U}_o.\underline{\gamma} + K\gamma^2\right)\left(\frac{\partial^2}{\partial z^2} - \gamma^2 - \frac{1}{4H_o^2} - \frac{1}{2}\frac{d}{dz}\frac{1}{H_o}\right) - i\left(\frac{1}{H_o}\frac{d\underline{U}_o}{dz} + \frac{d^2\underline{U}_o}{dz^2}\right).\underline{\gamma}\right\}\tilde{w} - \gamma^2 g B_o \tilde{h}$$

$$= 0 \qquad (4.12)$$

and $$\left(\frac{\partial}{\partial t} + i\underline{U}_o.\underline{\gamma} + K\gamma^2\right)\tilde{h} - \tilde{w} = 0, \qquad (4.13)$$

while the boundary conditions become

$$\tilde{w} = \tilde{h} = 0 \qquad \text{at} \qquad z = z_1, z_2. \qquad (4.14)$$

Here $$\frac{1}{H_o} = -\frac{1}{\rho_o}\frac{d\rho_o}{dz} \quad , \tag{4.15}$$

and $\tilde{w}$ and $\tilde{h}$ are the Fourier transforms of $\rho_o^{\frac{1}{2}}w$ and $-\rho_o^{\frac{1}{2}}\delta\phi/B_o$ (in the inviscid case, $\tilde{h}$ is the Fourier transform of $\rho_o^{\frac{1}{2}}$ times the height risen by a fluid element). Note that the mean flow $\underline{U}_o$ enters the equations only via $\underline{U}_o.\underline{\gamma}$. Hence the perturbation detects only the resolved part of $\underline{U}_o$ in the direction of propagation - a form of the theorem of Squire (1933), noted by Yih (1969) which considerably simplifies analysis of flows which change direction with height.

Further progress now requires use of one or other of the approaches taken up in chapters 5 and 6: consideration of a single exponentially growing mode, or examination of the growth of an initially localised perturbation. At present they will merely be introduced before turning to an account of other gravity wave models.

4.1.2 Linear Modes.

Consider a single exponentially growing mode with time dependence $\exp(-i\sigma t)$. Substituting in (4.12) and (4.13) gives

$$\left\{\left(\underline{U}_o.\underline{\gamma} - \sigma - iK\gamma^2\right)\left(\frac{d^2}{dz^2} - \gamma^2 - \frac{1}{4H_o^2} - \frac{1}{2}\frac{d}{dz}\frac{1}{H_o}\right) - \left(\frac{1}{H_o}\frac{d\underline{U}_o}{dz} + \frac{d^2\underline{U}_o}{dz^2}\right).\underline{\gamma}\right\}\tilde{w} + i\gamma^2 g B_o \tilde{h}$$

$$= 0 \tag{4.16}$$

$$\left(\underline{U}_o.\underline{\gamma} - \sigma - iK\gamma^2\right)\tilde{h} + i\tilde{w} = 0 \tag{4.17}$$

This is now an eigenvalue problem to determine $\sigma(\underline{\gamma})$ such that there are non-zero solutions satisfying the boundary conditions (4.14). Writing $\sigma = \sigma_r + i\sigma_i$, the growth rate is σ_i; a mode will be unstable or amplifying if σ_i is positive, neutral if σ_i is zero. Neutral modes have

$$\text{phase velocity} = \frac{\sigma_r}{\gamma^2}\underline{\gamma} \tag{4.18}$$

$$\text{group velocity} = \left(\frac{\partial\sigma_r}{\partial\alpha}, \frac{\partial\sigma_r}{\partial\beta}, 0\right) \tag{4.19}$$

(as for instance in Whitham 1974); these terms are not strictly applicable for amplifying modes, but will for convenience be retained. For antisymmetric mean flows, modes with phase velocity equal to the middle level mean flow velocity will be referred to as stationary, others as propagating.

Writing $$\sigma' = \sigma + iK\gamma^2 \tag{4.20}$$

and solving for $\tilde{w}$ and $\tilde{l} = \rho_o^{-\frac{1}{2}}\tilde{h}$ gives

$$\frac{d^2\tilde{w}}{dz^2} - \left\{\gamma^2 + \frac{1}{4H_0^2} + \frac{1}{2}\frac{d}{dz}\frac{1}{H_0} - \frac{gB_0\gamma^2}{(\underline{U}_0\cdot\underline{\gamma}-\sigma')^2} + \frac{\frac{d}{dz}\left(\frac{1}{\rho_0}\frac{d\underline{U}_0}{dz}\cdot\underline{\gamma}\right)}{\frac{1}{\rho_0}(\underline{U}_0\cdot\underline{\gamma}-\sigma')}\right\}\tilde{w} = 0 \tag{4.21}$$

$$\frac{d}{dz}\left\{\frac{1}{\rho_0}(\underline{U}_0\cdot\underline{\gamma}-\sigma')^2\frac{d}{dz}(\rho_0\tilde{l})\right\} - \left\{(\underline{U}_0\cdot\underline{\gamma}-\sigma')^2\left(\gamma^2+\frac{d}{dz}\frac{1}{H_0}\right) - gB_0\gamma^2\right\}\tilde{l} = 0 \tag{4.22}$$

These equations, valid (if K = 0) for adiabatic motion of a Boussinesq gas should be contrasted with those for motion of an inviscid incompressible liquid given by Taylor (1931) and Miles (1961):

$$\frac{d^2\tilde{w}}{dz^2} - \left\{\gamma^2 + \frac{1}{4H_0^2} + \frac{1}{2}\frac{d}{dz}\frac{1}{H_0} - \frac{gB_0\gamma^2}{(\underline{U}_0\cdot\underline{\gamma}-\sigma')^2} + \frac{\frac{d}{dz}\left(\rho_0\frac{d\underline{U}_0}{dz}\cdot\underline{\gamma}\right)}{\rho_0(\underline{U}_0\cdot\underline{\gamma}-\sigma')}\right\}\tilde{w} = 0 \tag{4.23}$$

$$\frac{d}{dz}\left\{\rho_0(\underline{U}_0\cdot\underline{\gamma}-\sigma')^2\frac{d\tilde{l}}{dz}\right\} - \rho_0\left\{(\underline{U}_0\cdot\underline{\gamma}-\sigma')^2\gamma^2 - gB_0\gamma^2\right\}\tilde{l} = 0 \tag{4.24}$$

where in this case

$$B_0 = -\frac{1}{\rho_0}\frac{d\rho_0}{dz} \tag{4.25}$$

The term $\frac{d}{dz}\left(\frac{1}{\rho_0}\frac{d\underline{U}_0}{dz}\cdot\underline{\gamma}\right)$ in (4.21), which may seem surprising at first sight, can be seen to arise naturally from the term $\frac{D}{Dt}\left(\frac{\underline{\xi}}{\rho_0}\right)$ in the Boussinesq vorticity equation:

$$\frac{D}{Dt}\left(\frac{\underline{\xi}}{\rho_0}\right) = \frac{\underline{\xi}}{\rho_0}\cdot\nabla\underline{u} - \frac{g}{\rho_0}\,\underline{k}\times\nabla\delta\phi \tag{4.26}$$

The factor $1/\rho_0$ means that for statically neutral flow ($B_0 = 0$) the necessary condition for existence of an unstable mode becomes

$$\frac{d}{dz}\left(\frac{1}{\rho_0}\frac{d\underline{U}_0}{dz}\cdot\underline{\gamma}\right) = 0\,, \tag{4.27}$$

instead of Rayleigh's (1880) condition in the constant density case that the velocity component in the direction of propagation should have a point of inflexion.

The effect of diffusion in (4.16), (4.17) is merely to reduce the growth rate σ_i by an amount $K\gamma^2$; this is a consequence of the form assumed for the diffusion terms in which only horizontal space derivatives were included. Results obtained with this approximation in chapter 5 show good qualitative agreement with those of Asai (1970a), who retained the $K\partial^2/\partial z^2$ terms, and this gives some justification for the widespread use of the inviscid equations, provided computed growth rates are suitably modified. A simple illustration of this modification is provided by longitudinal modes $\underline{U}_0\cdot\underline{\gamma} = 0$, for unidirectional flow, in which case (4.21) with constant B_0 and H_0 reduces to

$$\frac{d^2\tilde{w}}{dz^2} - \left\{\gamma^2 + \frac{1}{4H_0^2} - \frac{gB_0\gamma^2}{\sigma'^2}\right\}\tilde{w} = 0\,. \tag{4.28}$$

An infinite set of modes can be found satisfying the boundary conditions:

$$\tilde{w} = \text{constant} \times \sin n\pi \frac{z - z_1}{z_2 - z_1} \tag{4.29}$$

where n is an integer, and

$$\sigma = i\left\{\frac{-gB_0\gamma^2}{\gamma^2 + \frac{1}{4H_0^2} + \frac{n^2\pi^2}{(z_2 - z_1)^2}}\right\}^{\frac{1}{2}} - ik\gamma^2 \tag{4.30}$$

which in the statically unstable case $B_0 < 0$ gives growth but no propagation.

The effect of the mean density variation here is merely to reduce the growth rate via the term $\frac{1}{4H_0^2}$, which is negligible in comparison with $\frac{n^2\pi^2}{(z_2 - z_1)^2}$ for convection in the troposphere (where $H_0 \simeq 7$ km, $z_2 - z_1 \lesssim 10$ km). Setting $\frac{1}{H_0} = 0$ therefore, and introducing the following non-dimensional variables

$$\text{wavenumber} \qquad k = \tfrac{1}{2}(z_2 - z_1)\gamma \tag{4.31}$$

$$\text{Rayleigh number} \qquad Ra = \frac{-gB_0(z_2 - z_1)^4}{k^2}, \tag{4.32}$$

(4.30) implies a non-dimensional growth rate

$$\frac{\sigma_i}{(-gB_0)^{\frac{1}{2}}} = \frac{k}{(k^2 + \frac{1}{4}n^2\pi^2)^{\frac{1}{2}}} - \frac{4k^2}{Ra^{\frac{1}{2}}}. \tag{4.33}$$

This is plotted in fig 4.1 against log k for different values of Ra, for the first mode: n = 1. The log (to base 10) of the wavenumber is used here and subsequently to show more clearly the short-wave behaviour. In the absence of diffusion (Ra = ∞), growth rate increases with wavenumber, with $\frac{\sigma_i}{(-gB_0)^{\frac{1}{2}}} \to 1$ in the short wave limit $k \to \infty$. If diffusion is included, the short waves are damped for k greater than some critical wavenumber k_c, while maximum growth rate occurs at some finite wavenumber k_m; for $Ra^{\frac{1}{4}} \gg n\pi$, these are given approximately by

$$k_c \simeq \tfrac{1}{2}Ra^{\frac{1}{4}} \tag{4.34}$$

$$k_m \simeq (n\pi)^{\frac{1}{2}} 2^{-\frac{5}{4}} Ra^{\frac{1}{8}} \simeq 0.745\, n^{\frac{1}{2}} Ra^{\frac{1}{8}} \tag{4.35}$$

the maximum being approximately

$$\frac{\sigma_i}{(-gB_0)^{\frac{1}{2}}} \simeq 1 - 2^{-\frac{1}{2}} n\pi Ra^{-\frac{1}{4}} \simeq 1 - 2.22\, n Ra^{-\frac{1}{4}} \tag{4.36}$$

Many papers have been published on linear modes for more general mean flows, where in general, unlike the longitudinal case, no simple solutions of (4.21) exist. Reviews may be found as follows: unstratified flow - Lin (1955); inviscid flow - Drazin and Howard (1966), Yih (1969); general - Yih (1965), Betchov and Criminale (1967), Turner

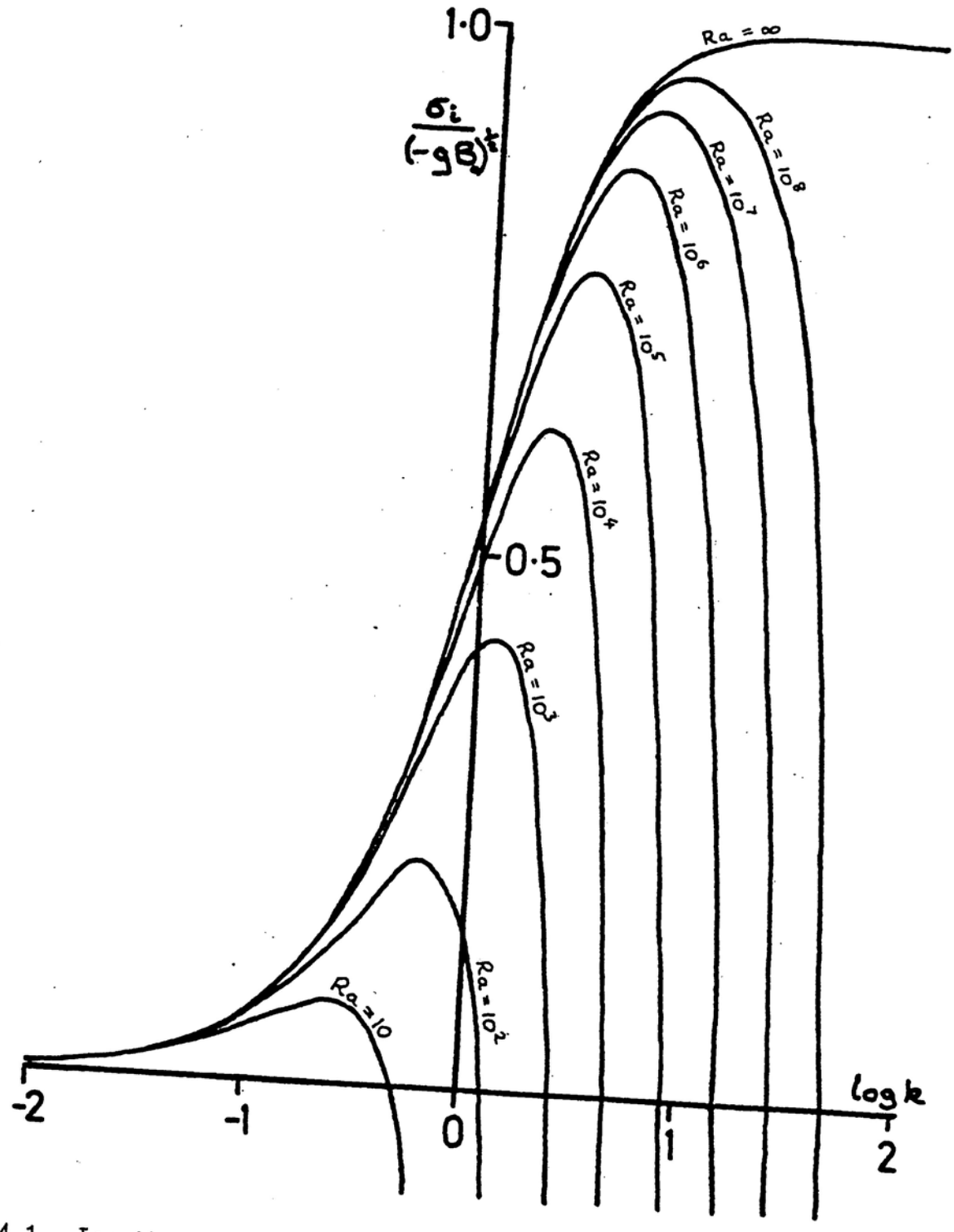


Fig 4.1. Longitudinal mode, n = 1: non-dimensional growth rate plotted against log wavenumber for different Rayleigh numbers.

(1973), Kelly (1978). It is not proposed to go over their conclusions here, except to mention two particular results which apparently present problems in the modelling of SQL's in view of observational findings such as those of Betts, Grover and Moncrieff (1976) mentioned in section 2.2.3c.

(a) SQL's occur when the mean wind field is nearly unidirectional, and are transverse to the mean wind; their energy is derived from buoyancy (chiefly from latent heat release) as suggested by the low level up-gradient momentum transfer (section 2.2.3c). However Kuo (1963) and Asai (1970 a,b; 1972) have shown that the preferred buoyancy-driven modes are longitudinal, since the transverse modes are stabilised by feeding of perturbation energy into the mean flow via a Reynolds stress. Modes with a preferred transverse orientation do occur for mean flows with a sufficiently pronounced inflexion point, but only for very small buoyancies, and these are inertially driven, transferring momentum down-gradient.

(b) Tropical SQL's usually travel faster than the mean wind at any level. Amplifying linear modes however must, by the theorem of Miles (1961) have a steering level, i.e. a level at which phase velocity, as defined by (4.18), is equal to the mean flow velocity.

These two points will be resolved in detail later; briefly the solution is that a SQL is not a single mode with a particular orientation, but rather an amplifying patch of convection consisting of many modes with different growth rates and phase velocities, the superposition of which introduces group velocities, which are not constrained by the Miles (1961) theorem.

The fact that superposition introduces group velocities will be demonstrated in the next section, but first it will be convenient to discuss a model which does make this assumption, namely that of Marroquin and Raymond (1979). Solving the Taylor-Goldstein equation (4.21) with latent heat release represented by a modified static stability (as in section 4.3.1), and with no diffusion, they computed phase velocities and growth rates of linear modes with various wavenumbers for velocity and thermodynamic profiles corresponding to several types of severe thunderstorms. Except for SQL's, they found that the group velocity (obtained by interpolation) showed little variation with wavenumber, so that the group velocity of the fastest growing mode could plausibly be used as an estimate of storm velocity, and did indeed provide a reasonable estimate for multicell and left-

moving storms, but not for severe right-moving storms, a fact which they attributed to a dynamical difference between supercells and other types of storms.

Marroquin and Raymond only modelled one SQL, namely the Venezuelan SQL of 24 July 1972 observed as disturbance no. 47 of VIMHEX (fig 4.2). They found that unlike the other types of storm, the group velocity vector here varied considerably with wavenumber, so that less certainty could be attached to the predicted SQL velocity, 10·3 m/s from 071°, and indeed the predicted speed fell well short of the observed 15·3 m/s, though good agreement was obtained with the observed direction 065°. Even for the other storms, one shortcoming of the model is evident, namely that the fastest growing mode corresponded to the short wave limit $\gamma \to \infty$, whereas more physically realistic results would have been obtained by inclusion of viscosity as in fig 4.1.

4.1.3 Growth of an Initially Localised Perturbation.

To justify Marroquin and Raymond's use of the group velocity of the fastest growing normal mode in determining the motion of a patch of convection, it is necessary to consider superposition of linear modes using Fourier integrals. In two dimensions, these take the form

$$I(x,z) = \int_{-\infty}^{\infty} \tilde{f}(\alpha)\, \tilde{w}_\alpha(z) \exp i\{\alpha x - \sigma(\alpha)t\} d\alpha \qquad (4.37)$$

where $\tilde{f}(\alpha)$ is the Fourier transform of the initial perturbation and $\sigma(\alpha)$, $\tilde{w}_\alpha(z)$ are found by solving the normal mode eigenvalue problem. The asymptotic theory for such integrals has been developed by Bers (1975) and McIntyre (1978) and is applicable to instabilities in fluids, plasmas and elsewhere. In this theory, attention is directed to a point moving with some horizontal speed $U = x/t$, so that (4.37) becomes

$$I(x,z) = \int_{-\infty}^{\infty} \tilde{f}(\alpha)\, \tilde{w}_\alpha(z) \exp\{-i\Omega(\alpha,U)t\} d\alpha \qquad (4.38)$$

where
$$\Omega(\alpha,U) = \sigma(\alpha) - \alpha U \qquad (4.39)$$
$$= \Omega_r + i\Omega_i \text{ , say.}$$

Assuming all functions sufficiently well-behaved, and growth rates bounded, the contour for the integration can be deformed off the real axis in a direction which diminishes Ω_i for all α, until one of two possibilities occurs

(i) A contour is reached where $\Omega_i \leq 0$ everywhere; therefore I does not grow as $t \to \infty$ and there is stability at a point moving with the particular speed U.

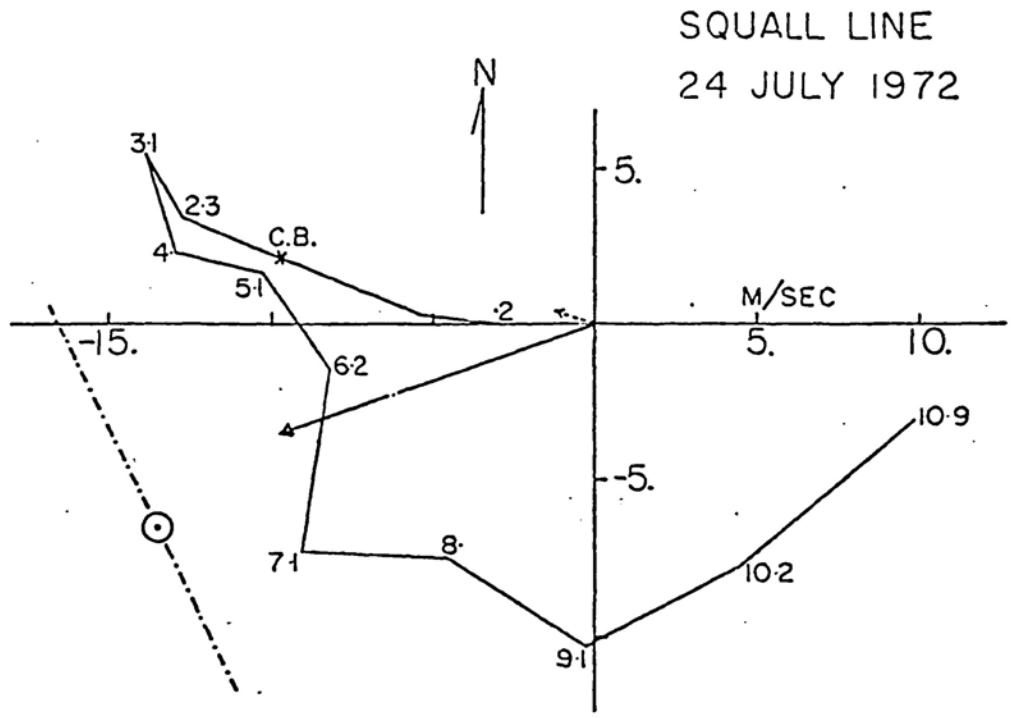


Fig 4.2. Propagation velocity for the Venezuelan squall line of 24 July 1972 (from Marroquin and Raymond 1979). The solid line is the wind hodograph, and the dash-dot line shows the observed squall line orientation (155-355°), with the circle giving the actual storm velocity. The full arrow gives the storm velocity as predicted by the unstable gravity wave model, while the dashed arrow gives the prediction of the wave-CISK model (section 4.2.2).

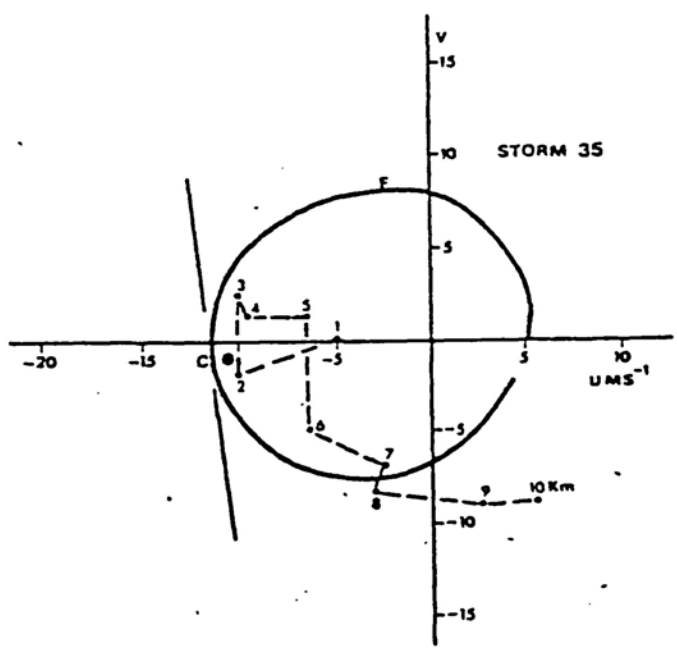


Fig 4.3. Propagation velocity for the Venezuelan squall line of 9 July 1972 as predicted by the wave-CISK model (from Fernandez and Thorpe 1979). The wind hodograph is indicated by a dashed line, while the dot gives the observed storm velocity. The propagation velocity curve is shown (full) with the point corresponding to maximum instability being marked F; the closest prediction to the observed velocity is marked C, the corresponding orientation being given by the straight line.

(ii) A saddle point is reached ($d\Omega/d\alpha = 0$) at $\alpha = \alpha_o$, say, with $\Omega_i(\alpha_o) > 0$. Applying the method of steepest descent, this saddle point makes an asymptotic contribution to the integral proportional to

$$t^{-\frac{1}{2}} \tilde{f}(\alpha_o)\, \tilde{\omega}_{\alpha_o}(z) \exp\{-i\Omega(\alpha_o, U)t\}$$

so that there is instability at a point moving with speed U.

Considering saddle points for varying U, the speed for which the instability is greatest is given by

$$\frac{d}{dU}\Omega_i(\alpha_o(U), U) = 0 \qquad (4.40)$$

which, with $\alpha_o = \alpha_{or} + i\alpha_{oi}$ gives

$$\frac{\partial\Omega_i}{\partial\alpha_{or}}\frac{d\alpha_{or}}{dU} + \frac{\partial\Omega_i}{\partial\alpha_{oi}}\frac{d\alpha_{oi}}{dU} + \frac{\partial\Omega_i}{\partial U} = 0 \qquad (4.41)$$

Now the saddle point condition $d\Omega/d\alpha = 0$ implies that the first two terms vanish, so by (4.39) the last term gives

$$\alpha_{oi} = 0 \qquad (4.42)$$

Applying the saddle point condition again, with real α_o, finally gives

$$\frac{d\sigma_r}{d\alpha_o} = U \qquad \frac{d\sigma_i}{d\alpha_o} = 0 \qquad (4.43)$$

Hence the point of greatest instability moves at the group velocity of the normal mode with the greatest amplification rate for a real wavenumber (assumed finite), provided the initial conditions do not give $f(\alpha_o) = 0$.

This summary of two-dimensional asymptotic theory is based on Simmons and Hoskins (1979) who applied both the initial value and normal mode techniques to development of unstable baroclinic waves. They concluded that linear theory is applicable in development of new depressions on the fringes of the region of motion, but that nonlinear effects were important in the centre.

Extension of the theory to three dimensions is straightforward. In this case, for a point moving with velocity $(U,V) = (x/t\ ,\ y/t)$, the integral (4.38) becomes

$$I(x,y,z) = \int_{-\infty}^{\infty}\int_{-\infty}^{\infty} \tilde{f}(\alpha,\beta)\,\tilde{\omega}_{\alpha\beta}(z) \exp\{-i\Omega(\alpha,\beta,U,V)t\}\, d\alpha\, d\beta \qquad (4.44)$$

where

$$\Omega(\alpha,\beta,U,V) = \sigma(\alpha,\beta) - \alpha U - \beta V\,. \qquad (4.45)$$

If integration is carried out first in α, then in β, and in each case a saddle point is reached, the asymptotic contribution to the integral is

$$t^{-1}\,\tilde{f}(\alpha_o,\beta_o)\,\tilde{\omega}_{\alpha_o\beta_o}(z)\,\exp\{-i\Omega(\alpha_o,\beta_o,U,V)t\}$$

where $\partial\Omega/\partial\alpha = \partial\Omega/\partial\beta = 0$ at $(\alpha,\beta) = (\alpha_o,\beta_o)$. Maximising this contribution with respect to U gives

$$\frac{\partial\Omega_i}{\partial\alpha_{or}}\frac{\partial\alpha_{or}}{\partial U} + \frac{\partial\Omega_i}{\partial\alpha_{oi}}\frac{\partial\alpha_{oi}}{\partial U} + \frac{\partial\Omega_i}{\partial\beta_{or}}\frac{\partial\beta_{or}}{\partial U} + \frac{\partial\Omega_i}{\partial\beta_{oi}}\frac{\partial\beta_{oi}}{\partial U} + \frac{\partial\Omega_i}{\partial U} = 0 \qquad (4.46)$$

which by the saddle point conditions gives $\partial\Omega_i/\partial U = 0$, and hence by (4.45), $\alpha_{oi} = 0$; application of $\partial\Omega/\partial\alpha = 0$ for real α then gives $\partial\sigma_r/\partial\alpha_o = U$, $\partial\sigma_i/\partial\alpha_o = 0$. Similarly maximising with respect to V gives $\beta_{oi} = 0$, $\partial\sigma_r/\partial\beta_o = V$, $\partial\sigma_i/\partial\beta_o = 0$. Hence as before, the point of maximum instability moves with the group velocity (4.19) of the fastest growing mode.

This conclusion on the role of group velocity in three dimensional asymptotic growth of a perturbation is confirmed by Benjamin (1961) and Criminale and Kovasznay (1962) in studies of the initial value problem for neutrally stratified viscous flows; further studies for such flows were made by Gaster (1968) and Gaster and Davey (1968). For unstably stratified flows, the only published results are the computed group velocities of Marroquin and Raymond (1979) which have already been presented in the previous section; they did not however extend their study to the initial value problem, and it is this which forms the subject of chapter 6 of this thesis. Presentation of results will therefore be deferred for the present, though it may be noted that care is needed here in the computation of group velocities, as will become apparent in section 5.6.2.

It should be mentioned that although the above asymptotic analysis is apparently adequate in cases where unstable modes exist, serious problems arise if they do not, and this can be seen very simply by consideration of statically neutral, constant shear inviscid mean flow. In this case, if $1/H_o = 0$, (4.21) reduces to

$$\frac{d^2\tilde{w}}{dz^2} - \gamma^2\tilde{w} = 0 \qquad (4.47)$$

which has no solutions satisfying the boundary conditions (4.14), i.e. no normal modes exist at all, whether amplifying, decaying or neutral. Physically however a solution must exist for development of an initial perturbation, and in fact in this constant shear case, if the mean flow

is in the x - direction, the vorticity equation for transverse perturbations reduces to

$$\left(\frac{\partial}{\partial t} + U_o \frac{\partial}{\partial x}\right) \delta\eta = 0 \tag{4.48}$$

with solution $$\delta\eta = \delta\eta_o (x - U_o t, z) \tag{4.49}$$

where $$\delta\eta = \frac{\partial}{\partial z} \delta u - \frac{\partial w}{\partial x} \tag{4.50}$$

Thus motion consists merely of advection of the initial vorticity perturbation with the mean flow. Because of the shear of the mean flow however, the form of the initial perturbation is not preserved, and the exponential mode approach fails.

This failure of the exponential mode approach is made especially serious by the fact that in the example given, perturbation kinetic energy grows without limit. For, whilst expressing (4.49) in terms of vertical velocity gives

$$\nabla^2 w = -\frac{\partial}{\partial x} \delta\eta_o (x - U_o t, z) \tag{4.51}$$

the solution of which will be bounded, the corresponding equation for perturbation horizontal velocity is

$$\nabla^2 \delta u = \left(\frac{\partial}{\partial z} - U_o' t \frac{\partial}{\partial x}\right) \delta\eta_o (x - U_o t, z) \tag{4.52}$$

which suggests solutions δu asymptotically proportional to t at points $x \sim U_o t$. This result is confirmed by Chimonas (1979), who, following the work of Case (1960 a,b) and Miles (1961) considered the initial value problem for arbitrary mean flows with stable or neutral stratification. Chimonas showed that, apart from exponential modes, there normally exist 'algebraic disturbances' with asymptotic time dependence in the two-dimensional case given by

$$\delta u (x - U_o t, z) \sim t^{2\nu} \tag{4.53}$$

where $$\nu^2 = \tfrac{1}{4} - J \tag{4.54}$$

and $$J = g\beta_o / U_o'^2 \tag{4.55}$$

Thus whereas Miles (1961), considering exponential modes showed that a necessary condition for instability is that the local Richardson number J be somewhere less than $\frac{1}{4}$, Chimonas' result implies that this is a sufficient condition for instability. An example of this 'algebraic instability' will be seen in section 6.3.2, where plane Couette flow is found to be 'algebraically unstable' even when neutrally stratified

(as anticipated above), whereas for exponential modes (Kuo 1963), it is only unstable for Richardson number J less than $-\frac{3}{4}$ (see section 5.2.2).

For unstable stratification, the situation is less clear. Eliassen et al (1953) considering plane Couette flow showed that the analysis may be extended to slightly unstable stratification; this cannot however hold true for arbitrarily large negative Richardson number, since in the limit $J \to -\infty$, no shear is available to deform the initial perturbation and permit non-modal disturbances, and the exponential modes do in fact form a complete set. Even when they are not complete, it does however seem reasonable to assume that, provided unstable exponential modes exist, they will eventually dominate any algebraic disturbance, as has been shown to hold for the baroclinic instability problem by Pedlosky (1964). Thus normal modes would give a correct asymptotic description as assumed in the analysis in this section, and the way is open for further study along these lines in chapters 5 and 6.

4.2 OTHER GRAVITY WAVE MODELS.

Two other gravity wave models have already been mentioned, and these will now be considered.

4.2.1 Stable Gravity Wave Model.

The stable gravity wave model corresponds to $B_o > 0$ at all levels in (4.3), and in this case, modes found from (4.21) in the absence of diffusion are normally neutral (i.e. not amplifying or decaying), and propagate, often faster than the mean flow at any level. It is tempting to use these to model SQL's, since the atmosphere is stably stratified to dry convection (except near the surface). Thus Hamilton and Archbold (1945) suggested that SQL's are short gravity waves propagating along the boundary-layer inversion, and produced realistic propagation speeds, though making use of the formula for long waves.

In a non-linear extension of the gravity wave concept, Tepper (1950) suggested a model of the SQL as a pressure jump generated by a cold front and travelling along an inversion 'whose genesis, propagation and destruction is independent of the precipitation which it produces'. He drew an analogy with hydraulic jumps in shallow water flow. Barrefors (1965), making use of the theory of characteristics, applied this model to West African SQL's and concluded that high ground, by reducing the depth of the flow, and hence the perturbation phase speed, favoured jump formation.

Stable gravity wave models have the serious drawback however that they lack an energy source. Consequently viscosity, and upwards energy propagation (which is to be expected for longer waves according to Lilly 1979) would result in decay within an hour or so. Furthermore, though the low-level convergence associated with gravity waves can trigger thunderstorm development, as observed by Uccellini (1975), and though thunderstorms in turn do generate gravity waves (Lilly 1979), Uccellini's (1975) study suggested that the gravity waves pass through the convective area, rather than there being any coupling of the two. It is therefore to be concluded that a stable gravity wave is inadequate as a model of a SQL.

4.2.2 Forced Gravity Wave (Wave-CISK) Model.

The obvious shortcoming of the stable gravity wave model is its failure to include latent heat release as a driving mechanism. The wave-CISK concept, so named by Lindzen (1974) attempts to remedy this deficiency by modelling a tropical convective system as a forced gravity wave in which low-level convergence triggers off cumulus convection, which in turn acts as a driving mechanism for the wave.

Mathematically, wave-CISK models introduce a forcing term into the thermodynamic equation (4.3) which, in the absence of diffusion becomes

$$\frac{D}{Dt}\,\delta\phi \;+\; B_0 w \;=\; Q \qquad (4.56)$$

where the forcing function Q represents some heat source which may, for instance, be taken to be proportional to w or dw/dz at some level. If linearisation is carried out and all the variables including Q are assumed to have a wavelike dependence $\exp\{i(\alpha x + \beta y - \sigma t)\}$, the forced versions of equations (4.21) and (4.22) are obtained:

$$\frac{d^2\tilde{w}}{dz^2} - \left\{\gamma^2 + \frac{1}{4H_0^2} - \frac{gB_0\gamma^2}{(\underline{U}_0.\underline{\gamma}-\sigma)^2} + \frac{\frac{d}{dz}\left(\frac{1}{\rho_0}\frac{d\underline{U}_0}{dz}.\underline{\gamma}\right)}{\frac{1}{\rho_0}(\underline{U}_0.\underline{\gamma}-\sigma)}\right\}\tilde{w} = \frac{g\gamma^2\tilde{Q}}{(\underline{U}_0.\underline{\gamma}-\sigma)^2} \qquad (4.57)$$

$$\frac{d}{dz}\left\{\frac{1}{\rho_0}(\underline{U}_0.\underline{\gamma}-\sigma)^2\frac{d}{dz}(\rho_0\tilde{l})\right\} - \left\{(\underline{U}_0.\underline{\gamma}-\sigma)^2 - gB_0\right\}\gamma^2\tilde{l} = \frac{-ig\rho_0^{-\frac{1}{2}}\gamma^2\tilde{Q}}{(\underline{U}_0.\underline{\gamma}-\sigma)} \qquad (4.58)$$

where H_0 has been assumed constant, and $\tilde{Q}$ is the Fourier transform of $\rho_0^{\frac{1}{2}}Q$.

Wave-CISK was applied to the modelling of SQL's by Raymond (1975) who, using various observed wind profiles, found eigenvalues of (4.57) in the long wave limit $\gamma = 0$, with Q proportional to the surface value

of dw/dz, and plotted propagation velocity curves using the computed group velocity for different directions of propagation. For multicell storms, results were poor, possibly because of the inappropriateness of the long wave approximation in this case. For supercell storms and SQL's, the situation was however better, with storm velocities generally lying near the propagation velocity curve, though not usually at the direction of propagation corresponding to the greatest growth rate. This can be seen clearly in results obtained by Fernandez and Thorpe (1979) for the Venezuelan SQL of 9 July 1972 (no. 35 of VIMHEX), shown in fig 4.3; the most unstable mode (F) gives a very poor prediction of storm velocity, but the point (C) on the propagation velocity curve corresponding to the observed direction of motion gives a good prediction for the storm speed. For the SQL of 24 July 1972 however, results did not permit determination of a propagation velocity curve, and the predicted storm velocity (dashed arrow in fig 4.2) gave very poor agreement with observation.

In a subsequent paper, Raymond (1976) examined actual development of an initial cell by numerical evaluation of an integral similar to (4.44) over a square grid, using eigenvalues computed as before. Development of a right-moving supercell, and of a splitting storm were thus realistically modelled, but no study was made of SQL's. The splitting storm simulation is shown in fig 4.4; the surface flow pattern (fig 4.4a) shows that splitting of an initial region of convergence gives rise to two separate convergence-divergence couplets moving at different speeds to the left and right; by t = 2000 s, the convergence in excess of 10^{-2} s^{-1} and the development of strong convection in the old downdraught air between the left and right moving storms suggests the breakdown of validity of the linear theory. A plot of non-dimensional growth rate against direction of propagation for individual modes (fig 4.4b) reveals unusually not one, but two peaks, which explains the formation of the two separate wave packets.

Returning to the modelling of tropical SQL's with their rapid propagation, Fernandez and Thorpe (1979) obtained amplifying modes with not only group speeds but also phase speeds greater than the mean flow speed at any level, as also did Lilly (1979). This is in contrast to amplifying unforced linear modes, which by the theorem of Miles (1961) must have a steering level (see section 4.1.2). Though the physical mechanisms of buoyancy which are being modelled in the two cases are quite distinct, the fact that the forcing in wave-CISK models is usually

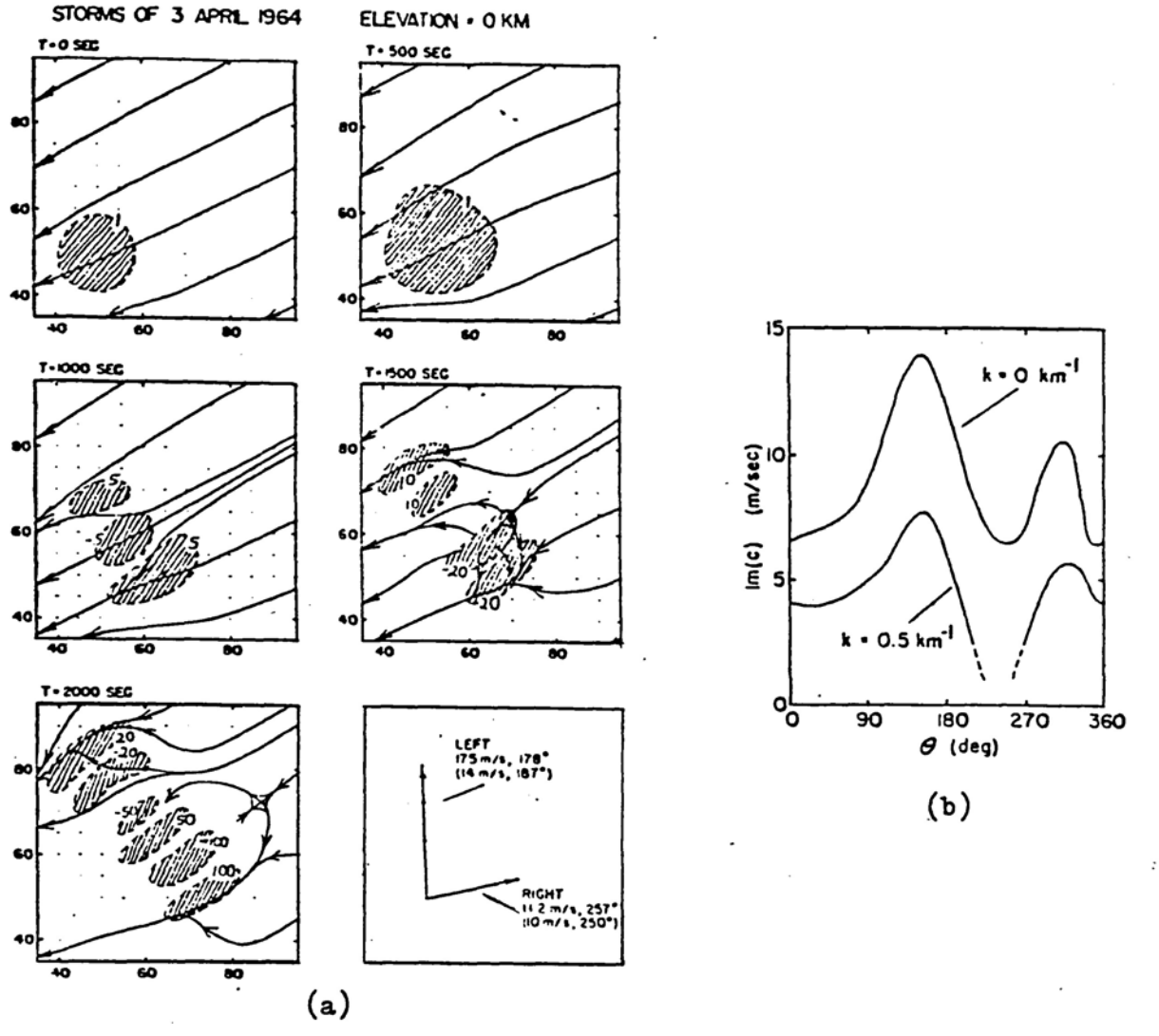


Fig 4.4. Oklahama storms of 3 April 1964 (from Raymond 1976)

(a) Simulated evolution of surface flow. Hatched areas indicate regions of convergence exceeding the labelled value, which is given in units of 10^{-4} s^{-1}. Divergence is indicated by a minus sign. The tracks of the two storms are plotted lower right, along with computed and (in parentheses) observed velocities. North is up, and distances are in km.

(b) Variation of computed non-dimensional growth rate Im(c) with direction of propagation for two different wavenumbers k.

chosen to depend on vertical velocity means that the two models are rather similar; indeed, were the forcing term actually proportional to the vertical velocity at each level, it would reduce to the stratification term of the unforced model. So why can non-steering level modes occur in spite of Miles' theorem?

To answer this question, Miles' (1961) method of proof will be applied to the height equation (4.58), as in Bolton (1980b). Multiplying by the complex conjugate $\rho_0 \tilde{l}^*$, integrating between the boundaries and making use of the boundary conditions (4.14) gives

$$-\int_{z_1}^{z_2} \frac{1}{\rho_0}(\underline{U}_0.\underline{\gamma}-\sigma)^2\left|\frac{d}{dz}(\rho_0\tilde{l})\right|^2 dz - \int_{z_1}^{z_2}\rho_0\left\{(\underline{U}_0.\underline{\gamma}-\sigma)^2 - g\beta_0\right\}\gamma^2\left|\tilde{l}\right|^2 dz = \int_{z_1}^{z_2}\frac{-ig\rho_0^{\frac{1}{2}}\tilde{Q}\tilde{l}^*}{\underline{U}_0.\underline{\gamma}-\sigma}\,dz \tag{4.59}$$

The imaginary part of this is

$$2\int_{z_1}^{z_2}\sigma_i(\underline{U}_0.\underline{\gamma}-\sigma_r)\left\{\frac{1}{\rho_0}\left|\frac{d}{dz}(\rho_0\tilde{l})\right|^2 + \rho_0\gamma^2\left|\tilde{l}\right|^2\right\}dz = Im\int_{z_1}^{z_2}\frac{-ig\rho_0^{\frac{1}{2}}\tilde{Q}\tilde{l}^*}{\underline{U}_0.\underline{\gamma}-\sigma}\,dz \tag{4.60}$$

Now suppose the phase of the forcing Q differs from that of the vertical velocity w by an amount θ, so that

$$\tilde{Q} = F e^{i\theta}\tilde{w} \quad , \text{ say} \tag{4.61}$$

where F and θ are real and may vary with height z. The right-hand side of (4.60) now becomes

$$\int_{z_1}^{z_2} g\rho_0\gamma^2\left|\tilde{l}\right|^2 F\sin\theta\,dz$$

where use has been made of the relation $\tilde{w} = i(\underline{U}_0.\underline{\gamma}-\sigma)\rho_0^{\frac{1}{2}}\tilde{l}$ (derived from (4.17)).

If $\theta \equiv 0$, the right-hand side of (4.60) vanishes, and therefore either $\sigma_i = 0$: no amplification, or $\underline{U}.\underline{\gamma}-\sigma_r = 0$ somewhere: a steering level exists. Hence for forcing to generate an amplifying, non-steering level perturbation, it is necessary that the forcing should be somewhere out of phase with w, as suggested by Moncrieff (1978).

If θ is constant, but not necessarily zero, and there is no stratification ($B_0 = 0$), multiplication of (4.59) by $e^{-i\theta}$ and taking the imaginary part gives

$$\int_{z_1}^{z_2}\left\{\sin\theta\left[(\underline{U}_0.\underline{\gamma}-\sigma_r)^2-\sigma_i^2\right] + 2\cos\theta\left[\sigma_i(\underline{U}_0.\underline{\gamma}-\sigma_r)\right]\right\}\left\{\frac{1}{\rho_0}\left|\frac{d}{dz}(\rho_0\tilde{l})\right|^2 + \rho_0\gamma^2\left|\tilde{l}\right|^2\right\}dz = 0 \tag{4.62}$$

which can only be satisfied if somewhere

$$\underline{U}_o.\underline{\gamma} - \sigma_r = \tan\tfrac{1}{2}\theta\ \sigma_i \quad \text{or} \quad -\cot\tfrac{1}{2}\theta\ \sigma_i \tag{4.63}$$

which is an extension of the result of Miles (1961). It should be noted that the differential equation satisfied by $\tilde{w}$ in this case is

$$\frac{d^2\tilde{w}}{dz^2} - \left\{\gamma^2 + \frac{1}{4H_o^2} + \frac{g\gamma^2 F e^{i\theta}}{(\underline{U}_o.\underline{\gamma}-\sigma)^2} + \frac{\frac{d}{dz}\left(\frac{1}{\rho_o}\frac{d\underline{U}_o}{dz}.\underline{\gamma}\right)}{\frac{1}{\rho_o}(\underline{U}_o.\underline{\gamma}-\sigma)}\right\}\tilde{w} = 0 \tag{4.64}$$

which is the Taylor-Goldstein equation with a complex static stability $-Fe^{i\theta}$. Thus the stratification which was excluded at the beginning of this paragraph by setting $B_o = 0$ has been regained in a more general form through the particular forcing (4.61) which was chosen.

For a general mean flow profile $U(z)$, (4.63) is not very informative since it admits both steering level and non-steering level amplifying perturbations. However, in the special case of longitudinal modes: $\underline{U}_o.\underline{\gamma} = 0$,

$$\sigma_r = -\tan\tfrac{1}{2}\theta\ \sigma_i \quad \text{or} \quad \cot\tfrac{1}{2}\theta\ \sigma_i \tag{4.65}$$

so that, for θ not a multiple of π , amplifying perturbations must also propagate.

If also F is a (positive) constant, exact solutions to (4.64) can be found as in (4.29), but with the eigenvalue relation (4.30) (with $K = 0$) replaced by

$$\sigma = i\left\{\frac{gF\gamma^2}{\gamma^2 + \frac{1}{4H_o^2} + \frac{n^2\pi^2}{(z_2-z_1)^2}}\right\}^{\frac{1}{2}} e^{\frac{1}{2}i\theta} \tag{4.66}$$

It can be seen that σ is purely imaginary (amplification but no propagation) for $\theta = 0$. However, σ_r increases (increasing propagation speed) as the phase shift θ increases from 0 to π , amplification rate σ_i correspondingly falling from its maximum to zero.

The results from this model are illustrated in fig 4.5. In the case $\theta = 0$ (fig 4.5a) corresponding to unstable gravity waves $B_o < 0$ in (4.30), the heating coincides with the upward motion, and there is amplification but no propagation. However, as heating becomes out of phase with the vertical motion (fig 4.5b), the perturbation, while still amplifying, tends to move so that the previous areas of maximum heating become areas of maximum upward motion. Finally, in the case $\theta = \pi$ (fig 4.5c) corresponding to stable gravity waves $B_o > 0$ in (4.30), the heating coincides with the downward motion, and there is propagation but no amplification.

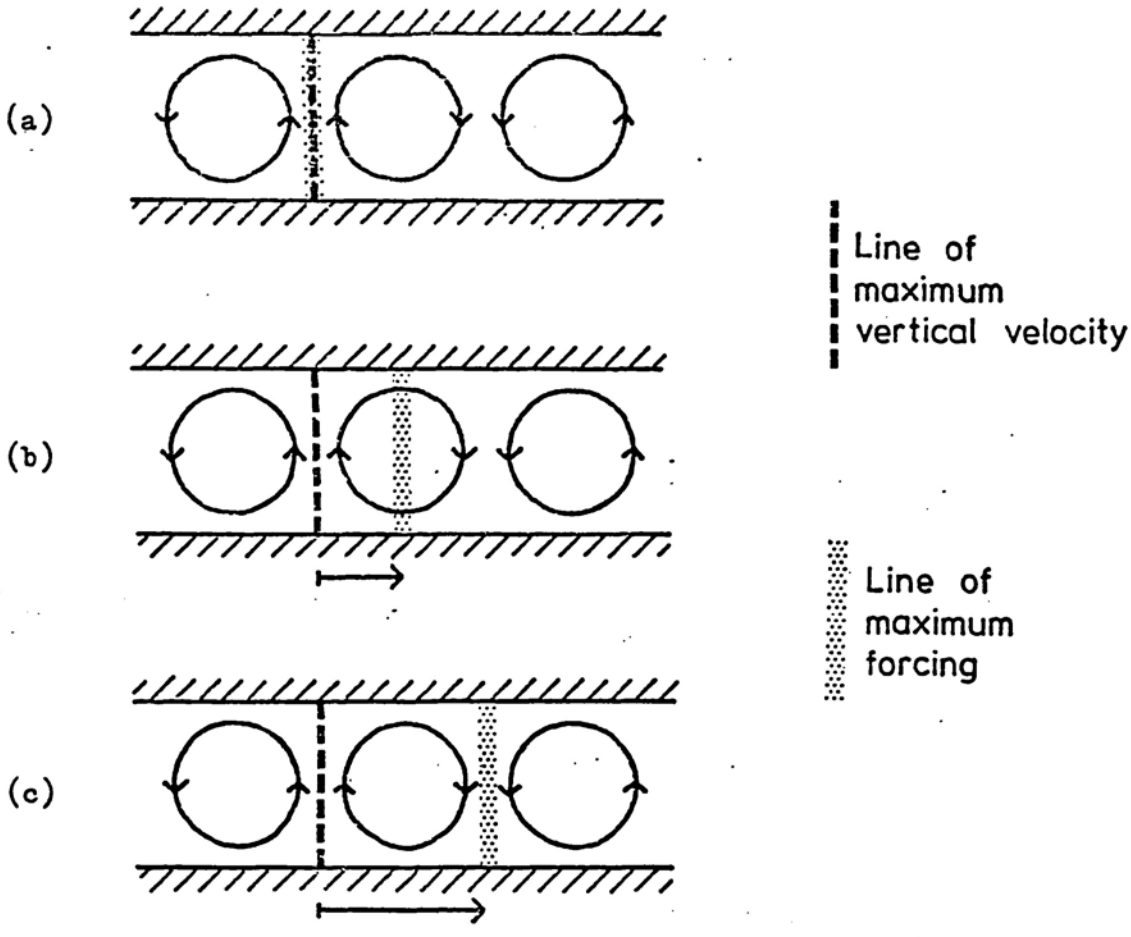


Fig 4.5. Phase-shifted linear perturbations of stratified flow (from Bolton 1980b).

(a) Statically unstable case (heating in phase with upward motion): growth but no propagation.

(b) Forced case (heating out of phase with upward motion): growth and propagation.

(c) Statically stable case (heating in phase with downward motion): propagation but no growth.

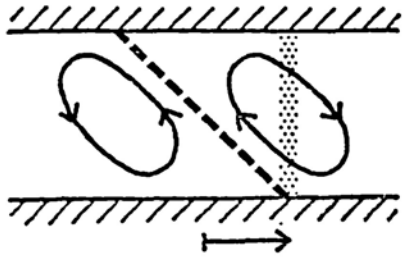


Fig 4.6. Forced linear perturbation of stratified flow in wave-CISK model, illustrating phase shift between heating and vertical motion, giving rise to both growth and propagation (from Bolton 1980b).

The above model does not exactly represent what happens in a conventional wave-CISK model since, even for unsheared mean flows, the lines of maximum w slope with height, as remarked by Lilly (1979). For Q proportional to w or dw/dz at some given level as is normally assumed, the lines of maximum forcing will not however slope with height, so a situation arises similar to fig 4.6, with a corresponding tendency for amplification to be accompanied by propagation.

A sloping of lines of maximum w with height could also arise from application of a radiation upper boundary condition in place of the rigid lid condition (4.14). Thus, assuming as before no phase change of forcing with height, there will again be a phase shift between vertical velocity and forcing, unless the phase tilt of velocity only accurs above the upper limit of any forcing. Such a phase shift is in any case still to be expected from the preceding analysis, provided there is negligible motion above a certain level, which is a reasonable approximation in view of the large reduction of amplitude of convective motion above the tropopause.

It is possible to suggest mechanisms which might lead to a phase shift between maximum forcing and maximum vertical motion. For example, considering downdraught cooling by evaporation of raindrops, the greatest cooling tends to correspond, not to the maximum vertical velocity (as in the case of heating in the updraught), but rather to the driest air, which is the incoming air at the edge of the cumulonimbus. Thus a phase shift not greater than $\frac{1}{2}\pi$ may occur in the downdraught cooling, and this could be modelled by an overall phase shift not greater than $\frac{1}{4}\pi$ for the updraught and downdraught combined. This shift is however rather small to account for the propagation of a tropical SQL. Moreover, a phase shift of this nature would not adequately justify the use of a wave-CISK model, since the phase shift in a wave-CISK model is not explicitly included, and varies with height in an unknown manner. If it is desirable to model a phase shift, a more satisfactory method would be to include it explicitly by use of a complex static stability parameter, as in (4.64). Thus the forced gravity wave model offers no advantage over the unstable model of section 4.1.1, which, being more straightforward is therefore to be preferred.

4.3 TWO-DIMENSIONAL MODELS.

4.3.1 Basic Equations.

In the gravity wave models, mathematical tractability was achieved by omission of the non-linear terms, results therefore being applicable

only to the initial growth stage. Another possibility, due to Dubreil-Jacotin (1935), and subsequently Long (1953), is to retain the non-linear terms and reduce the equations of motion to a single equation, but at the expense of constraining the motion to be two-dimensional and steady, so that only the mature stage is modelled. This approach has been applied to large amplitude lee-waves by Yih (1960 a,b) and Miles (1968 a,b), and forms the basis of the two-dimensional SQL models of Moncrieff and collaborators which are about to be described.

The Dubreil-Jacotin equations may conveniently be derived by making use of the Lagrangian description of fluid flow, in which (x,z) are replaced as independent variables by (x_o,z_o), the initial position of a fluid element at some given time t_o. In this system, the continuity equation becomes

$$\frac{\partial(x,z)}{\partial(x_o,z_o)} = \frac{\rho}{\rho_o} \tag{4.67}$$

and transformations between the coordinate systems may be deduced, for example

$$\frac{\partial z_o}{\partial x} = \frac{\partial(z_o,z)}{\partial(x,z)} = \frac{\rho_o}{\rho}\frac{\partial(z_o,z)}{\partial(x_o,z_o)} = -\frac{\rho_o}{\rho_o}\frac{\partial z}{\partial x_o} \tag{4.68}$$

where $\partial/\partial x$ = derivative holding z, $\partial/\partial x_o$ = derivative holding z_o. For steady flows with horizontal inflow $U_o(z_o)$, time only occurs in the combination $x_o + U_o t$, so that the derivative following the motion becomes

$$\frac{D}{Dt} = U_o \frac{D}{Dx_o} \tag{4.69}$$

and the fluid velocity is

$$\underline{u} = \frac{Dr}{Dt} = U_o\frac{\partial r}{\partial x_o} = \frac{\rho_o U_o}{\rho}\left(\frac{\partial z_o}{\partial z}, -\frac{\partial z_o}{\partial x}\right) \tag{4.70}$$

where use has been made of (4.68) and a similar equation for $\partial z_o/\partial z$.

In two dimensions the vorticity equation (4.26) becomes

$$\frac{D}{Dt}\frac{\eta}{\rho} = -\frac{g}{\rho}\frac{\partial}{\partial x}\delta\phi \tag{4.71}$$

where $\eta = \frac{\partial u}{\partial z} - \frac{\partial w}{\partial x}$, and the subscript $_o$ on the density has been dropped to avoid subsequent confusion with inflow values. In the absence of diffusion, the thermodynamic equation (4.3) may be written

$$\frac{D}{Dt}\left\{\phi_o(z) + \delta\phi\right\} = 0 \tag{4.72}$$

so that log potential temperature is conserved along each streamline and may be set equal to its inflow value $\phi_o(z_o)$. Hence

$$\delta\phi = \phi_o(z_o) - \phi_o(z) \tag{4.73}$$

and, making use of (4.68) and (4.69), the vorticity equation (4.71) becomes

$$\frac{D}{Dt}\left\{\frac{\eta}{\rho} - \frac{gB_o(z_o)z}{\rho_o(z_o)U_o(z_o)}\right\} = 0 \tag{4.74}$$

so that the quantity in brackets is conserved along each streamline. Setting it to its inflow value gives

$$\frac{\eta}{\rho} = \frac{\eta_o(z_o)}{\rho_o(z_o)} + \frac{gB_o(z_o)}{\rho_o(z_o)U_o(z_o)}(z - z_o) \tag{4.75}$$

or, using (4.70)

$$\frac{\rho_o U_o}{\rho}\nabla.\left(\frac{\rho_o U_o}{\rho}\nabla z_o\right) = \frac{d}{dz_o}\tfrac{1}{2}U_o^2 + gB_o(z_o)(z - z_o) \tag{4.76}$$

which is a form of the Dubreil-Jacotin equation. This is a nonlinear equation of the Helmholtz type which may, in principle, be solved for z_o subject to the boundary conditions (4.4).

For the inflow and outflow remote from any vertical motion, $\partial/\partial x \equiv 0$, and (4.76) may be written

$$\tfrac{1}{2}\frac{d}{dz_o}\left\{\left[\left(\frac{\rho_o}{\rho}\frac{dz_o}{dz}\right)^2 - 1\right]U_o^2\right\} = gB_o(z_o)(z - z_o) \tag{4.77}$$

Now from (4.70),

$$\frac{\rho_o}{\rho}\frac{dz_o}{dz}U_o = u \tag{4.78}$$

so, integrating, it follows that the change in kinetic energy along a streamline is given by

$$\tfrac{1}{2}\left(u^2 - U_o^2\right) = \int_{z_*}^{z_o} gB_o(z_o')(z' - z_o')\,dz_o' - \frac{\delta p_*}{\rho} \tag{4.79}$$

where z_* is any level for which $z = z_o$, and $\delta p_*/\rho$ is the change in $\delta p/\rho$ across the system at this level, this latter term (the arbitrary constant in the integral) having been evaluated by making use of the energy equation.

Equations (4.76) and (4.79) are generalisations of equations derived under a rather different formulation by Green and Pearce (1962), and used as the basis of an elegant series of mathematical models of SQL's in Moncrieff and Green (1972), Moncrieff and Miller (1976) and subsequent papers. Except for numerical integrations with assigned heat sources, they in fact considered a stably stratified environment $B_o > 0$, with a forcing term Q (as in (4.56)) to represent latent heat release. However, the particular form of the forcing chosen, $Q = \gamma w$ (γ constant) means that their thermodynamic equation reduces to (4.3)

with a modified static stability $B_o - \gamma$ replacing B_o, so that like the unforced linear models of section 4.1, these models are open to the criticism that they do not adequately represent latent heat release. Another limitation is that (4.76) only holds for two dimensional steady flows, whilst (4.79) only holds for inflow and outflow. A generalisation of the argument of Moncrieff and Miller (1976) does show (4.79) to hold for inflow and outflow of three dimensional flows provided they are steady; extension of (4.76) however results in a set of highly nonlinear equations, as shown in appendix B.

4.3.2 Overturning Models.

The Moncrieff overturning models considered two idealised situations, illustrated in fig 4.7, corresponding respectively to steering level and non-steering level storms.

(a) Steering Level Case (fig 4.7a). For the updraught in this case, Moncrieff and Green (1972) showed that if

$$U_o = S(z_* - z_o) \qquad \text{for } z_o \leq z_* \qquad (4.80)$$

(i.e. constant inflow shear), it is, in the case of constant density and static stability, possible to satisfy (4.77) with an inflow- outflow relation

$$z_* - z_o = \beta(z - z_*) \qquad (4.81)$$

Here the steering level z_* (level of no relative motion) and the parameter β may be related by the condition that inflow air at the surface $z_o = 0$ must leave at the upper boundary $z = H$ to give

$$z_* = H \frac{\beta}{\beta + 1} \qquad (4.82)$$

The condition for existence of such a solution is obtained by substitution in (4.77) as

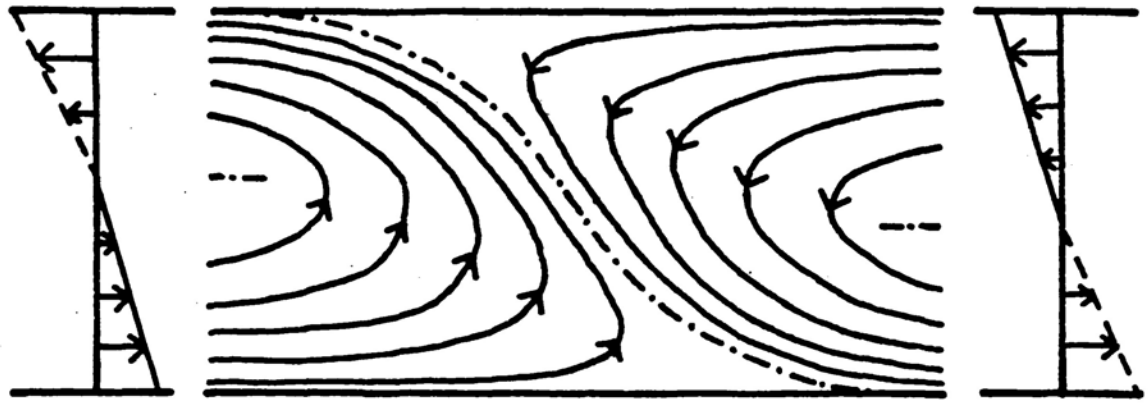
$$\beta(1 - \beta) = \frac{gB_o}{S^2} = R \quad , \text{ say} \qquad (4.83)$$

where R is a dimensionless number which may be taken as a Richardson number. For existence of real solutions for β, R must be less than $\frac{1}{4}$. This is satisfied in the buoyant case $R < 0$, and then $\beta > 1$, and the outflow velocity

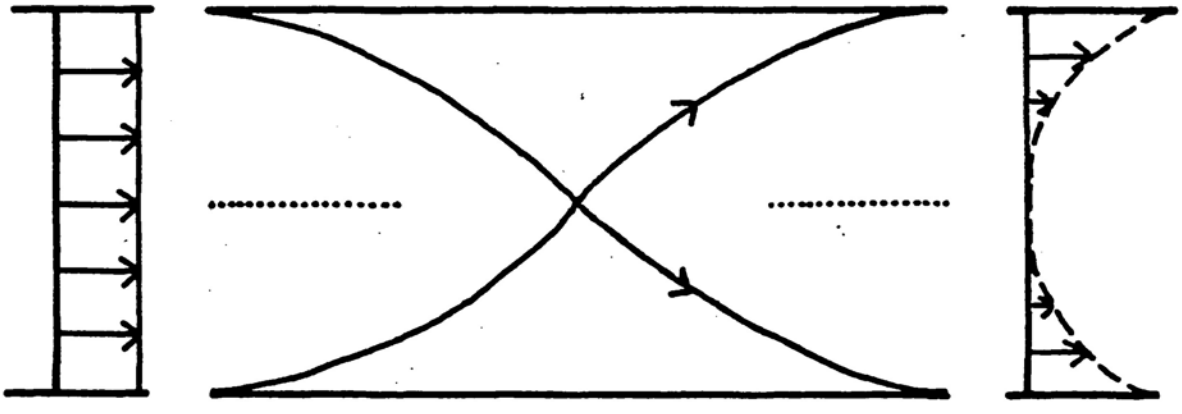
$$u = \beta^2 S(z - z_*) \qquad (4.84)$$

(from (4.78) and (4.81)) shows increased shear and thus, according to Moncrieff and Green (1972), up-gradient momentum transfer.

Including the effect of mean density variation with a constant scale height defined as in (4.15), Moncrieff and Green showed that



(a)



(b)

Fig 4.7. Airflow in two-dimensional steady overturning models.

(a) Steering level case: constant inflow shear, Richardson number $-\frac{1}{2}$ (after Moncrieff 1978).

(b) Non-steering level case: constant inflow velocity, maximum mechanical efficiency (after Moncrieff and Miller 1976).

Full lines are used for inflow profiles, dashed lines for outflow profiles; dash-dot lines separate inflow and outflow streamlines.

the storm speed relative to the surface flow is approximately

$$c = S z_* = SH \left\{ \frac{1 + (1-4R)^{1/2}}{3 + (1-4R)^{1/2}} - 0{\cdot}11 \frac{H}{H_0} \right\} \qquad (4.85)$$

where the first term on the right comes from (4.82), and the second term is an empirical fit to numerical results. Using this, they were able to infer propagation speeds to within 3 m/s for a variety of middle latitude storms, though not for a severe right-moving storm.

Moncrieff (1978) extended the work of Moncrieff and Green (1972) to compute the full storm circulation, with an updraught and downdraught separated by a free boundary under various boundary conditions; fig 4.4a actually shows the streamlines computed for $R = -\frac{1}{2}$ with both velocity and temperature discontinuous along the interface. Moncrieff found that negative vorticity generation along the updraught/downdraught interface gave rise to reversal of outflow for $-R > 1$, so that steady states could only exist for $-R \leqslant 1$. By two-dimensional numerical integration of the time dependent equations, as well as consideration of the steady state problem, he showed that the interface normally sloped downshear, as expected from the up-gradient momentum transfer, the only exception being when non-adiabatic forcing was applied, in which case the flow was transient. Since physically an upshear slope is required so that rain falling from the updraught can drive the downdraught, it therefore appears that a steady circulation can only be achieved in three dimensions with interlocking airstreams.

(b) Non-Steering Level Case (fig 4.7b). Here the need for a three-dimensional model is even more apparent because of the crossing of airstreams. The inflow and outflow may however still be two-dimensional, in which case (4.79) still applies, and may be solved analytically for unsheared inflow with constant density and static stability, as in Moncrieff and Miller (1976). Taking the boundaries at $z = 0, H$, so that air entering at $z = \frac{1}{2} H$ leaves at the same level, and writing δp_* as the pressure jump at this level, the solution is

$$z_0 = z - \frac{c}{(-gB_0)^{1/2}} \left\{ 1 - \left(1 - \frac{\delta p_*}{\frac{1}{2}\rho c^2} \right)^{\frac{1}{2}} \right\} \sinh \frac{(-gB_0)^{\frac{1}{2}}}{c} \left(z - \frac{H}{2} \right) \qquad (4.86)$$

where c is the storm speed relative to the inflow, the corresponding outflow being

$$u = c \left[1 - \left\{ 1 - \left(1 - \frac{\delta p_*}{\frac{1}{2}\rho c^2} \right)^{\frac{1}{2}} \right\} \cosh \frac{(-gB_0)^{\frac{1}{2}}}{c} \left(z - \frac{H}{2} \right) \right] \qquad (4.87)$$

In order to determine the amplitude of the system, it is necessary to specify $\frac{\delta p_*}{\frac{1}{2}\rho c^2}$; the case $\frac{\delta p_*}{\frac{1}{2}\rho c^2} = 1$, according to Moncrieff and Miller

(1976), defines a convective circulation of maximum mechanical efficiency, i.e. conversion of available potential energy into mean flow kinetic energy; this is illustrated in fig 4.7b. Applying the condition that air flowing in at the lower boundary must leave at the upper boundary, and vice-versa, gives the relation

$$\left\{1 - \left(1 - \frac{\delta p_*}{\frac{1}{2}\rho c^2}\right)^{\frac{1}{2}}\right\} \sinh \frac{(-gB_o)^{\frac{1}{2}}}{c}\frac{H}{2} = \frac{(-gB_o)^{\frac{1}{2}}}{c}H \,, \qquad (4.88)$$

which in the case $\frac{\delta p_*}{\frac{1}{2}\rho c^2} = 1$ implies

$$c = 0{\cdot}32\,(APE)^{\frac{1}{2}} \qquad (4.89)$$

where

$$APE = \tfrac{1}{2}(-gB_o)H^2 \qquad (4.90)$$

is the available potential energy, obtained by evaluating (3.1) for a parcel originating at the lower boundary.

If density variation and a small constant shear are included, Moncrieff and Miller (1976) found numerically that the storm speed relative to the mean inflow is still given adequately by (4.89). They suggested however that this would break down if $-R \lesssim 2.8$ (with R as in (4.83)), since a large shear would produce relative outflow at the front at some levels. Application of (4.89) to Venezuelan SQL's in Betts et al (1976) gave propagation speeds to within 4 m/s; the application to West African data has been considered in section 3.1.3.

Though the overturning models represent well several aspects of SQL dynamics, some important limitations should be mentioned which indicate the need for further study.

Firstly, though the models do agree with observations (section 2.1.1) in that they predict cut-off Richardson numbers, the division into steering level storms for $-R \lesssim 1$, propagating storms for $-R \gtrsim 2.8$ appears to contradict observational evidence that they both occur for comparable Richardson numbers, the difference lying in whether or not the velocity profile has a maximum. Studies with more representative velocity profiles are needed to clarify this point.

Secondly, while the models do indicate up-gradient momentum transfer, the inflow-outflow changes, particularly in the non-steering level case (fig 4.7b) bear little relation to those observed (e.g. fig 2.9). Again this may be partly attributed to use of an unrepresentative velocity profile, but a more important shortcoming (Lilly 1979) is the use of a constant static stability, which results in downdraught inflow from the upper boundary, rather from the middle levels as observed (fig 2.2).

Finally, though the models do give reasonable estimates of storm speeds, they do not indicate a preferred direction of propagation, and in particular do not explain why SQL's should be oriented transverse to the wind shear, whereas consideration of fastest growing linear modes appears to favour a longitudinal disturbance; an assumption such as that made in section 3.1.3 that their direction of motion is that of the mean wind is entirely arbitrary and has no mathematical basis. A three-dimensional study is needed to resolve this point, and, as previously mentioned, to model individual airstreams; this however runs into the difficulties hinted at the end of the previous section.

4.3.3 Density Current Models.

One area in which inability to resolve individual airstreams is unimportant is modelling of downdraught outflows, these being a much larger-scale feature of the motion. Following theoretical work on density currents by Benjamin (1968), experiments by Simpson (1969) and Simpson and Britter (1980), and observations by Charba (1974) and Miller and Betts (1977), Thorpe et al (1980) have applied the two-dimensional steady equations to modelling of both steering level and non-steering level cases. Both updraught and downdraught solutions to the equations are possible, but only the downdraught situation will initially be considered.

(a) Steering Level Case (fig 4.8a). Here, the inflow-outflow equations are the same as in the corresponding overturning model, with solutions for $R \leqslant \frac{1}{4}$; those solutions with $R > 0$ will be forced downdraughts, those with $R < 0$ convective downdraughts. The depth of the outflow ($H - z_*$ in the overturning model) will be

$$h_D = \frac{2}{3 + (1 - 4R)^{\frac{1}{2}}} \qquad (4.91)$$

As before the complete circulation may be found, but it differs from the overturning case in that there is no updraught/downdraught interface, and hence no upper limit on $-R$; also, whereas previously the inflow shear was prescribed, now it is regarded as a response to the vertical motion, effected by gravity waves during development of the flow. This model could apply to an isolated thunderstorm.

(b) Non-Steering Level 'Jump' Model. This would on the other hand be appropriate for modelling the propagating downdraught of a SLS. Now such a downdraught will have $(z - z_0)$ negative everywhere except at the boundaries, where it vanishes, so that $\frac{d}{dz}(z - z_0)$ must be negative

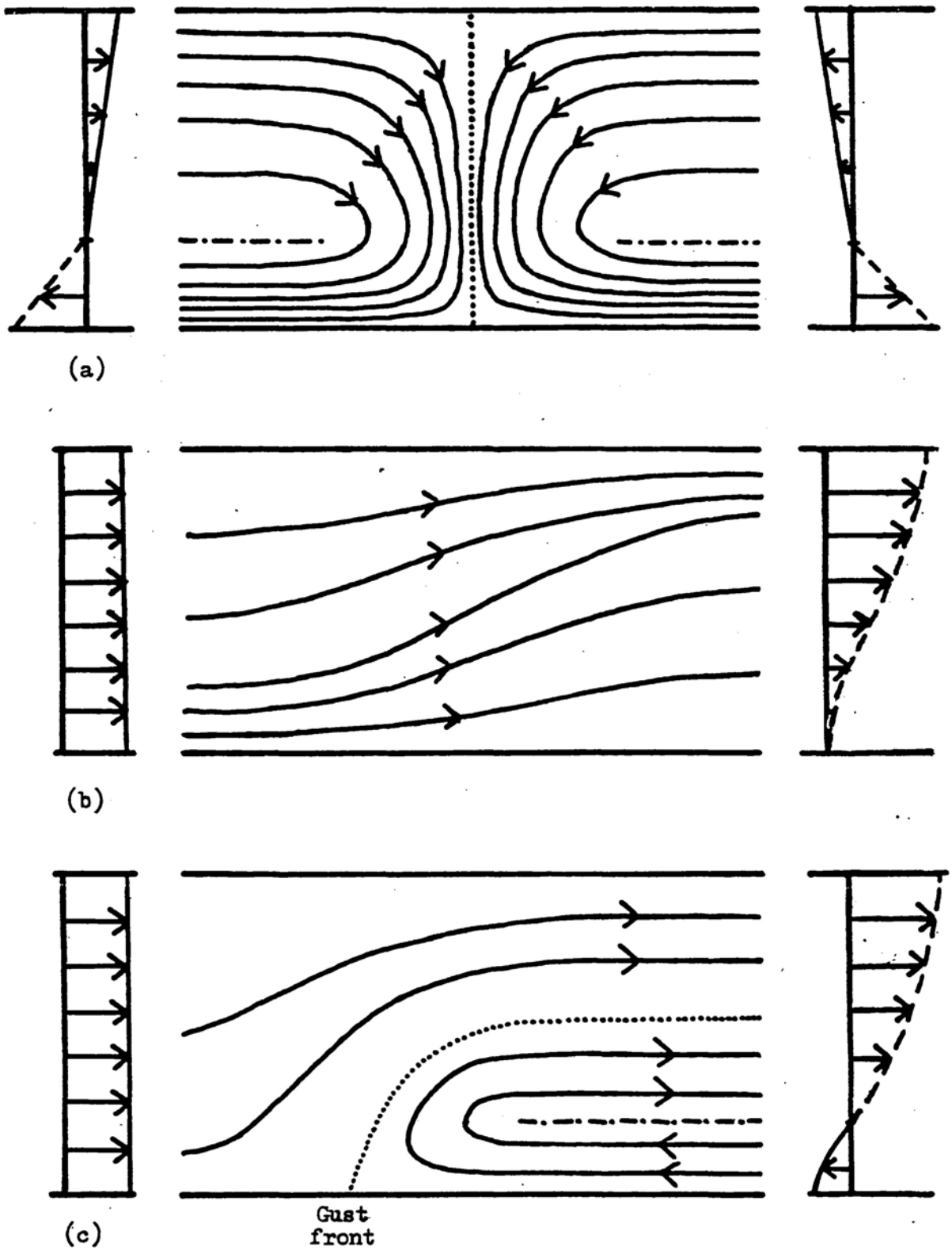


Fig 4.8. Airflow in two-dimensional steady density current models (after Thorpe et al 1980).

(a) Steering level downdraught.

(b) Non-steering level updraught.

(c) Density current head.

at the lower boundary, positive at the upper boundary. Hence at the lower boundary, $dz_o/dz > 1$, and so, by (4.78), noting that $\rho = \rho_o$ here, $u^2 - U_o^2 > 0$, which represents an increase in low-level storm-relative kinetic energy; substitution in (4.79) shows that there will be an associated pressure drop. Similarly at the upper boundary there will be a decrease in kinetic energy, and pressure jump. These changes correspond to the period of return to pre-storm conditions (section 2.2.3b), when motion is dominated by the mesoscale downdraught.

Furthermore, since $(u^2 - U_o^2)$ is negative at the upper boundary, positive at the lower boundary, $\frac{d}{dz}(u^2 - U_o^2)$ must be negative somewhere, and so, since $(z - z_o)$ is everywhere non-positive, B_o must be positive somewhere by (4.77). If static stability is constant, it must hence be positive everywhere, as inferred using a different argument by Thorpe et al (1980), implying that the mesoscale downdraught must be dynamically forced; this conclusion does not necessarily follow however if B_o is allowed to change sign.

Thorpe et al (1980) solved the inflow-outflow equations in the non-steering level case for an updraught, not a downdraught, with constant ρ , B_o, U_o . The solution may be written

$$z_o = z - \frac{c}{(gB_o)^{\frac{1}{2}}}\left\{1 - \left(1 - \frac{\delta p_o}{\frac{1}{2}\rho c^2}\right)^{\frac{1}{2}}\right\} \sin \frac{(gB_o)^{\frac{1}{2}}}{c} z \qquad (4.92)$$

$$u = c\left[1 - \left\{1 - \left(1 - \frac{\delta p_o}{\frac{1}{2}\rho c^2}\right)^{\frac{1}{2}}\right\} \cos \frac{(gB_o)^{\frac{1}{2}}}{c} z\right] \qquad (4.93)$$

where δp_o is the surface pressure jump, and the boundary conditions give

$$\frac{c}{(gB_o)^{\frac{1}{2}}H} = \frac{1}{n\pi} = F_A \quad , \text{ say} \qquad (4.94)$$

this quantity being a Froude number for the flow. As in the overturning model, $\frac{\delta p_o}{\frac{1}{2}\rho c^2}$ must be specified to determine the amplitude of the system; the case $\frac{\delta p_o}{\frac{1}{2}\rho c^2} = 1$ is illustrated for $n = 1$ in fig 4.8b.

Unlike overturning, there is no crossing of airstreams here and it should be possible to solve for the internal flow pattern. However in this case of constant inflow velocity, (4.76) becomes

$$\nabla^2 (z - z_o) + \frac{gB_o}{c^2}(z - z_o) = 0 \qquad (4.95)$$

which has no solution for an infinite x-domain with $(z - z_o)$ zero on inflow and finite on outflow. A way out of this difficulty could be to impose forcing over a finite length in the x-direction, but if this device is to be avoided it seems that a sheared inflow profile is

required for existence of a steady jump*. This may throw some light on why SLS's only occur in conditions of appreciable wind shear, though further investigation is required.

(c) Time Integration. Thorpe et al (1980) also integrated the time-dependent two-dimensional equations for stably stratified flow with constant ambient wind U_0 and a localised heat sink Q as in (4.56). Their results showed density currents propagating both upstream and downstream. The structure of a density current head relative to the gust front is show in fig 4.8c, and is intermediate between the steady steering level and non-steering level cases; a steady flow is however unlikely since overturning of the stably stratified low level air on the right would result in a statically unstable return flow which would break down into eddies (this argument would also apply to the stably stratified case, $R > 0$ of steering level overturning). In the absence of ambient wind ($U_0 = 0$) the heads propagated in each direction at a speed

$$c_\Delta \simeq 0{\cdot}8\, c' \tag{4.96}$$

where

$$c' = (g \times Q \times \text{area of sink})^{\frac{1}{3}} \tag{4.97}$$

is a characteristic velocity of the system; in contrast, for a liquid

$$c_\Delta \simeq \left(g H_\Delta \frac{\Delta\rho}{\rho}\right)^{\frac{1}{2}} \tag{4.98}$$

for a density current of depth H_Δ (Benjamin 1968). When an ambient flow $U_0 > 0$ was imposed, the speeds of both upstream and downstream heads were given empirically by

$$c = c_\Delta + 0{\cdot}7\, U_0 \tag{4.99}$$

which agrees with the results obtained experimentally by Simpson (1969) and Simpson and Britter (1980). If however $0.7\, U_0 \geq c_\Delta$, no upstream head was formed, though for slightly smaller values of U_0, there was a large surface convergence ahead of the head, corresponding to optimum

* Long (1965) was similarly unable to obtain solitary waves in the constant inflow case. He remarked that if the Boussinesq approximation is not made, (4.76) should be replaced by

$$\frac{\rho_0 U_0}{\rho} \nabla\cdot\left(\frac{\rho_0 U_0}{\rho}\nabla z_0\right) = \frac{d}{dz_0}\tfrac{1}{2}U_0^2 + B_0(z_0)\left\{g(z-z_0) + \tfrac{1}{2}\left(|\underline{u}|^2 - U_0^2\right)\right\}$$

and attributed the failure to obtain solitary waves to omission of the last term. However Lilly (1979) pointed out that the extra term is negligible, and can in any case be removed by the transformation $U_0' = \theta^{\frac{1}{2}} U_0$ (where $d/dz_0 \ln \theta_0 = B_0$), so that (4.95) still holds for the only slightly varying inflow profile $U_0 = \text{constant} \times \theta_0^{-\frac{1}{2}}$.

conditions for storm regeneration.

In the region behind the head, behaviour was related to a Froude number

$$F_N = \frac{U_o}{c'} \qquad (4.100)$$

(related to F_A in the steady analysis). For $U_o = 0$, F_N vanishes, and there was a symmetrical downward flow in the sink region as in fig 4.8a, with outflow depth close to that predicted by (4.91). For $F_N \gg 1$, after an initial period of adjustment flow, downward motion was displaced to the downstream head, and behind there was a jump-type upward motion, the outflow from which occupied nearly the whole fluid depth, as in fig 4.8b. Intermediate between these cases were other flow configurations which did not correspond to any simple steady model.

These results thus throw light on some aspects of the downdraught outflow such as its depth and propagation speed, indicating in particular the fairly critical matching of outflow and environmental wind speeds needed to provide optimum conditions for storm regeneration. Further study is however needed to provide a mathematical basis for the empirical results, and to produce a clearer link with observations.

4.3.4 Use of an Assumed Flow.

Green and Pearce (1962) approached the two-dimensional steady flow problem in one further way which did not make use of the Lagrangian equations. They assumed a complete two-dimensional steady motion field, and solved (4.71) and (4.56) to find the forcing Q needed to sustain the motion. Considering only the steering level overturning case, with an upshear tilt to the updraught/downdraught interface, they found that such a configuration was possible provided there was cooling at lower levels of both updraught and downdraught, and heating at upper levels of the updraught. The upshear tilt of the updraught meant that the low level cooling could be partly provided by evaporation of falling rain, but this would probably be inadequate to cool all the incoming upper level air; a three-dimensional structure is thus implied, with some of the incoming air deflected round the storm. The need for upper level heating may be a result of the unrealistic rigid upper boundary condition (which rules out deceleration of the updraught above the tropopause), or may indicate the need to include a closed eddy between updraught and downdraught at upper levels in the assumed flow.

This last point brings out the principal shortcoming of the method: the need to provide a realistic velocity field beforehand. Also, it does not necessarily follow that a forcing only slightly different from

that inferred would maintain a velocity field close to the original. The method can however easily be extended to three-dimensional unsteady flows, and further study in this direction could be worthwhile.

4.4 NUMERICAL MODELS.

4.4.1 Zero and One-Dimensional Models.

Turning now to fully numerical integrations, a variety of models exist for the purpose of studying different aspects of storm structure. Simplest dynamically are the zero and one-dimensional models (the latter having vertical variation only) used to examine in detail cloud microphysics and growth of convective elements. These are reviewed for instance by Lilly (1975) and Gokhale (1975), and provide the background for the parameterisations used in the two and three-dimensional models which follow. The emphasis in this account will however be on storm dynamics, and for this reason the zero and one-dimensional models will not be described, and nor will details of the two and three-dimensional models such as initial and boundary conditions, and integration schemes, which may be found in Lilly (1979).

4.4.2 Two-Dimensional Models.

The earliest dynamical model of a convective element was a two-dimensional study in a dry unsheared environment by Malkus and Witt (1959). Lilly (1962) made a similar study, whilst Arnason et al (1968) and Clark (1973) included moisture; their results showed development of a compensating downward motion on each side of the initial updraught. Similar results, though not directly applicable to SQL's were obtained with axisymmetric models, a comparison with results of two-dimensional models being found in Soong and Ogura (1973).

Asai (1964) extended the two-dimensional study by inclusion of constant shear in a moist but non-precipating model. He found that, as in Moncrieff's (1978) steady model (section 4.3.2a), the convection tilts downshear with height, with associated up-gradient momentum transfer. A consequence not evident in Moncrieff's model is that convection is suppressed in comparison to the unsheared case, a result which agrees with the observational conclusions of Byers and Battan (1949) (section 2.1.1) and the results on orientation of linear modes quoted in section 4.1.2.

With the inclusion of rain however, various models with uni-directional shear showed that, although convection in the sheared case

may not be so intense, it will in general persist much longer than it would in the absence of shear. Takeda (1965, 1966) found that a quasi-steady circulation could develop in which the lower part of the convective cell tilts upshear, so that rain falling from the updraught can enhance the downdraught on the upshear side as in fig 4.9a; this downdraught in turn enhances the updraught by increasing convergence at its base. Schlesinger (1973) confirmed existence of a quasi-steady circulation with moderate environmental shear and moisture supply; if shear is too weak however, there is an intense updraught, but formation of a downdraught downshear cuts off the moisture supply and causes dissipation; with inadequate moisture supply on the other hand, strong shear will disrupt the airflow so that no storm can exist. These results are consistent with the conclusion of section 2.1.1 that the Richardson number must lie within a certain range for existence of a SQL.

Not all models with unidirectional shear were however able to produce a quasi-steady circulation. Hane (1973) found rather that the system pulsates, with an upshear downdraught undercutting the updraught and triggering new development downshear, a situation which he attributed to the two-dimensional constraint. Takeda (1971) on the other hand, contrary to his earlier results found that the updraught sloped downshear, so that the downdraught was downshear, as in fig 4.9b, and cut off the moisture supply, leading to dissipation. If however there was a fairly low jet, the cloud was erect, and the downdraught could form in the direction of the low level shear (fig 4.9c), enhancing the updraught by increasing convergence at its base and permitting a quasi-steady circulation. The need for a jet agrees with observations of tropical SQL's (section 3.2.1), though Takeda's two-dimensional quasi-steady system could not move faster than the maximum wind or there would be crossing of airstreams.

None of these studies give any indication of how a two-dimensional transverse disturbance might emerge, when the fastest growing linear mode is normally longitudinal. Sasaki (1959) and Ogura and Charney (1960) did study development of a SQL in advance of a cold front, while Orville and Sloan (1970) initiated convection over a two-dimensional ridge. However. unless a two-dimensional structure is imposed like this, a three-dimensional study is necessary even for unidirectional mean flows, as remarked by Steiner (1973).

4.4.3 Three-Dimensional Models.

In a non-precipitating three-dimensional study, Steiner (1973) confirmed Asai's (1964) result that unidirectional shear inhibits

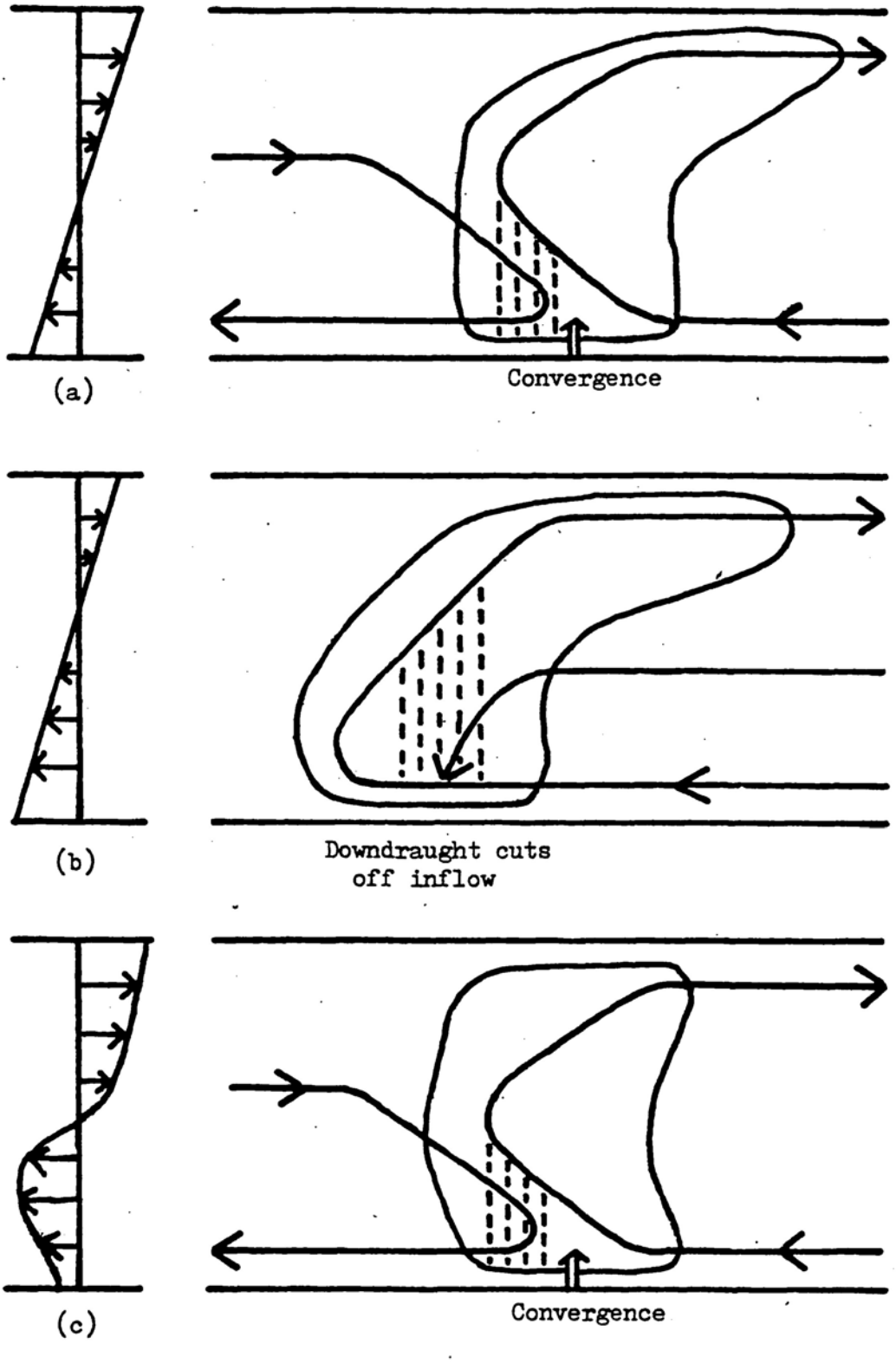


Fig 4.9. Storm-relative airflow in two-dimensional simulations.

(a) Constant inflow shear: long-lived storm (after Takeda 1966).

(b) Constant inflow shear: short-lived storm (after Takeda 1971).

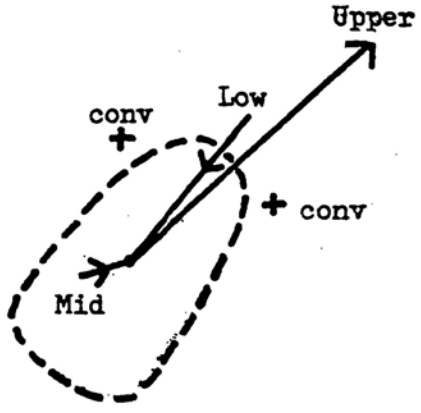
(c) Low-level jet: long-lived storm (after Takeda 1971).

convection. With precipitation however, Pastushkov (1975) showed that if there is sufficient buoyancy, convection is intensified, with formation of new updraughts downshear and to the sides of the initial updraught. Such results could be relevant to the initial development of a SQL, but subsequant results with similar models by Schlesinger, and Klemp and Wilhemson are more applicable to the severe right and left moving storms of Browning (1968).

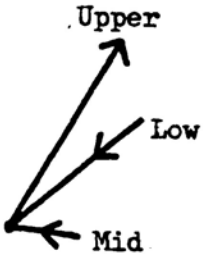
Schlesinger (1975, 1978) found that there was a quasi-erect initial updraught, weaker in the presence of shear, which acted as a barrier to middle level flow. In the absence of shear the downdraught formed under the updraught and further development was inhibited. With suitable unidirectional shear, the downdraught formed upshear and undercut the updraught, with the result that the updraught split into two rotating halves which moved apart and continued to grow for some time, sustained by convergence at the edge of the downdraught outflow. With a clockwise rotation of the wind at low levels, a split still occurred, but now the right hand flank was stronger and moved more slowly, as is commonly observed to happen (section 2.1.3a).

Wilhemson (1974) confirmed the splitting of the updraught, and Klemp and Wilhemson (1978 a,b) investigated further. Their results were similar to those of Schlesinger, except that the downdraught in the sheared cases formed directly under the updraught, and after splitting of the updraught, it also split and the halves moved with the updraughts, which continued to intensify. A subsequent study, Wilhemson and Klemp (1978), highlighted the role of the gust front formed by the downdraught outflow in generating the convergence needed to maintain the system.

The role of the downdraught outflow in splitting was confirmed by Thorpe and Miller (1978) in one of a series of studies using the model of Miller and Pearce (1974). They suggested that cells had an interlocking updraught/downdraught structure, and moved with a velocity close to the mean wind over the depth of the troposphere which they occupied at any given time. In the splitting storm study (fig 4.10a), cell relative outflow at upper levels overlaid the cell relative inflow at low levels, so that the cell sloped downshear, the downdraught formed downshear, and inflow to the updraught was cut off; new cells were formed by convergence on each flank of the wedge-shaped downdraught outflow, but in this case moved parallel to each other and did not rotate. Unfortunately this study, based on a profile appropriate to the Wokingham storm (Browning 1962) produced very poor correspondence

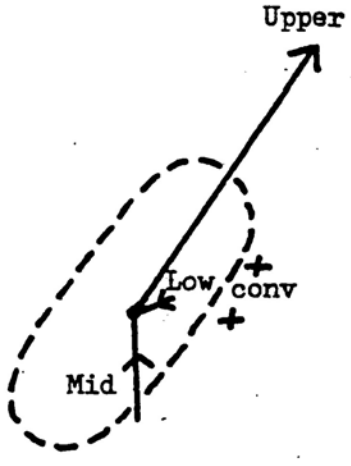


(a) Splitting storm: cell and storm relative

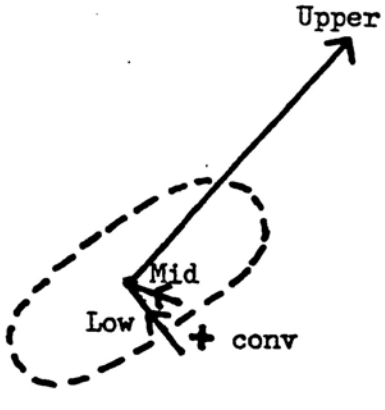


Hampstead storm

(b) Cell relative



(c) Storm relative



(d) Multicell storm: cell relative

Fig 4.10. Flow vectors for various three-dimensional simulations (after Thorpe and Miller 1978)

Low: 1000-850 mb; Mid: 750-600 mb; Upper: 400-250 mb.

— — — — : Outline of downdraught outflow

+ conv : Principal region of convergence.

with observation. Better results were obtained with the Hampstead stationary storm (Miller 1978); here again the cell relative updraught outflow overlaid the inflow (fig 4.10b) so that cell lifetimes were short; now however, the cell downdraughts merged in a cold pool, and a succession of cells formed on the south flank along a stationary line of convergence formed where the cold outflow met incoming low level air (fig 4.10c). If the direction of the low level inflow was changed (Thorpe and Miller 1978) so that it no longer lay under the upper level outflow (fig 4.10d), cells tended to last much longer, and each cell in turn triggered the next where its downdraught met incoming air on its right flank, leading to a right moving multicell storm.

With the same model, Moncrieff and Miller (1976) and Miller and Betts (1977) made the only three-dimensional study which deals specifically with a SQL, namely the Venezuelan SQL of 24 July 1972 also considered by Marroquin and Raymond (1979) - see section 4.1.2. They found that the fast-moving evaporatively-driven cell downdraughts formed a cold pool moving ahead and triggering pairs of new cells along the line where it met incoming low-level air; above, the descent of the cell downdraughts resulted in sucking down of a slower mesoscale downdraught so that, as inferred in section 4.3.3, this second downdraught was forced, not driven by evaporation of rain from the anvil as suggested by Zipser (1969)*. The line orientation 155 - 335° which was obtained agreed well with observation, but movement of the cells to the north along the line meant that the system as a whole moved from slightly south of east, as opposed to the observed direction from 065°. Moncrieff and Miller (1976) explained this discrepancy by suggesting that only part of the observed line had been simulated, possibly due to insufficient resolution, or because the whole line owed its existence to a trough. They suggested that the persistence of the SQL arose from a matching of the storm speed, as determined by locations of successive cells, with the speed of the downdraught outflow, determined by a density current model as in section 4.3.3. Significantly the model failed to generate a SQL using a West African profile (Thorpe, personal communication), in which a reversal of the wind direction at low levels would result in a smaller storm speed.

* In a recent numerical study, Brown (1979) did however show that much of the mesoscale descent could be accounted for by evaporation.

4.5 OTHER DYNAMICAL MODELS.

Before concluding this chapter, mention should be made of certain ad hoc models which, unlike the other models, start not from the complete set of equations of motion, but from some assumption on the nature of the motion.

4.5.1 Mixing Models.

Newton (1950) proposed that in a SQL or other SLS, vertical mixing of horizontal momentum of incoming air resulted in formation of regions of convergence and divergence (fig 4.11), leading to preferred downshear development. Thus, for flow which veered (Newton 1963), new growth was favoured on the right flank (fig 4.12). Modelling an individual SQL element as a rigid cylindrical barrier to the flow at each level, and making use of the formula for the induced pressure drop, Newton and Newton (1959) deduced that clouds with large diameters and vertical velocities will have smaller in-cloud shear, and hence less tendency for the tops to be blown off, thus apparently explaining the contradictory effect of shear in local thunderstorms and SLS's. Subsequent studies (Newton 1966; Warner 1972), considering parcel trajectories, showed that an upshear tilt of the updraught was possible. A mixing model such as this is however open to the serious objection that it represents down-gradient momentum transfer, whereas there is observational evidence, quoted for example in Moncrieff and Green (1972), of up-gradient transfer at upper levels; furthermore it is questionable whether the formula for the induced pressure drop is still valid when the rigid cylinder is replaced by an airstream, particularly bearing in mind that the motion of a convection cell as a whole will in general differ considerably from the velocities of individual air parcels in it, as noted by Raymond (1975).

4.5.2 Rigid Cylinder Models.

Other studies, though not applicable to SQL's, have also made use of properties of flow past a rigid cylinder. Fujita (1965) used the Magnus effect, whereby a rotating cylinder in a uniform stream is deflected perpendicular to the stream, to explain the formation of hook echoes in supercells by displacement of the rotating updraught core relative to the body of the storm. Extending this idea, Fujita and Grandoso (1968) explained storm splitting as the separation due to the Magnus effect of oppositely rotating vortices shed by an initial cylindrical updraught. As before, the validity of these studies depends

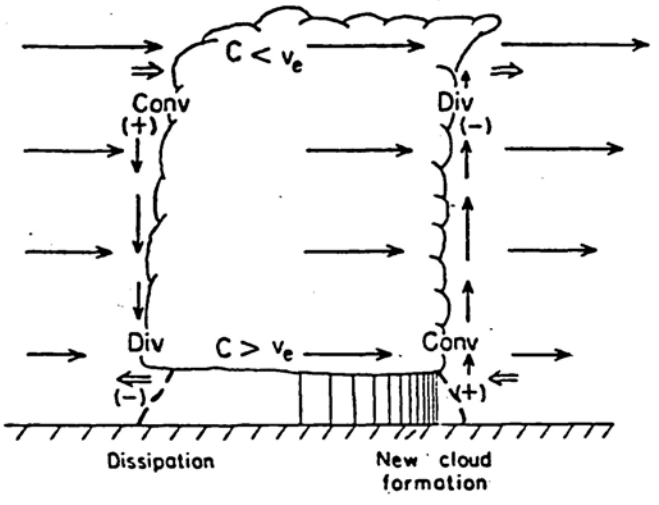


Fig 4.11. Schematic cross section through a squall line or large rainstorm. Lengths of horizontal arrows are proportional to wind speeds outside and inside the cloud system (from Newton and Newton 1959).

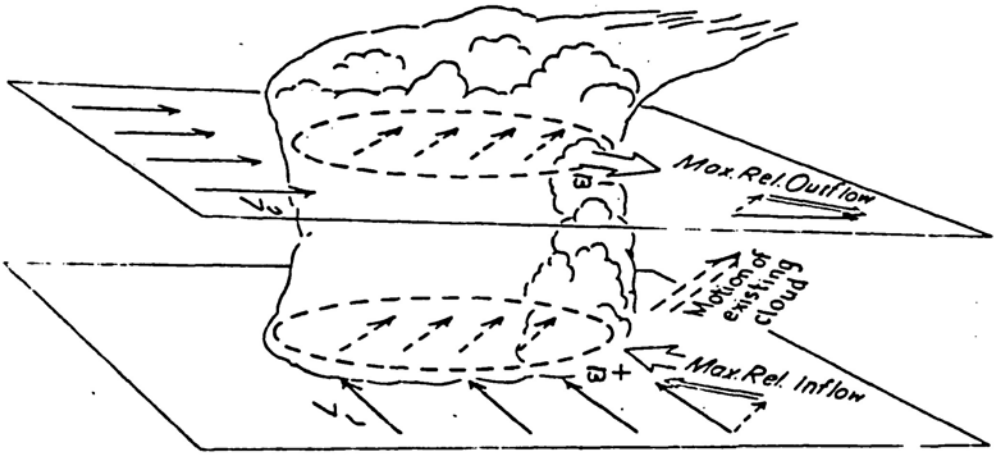


Fig 4.12. A large isolated thunderstorm or squall line element embedded in an environment in which the wind veers with height (from Newton 1963).

on the extent to which airstreams do have the properties of rigid flow barriers.

4.5.3 Sinking Jet Model.

Le Roux (1971) produced a model of an African SQL in which a cold core wind maximum in the African Easterly Jet sinks until it reaches the surface, forming an arc-shaped front where it meets the monsoon air; the monsoon air is forced to ascend, thus triggering convection. Energy is supplied by the AEJ, the convection being almost incidental to the process, which, as with the stable gravity wave model (section 4.2.1) is a serious shortcoming.

In conclusion therefore, the assumptions on which these three ad hoc models are based are open to serious doubt, and the mathematical and numerical models earlier described are to be preferred.

CHAPTER 5. LINEAR MODES OF AN UNSTABLY STRATIFIED SHEARED FLOW.

5.1 INTRODUCTION.

Turning now to the unstable gravity wave model, two properties of West African SQL's were mentioned in chapter 4 which apparently led to difficulties in modelling: orientation and propagation speed. In this chapter, these two questions will be examined in detail using as models linear modes of antisymmetric shear flows and of symmetric jets. The order of the chapter will, as mentioned in chapter 1, be roughly that in which the investigation was carried, but first it will be convenient to derive the basic equations, introduce the flows to be considered, and set down the numerical methods used.

5.1.1 Basic Equations.

(a) Non-Dimensional Variables.

For presentation of mathematical results, non-dimensional variables offer considerable simplification and will be used wherever possible. Though some of these variables are not used until chapter 6, it will be convenient to introduce them all here, defined rather carefully in terms of the variables of sections 4.1.1 and 4.1.2 as follows.

Position:
$$(X, Y, Z) = \frac{1}{\frac{1}{2}(z_2 - z_1)}(x, y, z - \tfrac{1}{2}(z_1 + z_2)) \qquad (5.1)$$

(defined so that the boundaries are at $Z = \pm 1$).

Density scale height:
$$r = \frac{\frac{1}{2}(z_2 - z_1)}{H_0} = -\frac{1}{\rho_0}\frac{d\rho_0}{dZ} \qquad (5.2)$$

Wavenumber:
$$k = \tfrac{1}{2}(z_2 - z_1)\gamma \qquad (5.3)$$

(this has already been introduced in (4.31)).

The other variables have to be referred to a characteristic shear and static stability, which will be defined respectively as

$$S = \frac{1}{z_2 - z_1}\int_{z_1}^{z_2}\left|\frac{dU_0}{dz}\right| dz \qquad (5.4)$$

and
$$B = \frac{\phi_0(z_2') - \phi_0(z_1')}{z_2' - z_1'} \qquad (5.5)$$

where S is chosen to be consistent with (3.4), while in B, z_1' and z_2' are chosen to make $\phi_0(z_1')-\phi_0(z_2')$ take as large a negative value as possible (since it is in the statically unstable situation that energy will be available for buoyancy driven modes). The corresponding Richardson number is

$$R = \frac{gB}{S^2} \tag{5.6}$$

This should be contrasted with the more usual

$$J = \min\left\{\frac{gB_0}{\left|\frac{d\underline{U}_0}{dz}\right|^2}\right\} \tag{5.7}$$

which has not been adopted since it is more difficult to determine with any precision for atmospheric data, and leads to mathematical difficulties with discontinuous profiles.

The non-dimensional lapse rate will be defined as

$$L(Z) = \frac{B_0(z)}{B} \tag{5.8}$$

while diffusion is represented by the Rayleigh number

$$Ra = \frac{-gB(z_2 - z_1)^4}{K^2} \tag{5.9}$$

as in (4.32).

Now B in (5.5) will be negative for virtually all the profiles which will be considered, both mathematical and atmospheric, the negative values in the latter case arising from the method chosen for parameterisation of latent heat release (section 4.3.1). Hence the Brunt-Vaisala frequency is imaginary, and use will be made instead of

$$N = (-gB)^{\frac{1}{2}} \tag{5.10}$$

Two non-dimensional times are now possible,

$$\tau = Nt \tag{5.11}$$

and

$$T = St \tag{5.12}$$

and these will be used respectively in chapters 5 and 6.

The non-dimensional mean flow will be

$$\underline{U}(Z) = (U(Z), V(Z)) = \frac{\underline{U}_0(z)\gamma}{kS} \tag{5.13}$$

with components along and perpendicular to the propagation vector

$$W(Z) = \frac{\underline{U}_0(z).\underline{\gamma}}{kS} = U(Z)\cos\theta + V(Z)\sin\theta \tag{5.14}$$

and

$$Q(Z) = \frac{|\underline{U}_0(z)\times\underline{\gamma}|}{kS} = U(Z)\sin\theta - V(Z)\cos\theta \tag{5.15}$$

where θ is defined by (4.11). The non-dimensionalisation of σ will be made consistent with that of $\underline{U}_0.\underline{\gamma}$, so define

$$c = c_r + ic_i = \frac{\sigma + iK\gamma^2}{kS} \tag{5.16}$$

The non-dimensional phase speed is then

$$c_r = \frac{\sigma_r}{kS} = \frac{\text{phase speed}}{\frac{1}{2}(z_2 - z_1)\gamma} \tag{5.17}$$

which is a convenient variable for plotting results. The growth rate is however divided by k, so better non-dimensional variables (corresponding to the non-dimensional times (5.11) and (5.12)) are

$$\text{either} \qquad \frac{\sigma_i}{N} = \frac{kc_i}{(-R)^{\frac{1}{2}}} - \frac{4k^2}{Ra^{\frac{1}{2}}} \tag{5.18}$$

$$\text{or} \qquad \frac{\sigma_i}{S} = kc_i - 4k^2\left(\frac{-R}{Ra}\right)^{\frac{1}{2}} \tag{5.19}$$

In general $\frac{\sigma_i}{N}$ will be used except in cases where non-negative values of B occur, notably for unstratified flow. Plotted growth rates will all assume no diffusion ($Ra = \infty$).

(b) Unidirectional Mean Flow.

The mean flows considered in this chapter are all unidirectional, with $V \equiv 0$. Furthermore mean density variation will be assumed as in section 4.1.2 to affect growth rates only slightly*, so will be ignored by setting $r = 0$ in (5.2). Thus the Taylor-Goldstein and height equations, (4.21) and (4.22) become

$$\frac{d^2\tilde{w}}{dz^2} - \left\{k^2 - \frac{R_\theta L(z)}{[U(z) - c_\theta]^2} + \frac{U''(z)}{U(z) - c_\theta}\right\}\tilde{w} = 0 \tag{5.20}$$

and

$$\frac{d}{dz}\left\{[U(z) - c_\theta]^2 \frac{d\tilde{l}}{dz}\right\} - \left\{k^2[U(z) - c_\theta]^2 - R_\theta L(z)\right\}\tilde{l} = 0 \tag{5.21}$$

with boundary conditions

$$\tilde{w}(\pm 1) = \tilde{l}(\pm 1) = 0 \tag{5.22}$$

Here

$$R_\theta = R \sec^2\theta \tag{5.23}$$

is a modified Richardson number appropriate to the particular direction of propagation, and correspondingly

$$c_\theta = c \sec\theta \tag{5.24}$$

For neutrally stratified flow ($R = 0$), the same equation (5.20) is satisfied for any direction of propagation θ, giving the same value for c_θ. Thus, if unstable modes exist, growth rate $\sigma_i = kS c_{\theta i} \cos\theta$ is greatest for $\theta = 0$, i.e. the 'two-dimensional mode', which is the result of Squire (1933). For stratified flows however, the appropriate

* But see section 6.2.4d for the effect on perturbation velocities.

modified Richardson number R_θ depends on the orientation θ, and the stability of a three-dimensional mode with Richardson number R is determined by the stability of a two-dimensional mode with a greater Richardson number R_θ. Now (5.20) determines c_θ as a function of k and R_θ, so

$$\sigma_i = k S c_{\theta i}(k, R_\theta)\cos\theta = k S c_{\theta i}(k, R\sec^2\theta)\cos\theta$$

$$= f(\cos\theta) \quad , \text{ say} \qquad (5.25)$$

giving

$$\frac{\partial\sigma}{\partial\theta} = -f'(\cos\theta)\sin\theta \qquad (5.26)$$

and provided $f'(1)$ is finite, it follows that the growth rate is stationary for $\theta=0$. However it cannot be deduced that this gives a maximum, and this will be illustrated in section 5.3.1, where it will be seen that there can be either a maximum or minimum of growth rate, depending on other conditions.

5.1.2 Hyperbolic Tangent Profiles.

As already mentioned, the actual profiles considered in this chapter take the form of antisymmetric shear flows and of symmetric jets. In each case, families of hyperbolic tangent profiles were studied, these being chosen as exhibiting, in the statically neutral case, a transition from normal mode stability to inflexion point instability. A general review of stability analyses for such profiles can be found in Drazin and Howard (1966), and some of this work will be summarised here, though it will be seen that attention in the past has largely been directed to stably and neutrally stratified flows, and not to the unstably stratified flows which form the subject of this present study.

(a) The Antisymmetric Shear Flows $\qquad U = \dfrac{\tanh \mu Z}{\tanh \mu} \qquad (5.27)$

The limiting case $\mu=0$ is the constant shear plane Couette flow

$$U = Z \qquad (5.28)$$

which has been studied in detail by Taylor (1931), Eliassen et al (1953), Kuo (1963) and Asai (1970a). The other limit $\mu\to\infty$ corresponds to a shear layer

$$U = \begin{cases} -1 & -1 \le Z < 0 \\ 1 & 0 < Z \le 1 \end{cases} \qquad (5.29)$$

though with continuous stratification, so this is not the classical Kelvin Helmholtz situation, as for instance in Lamb (1932).

For $\mu > 0$, the unstratified flow satisfies the Fjørtoft (1950) extension of the Rayleigh (1880) necessary condition for instability that there should exist a point of inflexion Z_s corresponding to a maximum of absolute vorticity $\left|\frac{dU}{dZ}\right|$. Nevertheless, for small μ, the profile is still stable, transition to instability accurring when the Rosenbluth and Simon (1964) long-wave criterion

$$\int_{-1}^{1} \frac{dZ}{U(Z) - U(Z_s)} > 0 \qquad (5.30)$$

is satisfied. The integrand here is singular at $Z = Z_s$, so the integral must be evaluated by parts, or by indenting the path of integration; applying the latter method, with U as in (5.27), gives instability if

$$\mu \, th\mu > 1 \qquad \text{i.e. if} \quad \mu > 1{\cdot}1997 \qquad (5.31)$$

This value of μ is confirmed by the Tollmien (1935) criterion that if at $Z = Z_s$ there exists a stationary neutral mode with wavenumber k_s, then for adjacent wavenumbers there exist unstable modes. In this case, solving (5.20) with $R_\theta = c_\theta = 0$, the stationary neutral modes for the hyperbolic tangent profile are obtained as

$$\tilde{w} \propto sh\, k_s Z \,(k_s \coth k_s Z - \mu th\mu Z) \qquad (5.32)$$

where the critical wavenumber k_s is given, as in Howard (1964) by the relationship

$$k_s \coth k_s = \mu th\mu \qquad (5.33)$$

which has a real root if μ is greater than the root of $\mu th\mu = 1$.

Other published work on the hyperbolic tangent profile has concentrated on stationary neutral modes for an unbounded flow domain, both unstratified (Garcia 1956; Drazin and Howard 1962), and with various stratifications (Drazin 1958; Thorpe 1969). Numerical studies of growing modes have been made for unstratified flow by Michalke (1964), and for stably stratified flows by Hazel (1972), Lalas and Einaudi (1976), and Tanaka (1975), this last study extending to finite amplitude. No numerical integrations have however been published for the unstably stratified flow.

(b) <u>The Symmetric Jet Profiles</u> $\qquad U = 1 - \frac{th^2 \mu Z}{th^2 \mu} \qquad (5.34)$

The limit $\mu = 0$ is plane Poiseuille flow

$$U = 1 - Z^2 \qquad (5.35)$$

which has been studied in some detail in the neutrally stratified viscous case, when there is instability for sufficiently large Rayleigh

number (see Lin 1955); Gage and Reid (1968) have investigated the effect of thermal stratification on this instability.

In the inviscid case for $\mu > 0$, Howard (1964) has shown that there are two possible stationary neutral modes. The sinuous (symmetric) mode has

$$\tilde{w} \propto \operatorname{ch} k_s z \left\{ 1 - 3\mu \operatorname{th}\mu z \, \frac{k_s \operatorname{th} k_s z - \mu \operatorname{th}\mu z}{k_s^2 - \mu^2} \right\} \qquad (5.36)$$

with k_s given by

$$k_s^2 - 3 k_s \operatorname{th} k_s \, \mu \operatorname{th}\mu + \mu^2 (3 \operatorname{th}^2 \mu - 1) = 0 \qquad (5.37)$$

Considering graphs of k_s^2, $k_s \operatorname{th} k_s$, this can be seen to have real roots k_s with $0 < k_s < 2\mu$ if

$$3 \operatorname{th}^2 \mu > 1 \quad \text{i.e. if} \quad \mu \geq 0{\cdot}658 \qquad (5.38)$$

which is also the condition that the points of inflexion lie within the flow domain.

For the varicose (antisymmetric) mode

$$\tilde{w} \propto \operatorname{sh} k_s z \left\{ 1 - 3\mu \operatorname{th}\mu z \, \frac{k_s \coth k_s z - \mu \coth \mu z}{k_s^2 - \mu^2} \right\} \qquad (5.39)$$

with k_s given by

$$k_s^2 - 3 k_s \coth k_s \, \mu \operatorname{th}\mu + \mu^2 (3 \operatorname{th}^2 \mu - 1) = 0 \qquad (5.40)$$

This has real roots for k_s, with $0 < k_s < \mu$, only if

$$3 \operatorname{th}^2 \mu - 1 > \frac{3}{\mu} \operatorname{th}\mu \quad \text{i.e if} \quad \mu \geq 1{\cdot}717. \qquad (5.41)$$

Hence by the Tollmein (1935) criterion, the sinuous mode is unstable for the smaller μ, being in fact unstable whenever the inflexion point lies within the flow domain, a result which is generally true for symmetric jet profiles, as shown by Howard (1964).

Other studies of the th^2 jet profile have dealt with an unbounded flow domain, stationary neutral modes being given in the unstratified case by Savic (1941) and Savic and Murphy (1943), and for various stratifications by Drazin and Howard (1962) and Miles (1963). A numerical study for stably stratified flow was made by Hazel (1972), but no results of integrations for unstably stratified flow have been published.

5.1.3 Numerical Methods.

Apart from certain special cases, notably the stationary neutral modes considered above, solutions to the stability equations for

hyperbolic tangent profiles must be sought numerically. No single method was found to be universally applicable; rather, use was made of three different types of numerical method, supplemented by short-wave approximations as follows.

(a) Matrix Methods.

With the non-dimensionalisation of section 5.1.1, equations (4.16) and (4.17) become

$$\left\{\left[U(\bar{z}) - c_\theta\right]\left(\frac{d^2}{d\bar{z}^2} - k^2\right) - U''(\bar{z})\right\}\tilde{w} - R_\theta L(\bar{z})\tilde{q} = 0 \qquad (5.42)$$

$$\left[U(\bar{z}) - c_\theta\right]\tilde{q} + \tilde{w} = 0 \qquad (5.43)$$

where

$$\tilde{q} = -ikS\tilde{h} . \qquad (5.44)$$

This may be reduced to an eigenvalue problem for a real matrix as in Asai (1970a).

An improvement can be made by application of Galerkin's method (see Connor and Brebbia 1976). Here $\tilde{w}$ and $\tilde{q}$ are approximated by finite Fourier series

$$\begin{Bmatrix}\tilde{w}\\ \tilde{q}\end{Bmatrix} = \sum_{n=1}^{M}\begin{Bmatrix}w_n\\ q_n\end{Bmatrix}\sin\tfrac{1}{2}n\pi(\bar{z}+1) \qquad (5.45)$$

where of the terms satisfies both boundary conditions. Now, (5.42) and (5.43) imply

$$\int_{-1}^{1}\left\{\left[(U - c_\theta)\left(\frac{d^2}{d\bar{z}^2} - k^2\right) - U''\right]\tilde{w} - R_\theta L\tilde{q}\right\}\sin\tfrac{1}{2}m\pi(\bar{z}+1) = 0 \qquad (5.46)$$

and

$$\int_{-1}^{1}\left\{(U - c_\theta)\tilde{q} + \tilde{w}\right\}\sin\tfrac{1}{2}m\pi(\bar{z}+1) = 0 \qquad (5.47)$$

$$m = 1, 2, \ldots M.$$

Substituting (5.45) and integrating (5.46) twice by parts to eliminate derivatives of U thus leads to

$$\tfrac{1}{2}\sum_{n=1}^{M}\left\{\left[k^2 + \tfrac{1}{4}m(2n-m)\pi^2\right]I_{|n-m|} - \left[k^2 - \tfrac{1}{4}m(2n+m)\pi^2\right]I_{n+m}\right\}w_n + \tfrac{1}{2}R_\theta\sum_{n=1}^{M}\left\{H_{|n-m|} - H_{n+m}\right\} = \left(k^2 + \tfrac{1}{4}m^2\pi^2\right)c_\theta w_m \qquad (5.48)$$

$$\tfrac{1}{2}\sum_{n=1}^{M}\left\{I_{|n-m|} - I_{n+m}\right\}q_n + w_m = c_\theta q_m \qquad (5.49)$$

$$m = 1, 2, \ldots M,$$

where I_n and H_n are Fourier cosine coefficients such that

$$\begin{Bmatrix} U(\bar{z}) \\ L(\bar{z}) \end{Bmatrix} = \sum_{n=1}^{M} \begin{Bmatrix} I_n \\ H_n \end{Bmatrix} \cos \tfrac{1}{2} n\pi(\bar{z}+1) \qquad (5.50)$$

As before this is an eigenvalue problem for a real matrix.

In both Asai's and Galerkin's methods, the eigenvalues of the matrix may be found by the Q-R method (see e.g. Froberg 1969); results may be checked and spurious eigenvalues eliminated by repeating the calculation with a different order matrix. In general, numerical results suggested that Galerkin's method gave a comparable accuracy to Asai's with a matrix of half the order, so is to be preferred.

(b) Shooting Method.

Here an approximation to an eigenvalue c_θ is taken, and a stability equation is integrated with suitable lower boundary conditions, giving a non-zero value for the solution at the upper boundary; iteration for c_θ is then carried out to reduce the upper boundary value of the solution to zero.

An alternative formulation transforms to a first order equation by substituting

$$\tilde{f} = \frac{\tilde{t}}{(U-c_\theta)^2 \frac{d\tilde{t}}{d\bar{z}}} \qquad (5.51)$$

into (5.21) to give

$$\frac{d\tilde{f}}{d\bar{z}} - \frac{1}{(U-c_\theta)^2} + \left\{k^2(U-c_\theta)^2 - R_\theta L\right\}\tilde{f}^2 = 0 \qquad (5.52)$$

(Note that, unlike the usual Riccati substitution, (5.51) has $\tilde{t}$ in the numerator, $\frac{d\tilde{t}}{d\bar{z}}$ in the denominator so that singularities at the boundaries are avoided). The lower boundary condition is now just $\tilde{f}(-1) = 0$, and iteration for c_θ is carried out to reduce $\tilde{f}(1)$ to zero. This alternative formulation is easier to program than the conventional method, but can require considerably more steps in the numerical integration to achieve satisfactory results.

The shooting method is useful for improving estimates to eigenvalues obtained by a matrix method (previous section) or from a mathematical expansion (e.g. the short wave approximation (5.75)), its advantage lying in the fact that integration may be carried out using a high order scheme such as Runge-Kutta. However the equation becomes singular for a stationary neutral mode in the neighbourhood of the critical level, and it then becomes necessary to deform the contour off the real axis, or use a Frobenius type expansion to link the numerical solutions on either side of the critical level, as in Einaudi and Lalas (1976).

Once an eigenvalue has been located, it may be 'tracked' as k or R_θ varies, extrapolating old values to give an estimate of the new one, a technique which proved to be extremely powerful in computing the results in this chapter.

(c) Graphical Method for Stationary Modes with Antisymmetric Profiles.

When seeking stationary modes of antisymmetric profiles with a constant lapse rate, a simplification of the shooting method is possible. Setting

$$\lambda = ic_\theta \qquad \zeta = iZ \tag{5.53}$$

and noting that for antisymmetric U,

$$U(Z) = U(-i\zeta) = -i\Omega(\zeta) \tag{5.54}$$

where Ω is some real function of ζ, (5.20) with L = 1 becomes

$$\frac{d^2\tilde{w}}{d\zeta^2} + \left\{k^2 + \frac{R_\theta}{(\Omega-\lambda)^2} - \frac{\Omega''}{\Omega-\lambda}\right\}\tilde{w} = 0 \tag{5.55}$$

with boundary conditions

$$w = 0 \qquad \text{at} \qquad \zeta = \pm i\,. \tag{5.56}$$

For stationary amplifying modes, c_θ is imaginary, and hence λ is real. So (5.55) is a linear ordinary differential equation with real coefficients, and two solutions $\tilde{w}_1(\zeta)$ and $\tilde{w}_2(\zeta)$ can be found as real functions of ζ (i.e. having series expansions with real coefficients), by numerical integration with suitable real initial conditions, e.g.

$$\begin{aligned} \tilde{w}_1(0) &= 1 & \tilde{w}_2(0) &= 0 \\ \tilde{w}_1'(0) &= 0 & \tilde{w}_2'(0) &= 1 \end{aligned} \tag{5.57}$$

Now since $\tilde{w}_1(\zeta)$ is a real function, $\tilde{w}_1(-i)$ is the complex conjugate of $\tilde{w}_1(i)$, and similarly for $\tilde{w}_2$, so application of the boundary conditions gives

$$F(\lambda, k, R_\theta) = Re[\tilde{w}_1(i)]\,Im[\tilde{w}_2(i)] - Im[\tilde{w}_1(i)]\,Re[\tilde{w}_2(i)] = 0 \tag{5.58}$$

which is now a purely real equation.

Hence for given R_θ, a graph of λ against k can be plotted by examining the sign of the function $F(\lambda, k, R_\theta)$. It was found convenient to do this using the line printer. Since the graph has several branches, a simple search in one direction is not however adequate; instead, for each point of a suitable rectangular grid, four adjacent positions (above, below, and to each side) were taken, and if F did not have the same sign at all these adjacent positions, the point was plotted. This method is very useful in finding all the stationary modes for a chosen area of the λ-k plane, and is particularly helpful in resolving

situations where neighbouring modes are close together, as in fig 5.5d, where all other methods failed. It will not however find propagating modes, and, like the shooting method does break down in the neighbourhood of stationary neutral modes.

For the constant shear profile (5.28), (5.55) reduces to

$$\frac{d^2\tilde{w}}{dz^2} + \left\{k^2 + \frac{R_\theta}{(z-\lambda)^2}\right\}\tilde{w} = 0 \qquad (5.59)$$

which has real solutions expressible in terms of Bessel functions, so that (5.58) may be replaced by the simpler

$$F(\lambda, k, R_\theta) = Re\left[J_\nu\{k(\lambda+i)\}\right] Im\left[Y_\nu\{k(\lambda+i)\}\right]$$

$$- Im\left[J_\nu\{k(\lambda+i)\}\right] Re\left[Y_\nu\{k(\lambda+i)\}\right] = 0 \qquad (5.60)$$

Eisler (1965) made use of a similar simplification for piecewise linear profiles.

(d) Short Wave Approximations.

All the numerical methods hitherto described break down for large wavenumber k, since a prohibitively large number of points would need to be taken to resolve the rapid variation of $\tilde{w}$. Physically however, one would expect short wave modes to be confined to a very small height range, and numerical results confirm this, suggesting that in the short wave limit, modes can only travel either near to one of the boundaries, or at a level at which the mean flow has a maximum (or minimum).

When attempting to confirm these results mathematically, the boundary case was found to be the simpler, provided the shear did not vanish there. With this assumption, define Z_* (complex) such that

$$U(Z_*) = c_\theta \qquad (5.61)$$

and expand

$$U(Z) - c_\theta = U'(Z_*)(Z-Z_*) + \tfrac{1}{2}U''(Z_*)(Z-Z_*)^2 + \cdots \qquad (5.62)$$

$$L(Z) = L(Z_*) + L'(Z_*)(Z-Z_*) + \cdots \qquad (5.63)$$

Substitution in (5.20) now gives

$$\frac{d^2\tilde{w}}{dZ^2} - \left\{k^2 - \frac{J(Z_*)}{(Z-Z_*)^2} + \frac{I(Z_*)}{(Z-Z_*)} + G(Z_*)\right\}\tilde{w} = 0 \qquad (5.64)$$

where

$$J(Z_*) = \frac{R_\theta L(Z_*)}{\left[U'(Z_*)\right]^2} \qquad (5.65)$$

is the local Richardson number,

$$I(Z_*) = \frac{U''(Z_*)}{U'(Z_*)} + \frac{R_\theta}{[U'(Z_*)]^2}\left\{\frac{U''(Z_*)}{U'(Z_*)}L(Z_*) - L'(Z_*)\right\} \tag{5.66}$$

and $$G(Z_*) = O(1) \tag{5.67}$$

In the case of constant shear and lapse rate, the local Richardson number J reduces to R_θ (constant), while I and G both vanish. Then (5.64) has solutions

$$\tilde{w} = \left[ik(Z - Z_*)\right]^{\frac{1}{2}} H_\nu^{(2)}\left[ik(Z - Z_*)\right] \tag{5.68}$$

where $$\nu^2 = \tfrac{1}{4} - J \tag{5.69}$$

and $H_\nu^{(1)}$, $H_\nu^{(2)}$ are Hankel functions with the following asymptotic expansions:

$$\left[ik(Z - Z_*)\right]^{\frac{1}{2}} H_\nu^{(2)}\left[ik(Z - Z_*)\right] = e^{\mp kZ}\chi_{\frac{1}{2}}(Z) \tag{5.70}$$

where

$$\chi_{\frac{1}{2}}(Z) \sim \text{constant} \times \left\{1 \pm \frac{(-J)}{2k(Z - Z_*)} + \frac{(-J)(-J-2)}{2!\left[2k(Z - Z_*)\right]^2} \pm \frac{(-J)(-J-2)(-J-6)}{3!\left[2k(Z - Z_*)\right]^3} + \cdots\right\} \tag{5.71}$$

Applying the boundary conditions gives

$$e^{-4k}\chi_1(1)\,\chi_2(-1) = \chi_1(-1)\,\chi_2(1) \tag{5.72}$$

Thus as $k \to \infty$ for fixed R_θ ,

$$\chi_1(-1) \lesssim e^{-2k} \quad \text{or} \quad \chi_2(1) \lesssim e^{-2k} \tag{5.73}$$

or equivalently $$H_\nu^{(2)}\left[ik(\mp 1 - Z_*)\right] \lesssim e^{-2k} \tag{5.74}$$

Examination of (5.71) shows that (5.73) can only be satisfied if $|Z_* \pm 1| \lesssim \frac{1}{k}$, so if $\kappa^{(2)}$ is a zero of $H_\nu^{(2)}$,

$$c = U(Z_*) \sim U(\mp 1) + \frac{i}{k}U'(\mp 1)\kappa^{(2)} + O\left(\frac{1}{k^2}\right) \tag{5.75}$$

This does give propagation along the boundary in the short-wave limit, with growth rate

$$\frac{\sigma_i}{N} \sim \frac{\mathrm{Im}\left[\kappa^{(2)}\right]}{(-R_\theta)^{\frac{1}{2}}} \tag{5.76}$$

which was the result obtained by Kuo (1963).

If R_θ is of the form $-m(m+1)$, where m is an integer, the series (5.71) terminates; applying the boundary condition reduces to finding m zeros of a polynomial, giving m modes at each boundary, of which $\frac{1}{2}m$, or the next integer below it, will be amplifying. For other values of R_θ, the zeros of the Hankel function must be found numerically; approximate values of growth rates for the first mode

may be read off the curve $\mu = 0$: propagating in fig 5.8a, this being the curve which was obtained for maximum growth rates of short wave modes for the constant shear profile.

If shear or lapse rate is not constant, the remainder term $I(Z_*)$ will no longer vanish, and the asymptotic expansion (5.71) has to be modified. Results suggest that, provided J in (5.69) and (5.71) is interpreted as $J(\pm 1)$, the local Richardson number at the boundary, then (5.75) will still hold, but with an error term $O\left[I(\pm 1)\frac{\ln k}{k^2}\right]$. Thus there is propagation along the boundary, with growth rate as if the shear and lapse rate were held at their boundary values throughout the fluid. A satisfactory analysis however could only be carried out in the case of large J, and this will be presented in section 5.4.2.

For short waves at a velocity maximum, at Z_o, say, one would expect, by analogy with unsheared flows (section 4.1.2) that in the short wave limit

$$c \sim U(Z_o) + i\frac{(-R_\theta)^{\frac{1}{2}}}{k} \qquad (5.77)$$

corresponding to propagation at the maximum mean flow velocity, with non-dimensional growth rate

$$\frac{\sigma_i}{N} \sim 1 . \qquad (5.78)$$

It was however only found possible to derive this result in the case of large Richardson number, and this will again be presented in section 5.4.2.

In general, the technique adopted in making use of these various numerical methods was to locate an eigenvalue approximately via either the Galerkin method (for small wavenumber) or a short wave approximation, then to 'track' as far as possible for both increasing and decreasing wavenumber using the shooting method. For stationary modes of anti-symmetric profiles, the graphical method alone sufficed.

5.2 NUMERICAL RESULTS FOR MONOTONIC PROFILES.

5.2.1 Introduction.

As a first attempt at modelling SQL's, the antisymmetric profiles (5.27) were considered, the corresponding Taylor-Goldstein equation being

$$\frac{d^2\tilde{\omega}}{dZ^2} - \left\{k^2 - \frac{R_\theta}{\left(\frac{th\mu Z}{th\mu} - c_\theta\right)^2} - \frac{2\mu^2\frac{th\mu Z}{th\mu}\operatorname{sech}^2\mu Z}{\frac{th\mu Z}{th\mu} - c_\theta}\right\}\tilde{\omega} = 0 \qquad (5.79)$$

Though these profiles do not approximate very satisfactorily the observed West African wind profiles, they had the advantage that long wave modes were generally stationary and could be found by the graphical method (section 5.1.3c), and the results, which form the subject of the present section, throw some light on the modelling of SQL's (section 5.3.1).

Considering first neutrally stratified flow, the graphical method was used to obtain fig 5.1, where growth rate σ_i/S, non-dimensionalised with respect to shear since there is no buoyancy, is plotted against $\log_{10}$ of wavenumber k for different μ. (Here, as elsewhere, the logarithmic wavenumber scale is used to show more clearly short wave behaviour.) Results confirm the appearance of instability for long waves for μ greater than 1·2, with, for finite μ, a short-wave cut-off at the stationary neutral mode, the cut-off wavenumber k_s being given by (5.33); such a cut-off was shown by Garcia (1956) to occur for sufficiently large wavenumber for all continuous flow profiles. In contrast, for the shear layer $\mu = \infty$ (the case $R_\theta = 0$ of the flow considered in section 5.2.4), growth rate increases indefinitely with wavenumber; this illustrates the danger of approximating a continuous profile by a discontinuous one.

For stratified flows, three particular values of μ were chosen: 0, 2 and ∞, growth rates and phase speeds being shown in figs 5.2-5.7. Apart from $\mu = \infty$, which will be dealt with in section 5.2.4, stationary modes were computed by the graphical method (section 5.1.3c), propagating modes by using the short-wave approximation (section 5.1.3d) to locate an eigenvalue, then 'tracking' this eigenvalue with varying k using the shooting method (section 5.1.3b).

5.2.2 Plane Couette Flow: $\mu = 0$.

For plane Couette flow (5.28), equation (5.79) reduces to

$$\frac{d^2\tilde{w}}{dz^2} - \left\{k^2 - \frac{R_\theta}{(z - c_\theta)^2}\right\}\tilde{w} = 0 \qquad (5.80)$$

which, in the long-wave limit $k = 0$ has solutions

$$\tilde{w} \propto (z - c_\theta)^{\frac{1}{2} \pm \nu} \qquad (5.81)$$

where

$$\nu^2 = \tfrac{1}{4} - R_\theta \qquad (5.82)$$

Applying the boundary conditions gives

$$c = \pm i \cot \frac{\pi n}{2\nu} \qquad (5.83)$$

where n takes integer values such that $0 < n < \nu$. This is only possible

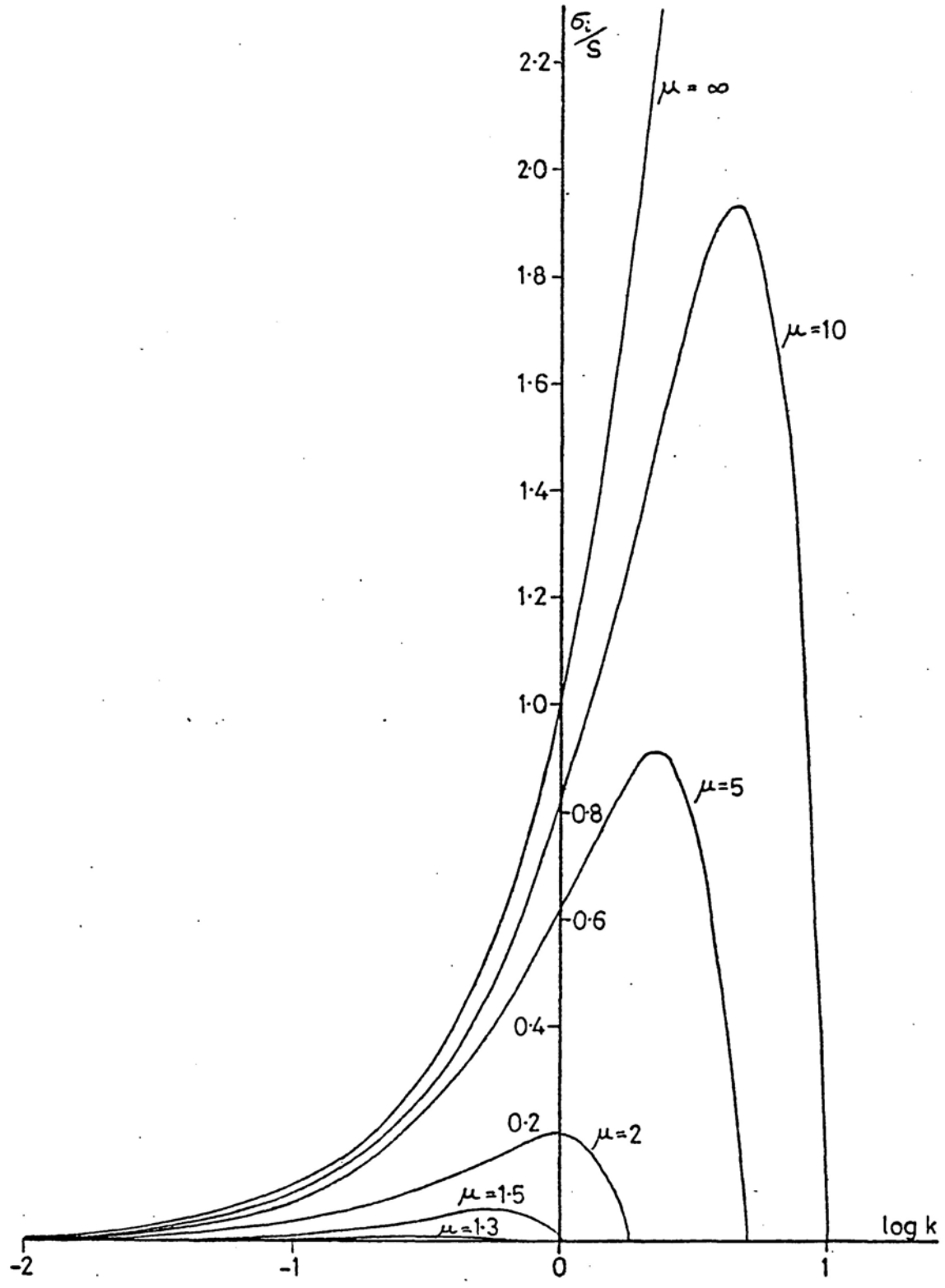


Fig 5.1. Hyperbolic tangent profiles: non-dimensional growth rate σ_i/S plotted against $\log_{10}$ of wavenumber k for different μ in unstratified case ($R_\theta = 0$).

for $\nu > 1$, which leads to Kuo's (1963) condition $R_\theta < -\frac{3}{4}$ for existence of unstable exponential modes. As noted in section 4.1.3 there is however 'algebraic instability' for $R_\theta < \frac{1}{4}$ (Chimonas 1979). The long wave approximation to the growth rate

$$\frac{\sigma_i}{N} = \frac{k}{(-R_\theta)^{\frac{1}{2}}} \cot \frac{\pi n}{2\nu} \qquad (5.84)$$

is plotted (dashed) for $n = 1, 5, 9$ together with various large Richardson number approximations in fig 5.13. It can be seen to give good results for $k < 1$, particularly for lower branches of the growth rate graph (those with smaller growth rates) where, interestingly, the large Richardson number approximations which form the main subject of the diagram tend to break down.

Numerically computed growth rates and phase speeds are shown as a function of $\log_{10} k$ for different R_θ in figs 5.2 and 5.3; the graph $R_\theta = -\infty$ is obtained from the longitudinal mode (4.33). In general the graphs have several branches, whereas in Kuo (1963) only the upper branches (those with largest growth rates) are shown. The long waves are stationary, with the number of amplifying modes given, as above, by the next integer below ν . Corresponding to every two long wave modes is a pair of short wave modes, each having the same growth rate, indistinguishable from the short wave limit (5.76) except in the neighbourhood of the branch points, and always less than the maximum growth rate of the faster growing of the two corresponding long wave branches; these short wave modes have opposite phase speeds, increasing from 0 at the branch point to ± 1 in the short wave limit, indicating a movement from the middle to the boundaries of the fluid with increasing wavenumber. In contrast, the modes for $R_\theta = -\infty$ are stationary for all wavenumbers and do not branch.

The fastest growing branches for the various modified Richardson numbers in fig 5.2 are collected together in fig 5.4. All growth rates increase with $-R_\theta$, and the curves are bounded above by the curve $R_\theta = -\infty$, which shows that, for the constant shear profile, increasing the shear for a given unstable stratification always reduces the growth rate of unstable modes, so that they are clearly buoyancy driven, The advantage of using σ_i/N as non-dimensional growth rate rather than σ_i/S (section 5.1.1) can be seen from the fact that all the curves are bounded here by the curve $R_\theta = -\infty$, whereas if σ_i/S were plotted, they would be unbounded.

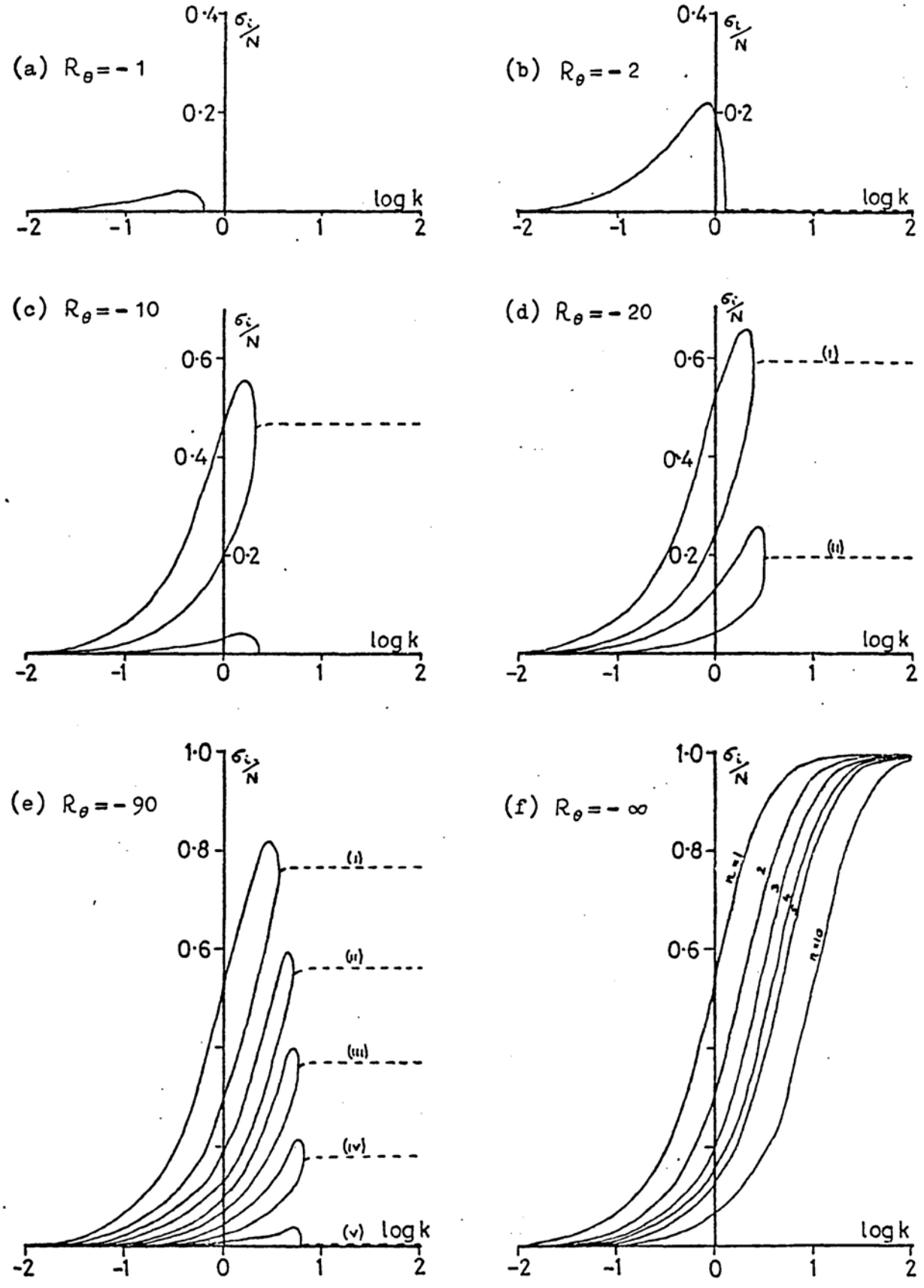


Fig 5.2. Plane Couette flow: non-dimensional growth rate σ_i/N plotted against $\log_{10}$ of wavenumber k for various modified Richardson numbers R_θ.

——— Stationary mode ------- Propagating mode.

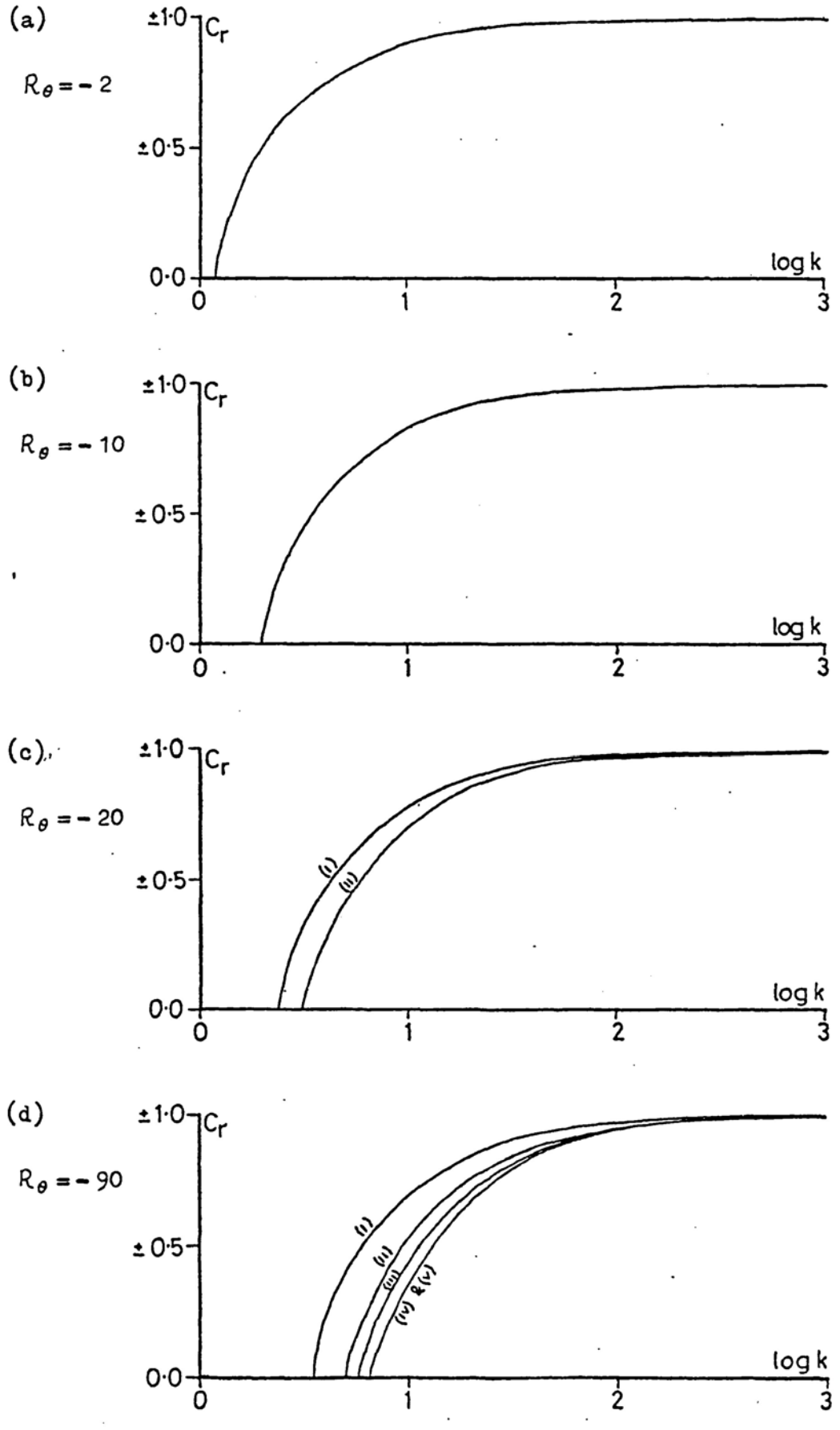


Fig 5.3. Plane Couette flow: non-dimensional phase speed c_r plotted against $\log_{10}$ of wavenumber k for various modified Richardson numbers R_θ.

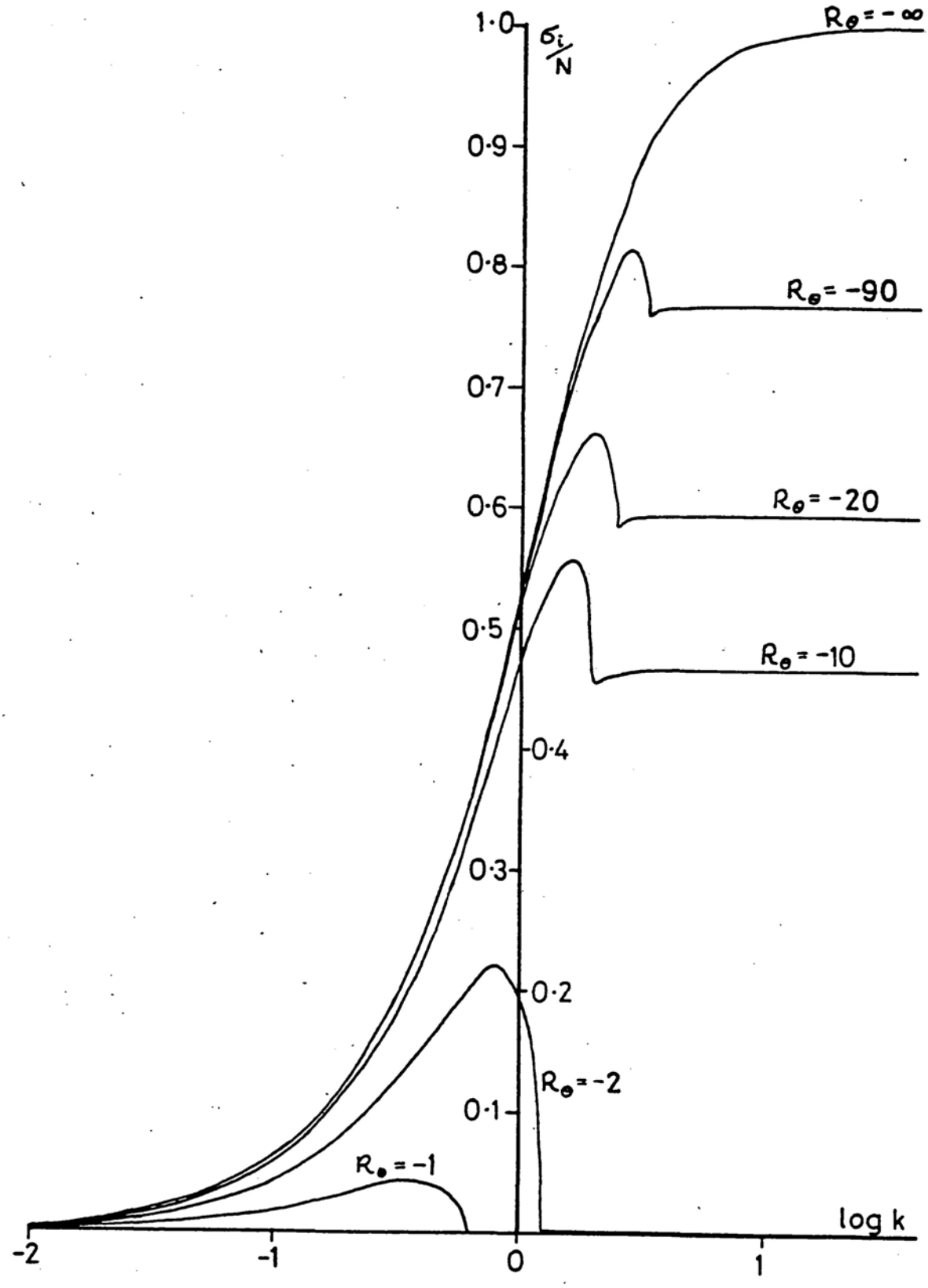


Fig 5.4 Plane Couette flow: largest growth rates σ_i/N as a function of $\log_{10}$ of wavenumber k for different modified Richardson numbers R_θ .

5.2.3 Hyperbolic Tangent Profile: $\mu = 2$.

Numerical results for hyperbolic tangent flow (5.27) with $\mu = 2$ are shown in figs 5.5 and 5.6 for different modified Richardson numbers. It was found that there was instability for $R_\theta \lesssim 1$. In the stably stratified cases (not illustrated), and for very slightly unstable stratification, there is a single stationary mode, the growth rate graph being similar in form to that obtained in the unstratified case ($\mu = 2$ in fig 5.1); the growth rate decreases as R_θ increases, confirming that this stationary mode is shear driven.

If there is significant buoyancy, propagating modes appear for all wavenumbers. These all have growth rate increasing with wavenumber, the short wave limit being given by (5.76); the phase speed is nearly constant for small wavenumber, but approaches ± 1 in the large wavenumber limit, indicating again a movement of short waves to the boundaries of the fluid. Their existence in the short wave limit, where they would have insufficient vertical extent to feed off the shear suggests that they are buoyancy driven, and this is confirmed by the increase of growth rate with $-R_\theta$. The short wave limit to the growth rate, (5.76) has a solution for $-R_\theta \gtrsim 0{\cdot}43$, which is therefore presumably the condition that a propagating mode should exist; for $-R_\theta \gtrsim 0{\cdot}25$, further solutions to (5.76) appear, suggesting that there should then be more than one propagating mode, though a second mode was only actually found for $-R_\theta \gtrsim 20$. If $-R_\theta \gtrsim 0{\cdot}25$, the short propagating mode is the fastest growing mode.

For $-R_\theta \gtrsim 20$, the graph of the stationary mode begins to branch, and, simultaneously, propagating modes which pass near to the branch points begin to have very sharp phase speed minima there; this is seen most clearly in curve (ii) for $R_\theta = -90$, where it appears that two stationary and two propagating long wave modes meet at the branch point. For $R_\theta = -240$, a further separate short-wave stationary branch of the graph has appeared; this was found by the graphical method, and it has not been possible to confirm it by any other method, so there is a possibility that it is spurious. In these large $-R_\theta$ cases, the increase of growth rate with $-R_\theta$ suggests that the stationary modes, as well as the propagating modes are buoyancy driven, a result which is confirmed in section 5.3.2.

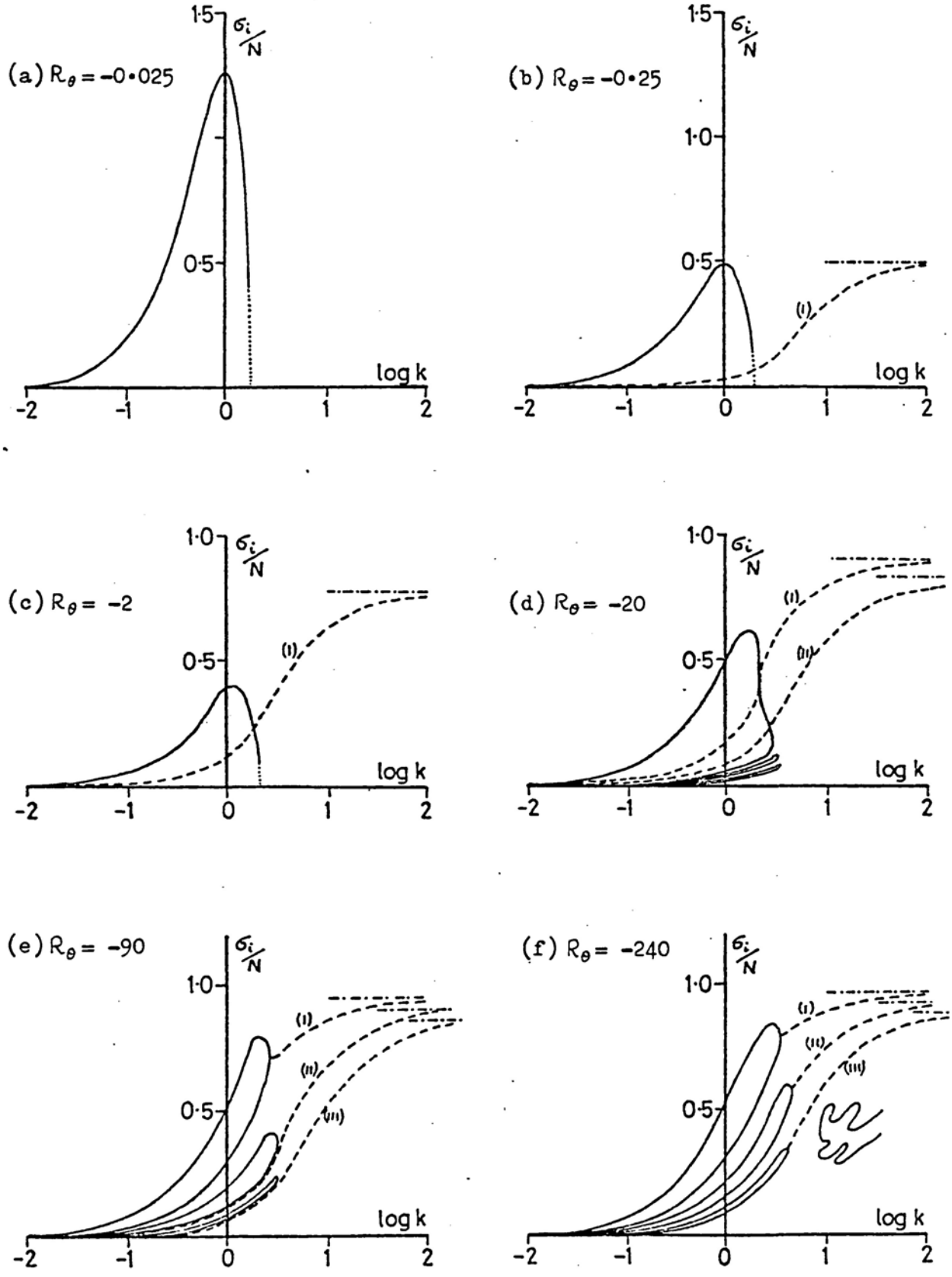
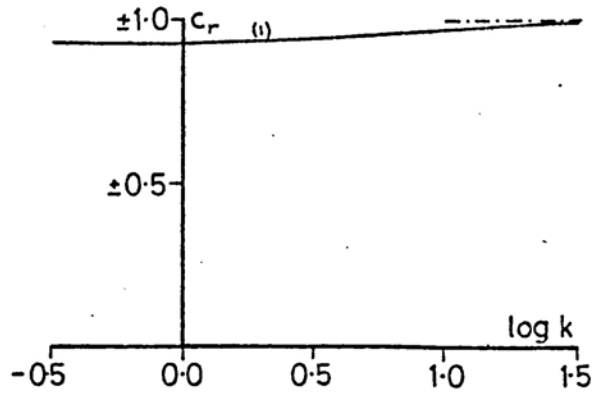


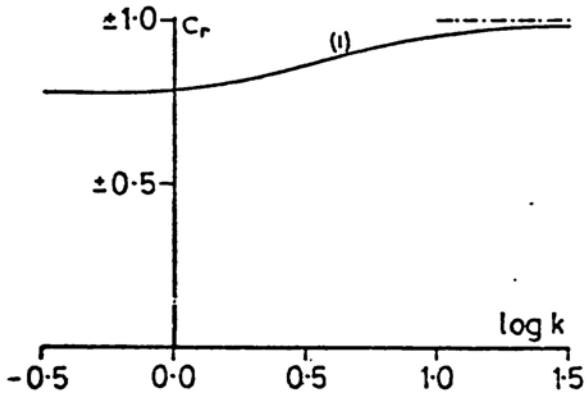
Fig 5.5. Hyperbolic tangent profile: non-dimensional growth rate $\frac{\sigma_i}{N}$ plotted against $\log_{10}$ of wavenumber k for various modified Richardson numbers R_θ.

——— Stationary mode - - - - - - Propagating mode

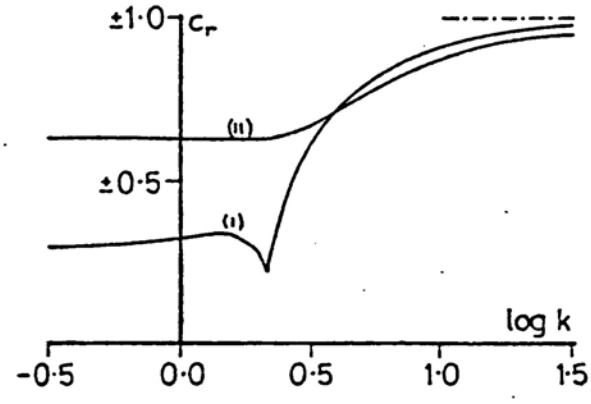
-·-·-·- Asymptotic limit ..... Extrapolated value.



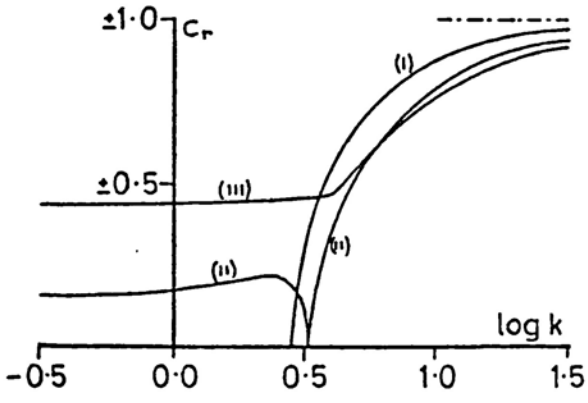
(b) $R_\theta = -0{\cdot}25$



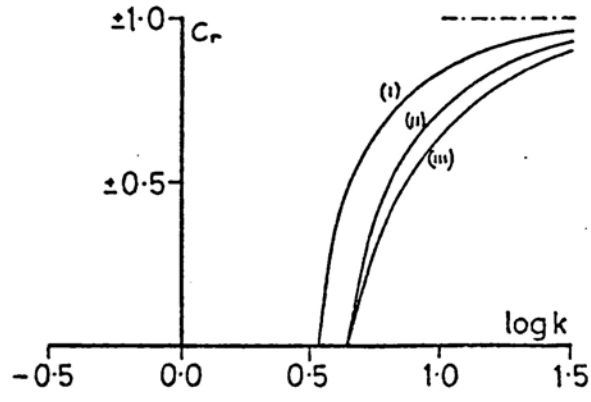
(c) $R_\theta = -2$



(d) $R_\theta = -20$



(e) $R_\theta = -90$



(f) $R_\theta = -240$

Fig 5.6. Hyperbolic tangent profile: non-dimensional phase speed c_r plotted against $\log_{10}$ of wavenumber k for various modidied Richardson numbers R_θ .

—·—·—·— Asymptotic limit.

5.2.4 Shear Layer: $\mu = \infty$.

For the shear layer (5.29), the Taylor-Goldstein equation becomes

$$\frac{d^2\tilde{\omega}}{d\bar{z}^2} - \left\{k^2 - \frac{R_\theta}{(\pm 1 - c_\theta)^2}\right\}\tilde{\omega} = 0 \qquad (5.85)$$

In addition to the boundary conditions (5.22), two conditions must be applied across the interface, and these may be expressed in terms of dimensional variables as follows. Kinematical condition: $w = \frac{Dh_0}{Dt}$ at $z = h_0$, where $h_0 \ll z_2 - z_1$ is the height of the interface; dynamical condition: pressure continuous at $z = h_0$. Taking sinusoidal horizontal dependence, linearising and non-dimensionalising, these give respectively continuity of $\frac{\tilde{\omega}}{(\pm 1 - c_\theta)}$ and of $(\pm 1 - c_\theta)\frac{d\tilde{\omega}}{d\bar{z}}$ at $\bar{z} = 0$. Solving (5.85) for the two layers and applying these conditions then gives

$$(1 - c_\theta)^2\left\{k^2 - \frac{R_\theta}{(1-c_\theta)^2}\right\}^{\frac{1}{2}}\coth\left\{k^2 - \frac{R_\theta}{(1-c_\theta)^2}\right\}^{\frac{1}{2}} + (-1-c_\theta)^2\left\{k^2 - \frac{R_\theta}{(-1-c_\theta)^2}\right\}^{\frac{1}{2}}\coth\left\{k^2 - \frac{R_\theta}{(-1-c_\theta)^2}\right\}^{\frac{1}{2}} = 0 \qquad (5.86)$$

For $R_\theta = 0$, this reduces to the classical unstratified Kelvin-Helmholtz problem, with solution

$$c = \pm i \qquad (5.87)$$

giving non-dimensional growth rate

$$\frac{\sigma_i}{S} = \pm k \qquad (5.88)$$

as plotted in fig 5.1. Otherwise it is necessary to solve (5.86) iteratively, though for stationary modes, it reduces under the substitution $\lambda = ic_\theta$ to

$$Re\left[(\lambda+i)^2\left\{k^2 + \frac{R_\theta}{(\lambda+i)^2}\right\}^{\frac{1}{2}}\coth\left\{k^2 + \frac{R_\theta}{(\lambda+i)^2}\right\}^{\frac{1}{2}}\right] = 0 \qquad (5.89)$$

which may be solved graphically as in section 5.1.3c. This was the method used to obtain the results shown in fig 5.7.

For small $-R_\theta$, all modes are stationary and have growth rate increasing with k. This is confirmed by small Richardson number expansions in the long and short wave cases which give growth rates

$$\frac{\sigma_i}{S} = \pm k\left\{1 + \tfrac{1}{6}(-R_\theta)(1 - \tfrac{1}{3}k^2) + \cdots\right\} \quad \text{for} \quad k^2, -R_\theta \ll 1 \qquad (5.90)$$

$$\frac{\sigma_i}{S} = \pm k\left\{1 + \frac{-R_\theta}{4k^2} + \cdots\right\} \quad \text{for} \quad -R_\theta, 1 \ll k^2 \qquad (5.91)$$

Non-dimensionalising the growth rate with respect to shear here shows that for small $-R_\theta$ these modes are shear driven. In particular, for the short waves (5.91), the effect of buoyancy only becomes appreciable

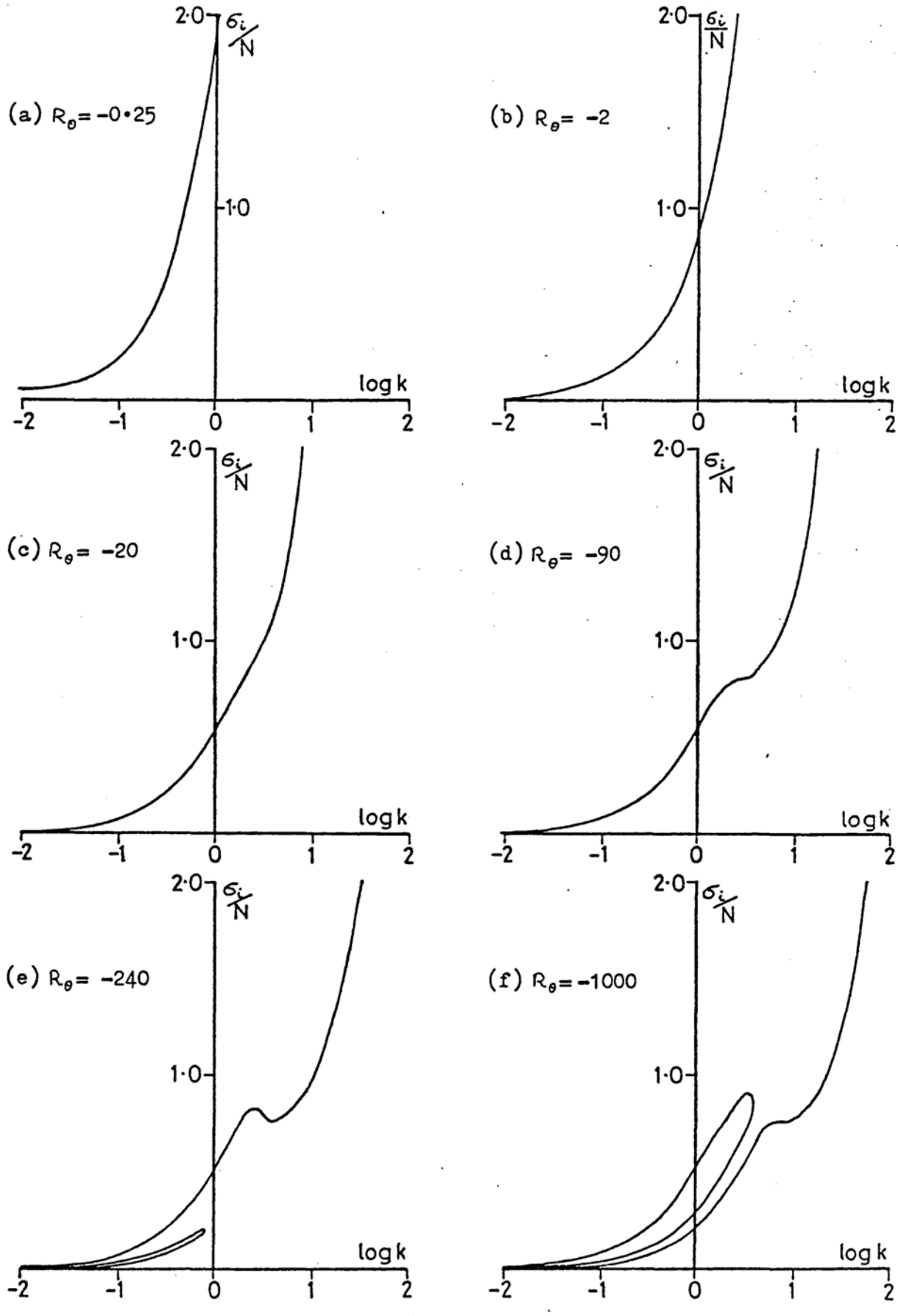


Fig 5.7. Shear layer: non-dimensional growth rate $\frac{\sigma_i}{N}$ plotted against $\log_{10}$ of wavenumber k for various modified Richardson numbers R_θ.

for $-R_\theta \sim k^2$; this is in contrast to the short wave modes for continuous profiles which are always buoyancy driven and propagate along one or other boundary.

If $-R_\theta$ is increased above about 90, the situation changes. Now the growth rate graph for stationary modes has a local maximum and, increasing $-R_\theta$ still further, the graph branches. Attempts to find propagating modes were unsuccessful, though it is likely that in this case, when the short wave approximation (5.91) is no longer valid, further work would reveal buoyancy driven short wave modes propagating close to the boundaries.

5.3 ORIENTATION OF THE FASTEST GROWING MODE.

5.3.1 Free and Forced Convection.

To apply the results of sections 5.2.1 - 5.2.4 to the modelling of SQL's, it is now necessary to find which is the fastest growing mode in a given situation. First, variation with modified Richardson number will be considered, then the results will be used to find variation with direction of propagation.

In fig 5.8a, maximum growth rate is plotted against $\log_{10}(-R_\theta)$ for both stationary and propagating modes for $\mu = 0$ and 2, the logarithmic scale being used so that the large $-R_\theta$ limit of 1 can be clearly seen. For $\mu = 0$, growth rate always increases with $-R_\theta$ and the stationary mode always has a greater growth rate than the propagating one. For $\mu = 2$, the stationary mode has a growth rate which is large for small $-R_\theta$, then falls to a minimum around $R_\theta = -1{\cdot}5$ before again increasing to the asymptotic maximum; the propagating mode has growth rate always increasing with $-R_\theta$, and for $-R_\theta \gtrsim 0{\cdot}25$, it grows more rapidly than the stationary mode.

For $\mu = \infty$ the maximum growth rate is infinite for short waves, so in this case it is necessary to fix the wavenumber k, and the value 1 was chosen; the graph (fig 5.8b) shows the growth rate to be large for small $-R_\theta$, and decreasing monotonically to the large $-R_\theta$ limit of $\left(1 + \frac{\pi^2}{4}\right)^{-\frac{1}{2}} = 0{\cdot}537$. The imposition of a fixed wavenumber may seem somewhat arbitrary, but some justification is provided by the fact that if horizontal diffusion is included as in the $4k^2/Ra^{\frac{1}{2}}$ term in (4.33), the short wave modes would be damped, and the wavenumber of maximum amplification could be arranged to be 1 by suitable choice of Rayleigh number; furthermore, the graphs for $\mu = 0$ and 2, which are also shown, display the same behaviour as they do in the optimised case above

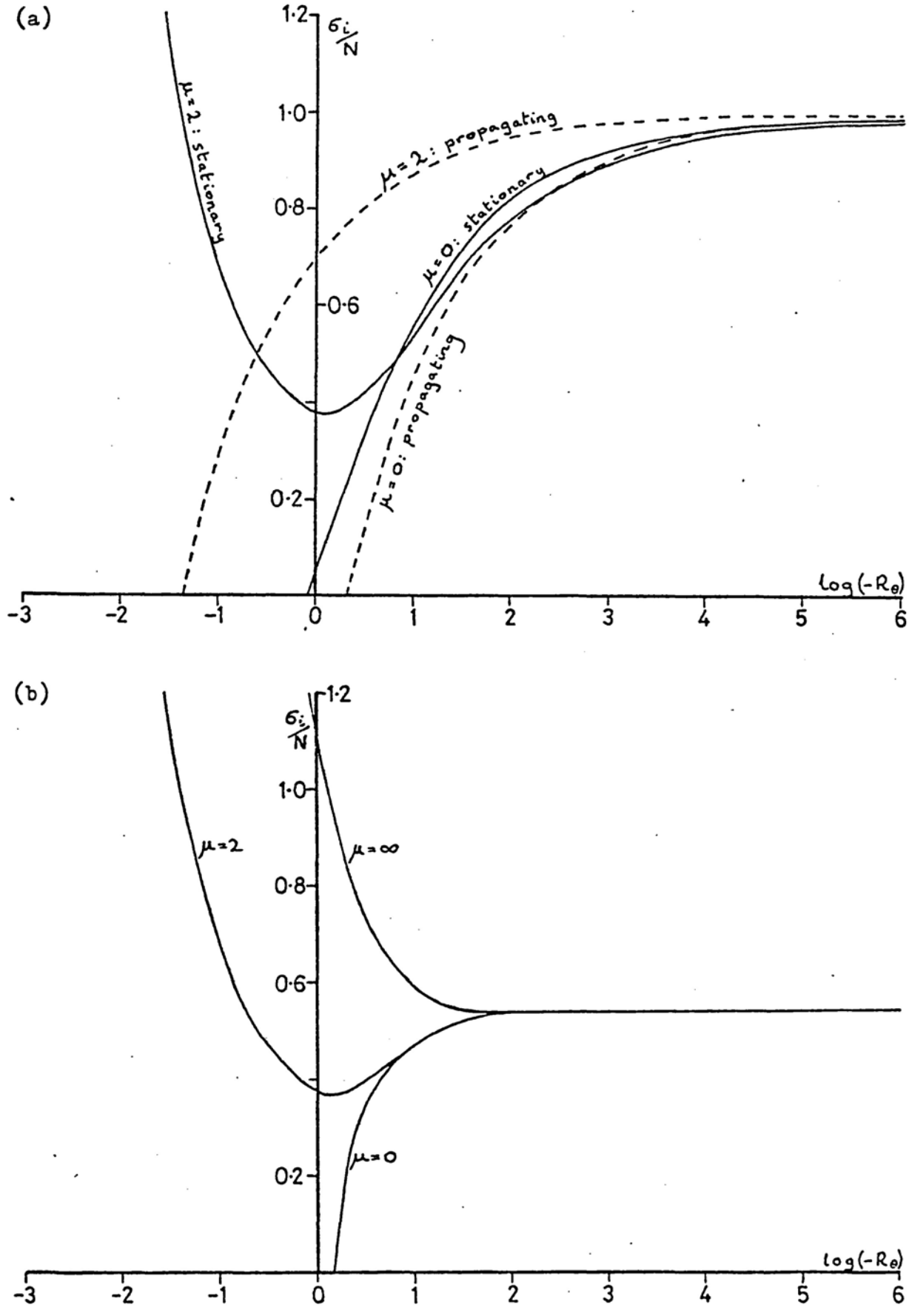


Fig 5.8. Non-dimensional growth rate $\frac{\sigma_i}{N}$ plotted against $\log_{10}$ of minus modified Richardson number for various antisymmetric profiles.

(a) Optimum growth rates over all wavenumbers

(b) Growth rates for wavenumber k = 1 (stationary modes only).

(though the large $-R_\theta$ limit is now 0·537).

The modes where $\frac{\sigma_i}{N}$ has a cut-off for small $-R_\theta$ and increases monotonically with $-R_\theta$ are clearly buoyancy driven, since increasing the shear for a given buoyancy decreases the growth rate; this applies to all modes for $\mu = 0$, and to the propagating mode for $\mu = 2$. Also, in the large $-R_\theta$ limit, all modes are buoyancy driven, as changing the shear for given buoyancy has no effect on growth rate. Care however is needed in interpreting the results where $\frac{\sigma_i}{N}$ decreases with $-R_\theta$, since $\frac{\sigma_i}{S}$, in contrast increases, as seen in fig 5.9 (note that here there is no longer a large $-R_\theta$ limit, so $-R_\theta$ rather than its log was used for the axis, thus making it possible to include cases of stable stratification). So, increase of buoyancy for given shear always causes an increase in growth rate, and buoyancy never inhibits convection. Shear will dominate as the driving mechanism in cases where $\frac{\sigma_i}{N}$ is large for small $-R_\theta$, i.e. for the stationary modes for $\mu = 2$ and ∞. However, whereas for $\mu = \infty$ shear and buoyancy always cooperate, as seen from the steady fall of the $\frac{\sigma_i}{N}$ graph, for $\mu = 2$, after cooperating for small $-R_\theta$, a point is reached where shear actually inhibits the convection, as seen by the increase in $\frac{\sigma_i}{N}$ with $-R_\theta$.

The implications of these results on orientation of the fastest growing mode are now investigated in figs 5.10 and 5.11, where maximum growth rate is plotted against inclination θ (as defined in (4.11)) of the propagation vector $\underline{\gamma}$ to the x axis. The Richardson number R which is used is that for the flow as a whole; for a given θ, the modified Richardson number is given by (5.23), and the growth rate can then be read off fig 5.8.

For the constant shear profile, $\mu = 0$ (fig 5.10a), all modes are buoyancy driven, so growth rate increases with θ, the maximum occurring for longitudinal rolls $\theta = 90°$, as in Kuo (1963). For the shear layer $\mu = \infty$ on the other hand (fig 5.10b), where shear and buoyancy cooperate as driving mechanisms, growth rate (shown again for k = 1) decreases with θ; the fastest growing mode is now transverse, $\theta = 0°$, and might be considered as a possible starting point in modelling a SQL.

For the continuous hyperbolic tangent profile however, the situation is more complicated, the case $\mu = 2$ being shown in fig 5.11a. For small $-R_\theta$, the shear driven stationary mode is dominant for small θ; in fact it is the only mode if $R_\theta \geq 0$, as can be seen in fig 5.11b, where $\frac{\sigma_i}{S}$ is used as the non-dimensional growth rate. If stratification is unstable however, there is always a transition as θ increases, so that

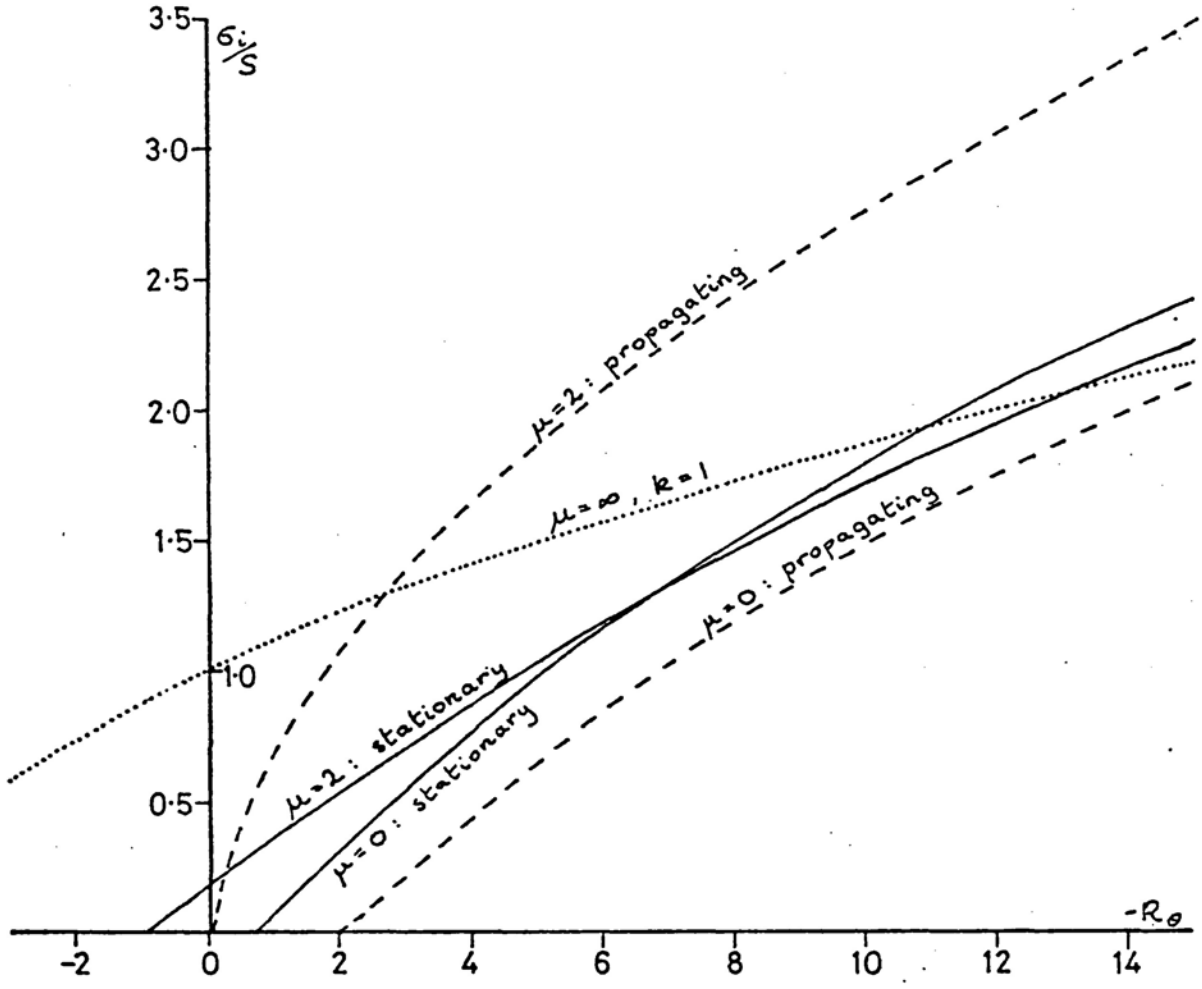
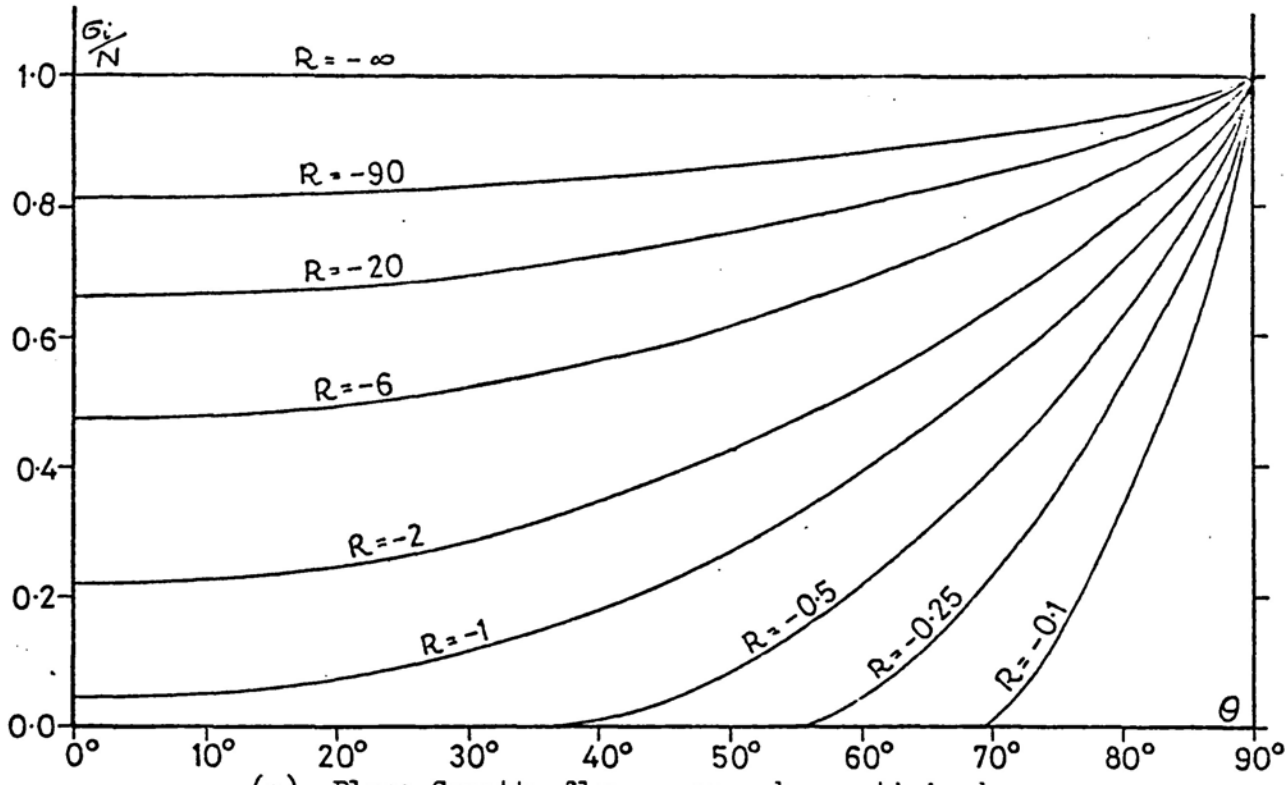
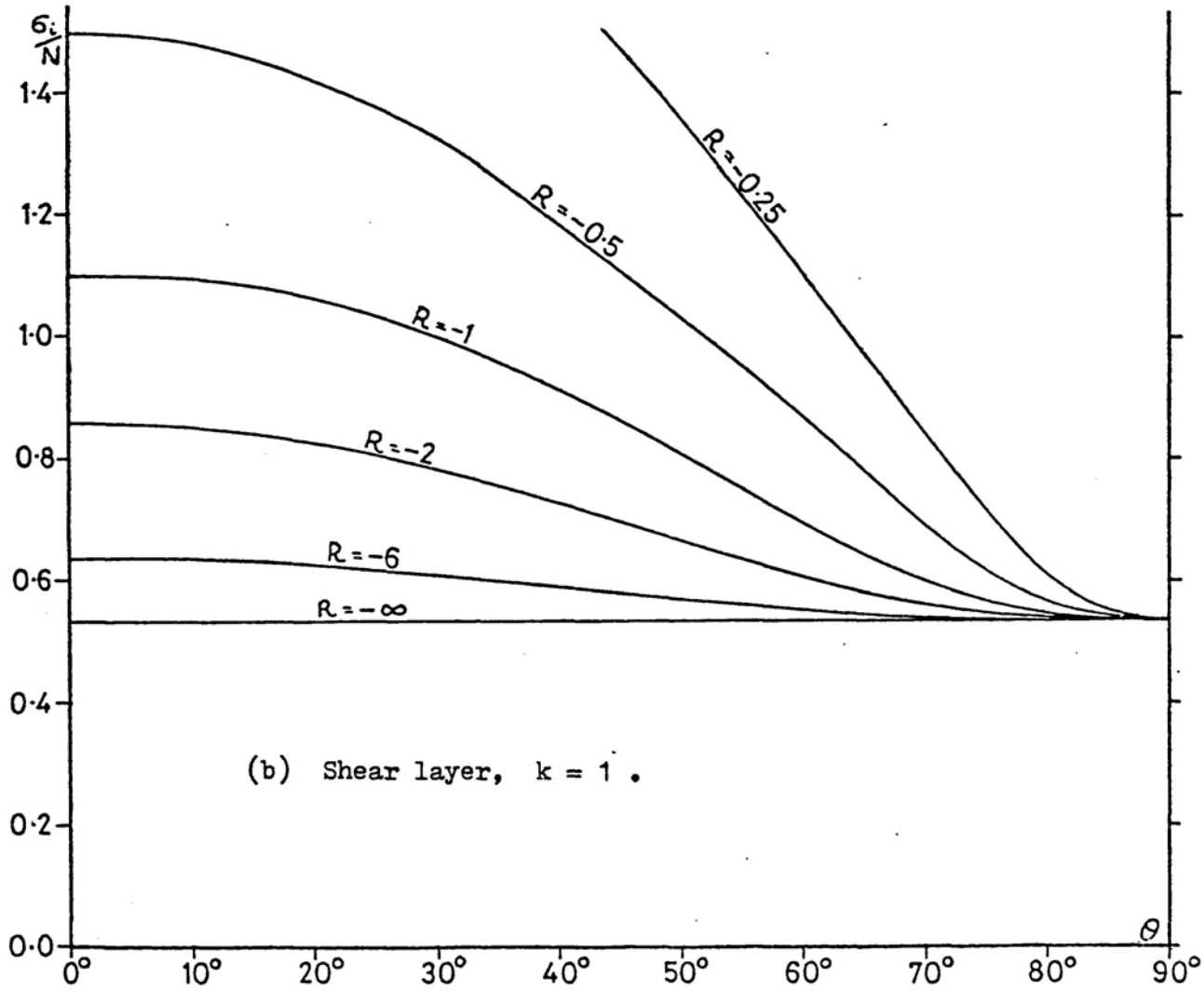


Fig 5.9. Non-dimensional growth rate $\frac{\sigma_i}{S}$ plotted against minus modified Richardson number for various antisymmetric profiles. For $\mu = 0$, 2 optimum growth rates over all wavenumbers k are plotted; for $\mu = \infty$, k is taken to be 1.

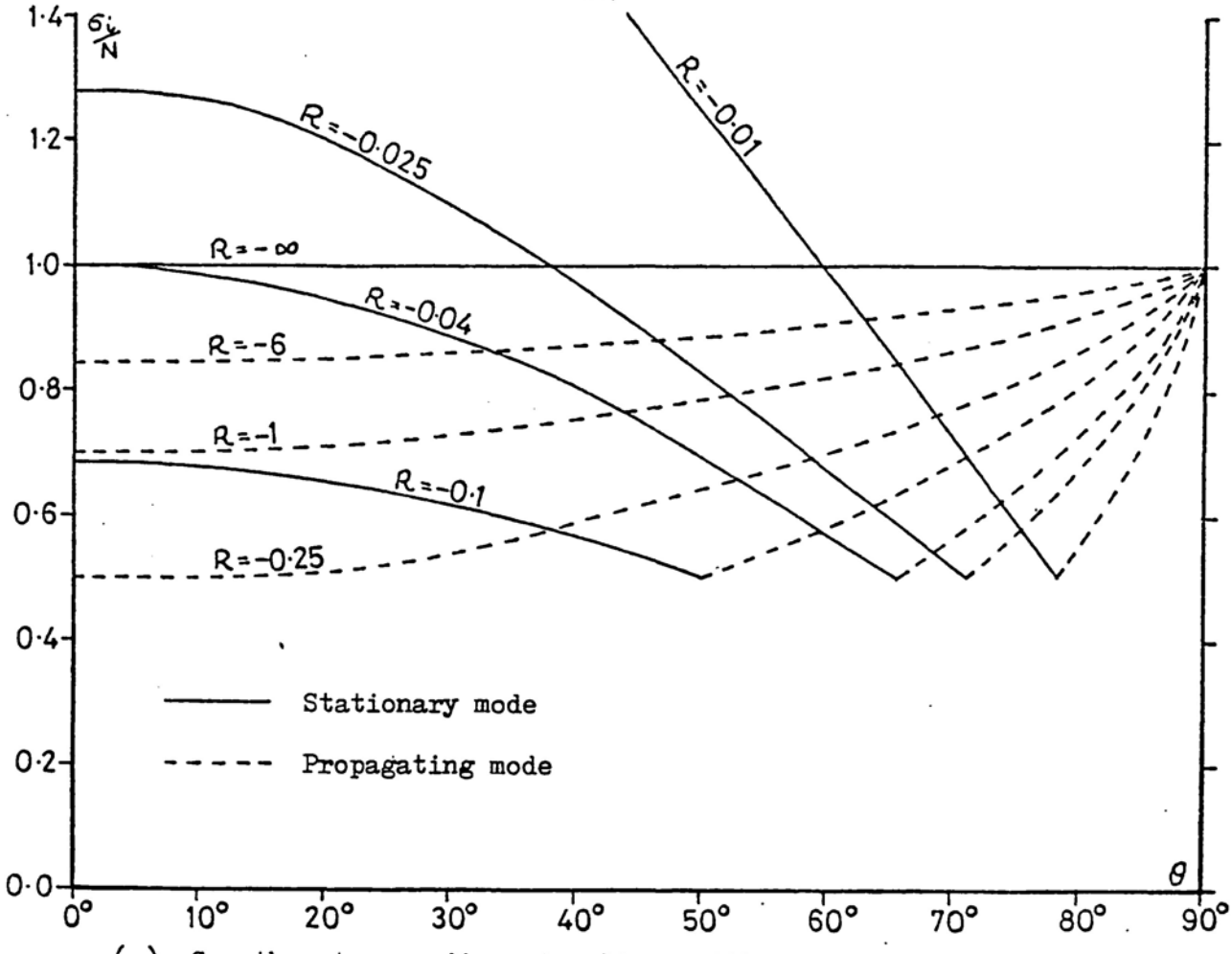


(a) Plane Couette flow, wavenumber optimised.

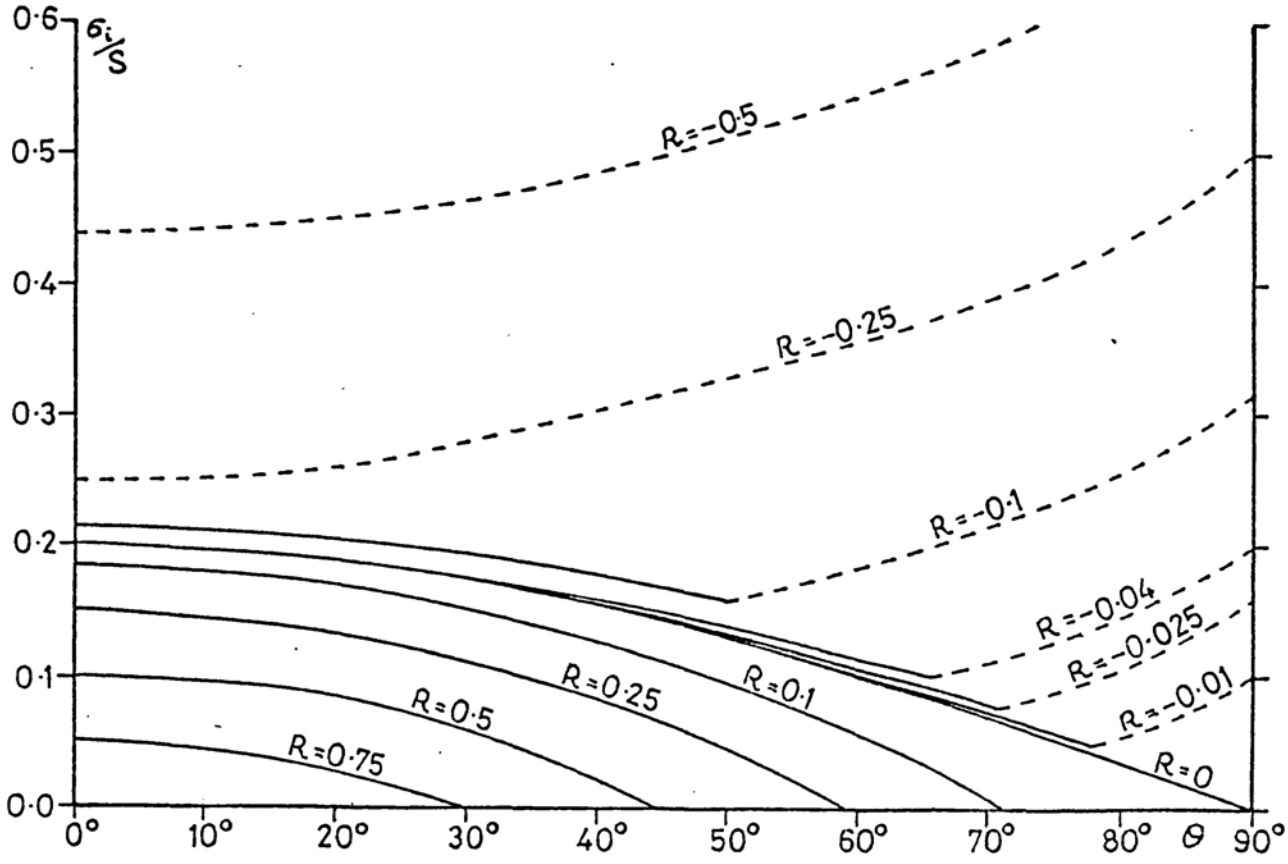


(b) Shear layer, $k = 1$.

Fig 5.10. Largest growth rate σ_i/N plotted against direction of propagation θ for various Richardson numbers R.



(a) Growth rate non-dimensionalised with respect to buoyancy



(b) Growth rate non-dimensionalised with respect to shear

Fig 5.11. Hyperbolic tangent profile: largest growth rate plotted against direction of propagation θ for various Richardson numbers R.

for large θ the buoyancy driven propagating mode is dominant, and indeed for $-R \gtrsim 0{\cdot}25$ it dominates for all θ. The greatest growth rate is for the buoyancy driven short longitudinal rolls for $-R \gtrsim 0{\cdot}04$, and for the shear driven long transverse mode otherwise. The transition is a consequence of the inhibiting effect of shear on convection for large $-R_\theta$ earlier noted for this profile, and always occurs for finite μ no matter how large the value. Unfortunately as noted in section 4.1.2, neither of the fastest growing modes is adequate as a model of a SQL, the buoyancy driven mode being longitudinal, and the transverse mode only occurring for negligible buoyancy, so the apparently promising results with the shear seem to have led nowhere after all.

One interesting point does nevertheless emerge from the results: the Richardson number $-0{\cdot}04$ which marks the transition from longitudinal to transverse modes lies in the range $-0{\cdot}02 \geqslant R \geqslant -0{\cdot}05$ given by Priestley (1959) for transition from free (buoyancy-driven) to forced (shear-driven) convection. Eisler (1965) obtained a similar transition with a piecewise linear velocity profile, as did Thorpe and Guymer (1977) with the symmetric profile $U = Z^2(1 - Z^2)$.

Further investigation reveals that the transition Richardson number of $-0{\cdot}04$ in fig 5.11 is somewhat fortuitous. Basically, buoyancy driven longitudinal modes have a maximum growth rate $\frac{\sigma_i}{N}$ of 1 (the short wave limit), while for the shear driven transverse modes, $-R_\theta$ is so small that the growth rate is approximately that of the unstratified case (fig 5.1), with maximum growth rate $\left(\frac{\sigma_i}{S}\right)_{max}$ occurring for some finite k. The transition occurs when $\frac{\sigma_i}{S}$ in each case is the same, which, since $\frac{N^2}{S^2} = -R$, implies a critical Richardson number

$$R_{crit} = -\left(\frac{\sigma_i}{S}\right)^2_{max} \qquad (5.92)$$

Now for $\mu = 2$, $\left(\frac{\sigma_i}{S}\right)_{max} = 0{\cdot}2$, so $R_{crit} = -0{\cdot}04$ as obtained above; however $-R_{crit}$ increases with μ and, for example $R_{crit} = -4$ for $\mu = 10$. A more consistent result may be obtained by using the local Richardson number J corresponding to the maximum shear instead of the mean Richardson number R, the two being related here by

$$J = \frac{1}{\mu^2} \tanh^2 \mu \, R \,. \qquad (5.93)$$

The critical Richardson number J_{crit} is then approximately $-0{\cdot}01$ for $\mu = 2$, and $-0{\cdot}04$ for $\mu = 10$, with a limit around $-0{\cdot}05$ as $\mu \to \infty$, or correspondingly as the depth of the fluid layer becomes infinite for a given finite shear layer. Thus Priestley's (1959) value for the critical Richardson number re-emerges, but as the value appropriate to the maximum shear in an unbounded atmosphere.

5.3.2 Mean Flow Forcing.

The previous section has served to emphasise the clear distinction between buoyancy and shear driven modes, and it will be profitable at this stage to ask why there is such a clear division. Why, except in the case of the shear layer do the fastest growing buoyancy driven modes orient themselves longitudinally, even though the mean flow field has a point of inflexion, which might have been expected to lead to greater instability for the transverse mode? The answer, as shown by Asai (1970 a,b; 1972), and mentioned in section 4.1.2, is that transverse modes are stabilised through feeding of energy into the mean flow. This point will be demonstrated by deriving the equations for the mean flow forcing in the absence of diffusion (without in this case non-dimensionalising), and applying them to the numerical results.

If the energy equation

$$\frac{D}{Dt}\tfrac{1}{2}|\underline{u}|^2 + \underline{u}.\nabla\frac{\delta p}{\rho_o} - g\delta\phi\, w = 0 \qquad (5.94)$$

is averaged over the whole flow domain (denoted by a double overbar), retaining only second order terms, and use is made of the continuity equation (4.2), a law of conservation of total energy is obtained:

$$\frac{\partial}{\partial t}\tfrac{1}{2}\rho\,\overline{\overline{(|\underline{u}|^2 + gB_o h^2)}} = 0 \qquad (5.95)$$

For convenience the potential energy (PE) here has been written in the form of the isobaric energy of Gossard and Hooke (1975), though other forms are possible, e.g. $\frac{1}{2}\rho g\frac{(\delta\phi)^2}{B_o}$ (Blackburn 1979) or $\rho g z\delta\phi$ (Green 1970).

Attempts to partition the PE into mean flow and perturbation contributions run into questions of definition of the PE release mechanism, so are not very helpful. Consideration of the kinetic energy (KE) is however more straightforward, and for this only xy averages will be taken, these being denoted by a single overbar. For the total KE, (5.94) gives

$$\frac{\partial}{\partial t}\tfrac{1}{2}\rho\overline{|\underline{u}|^2} = -\tfrac{1}{2}\rho g B_o\overline{wh} - \frac{\partial}{\partial z}\left\{\overline{w\delta p} + \rho\underline{U}_o.\overline{w(\delta u,\delta v)}\right\} \qquad (5.96)$$

while (4.1) gives for the mean flow KE

$$\frac{\partial}{\partial t}\tfrac{1}{2}\rho(U_o^2 + V_o^2) = -\underline{U}_o.\frac{\partial}{\partial z}\overline{\rho w(\delta u,\delta v)} \qquad (5.97)$$

where it is assumed here and for the remainder of this section that axes are taken such that $\sigma_r = 0$. Subtracting, the equation for perturbation KE is thus

$$\frac{\partial}{\partial t}\tfrac{1}{2}\rho\overline{|\delta\underline{u}|^2} = -\tfrac{1}{2}\rho g B_o\overline{wh} - \frac{d\underline{U}_o}{dz}\cdot\rho\overline{w(\delta u,\delta v)} - \frac{\partial}{\partial z}\overline{w\delta p} \qquad (5.98)$$

For amplifying sinusoidal modes in the absence of diffusion, (4.17) gives

$$\overline{wh} = \sigma_i\,\overline{h^2}$$

which is always positive. Hence, ignoring the $\frac{\partial}{\partial z}\overline{w\delta p}$ term, which disappears on z averaging, the conversions in (5.98) for an unstably stratified flow are from PE to perturbation KE, and in either direction between perturbation and mean flow KE.

Considering now a single Fourier mode, the mean flow KE term (5.97) will now be examined further, splitting it for convenience into terms arising from velocity components parallel and perpendicular to the unit vector $\hat{\underline{\gamma}}$ in the direction of propagation:

$$\begin{aligned}\frac{\partial}{\partial t}\tfrac{1}{2}\rho(U_o^2+V_o^2) &= \frac{\partial}{\partial t}\tfrac{1}{2}\rho\left\{|\underline{U}_o\times\hat{\underline{\gamma}}|^2 + |\underline{U}_o\cdot\hat{\underline{\gamma}}|^2\right\} \\ &= \left|\underline{U}_o\times\hat{\underline{\gamma}}\right|\left|\frac{\partial}{\partial z}\overline{\tilde{w}(\delta\tilde{u},\delta\tilde{v})}\times\hat{\underline{\gamma}}\right| + (\underline{U}_o\cdot\hat{\underline{\gamma}})\frac{\partial}{\partial z}\overline{\tilde{w}(\delta\tilde{u},\delta\tilde{v})}\cdot\hat{\underline{\gamma}}\end{aligned} \qquad (5.99)$$

where use has been made of the time average of (4.1), and for consistency with section 4.1.1, $\tilde{\Psi}$ will denote the Fourier mode of $\rho^{\frac{1}{2}}\psi$ for any field variable ψ. Now, solving (4.5) - (4.8) for $(\delta u, \delta v)$ and Fourier transforming gives

$$(\delta\tilde{u},\delta\tilde{v}) = \left(\frac{d\underline{U}_o}{dz}\times\hat{\underline{\gamma}}\right)\times\hat{\underline{\gamma}}\,\tilde{h} + i\frac{\hat{\underline{\gamma}}}{\gamma}\left(\frac{\partial\tilde{w}}{\partial z} - \tfrac{1}{2}r\tilde{w}\right) \qquad (5.100)$$

so

$$\begin{aligned}\frac{\partial}{\partial z}\overline{\tilde{w}(\delta\tilde{u},\delta\tilde{v})} &= \frac{\partial}{\partial z}\left\{\left(\frac{d\underline{U}_o}{dz}\times\hat{\underline{\gamma}}\right)\times\hat{\underline{\gamma}}\;\tfrac{1}{2}Re\left[i(\underline{U}_o\cdot\underline{\gamma}-\sigma)\right]|\tilde{h}|^2\right\} \\ &\quad -\frac{\hat{\underline{\gamma}}}{\gamma}\tfrac{1}{2}Im\left\{\gamma^2+\frac{1}{4H_o^2}-\tfrac{1}{2}\frac{d}{dz}\frac{1}{H_o}-\frac{gB_o}{(\underline{U}_o\cdot\underline{\gamma}-\sigma)^2}-\frac{\frac{d}{dz}\left(\frac{1}{\rho_o}\frac{d\underline{U}_o}{dz}\cdot\underline{\gamma}\right)}{\frac{1}{\rho_o}(\underline{U}_o\cdot\underline{\gamma}-\sigma)}\right\}|\tilde{w}|^2\end{aligned} \qquad (5.101)$$

where use has been made of (4.17) and the Taylor-Goldstein equation (4.21). The terms which comprise the change in KE are thus

$$\frac{\partial}{\partial t}\tfrac{1}{2}\rho|\underline{U}_o\times\hat{\underline{\gamma}}|^2 = \tfrac{1}{2}\sigma_i\left\{\frac{\partial}{\partial z}\left[(\underline{U}_o\times\hat{\underline{\gamma}})\cdot\left(\frac{d\underline{U}_o}{dz}\times\hat{\underline{\gamma}}\right)\right] - \left|\frac{d\underline{U}_o}{dz}\times\hat{\underline{\gamma}}\right|^2\right\}|\tilde{h}|^2 \qquad (5.102)$$

and

$$\frac{\partial}{\partial t}\tfrac{1}{2}\rho(\underline{U}_o\cdot\hat{\underline{\gamma}})^2 = \sigma_i(-gB_o)\frac{(\underline{U}_o\cdot\underline{\gamma})^2}{|\underline{U}_o\cdot\underline{\gamma}-\sigma|^2}|\tilde{h}|^2 + \tfrac{1}{2}\sigma_i(\underline{U}_o\cdot\hat{\underline{\gamma}})\rho_o\frac{d}{dz}\left(\frac{1}{\rho_o}\frac{d\underline{U}_o}{dz}\cdot\hat{\underline{\gamma}}\right)|\tilde{h}|^2 \qquad (5.103)$$

For (5.102) it may be shown that, if averaging is carried out in the vertical as well,

$$\frac{\partial}{\partial t}\tfrac{1}{2}\rho\overline{\overline{\left|\underline{U}_o\times\hat{\underline{\gamma}}\right|^2}} = -\frac{\partial}{\partial t}\tfrac{1}{2}\rho\overline{\overline{\left|(\delta\tilde{u},\delta\tilde{v})\times\hat{\underline{\gamma}}\right|^2}} \qquad (5.104)$$

which merely represents transfer of KE due to the wavelike redistribution

of the component of mean velocity perpendicular to the propagation vector, and does not affect the instability since this velocity component is absent in the stability equations (4.16) - (4.22).

The important KE transfer is thus given by (5.103). The first (buoyancy) term here shows that part of the KE gained by the perturbation from PE (first term on the right in (5.98)) is immediately transferred to mean flow KE (via the second term on the right in (5.98)). The second (shear) term in (5.103), (negative at an inflexion point) is the transfer of mean flow inflexion point KE to perturbation KE. This shear term vanishes if $\frac{1}{\rho_0}\frac{d\underline{U}_0}{dz}$ is constant, and changes sign, so that its z average is small, if the steering level is well away from the inflexion point, as occurs with short waves; in these cases therefore, the energy derived from the shear is negligible, so modes must be buoyancy driven. The buoyancy term when it predominates represents a loss of energy from the perturbation to the mean flow, with consequent reduction in growth rate, unless $\underline{U}_0 \cdot \underline{\gamma} = 0$, which explains the preferred longitudinal orientation of buoyancy modes for a unidirectional mean flow.

Turning now to some numerical results, it is convenient to non-dimensionalise as in section 5.1.1. Restricting attention to transverse modes (as only the unimportant transfer (5.102) remains for longitudinal modes), (5.103) becomes

$$\frac{1}{c_i}\frac{d}{d\tau}\tfrac{1}{2}U^2 = -R\frac{U^2}{|U-c|^2}\left|\tilde{h}\right|^2 + \tfrac{1}{2}U\frac{d^2U}{dZ^2}\left|\tilde{h}\right|^2 \qquad (5.105)$$

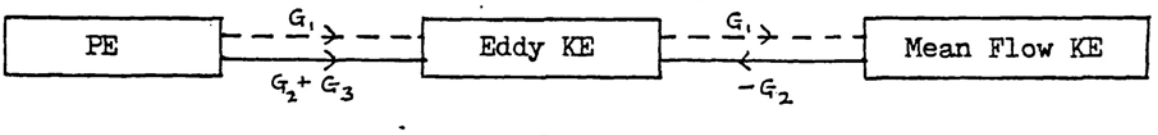
$$= G_1 + G_2 \text{ , say}$$

where G_1 and G_2 are the KE gained by the mean flow from the perturbation through the buoyancy and shear terms respectively. Also, for the transverse modes, noting that all perturbation quantities have time dependence $\exp(c\tau)$, the total gain in KE of the perturbation (from mean flow KE and PE combined) is simply

$$\frac{1}{c_i}\frac{d}{d\tau}\tfrac{1}{2}\left|\delta\underline{u}\right|^2 = \tfrac{1}{2}\left|\delta\underline{u}\right|^2 = \tfrac{1}{2}\left\{\left|\tilde{\omega}\right|^2 + \frac{1}{k^2}\left|\frac{d\tilde{\omega}}{dZ}\right|^2\right\} \qquad (5.106)$$

$$= G_3 \text{ , say}$$

The energy exchanges may then be represented as



Here the part G_1 of the KE which the perturbation gains from PE is immediately transferred to mean flow KE, leaving a gain G_2+G_3 from PE and $-G_2$ from mean flow KE. The three terms G_1, G_2, G_3, normalised so that the Z average $\overline{G_3} = 1$, are plotted in fig 5.12 for various modes for the hyperbolic tangent profile, $\mu = 2$.

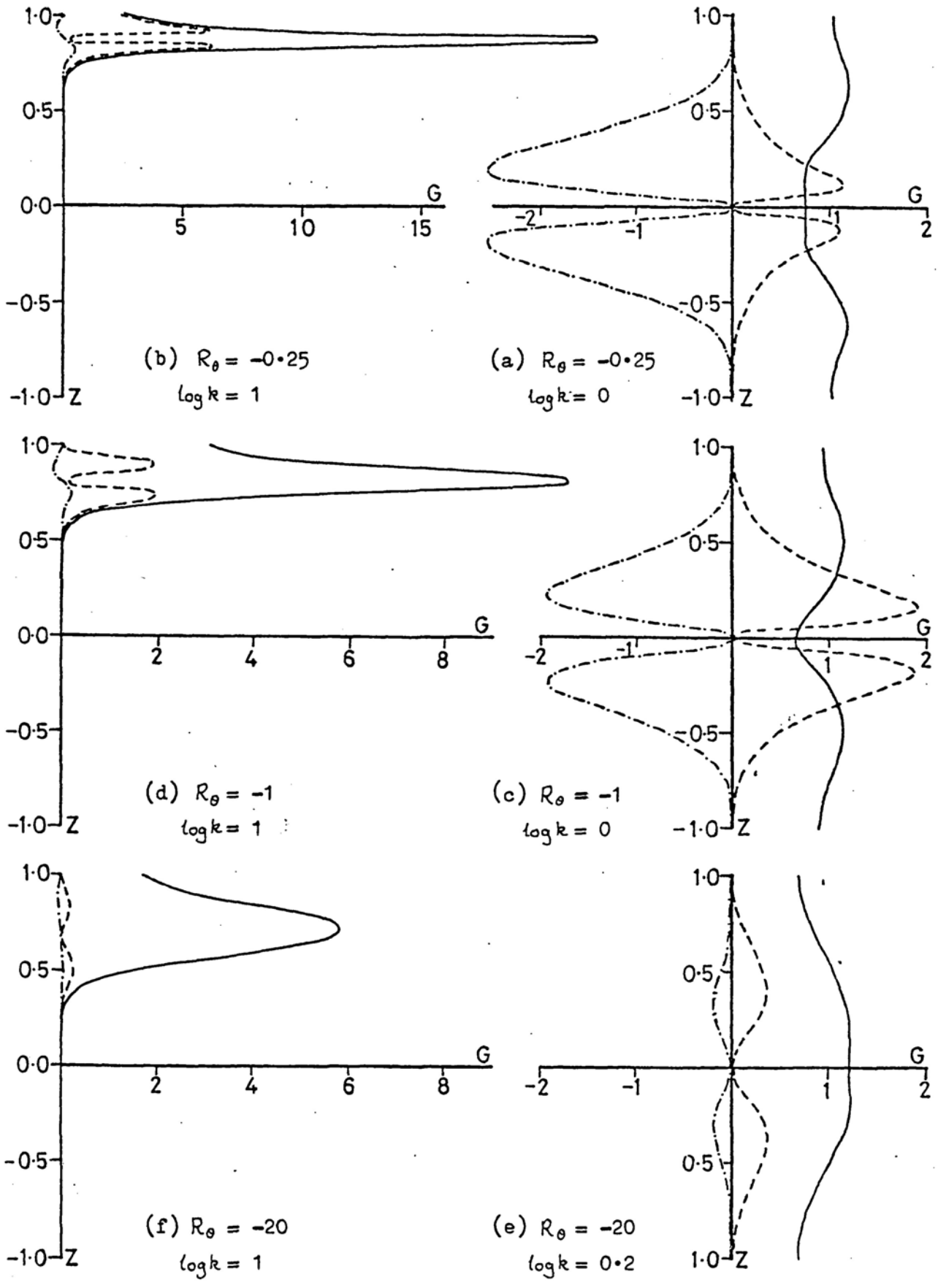


Fig 5.12. Hyperbolic tangent profile: energy transfers for various modified Richardson numbers and wavenumbers.

G_1, G_2 } KE gained by mean flow from perturbation through { buoyancy / shear } terms

G_3: Total KE gained by perturbation

For the long wave modes, fig 5.12 a,c and e, the wavenumber chosen is approximately that which gives the maximum growth rate. For the small $-R_\theta$ case, fig 5.12a, the shear term G_2 dominates the buoyancy term G_1, and $\overline{G_2}$ and $\overline{G_3}$ are approximately equal and opposite, indicating that all the increase in perturbation KE is provided by mean flow KE, the perturbation KE gained from PE being immediately transferred to mean flow KE. For the large $-R_\theta$ case, fig 5.12e, G_1 dominates G_2, though G_3 is much larger than either; hence the perturbation gains its KE from PE, and loses some KE to the mean flow; the dominance of G_3 is not surprising, since in the limit $R_\theta \to -\infty$, there is no mean flow, so that G_1 and G_2 would disappear altogether. The intermediate case $R_\theta = -1$ was chosen to be near the smallest growth rate in fig 5.8a; it is significant that in this case, the buoyancy and shear terms G_1 and G_2 almost balance indicating no net KE gain or loss by the mean flow; also $\overline{G_2}$ is numerically rather smaller than $\overline{G_3}$, so the perturbation gains its energy from both mean flow KE and from PE - though clearly not very efficiently from either!

For the short wave modes, fig 5.12 b,d and f, the largest growth rate corresponds to the limit $k \to \infty$, with motion cramped against the boundary, so a finite value, 10, had to be chosen for k. Now in all cases, G_2 changes sign, indicating negligible net gain in perturbation KE from the mean flow; the dominant term is always G_3, indicating PE as the source of eddy KE, and there is always a certain amount G_1 lost to mean flow KE, though this becomes less important with increasing $-R_\theta$, hence the increased growth rate. The vertical extent of the motion increases with increasing $-R_\theta$, which is to be expected from the large $-R_\theta$ short wave expansion (5.137), where an extent of order $\frac{(-R_\theta)^{1/6}}{k}$ is suggested.

In conclusion, these results confirm Asai's (1970 a,b; 1972) stabilisation of transverse buoyancy driven modes by feeding of energy to the mean flow. For large Richardson number this loss of energy from the perturbation is negligible, as is its gain from mean flow KE, so the growth rate is large. Decreasing $-R_\theta$ results in increased feeding of energy into the mean flow with a consequent reduction in growth rate; for the stationary modes however, a point is eventually reached where the loss of energy to the mean flow is more than offset by the gain from mean flow KE and growth rate rises again.

Returning now to the modelling of SQL's, of the two classes of fastest growing modes, those which are shear driven are unlikely to be relevant, occurring only for negligible buoyancy. Attention will thus be directed to the large Richardson number buoyancy driven modes.

5.4 LARGE RICHARDSON NUMBER EXPANSIONS.

Though no single linear mode is adequate as a model of a SQL, when superposition is carried out, the picture is much more promising. So now, in order to prepare the way for this superposition, it is necessary to examine the buoyancy driven modes for modified Richardson number approaching the longitudinal mode limit $R_\theta \to -\infty$. No general expansion is available, but various special cases may be considered; as usual, density variation and diffusion terms will be omitted.

5.4.1 Long Wave Expansion, $-R_\theta \gg k^2$.

For the long wave expansion, it is necessary to restrict attention to the case of constant lapse rate (L = 1 in (5.20)). The expansion for stable stratification was considered by Banks et al (1976), concentrating mainly on the profile $U = \sin \pi Z$, in which the repeated integrals which arise can be evaluated explicitly. A general expansion will now be derived in the case of unstably stratified flow.

The zero order approximation is the longitudinal mode for which

$$c_\theta = i \frac{(-R_\theta)^{\frac{1}{2}}}{k} \lambda_0 \tag{5.107}$$

where by (4.33),

$$\lambda_0 = \left(1 + \frac{n^2\pi^2}{4k^2}\right)^{-\frac{1}{2}} \tag{5.108}$$

the corresponding vertical velocity being

$$\tilde{\omega}_0(Z) = \sin \tfrac{1}{2} n\pi (Z+1) \tag{5.109}$$

The general expansion is then

$$c_\theta = i \frac{(-R_\theta)^{\frac{1}{2}}}{k} \left\{ \lambda_0 - i \frac{k}{(-R_\theta)^{\frac{1}{2}}} \lambda_1 - \frac{k^2}{(-R_\theta)} \lambda_2 + \cdots \right\} \tag{5.110}$$

where $$\tilde{\omega}(Z) = \tilde{\omega}_0(Z) - i \frac{k}{(-R_\theta)^{\frac{1}{2}}} \tilde{\omega}_1(Z) - \frac{k^2}{(-R_\theta)} \tilde{\omega}_2(Z) + \cdots \tag{5.111}$$

Substituting into (5.20), equating powers of $k/(-R_\theta)^{\frac{1}{2}}$, and applying the lower boundary condition now gives

$$\tilde{\omega}_1(Z) = \frac{2}{n\pi\lambda_0} \int_{-1}^{Z} \left\{ 2(k^2 + \tfrac{1}{4}n^2\pi^2)(U - \lambda_1) + U'' \right\} \sin \tfrac{1}{2} n\pi (\zeta+1) \sin \tfrac{1}{2} n\pi (\zeta - Z)\, d\zeta \tag{5.112}$$

$$\tilde{\omega}_2(Z) = \frac{2}{n\pi\lambda_0} \int_{-1}^{Z} \left\{ 3(k^2 + \tfrac{1}{4}n^2\pi^2)(U-\lambda_1)^2 + U''(U-\lambda_1) - \frac{2\lambda_2}{\lambda_0} k^2 \right\} \sin \tfrac{1}{2} n\pi (\zeta+1) \sin \tfrac{1}{2} n\pi (\zeta - Z)\, d\zeta$$

$$+ \frac{2}{n\pi\lambda_0} \int_{-1}^{Z} \left\{ 2(k^2 + \tfrac{1}{4}n^2\pi^2)(U-\lambda_1) + U'' \right\} \tilde{\omega}_1(\zeta) \sin \tfrac{1}{2} n\pi (\zeta - Z)\, d\zeta \tag{5.113}$$

Applying the upper boundary condition to these eventually gives, after much algebra

$$\lambda_1 = \tfrac{1}{2}\int_{-1}^{1}\left\{1 - \frac{k^2-\frac{1}{4}n^2\pi^2}{k^2+\frac{1}{4}n^2\pi^2}\,\frac{\cos n\pi\zeta}{\cos n\pi}\right\}U(\zeta)\,d\zeta \qquad (5.114)$$

$$\lambda_2 = \frac{\lambda_0}{4k^2}\int_{-1}^{1}\left\{\left(-k^2+\tfrac{3}{4}n^2\pi^2\right)+\left(k^2+\tfrac{3}{4}n^2\pi^2\right)\frac{\cos n\pi\zeta}{\cos n\pi}\right\}\left\{U(\zeta)-\lambda_1\right\}^2 d\zeta \qquad (5.115)$$

$$+\frac{2\lambda_0}{n\pi k^2}\left(k^2-\tfrac{1}{4}n^2\pi^2\right)\int_{-1}^{1}\frac{\sin n\pi\zeta}{\cos n\pi}\left\{U(\zeta)-\lambda_1\right\}\int_{-1}^{\zeta}\left\{\left(k^2+\tfrac{1}{4}n^2\pi^2\right)-\left(k^2-\tfrac{1}{4}n^2\pi^2\right)\frac{\cos n\pi\xi}{\cos n\pi}\right\}\left\{U(\xi)-\lambda_1\right\}d\xi\,d\zeta$$

Since λ_1 and λ_2 are both real, substitution in (5.110) shows that λ_1 is the first order approximation to the phase speed, while $\frac{k^2}{(-R_0)}\lambda_2$ is the second order correction to the growth rate.

For antisymmetric profiles, (5.114) gives $\lambda_1 = 0$, so that, for large $-R_0$, long waves must be stationary, as seen in figs 5.2 and 5.5, though in the latter case (hyperbolic tangent profile) there are long wave propagating modes for moderately large $-R_0$ which are not given by this approximation.

For any profile, $\lambda_1 = \overline{U}$ when $k = \frac{1}{2}n\pi$. Considering only the first mode, (5.114) may be rewritten

$$\lambda_1 = \int_{-1}^{1}\frac{k^2\cos^2\frac{1}{2}\pi\zeta + \frac{1}{4}\pi^2\sin^2\frac{1}{2}\pi\zeta}{k^2+\frac{1}{4}\pi^2}\,U(\zeta)\,d\zeta \qquad (5.116)$$

For small k, this shows that phase speed is mainly influenced by the speed of the mean flow near the boundaries (where $\sin^2\frac{1}{2}\pi\zeta$ is greatest), while for large k the main influence is from the mean flow at the mid level (where $\cos^2\frac{1}{2}\pi\zeta$ is largest). In particular, as k increases for mean flows with a single mid level maximum, phase speed moves closer to the maximum mean flow speed, an effect which will be noted for the parabolic profile in fig 5.19. However, by Miles' (1961) steering level theorem, this maximum speed is never actually attained, and in any case, the expansion breaks down for $k \gtrsim (-R_0)^{\frac{1}{2}}$.

For the correction to the growth rate, the second term in (5.115) is difficult to visualise, so attention will be restricted to the special case $k = \frac{1}{2}n\pi$, when it vanishes. For the first mode, the first term then becomes

$$\lambda_2 = \frac{\lambda_0\pi^2}{16k^2}\int_{-1}^{1}\left(3\sin^2\tfrac{1}{2}\pi\zeta - \cos^2\tfrac{1}{2}\pi\zeta\right)\left\{U(\zeta)-\overline{U}\right\}^2 d\zeta \qquad (5.117)$$

which will usually be positive, giving a reduction in growth rate as orientation of the mode is changed from longitudinal towards transverse. If however there is a sharp jet at the middle level (where $\sin^2\frac{1}{2}\pi\zeta$

vanishes), λ_2 could be negative, with growth rate increasing as orientation shifts from longitudinal, indicating that for this wavenumber, shear and buoyancy actually can cooperate. This is indeed found to be true for $\mu \geq 4$ for the th^2 profile (5.34) - see section 5.5.3; for larger wavenumbers however λ_2 is found to become positive so that the largest growth rate for a buoyancy driven mode does, even then occur for the longitudinal roll.

For two of the cases which have been considered, the integrals in (5.115) can be fairly easily evaluated

(a) Constant shear profile (5.28). Here

$$\lambda_2 = \frac{2\lambda_0}{n^4\pi^2 k^2}\left(k^2 + \tfrac{1}{4}n^2\pi^2\right)\left\{\left(5 - \tfrac{1}{3}n^2\pi^2\right)k^2 + \left(\tfrac{1}{3}n^2\pi^2 - 1\right)\tfrac{1}{4}n^2\pi^2\right\} \qquad (5.118)$$

which is plotted in fig 5.13 (dash-dot line) for $R_\theta = -90$. A very good approximation is obtained for the upper branches of the graph for $\log k \leq 0{\cdot}4$, which is to be expected since the ratio of successive real terms in (5.110) is then $\frac{k^2}{-R_\theta} \leq 0{\cdot}05$. For the first mode, $n = 1$, λ_2 is always positive, implying a reduction in growth rate; for the other modes, λ_2 is negative for sufficiently large k, but the expansion has broken down before the growth rate is larger than that of the first mode; hence as expected, constant shear has reduced the growth rate of the fastest growing mode. Interestingly, the descending part of the $n = 1$ curve, together with the parts of the $n \geq 2$ curves to the left of it, do give a rough idea of the behaviour in the region of the branch points; examination of results for other R_θ suggests that this is not merely fortuitous.

(b) Shear layer (5.29). For this

$$\lambda_2 = \begin{cases} \frac{2\lambda_0}{n^2\pi^2}\left(k^2 + \frac{1}{4}n^2\pi^2\right) & n \text{ odd} \\ \frac{2\lambda_0}{n^2\pi^2 k^2}\left(k^2 + \frac{1}{4}n^2\pi^2\right)\left(n^2\pi^2 - 3k^2\right) & n \text{ even} \end{cases} \qquad (5.119)$$

which is always positive for n odd, but negative for sufficiently large k for n even. Thus, surprisingly, even here, for large $-R_\theta$ shear reduces the growth rate of the first mode, and examination of fig 5.7 provides evidence for this in the existence of local maxima in the growth rate curves for $-R_\theta \geq 90$.

5.4.2 Short Wave Expansions.

As mentioned in section 5.1.3d, short waves may travel near to one of the boundaries or at a level of maximum mean flow; different expansions are needed in the two cases.

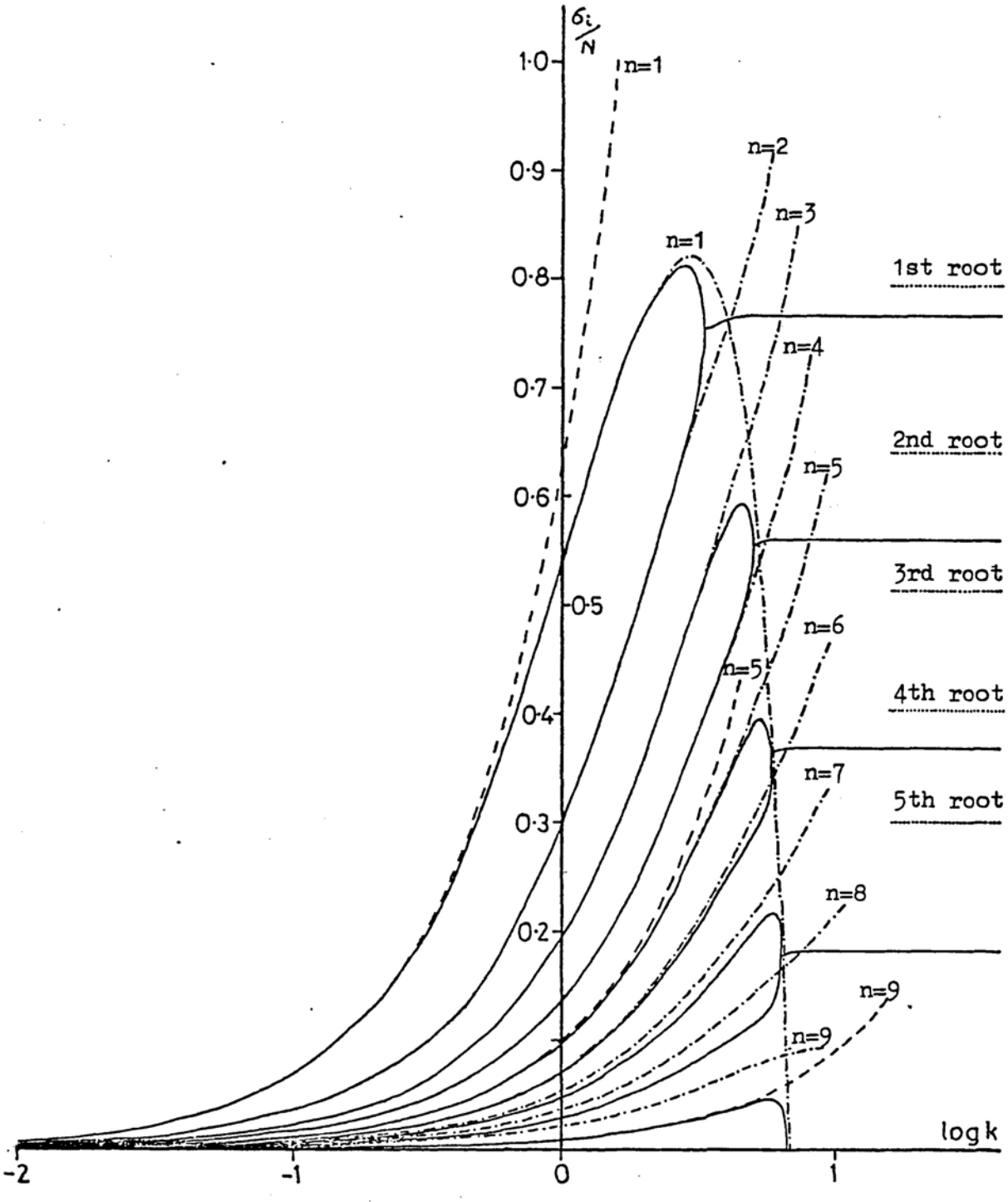


Fig 5.13. Plane Couette flow: various large Richardson number approximations to the non-dimensional growth rate for modified Richardson number $R_\theta = -90$.

——— Exact value

- - - - - - Long wave approximation

—·—·—·— Long wave } large $-R_\theta$ approximation.

····· Short wave }

(a) Expansion for Short Waves near a Boundary $k \gg J^{-1/6} \gg 1$.

For short waves near a boundary, a first approximation was obtained in section 5.1.3d by expanding about the pole Z_* of

$$f(Z) = k^2 - \frac{R_\theta L(Z)}{[U(Z)-c_\theta]^2} + \frac{U''(Z)}{U(Z)-c_\theta} \qquad (5.120)$$

For large $-R_\theta$, the Hankel functions obtained may be expanded in terms of Airy functions. A better error estimate however is found by deriving the Airy functions directly using Olver's (1974) method of expanding about one of the turning points where f(Z) vanishes. The two turning points $Z_\pm$ corresponding to the decaying and amplifying modes at the upper boundary are sketched, together with the appropriate pole Z_* in fig 5.14; lines through these points along which f(Z) is real are also indicated, dashed for $f(Z) > 0$, dotted for $f(Z) < 0$.

If k^2 and $-R_\theta$ are both large, the turning points are given from (5.120) approximately by

$$U(Z_\pm) = c_\theta \pm i\, U'(1) \frac{(-J)^{1/2}}{k} \left\{ 1 + O\left(\frac{L'(1)}{L(1)} \frac{(-J)^{1/6}}{k}, \frac{U''(1)}{U'(1)} \frac{1}{k(-J)^{1/2}} \right) \right\} \qquad (5.121)$$

the negative sign corresponding to the amplifying mode. In this

$$J = \frac{R_\theta L(1)}{[U'(1)]^2} \qquad (5.122)$$

is the local Richardson number at the boundary, and for simplicity both here and later, error terms are stated without proof.

Introducing new variables $\zeta, \tilde{u}$ such that

$$\tilde{w} = \left(\frac{d\zeta}{dZ}\right)^{-1/2} \tilde{u} \qquad (5.123)$$

and

$$\zeta \left(\frac{d\zeta}{dZ}\right)^2 = \frac{f(Z)}{k^2} \qquad (5.124)$$

with $\zeta = 0$ when $Z = Z_-$, (5.20) transforms to

$$\frac{d^2\tilde{u}}{d\zeta^2} = k^2 \zeta \tilde{u} + \left(\frac{dZ}{d\zeta}\right)^{1/2} \frac{d^2}{d\zeta^2} \left(\frac{dZ}{d\zeta}\right)^{-1/2} \tilde{u} \qquad (5.125)$$

Ignoring the last term (the error from which is negligible compared with errors introduced elsewhere - see Olver 1974), this has solutions $Ai(k^{2/3}\zeta)$, $Bi(k^{2/3}\zeta)$. Application of the boundary conditions gives

$$Ai(k^{2/3}\zeta_1)\, Bi(k^{2/3}\zeta_2) - Ai(k^{2/3}\zeta_2)\, Bi(k^{2/3}\zeta_1) = 0 \qquad (5.126)$$

where $\zeta = \begin{Bmatrix} \zeta_1 \\ \zeta_2 \end{Bmatrix}$ when $Z = \begin{Bmatrix} -1 \\ 1 \end{Bmatrix}$

and ζ_1, ζ_2 are given on integration of (5.124) by

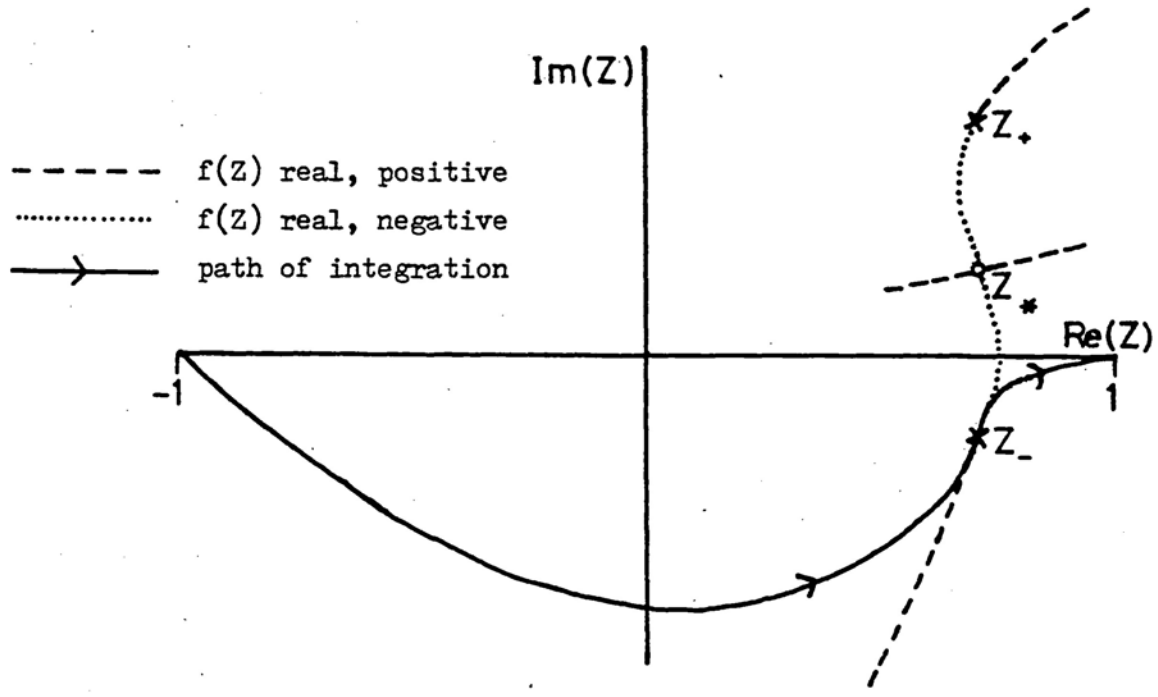


Fig 5.14. Complex Z plane showing turning points $Z_{\pm}$ and pole Z_{*} of f(Z), and lines through these where f(Z) is real.

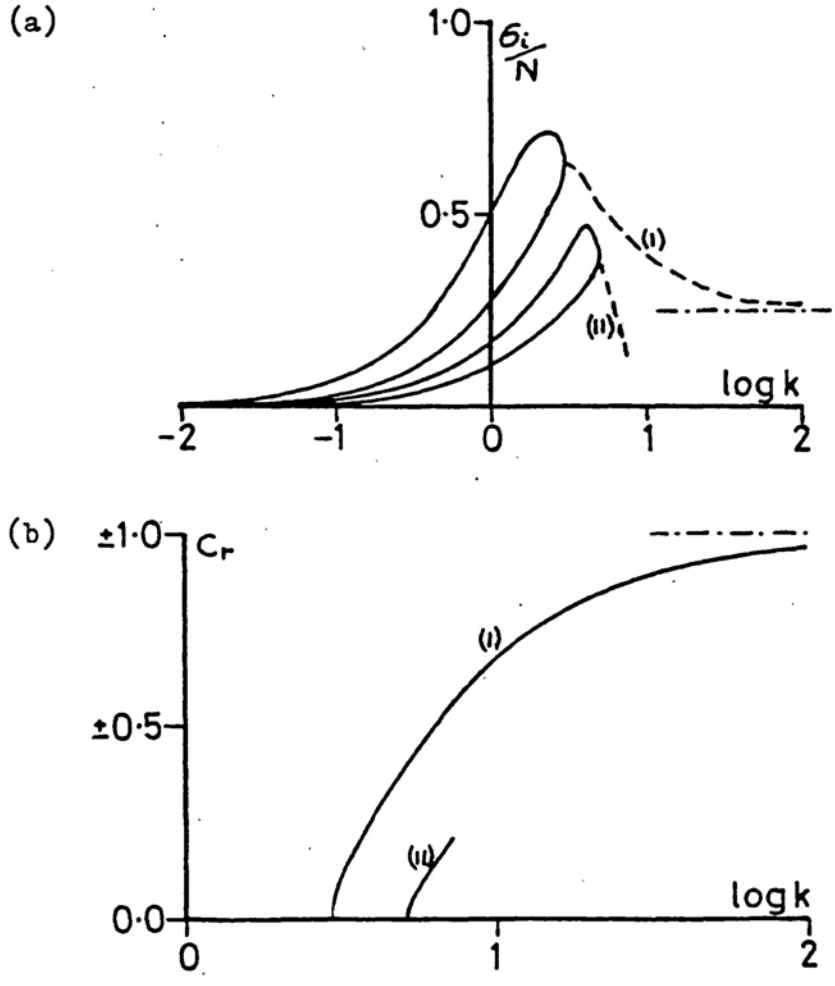


Fig 5.15. Tangent profile: non-dimensional (a) growth rate σ_i/N (b) phase speed c_r versus $\log_{10}$ of wavenumber k for $R_\theta = -20$.

$$\tfrac{2}{3}\zeta_1^{3/2} = \frac{1}{k}\int_{-1}^{Z_-}\left[f(Z)\right]^{\frac{1}{2}}dZ \qquad (5.127)$$

$$\tfrac{2}{3}(-\zeta_2)^{3/2} = \frac{1}{k}\int_{Z_-}^{1}\left[-f(Z)\right]^{\frac{1}{2}}dZ \qquad (5.128)$$

The paths of integration are shown in fig 5.14, they, and the negative square root in (5.128) being chosen so that $Re(\zeta)$ has the opposite sign to $Re(Z-Z_-)$, and so that the integrand is real in the neighbourhood of the turning point.

At this point it becomes necessary to anticipate the result (5.132) which, with (5.135) shows that for the mode near the upper boundary

$$Z_- \sim 1 + O\left(\frac{(-J)^{\frac{1}{6}}}{k}\right) \qquad (5.129)$$

Now in (5.127), except in a small neighbourhood of the turning point, $f(Z)$ may be approximated by k^2, and thus

$$\zeta_1 = 3^{2/3} + O\left(\frac{(-J)^{\frac{1}{6}}}{k}\right) \qquad (5.130)$$

In (5.128) however, the whole path of integration is within a small neighbourhood of the turning point Z_-, so it is convenient to expand about Z_- :

$$f(Z) \sim (Z-Z_-)f'(Z_-)\left\{1 + O\left((Z-Z_-)\frac{f''(Z_-)}{f'(Z_-)}\right)\right\} \qquad (5.131)$$

Hence (5.128) gives

$$\zeta_2 = (Z_- - 1)\frac{\left[-f'(Z_-)\right]^{\frac{1}{3}}}{k^{2/3}}\left\{1 + O\left((Z_- - 1)\frac{f''(Z_-)}{f'(Z_-)}\right)\right\}$$

$$= (Z_- - 1)\frac{(2k)^{\frac{1}{3}}}{(-J)^{\frac{1}{6}}}e^{-i\pi/6}\left\{1 + O\left(\frac{1}{(-J)^{\frac{1}{3}}}, \frac{L'(1)}{L(1)}\frac{(-J)^{\frac{1}{2}}}{k}, \frac{U''(1)}{U'(1)}\frac{(-J)^{\frac{1}{6}}}{k}\right)\right\} \qquad (5.132)$$

where use has been made of (5.120) and (5.121), and the factor $e^{-i\pi/6}$ has been chosen to make $Re(\zeta_2) < 0$ when $Re(1-Z_-) > 0$.

Now with ζ_1 given by (5.130), for large k,

$$Ai(k^{2/3}\zeta_1) \sim e^{-2k}, \quad Bi(k^{2/3}\zeta_1) \sim e^{2k} \qquad (5.133)$$

so applying the boundary conditions (5.126) gives

$$Ai(k^{2/3}\zeta_2) \to 0 \quad \text{as} \quad k \to \infty \qquad (5.134)$$

The first three roots (zeros of the Airy function) are

$$k^{2/3}\zeta_2 = \begin{Bmatrix} -2{\cdot}3381 \\ -4{\cdot}0879 \\ -5{\cdot}5206 \end{Bmatrix} \qquad (5.135)$$

Substituting in (5.132), solving for Z_- and making use of (5.121) finally gives for the first three modes at the upper boundary

$$c = U(1) + i\left|U'(1)\right|\frac{(-J)^{\frac{1}{2}}}{k}\left[1 - \frac{1}{(-J)^{\frac{1}{3}}}\begin{Bmatrix}0{\cdot}9279-1{\cdot}6071i\\1{\cdot}6223-2{\cdot}8099i\\2{\cdot}1908-3{\cdot}7946i\end{Bmatrix} + O\left(\frac{1}{(-J)^{\frac{2}{3}}}, \frac{L'(1)}{L(1)}\frac{(-J)^{\frac{1}{6}}}{k}, \frac{U''(1)}{U'(1)}\frac{1}{k(-J)^{1/6}}\right)\right] \tag{5.136}$$

(a corresponding expression with 1 replaced by -1 holding for modes at the lower boundary). Hence phase speed is

$$c_r \sim U(1) - \left|U'(1)\right|\left[\frac{(-J)^{\frac{1}{6}}}{k}\begin{Bmatrix}1{\cdot}6071\\2{\cdot}8099\\3{\cdot}7946\end{Bmatrix} + O\left(\frac{1}{k(-J)^{\frac{1}{6}}}, \frac{L'(1)}{L(1)}\frac{(-J)^{\frac{2}{3}}}{k^2}, \frac{U''(1)}{U'(1)}\frac{(-J)^{\frac{1}{3}}}{k^2}\right)\right] \tag{5.137}$$

while growth rate, non-dimensionalised with respect to buoyancy at the boundary is

$$\frac{\sigma_i}{\left[-g\beta_0 L(1)\right]^{\frac{1}{2}}} \sim 1 - \frac{1}{(-J)^{\frac{1}{3}}}\begin{Bmatrix}0{\cdot}9279\\1{\cdot}6233\\2{\cdot}1908\end{Bmatrix} + O\left(\frac{1}{(-J)^{\frac{2}{3}}}, \frac{L'(1)}{L(1)}\frac{(-J)^{\frac{1}{6}}}{k}, \frac{U''(1)}{U'(1)}\frac{1}{k(-J)^{1/6}}\right) \tag{5.138}$$

These results confirm that in the short wave limit, the waves travel along a boundary, with growth rate reduced from that in the unsheared case by a term proportional to $(-J)^{-1/3}$. These short wave limits of the growth rates are shown in fig 5.13 (dotted lines) for the case of constant shear with $R_\theta = -90$; errors are large, particularly for modes other than the first, in contrast to the long wave expansion where the error, being proportional to $(-R_\theta)^{-1}$, is small. Because (5.138) always gives a reduction in growth rate from that of the large -J limit, the short transverse modes always grow less rapidly than the longitudinal mode.

As the wavenumber is decreased from infinity, the perturbation moves away from the boundary, as shown by the second term in (5.137). The modification to the growth rate however depends on the next order term, which is difficult to evaluate, though one comment may be made: in the case of constant static stability, the $\frac{L'(1)}{L(1)}\frac{(-J)^{1/6}}{k}$ error term in (5.138) vanishes, leaving as the most important term the $\frac{U''(1)}{U'(1)}\frac{1}{k(-J)^{1/6}}$. Since this gives a reduction in growth rate for the hyperbolic tangent profile as k is reduced, it may be expected to do so for all profiles for which $\frac{U''(1)}{U'(1)}$ is negative. Correspondingly, profiles for which $\frac{U''(1)}{U'(1)}$ is positive would be expected to show an increase in growth rate, which is plausible also because a decrease in wavenumber causes the perturbation to move away from the boundary into a region of reduced shear. This is borne out by results shown in fig 5.15 for the profile $U = \tan z/\tan 1$ with $R_\theta = -20$. For small wavenumbers, modes are stationary and very similar to those with $R_\theta = -20$ for the constant shear profile (fig 5.2d). Beyond the branch points however, growth

rates fall, approaching, for the first mode, a limit given by the short wave approximation (5.76), with $J \simeq 4{\cdot}134$ in (5.69) (this boundary value of J is too small for the large Richardson number short wave approximation (5.138) to be applicable); the second mode apparently cuts off at $k \simeq 1$, which is to be expected since (5.76) only gives one mode for this J.

(b) Expansion for Short Waves near a Velocity Maximum.

In the case of a velocity maximum, the lack of shear prevents the use of the elegant turning point expansion of the previous section. Instead, restricting attention to the case of constant lapse rate $L = 1$, an ad hoc expansion will be carried out about the velocity maximum itself, without attempting an error analysis.

Defining Z_o such that

$$U'(Z_o) = 0 \tag{5.139}$$

expand $$U(Z) - c_\theta = U(Z_o) - c_\theta + \tfrac{1}{2}U''(Z_o)(Z - Z_o)^2 \tag{5.140}$$

where for a velocity maximum

$$U''(Z_o) < 0 \tag{5.141}$$

Now, for constant lapse rate, (5.20) may be written

$$\frac{d^2\tilde{w}}{dZ^2} - \frac{k^2\left[U(Z) - c_\theta + i\frac{(-R_\theta)^{\frac{1}{2}}}{k}\right]\left[U(Z) - c_\theta - i\frac{(-R_\theta)^{\frac{1}{2}}}{k}\right] + U''(Z)\left[U(Z) - c_\theta\right]}{\left[U(Z) - c_\theta\right]^2}\tilde{w} = 0 \tag{5.142}$$

so set $$U(Z_o) - c_\theta + i\frac{(-R_\theta)^{\frac{1}{2}}}{k} = \varepsilon \tag{5.143}$$

where, for amplifying modes, anticipating the result (5.152),

$$\varepsilon \sim \frac{(-R_\theta)^{\frac{1}{4}}\left[-U''(Z_o)\right]^{\frac{1}{2}}}{k^{3/2}} \tag{5.144}$$

Substituting in (5.142) then gives

$$\frac{d^2\tilde{w}}{dZ^2} - \frac{2ik^3}{(-R_\theta)^{\frac{1}{2}}}\left[\varepsilon + \tfrac{1}{2}U''(Z_o)(Z - Z_o)^2\right]\left\{1 + O\left(\frac{\left[-U''(Z_o)\right]^{\frac{1}{2}}}{k^{3/2}(-R_\theta)^{\frac{1}{4}}}\right)\right\}\tilde{w} = 0 \tag{5.145}$$

which, under the transformation

$$\zeta = e^{-i\pi/8}\frac{2^{\frac{1}{2}}k^{\frac{3}{4}}}{(-R_\theta)^{\frac{1}{8}}}\left[-U''(Z_o)\right]^{\frac{1}{4}}(Z - Z_o) \tag{5.146}$$

becomes $$\frac{d^2\tilde{w}}{d\zeta^2} - \left(\tfrac{1}{4}\zeta^2 + a\right)\tilde{w} \simeq 0 \tag{5.147}$$

where $$a = e^{-i\pi/4}\frac{k^{3/2}\varepsilon}{(-R_\theta)^{\frac{1}{4}}\left[U''(Z_o)\right]^{\frac{1}{2}}} \tag{5.148}$$

and the factor $e^{-i\pi/8}$ in (5.146) was chosen so that $Re(\zeta^2) > 0$ when $Z = \pm 1$.

According to Abramowitz and Stegun (1964), (5.147) has parabolic cylinder function solutions

$$Y_1(a,\zeta) = e^{-\frac{1}{4}\zeta^2}\left\{1 + (a+\tfrac{1}{2})\frac{\zeta^2}{2!} + (a+\tfrac{1}{2})(a+\tfrac{5}{2})\frac{\zeta^4}{4!} + \cdots\right\}$$

$$Y_2(a,\zeta) = e^{-\frac{1}{4}\zeta^2}\left\{\zeta + (a+\tfrac{3}{2})\frac{\zeta^3}{3!} + (a+\tfrac{3}{2})(a+\tfrac{7}{2})\frac{\zeta^5}{5!} + \cdots\right\} \quad (5.149)$$

Now, one or other of these series, say $Y(a,\zeta)$ terminates if

$$a = -n + \tfrac{1}{2} \quad (5.150)$$

where n is a positive integer. Then for $Z = \pm 1$, the form of ζ chosen in (5.146) ensures that

$$Y(a,\zeta) \to 0 \quad \text{as} \quad k \to \infty \quad (5.151)$$

so that, in the short wave limit, the boundary conditions (5.22) are satisfied. Thus from (5.143), (5.148) and (5.150),

$$c \simeq U(Z_0) + i\frac{(-R_\theta)^{\frac{1}{2}}}{k} - e^{i\pi/4}(n-\tfrac{1}{2})\frac{[-U''(Z_0)]^{\frac{1}{2}}(-R_\theta)^{\frac{1}{4}}}{k^{3/2}} \quad (5.152)$$

giving non-dimensional phase speed

$$c_r \simeq U(Z_0) - (n-\tfrac{1}{2})\frac{[-\frac{1}{2}U''(Z_0)]^{\frac{1}{2}}(-R_\theta)^{\frac{1}{4}}}{k^{3/2}} \quad (5.153)$$

and growth rate

$$\frac{\sigma_i}{N} \simeq 1 - (n-\tfrac{1}{2})\frac{[-\frac{1}{2}U''(Z_0)]^{\frac{1}{2}}}{k^{\frac{1}{2}}(-R_\theta)^{\frac{1}{4}}} \quad (5.154)$$

To the extent to which this approximation is true, it confirms the conjecture of section 5.1.3d (equation (5.77)) that, in the short wave limit, modes will propagate at the maximum mean flow velocity, and have the same growth rate as if there were no shear. Reducing wavenumber k however, the modes move away from the velocity maximum, and growth rate falls more rapidly than if there were no shear (when by (4.33), $\frac{\sigma_i}{N} \sim 1 - \frac{n^2\pi^2}{4k^2}$). These results are borne out in section 5.5.2 for the parabolic profile.

5.4.3 General Remarks.

It has been seen that while for long waves a single large Richardson number expansion will suffice for all mean flows (assuming constant lapse rate), short wave behaviour for monotonic profiles is quite different to that for profiles with a maximum. For intermediate wavenumbers, no large Richardson number expansion is possible, but

numerical results show the same distinction as found in the short wave case. For monotonic profiles, the fastest growing long wave modes meet in pairs at a branch point and give way to pairs of short wave modes which move to the boundaries for large k, as seen from results in sections 5.2.2 and 5.2.3. For profiles with a maximum however, results to be presented in section 5.5.2 show that each of the fastest growing long wave modes corresponds to a single short wave mode, with a steady movement of the mode to the level of the maximum as wavenumber is increased. This clear distinction between the two types of profile has crucial implications in the modelling of SQL's, as will be seen when superposition is carried out at the end of this chapter. First however, the results for profiles with a maximum will be presented.

5.5 NUMERICAL RESULTS FOR JET PROFILES.

5.5.1 Introduction.

With the failure of linear modes of monotonic profiles to adequately model West African SQL's, attention was now directed to profiles with a velocity maximum, bearing in mind the quite different large Richardson number behaviour noted in the previous section. The profiles considered were the symmetric jets (5.34).

Non-dimensional growth rates and phase speeds for neutral stratification are shown in figs 5.16 and 5.17 for $\mu = 1$, 2, 5 and 10; the limit $\mu \to \infty$ corresponds to unsheared flow, which has no exponential modes for $R_\theta = 0$, so is not included. Results are consistent with existence of a sinuous mode (S) for $\mu \geq 0{\cdot}658$, and of a varicose mode as well for $\mu \geq 1{\cdot}717$, as noted in section 5.1.2b. The sinuous mode has the larger maximum growth rate, though the varicose mode has a larger growth rate for small wavenumber. As wavenumber tends to the cut-off values given by (5.37) and (5.40), the phase speed approaches the mean-flow speed $1 - \frac{1}{3}\coth^2\mu$ at the point of inflexion; for $\mu = 2$ the phase speed of the varicose mode varies little from this value. For $\log k \lesssim 0{\cdot}4$, the sinuous mode for $\mu = 10$ has a smaller growth rate than that for $\mu = 5$, suggesting that, at least for long wave modes, growth rate falls to zero as the limit $\mu \to \infty$ is approached.

Growth rates and phase speeds are now shown for various modified Richardson numbers for $\mu = 0$ and 5 (figs 5.18 - 5.21). Results were obtained by roughly locating the eigenvalue by the Galerkin method (section 5.1.3a) or the short wave approximation (section 5.1.3d), then 'tracking' for varying k using the shooting method (section 5.1.3b).

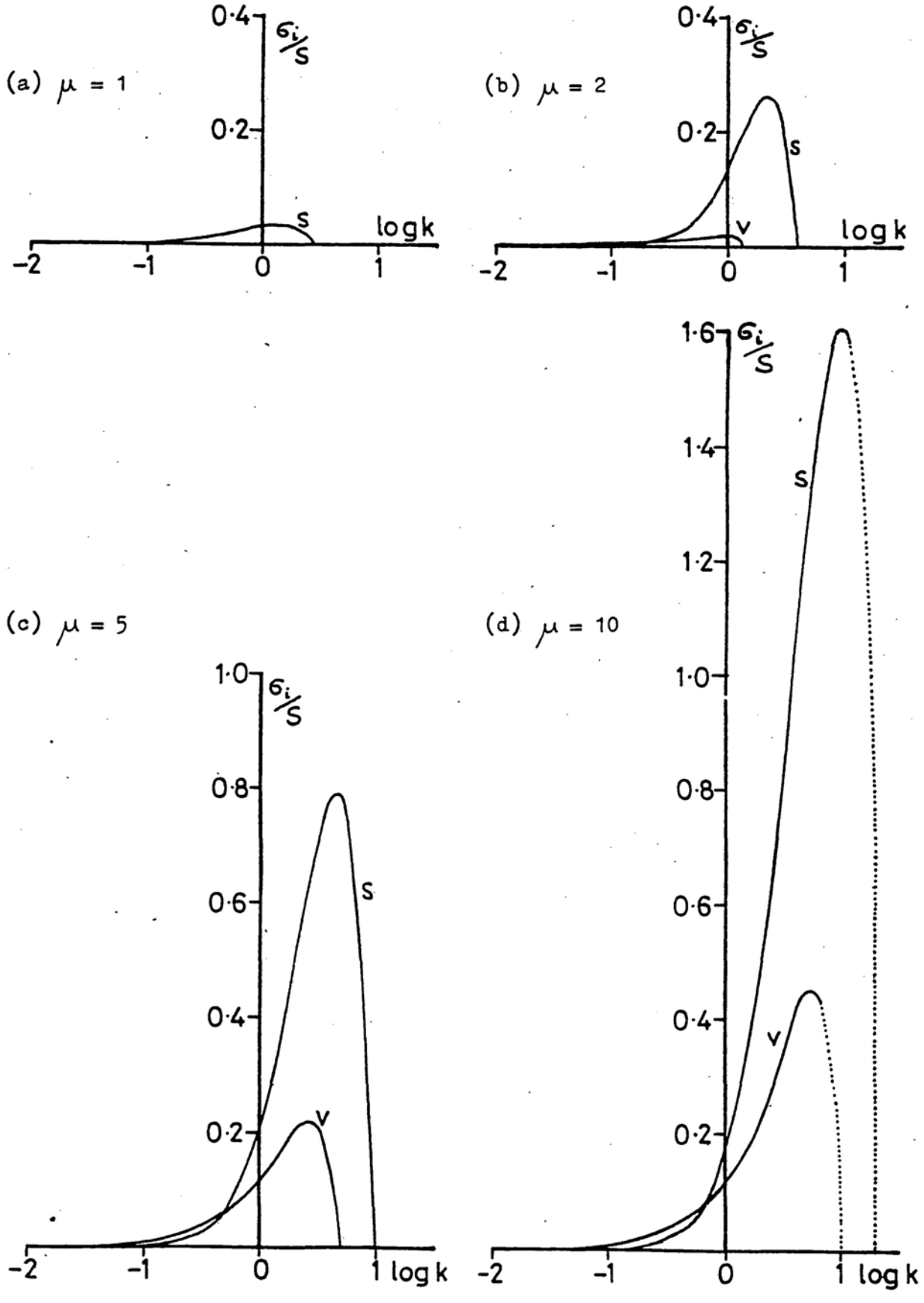


Fig 5.16. Th^2 jet profiles: non-dimensional growth rate $\frac{\sigma_i}{S}$ plotted against $\log_{10}$ of wavenumber k for different μ in unstratified case $(R_\theta = 0)$.

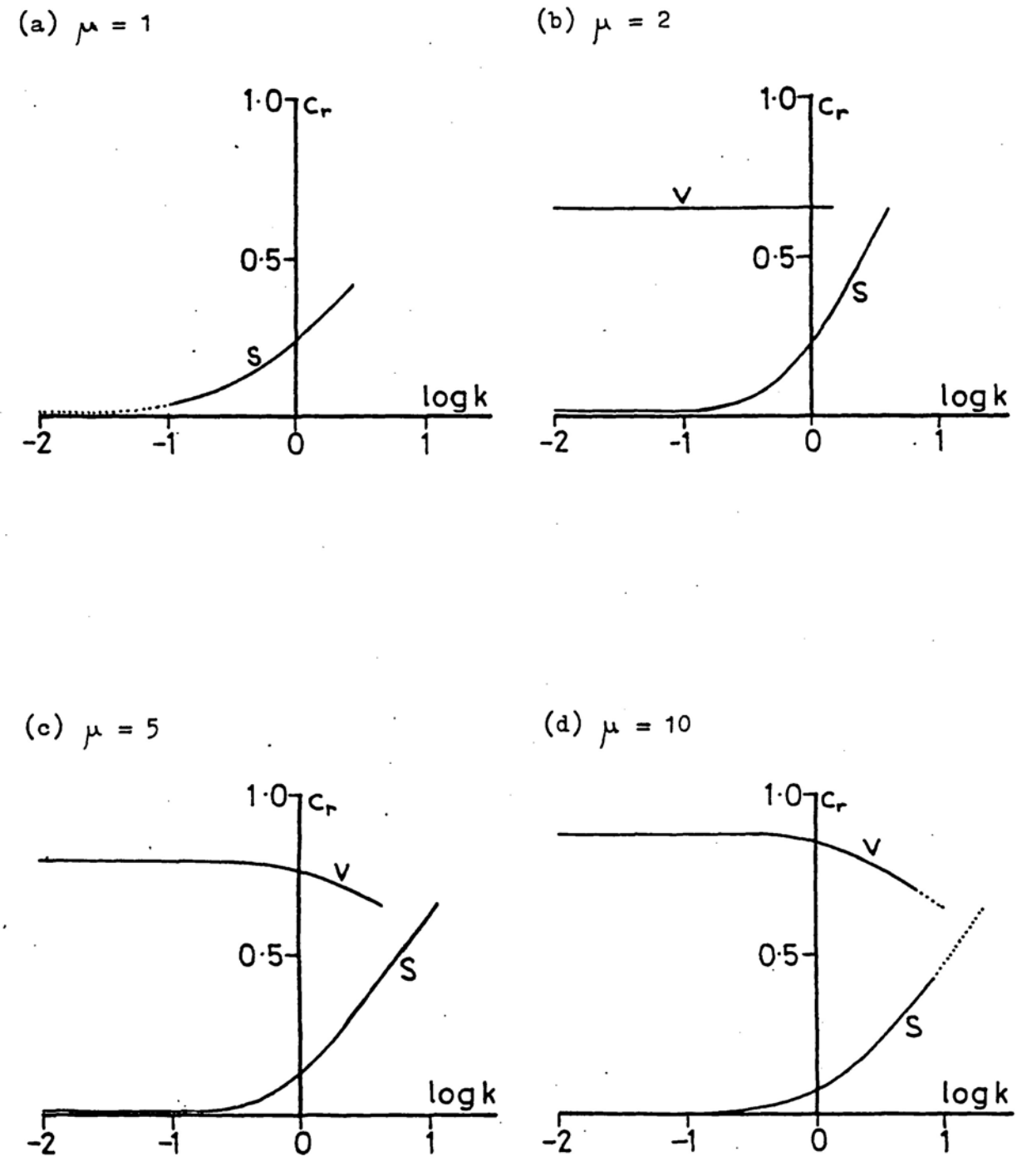


Fig 5.17. Th^2 jet profiles: non-dimensional phase speed c_r plotted against $\log_{10}$ of wavenumber k for different μ in unstratified case.

The graphical method (section 5.1.3c) which was used for the antisymmetric profiles could not be applied here, and this means that there is less certainty that all the branches of the graphs were located; indeed, for the larger Richardson numbers, there were so many modes that it is not possible to show them all in any case.

5.5.2 Plane Poiseuille Flow: $\mu = 0$.

Numerical results for the parabolic profile (5.35) are shown in figs 5.18 and 5.19. By Rayleigh's criterion, there are no unstable modes for $R_\theta = 0$, but one unstable mode has appeared for $R_\theta = -0{\cdot}5$; in contrast to plane Couette flow (section 5.2.2), the exact cut-off Richardson number cannot easily be determined analytically, and it was not investigated. For $R_\theta = -1$, again only one unstable mode could be found, but whereas the mode with $R_\theta = -0{\cdot}5$ had a short-wave cut-off, that with $R_\theta = -1$ has growth rate increasing monotonically to 1 in the short wave limit, with phase speed correspondingly approaching the maximum mean flow speed, as suggested by the short wave large Richardson number approximation (5.152). In spite of the smallness of $-R_\theta$, the growth rate and phase speed for $k \geq 10$ are given surprisingly well by this approximation, and it was used to extrapolate the graphs (dotted lines). A second mode has appeared for $R_\theta = -2$, and this too has monotonically increasing growth rate and, for $k \geq 10$, growth rate and phase speed corresponding well with the short wave approximation.

For $-R_\theta \geq 6$, a considerable number of modes was found, and only the first few are plotted. In all cases, the first two modes have growth rate increasing monotonically with wavenumber while phase speed approaches the maximum mean flow speed, as anticipated in section 5.4.3; the third mode has a local maximum similar to that obtained for $-R_\theta \geq 90$ with the shear layer (section 5.2.4). All these three modes have growth rate and phase speed for $k \geq 10$ given well by the short wave approximation (5.152).

Modes (iv) and (v) however always meet at a branch point. The phase speeds of the two long wave branches are so similar that it was not possible to plot them separately. Only one short wave branch was found and unlike modes (i) - (iii), this has phase speed approaching the mean flow speed at the boundary, while its growth rate decreases with wavenumber, which is to be expected since the mean flow shear is greatest at the boundary, as for the tangent profile (fig 5.15). For $R_\theta = -6$, the local Richardson number at the boundary at the boundary is $-1{\cdot}5$, which is too close to zero for existence of a short wave limit

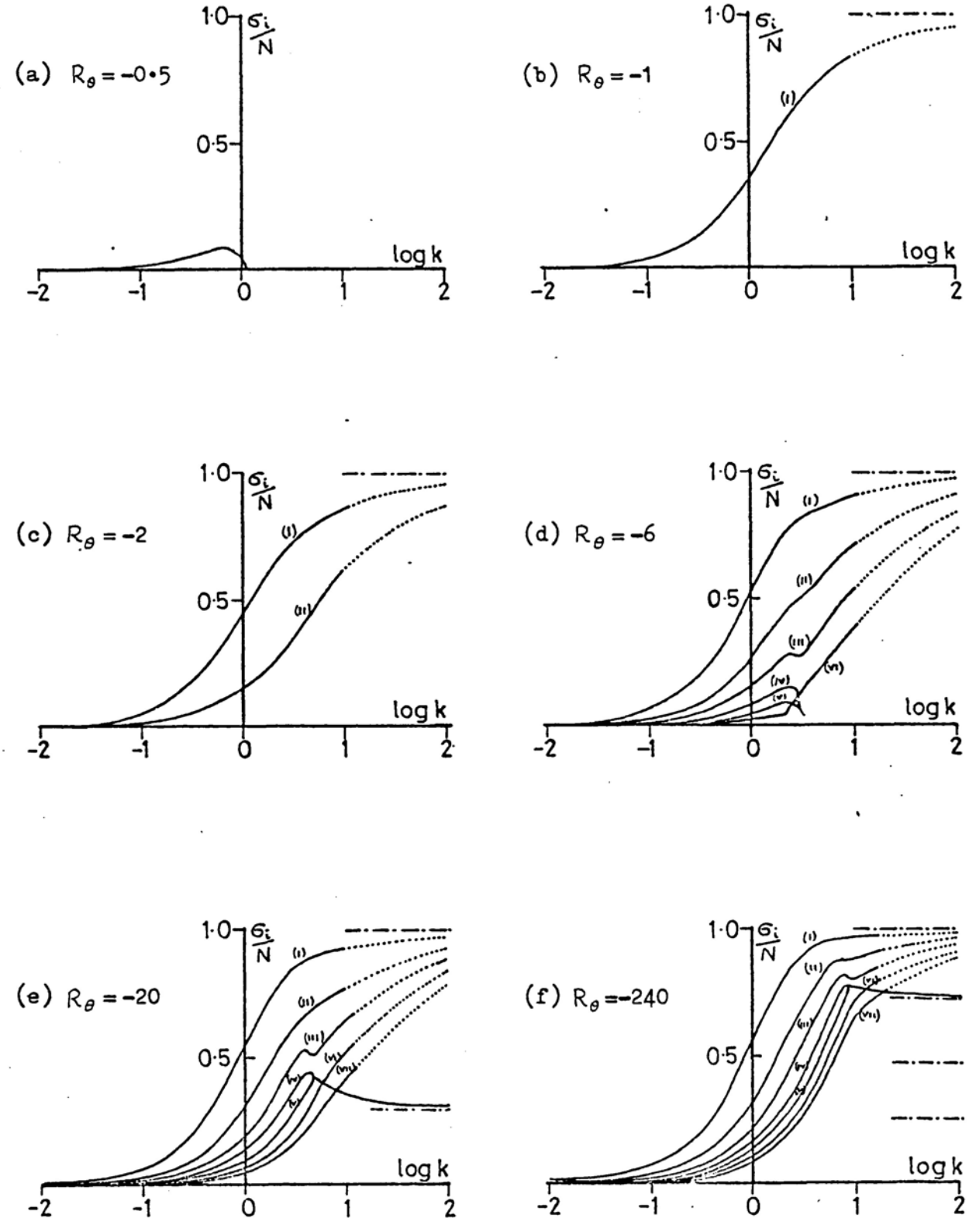


Fig 5.18. Plane Poiseuille flow: non-dimensional growth rate $\frac{\sigma_i}{N}$ plotted against $\log_{10}$ of wavenumber k for various modified Richardson numbers R_θ.

—·—·— Asymptotic limit ····· Extrapolated value

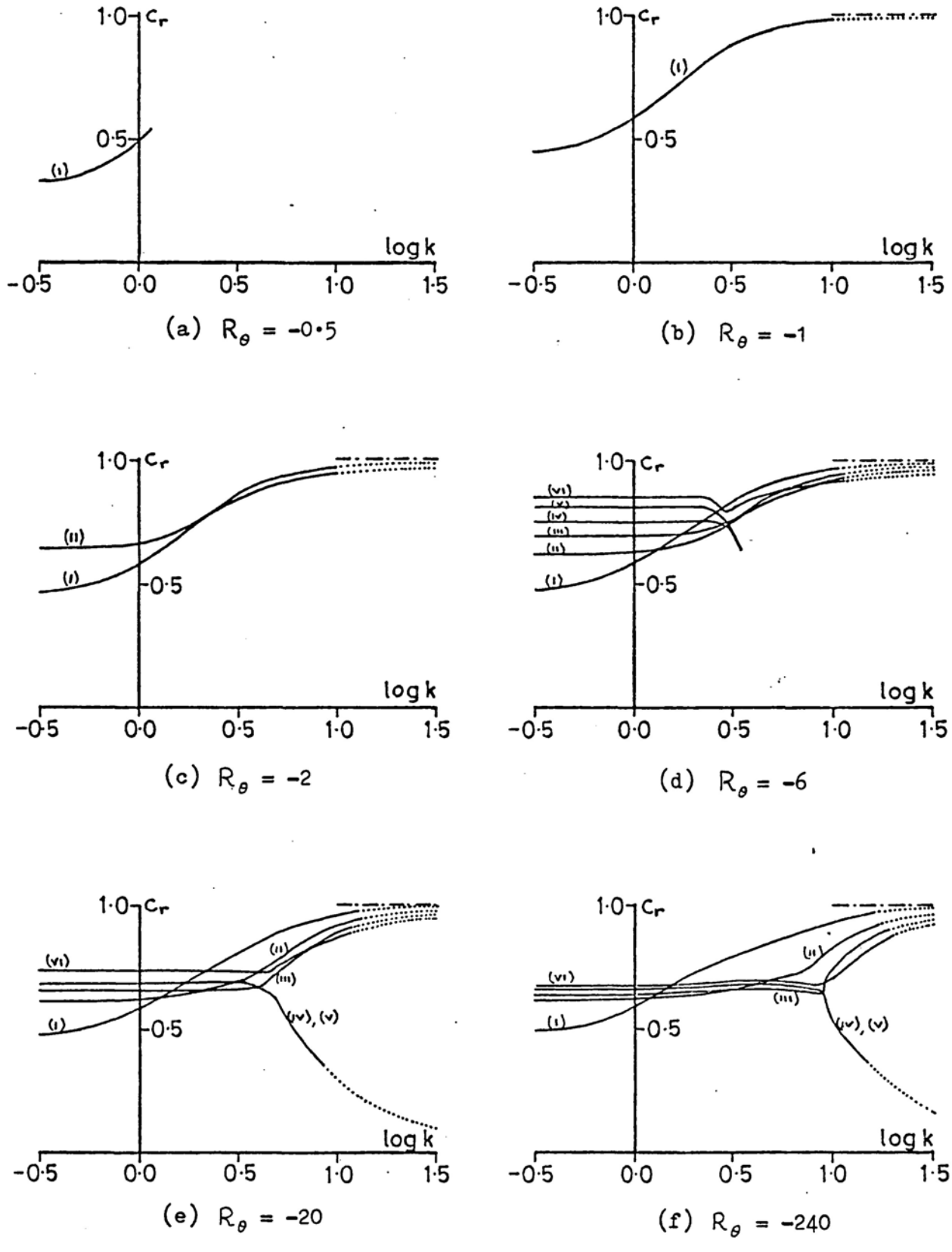


Fig 5.19. Plane Poiseuille flow: non-dimensional phase speed c_r plotted against $\log_{10}$ of wavenumber k for various modified Richardson numbers R_θ .

—·—·— Asymptotic limit ..... Extrapolated value.

(i.e. a solution of (5.75)), and the growth rate graph apparently has a corresponding short wave cut-off, as for the second short wave mode for the tangent profile, fig 5.15a. For $R_\theta = -20$ on the other hand, a short wave limit does exist (dash-dot line), and the growth rate graph approaches it, as for the first short wave mode in fig 5.15a; correspondingly phase speed approaches the mean flow speed at the boundary, though more slowly ($\sim k^{-1}$) than the approach of the modes at the maximum to their limit ($\sim k^{-3/2}$). For $R_\theta = -240$, there are three short wave boundary modes (solutions to (5.75)), indicated by dash-dot lines, and the growth rate graph approaches the first of these limits; presumably other modes exist which approach the other two, but they were not found.

After mode (v), all the remaining modes which have been found have growth rate monotonically increasing with wavenumber and approaching 1, short wave behaviour being given approximately (though not as well as for modes (i) - (iii)) by the short wave velocity maximum approximation (5.152). The higher modes have phase speeds in the long wave limit progressively nearer the maximum mean flow speed, and retain these long wave phase speeds for progressively larger wavenumbers; for short waves however, the higher the mode, the more slowly does phase speed approach its short wave limit of the maximum mean flow speed.

5.5.3 Th^2 Jet Profile: $\mu = 5$.

For the th^2 profile (5.34), the value 5 chosen for μ was taken to be sufficiently large that (5.117) gives an increase in growth rate as orientation of the mode is changed from longitudinal towards transverse; results are shown in figs 5.20 and 5.21.

For $R_\theta = -0{\cdot}025$, the dominant modes are the symmetric sinuous (S) and antisymmetric varicose (V) shear-driven modes obtained for unstratified flow (fig 5.16c), and having similar short-wave cut-offs. Even for such a small modified Richardson number however, the shear at the boundaries is so low as to permit existence there of a pair of buoyancy driven modes, one antisymmetric and one symmetric, with the antisymmetric mode having the larger long wave growth rate (in contrast to the smaller growth rate of the varicose mode); as wavenumber increases, the growth rates and phase speeds approach each other, but, as far as can be ascertained, a clear antisymmetric/symmetric distinction can still be made.

As $-R_\theta$ is increased, further pairs of buoyancy driven modes

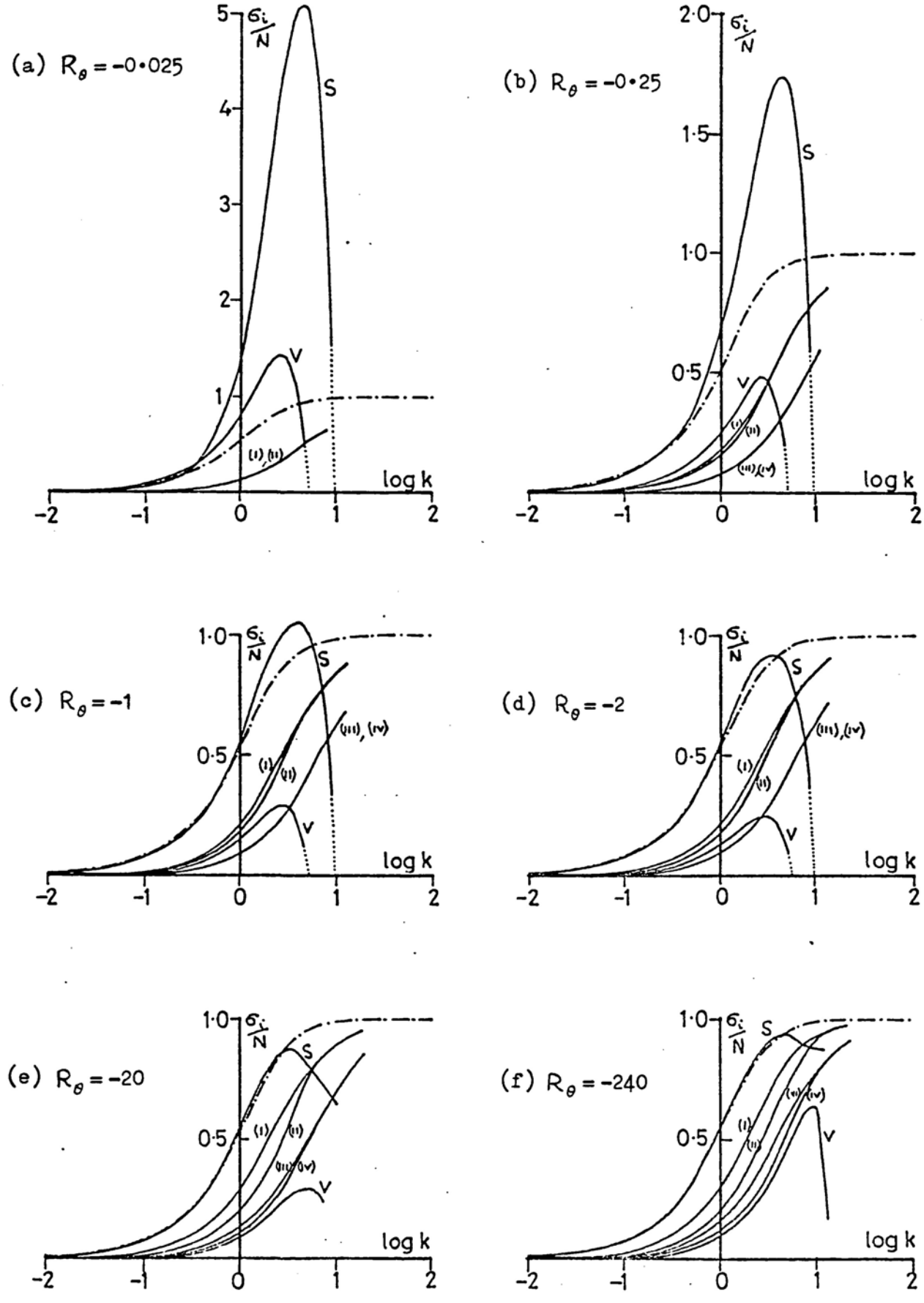
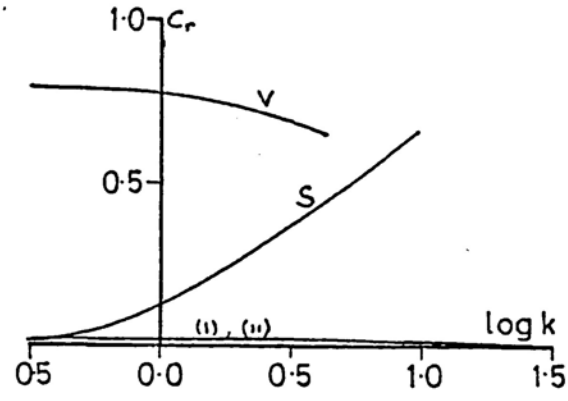
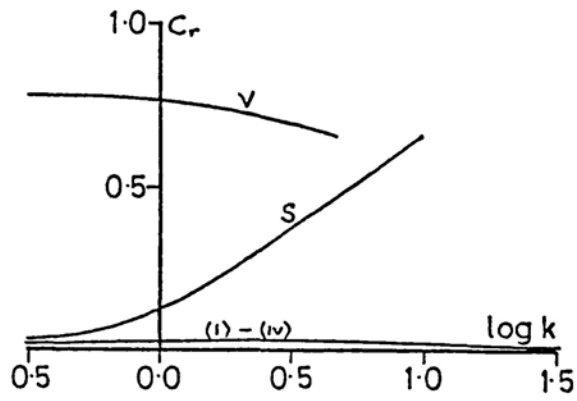


Fig 5.20. Th^2 jet profile: non-dimensional growth rate $\frac{\sigma_i}{N}$ plotted against $\log_{10}$ of wavenumber k for various modified Richardson numbers R_θ .

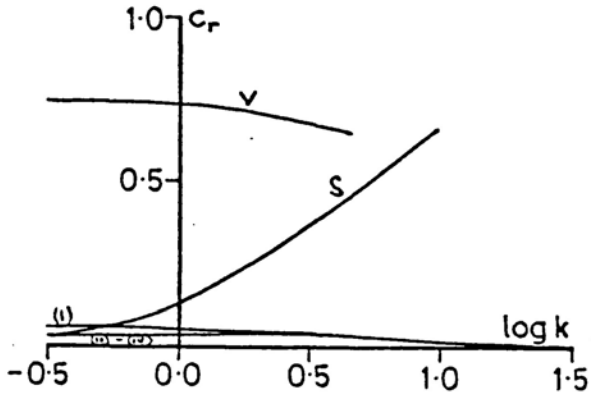
—·—·— $R_\theta = -\infty$, first mode ..... Extrapolated value



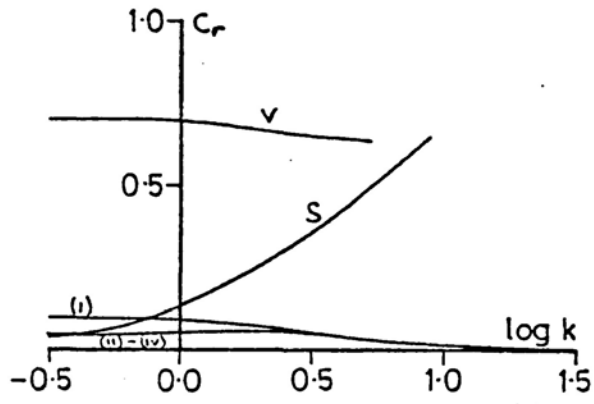
(a) $R_\theta = -0{\cdot}025$



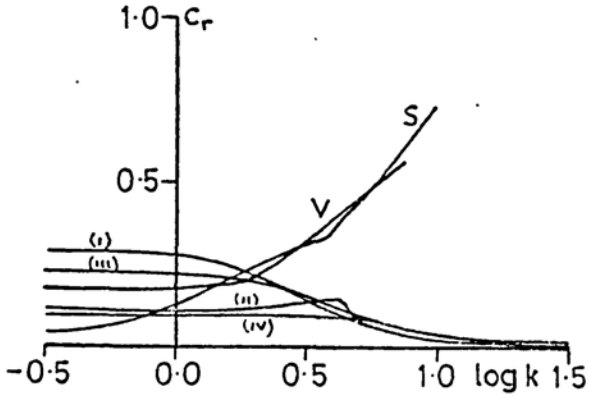
(b) $R_\theta = -0{\cdot}25$



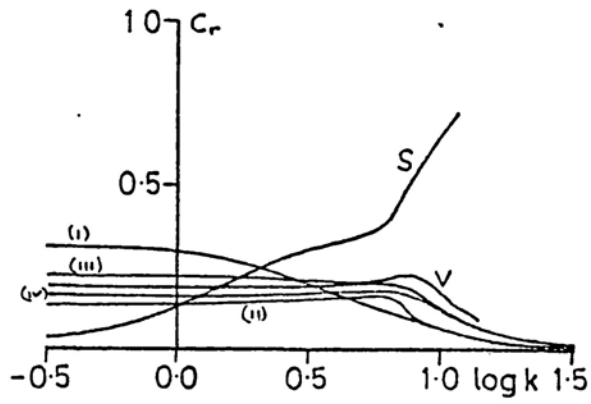
(c) $R_\theta = -1$



(d) $R_\theta = -2$



(e) $R_\theta = -20$



(f) $R_\theta = -240$

Fig 5.21. Th^2 jet profile: non-dimensional phase speed c_r plotted against $\log_{10}$ of wavenumber k for various modified Richardson numbers R_θ.

appear, with properties similar to those of the first pair; only the first two pairs in each case are shown. With increasing $-R_\theta$, growth rates of all the buoyancy driven modes increase, long wave phase speeds move away from the mean flow speed at the boundary, and antisymmetric/symmetric differences in long wave growth rates become more pronounced.

For the sinuous and varicose modes, the situation is more complicated. The phase speed of the sinuous mode alters little with modified Richardson number, but its growth rate decreases up to $R_\theta = -20$, then increases again for $R_\theta = -240$. For the varicose mode however, phase speed remains unaltered and growth rate decreases only up to $R_\theta = -2$; beyond this value, not only does the maximum growth rate increase, but also the long wave phase speed is much closer to the boundary mean flow speed; for $R_\theta = -240$ the short wave phase speed is also much closer to this boundary speed. For both sinuous and varicose modes, the short wave cut-offs are assumed to alter little up to $R_\theta = -2$, but thereafter they apparently shift to larger wavenumber, and for $R_\theta = -240$, the growth rate of the sinuous mode seems to approach some short wave limit between 0·8 and 0·9; further clarification is needed here however as the phase speed graph indicates, in the short wave limit, movement of the mode towards the mean flow maximum speed, which, by (5.154) would demand a limit of 1 for the growth rate.

These results are now used to find variation of growth rate with direction of propagation. If wavenumber is fixed to be 1 (dashed line in fig 5.22), growth rate of the sinuous mode decreases monotonically with $\log(-R_\theta)$ to its large Richardson number limit of 0·537, indicating shear and buoyancy cooperating as driving mechanisms. Growth rate thus decreases with angle of orientation θ, as seen in fig 5.23 (dashed line) for $R = -0{\cdot}25$. This is consistent with the increase of growth rate as orientation changes from longitudinal towards transverse predicted in (5.117), and suggests the fastest growing transverse mode as a possible start for a SQL model. However if the sinuous mode for k = 1 in any of figs 5.21 is examined, it can be seen that the phase speed is fairly close to the boundary level mean flow speed, and certainly nowhere near the maximum mean flow speed required. Furthermore, the model is critically dependent on the exceptionally sharp jet which the th^2 profile has for $\mu = 5$, and on the unrealistically large viscosity (small Rayleigh number) which would be needed to fix the wavenumber of maximum amplification to be 1.

The importance of the choice of wavenumber may be appreciated if,

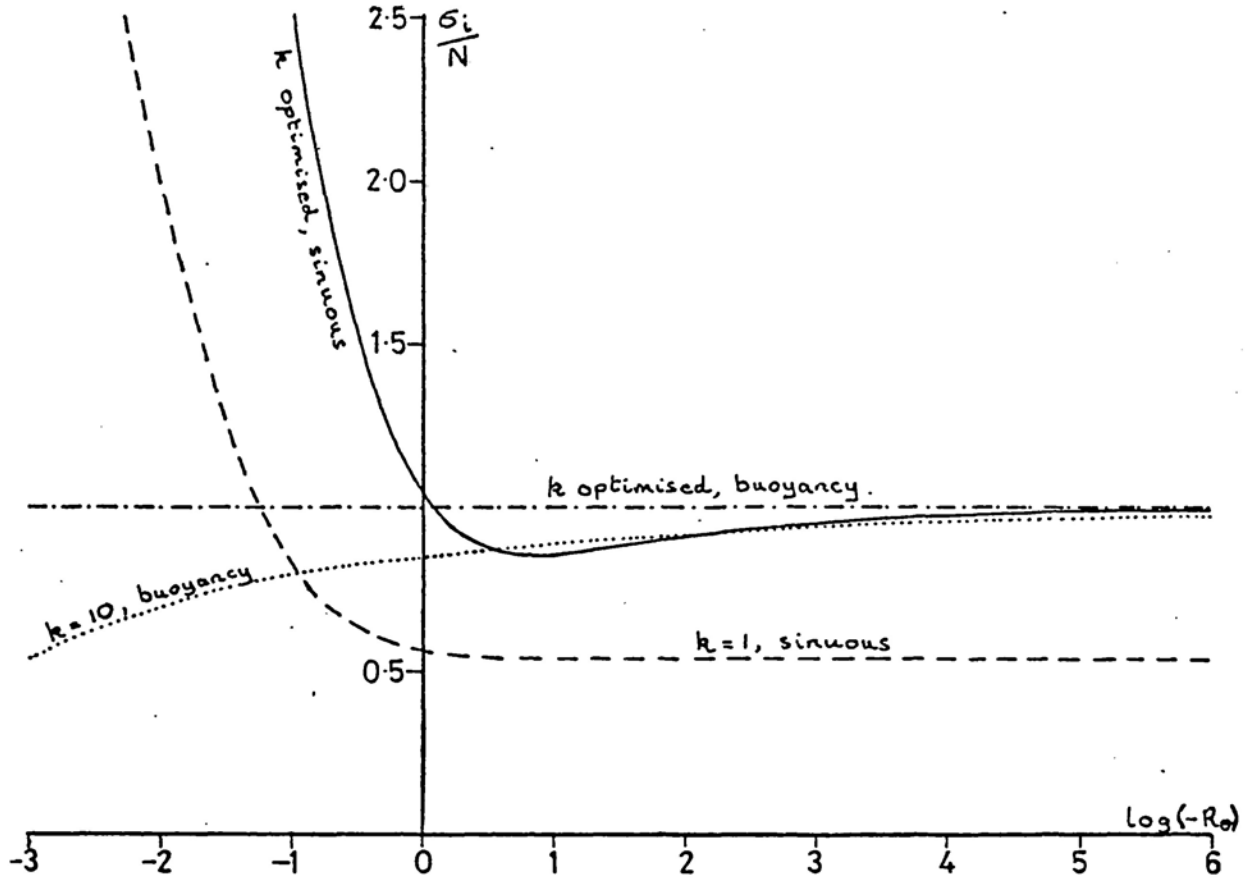


Fig 5.22. Non-dimensional growth rate $\frac{\sigma_i}{N}$ versus $\log_{10}$ of minus modified Richardson number for various modes of the th^2 jet profile.

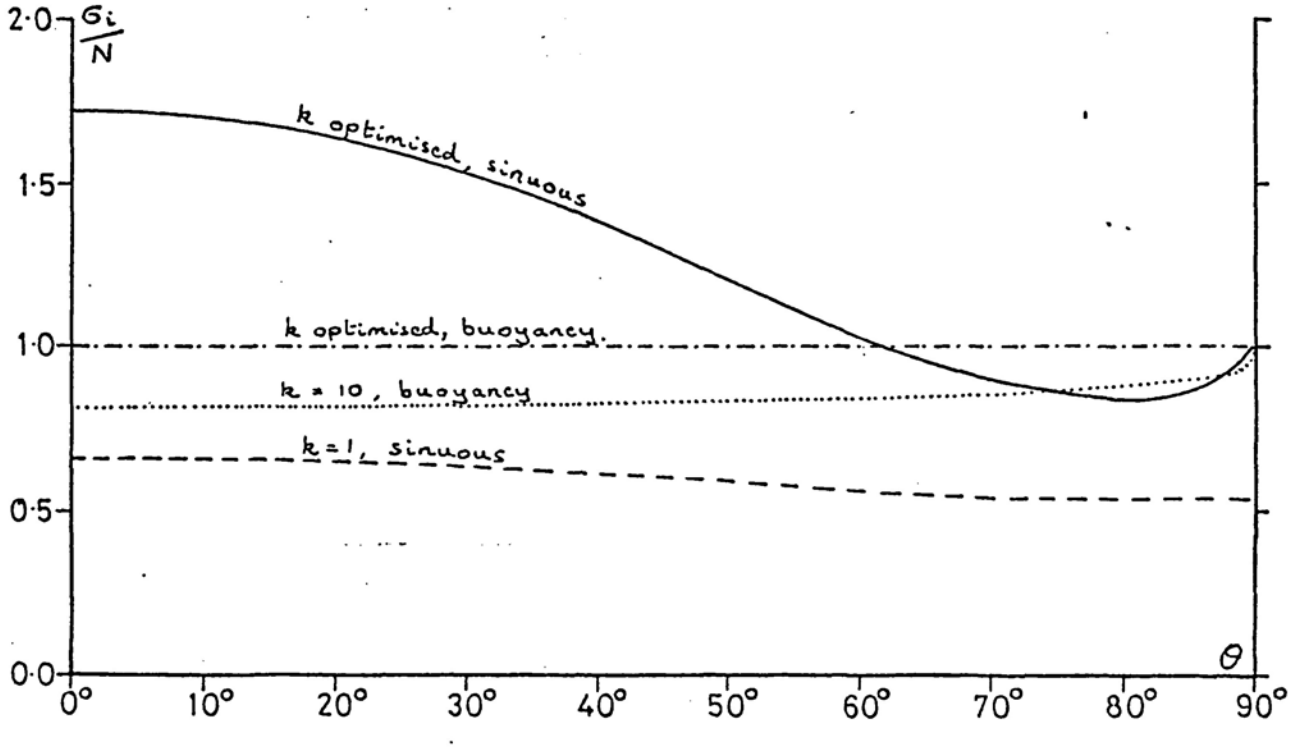


Fig 5.23. Non-dimensional growth rate $\frac{\sigma_i}{N}$ versus direction of propagation for various modes of the th^2 jet profile for Richardson number R = -0·25.

instead of fixing k, it is chosen to give maximum growth rate for the sinuous mode. Now the graph of $\frac{\sigma_i}{N}$ against $\log(-R_\theta)$ (full line in fig 5.22) shows growth rate falling to a minimum for $R_\theta \simeq -7$, before rising to its large Richardson number limit of 1. Thus, for $-R \lesssim 7$, the graph of $\frac{\sigma_i}{N}$ against direction of propagation, shown in fig 5.23 (full line) for $R = -0{\cdot}25$, reveals a minimum growth rate for some θ intermediate between 0° and 90°, suggesting a distinction between buoyancy and shear driven modes, as obtained for the hyperbolic tangent profile in fig 5.11.

In this case of optimised wavenumber, a further complication arises. For $-R_\theta \gtrsim 2$, the greatest growth rate for the sinuous mode is less than the large wavenumber growth rate of the buoyancy modes, for which, irrespective of R_θ, $\frac{\sigma_i}{N}$ is close to 1 (dash-dot line in fig 5.22). Including this in fig 5.23 (dash-dot line), the minimum growth rate for intermediate θ is apparently removed, being replaced by a constant value. However, in the physically more realistic case of a fixed wavenumber k = 10 (which is sufficiently large that it could plausibly be made the wavenumber of maximum amplification with a suitably chosen large Rayleigh number), the effect of including the buoyancy mode (monotonically increasing dotted line in fig 5.23) is merely to make the minimum in the graph of $\frac{\sigma_i}{N}$ against θ less sharp (by cutting off the section of the full line where the dotted line is higher), and the clear distinction between buoyancy and shear driven modes is thus recovered.

This distinction between buoyancy and shear driven modes is also evident if the mean flow forcing is examined (fig 5.24), the notation being that of equations (5.105) and (5.106).

The situation for the sinuous mode (drawn with wavenumber near to that which gives maximum growth rate) is similar to that for the stationary mode in fig 5.12. For small $-R_\theta$ (fig 5.24a), $|\overline{G_2}|$ and $\overline{G_3}$ are nearly equal, and dominate $\overline{G_1}$, indicating that the perturbation is driven by mean flow KE. For large $-R_\theta$ (fig 5.24c), $\overline{G_1}$ (0·029) is numerically larger than $\overline{G_2}$ (-0·021), but both are dominated by $\overline{G_3}$, so that the perturbation gains its KE from PE and loses some to the mean flow. The intermediate case (fig 5.24b) has $\overline{G_2}$ numerically smaller than $\overline{G_3}$, so derives perturbation KE from both PE and mean flow KE; however $\overline{G_1}$ is smaller than $|\overline{G_2}|$ so there is a net loss of KE by the mean flow, in contrast to the intermediate case in fig 5.12c; the difference may be related to the fact that $R_\theta = -1$ in fig 5.12c corresponds to minimum growth rate, whereas least growth rate for the sinuous mode in fig 5.20 corresponds to $-R_\theta$ significantly greater than 20.

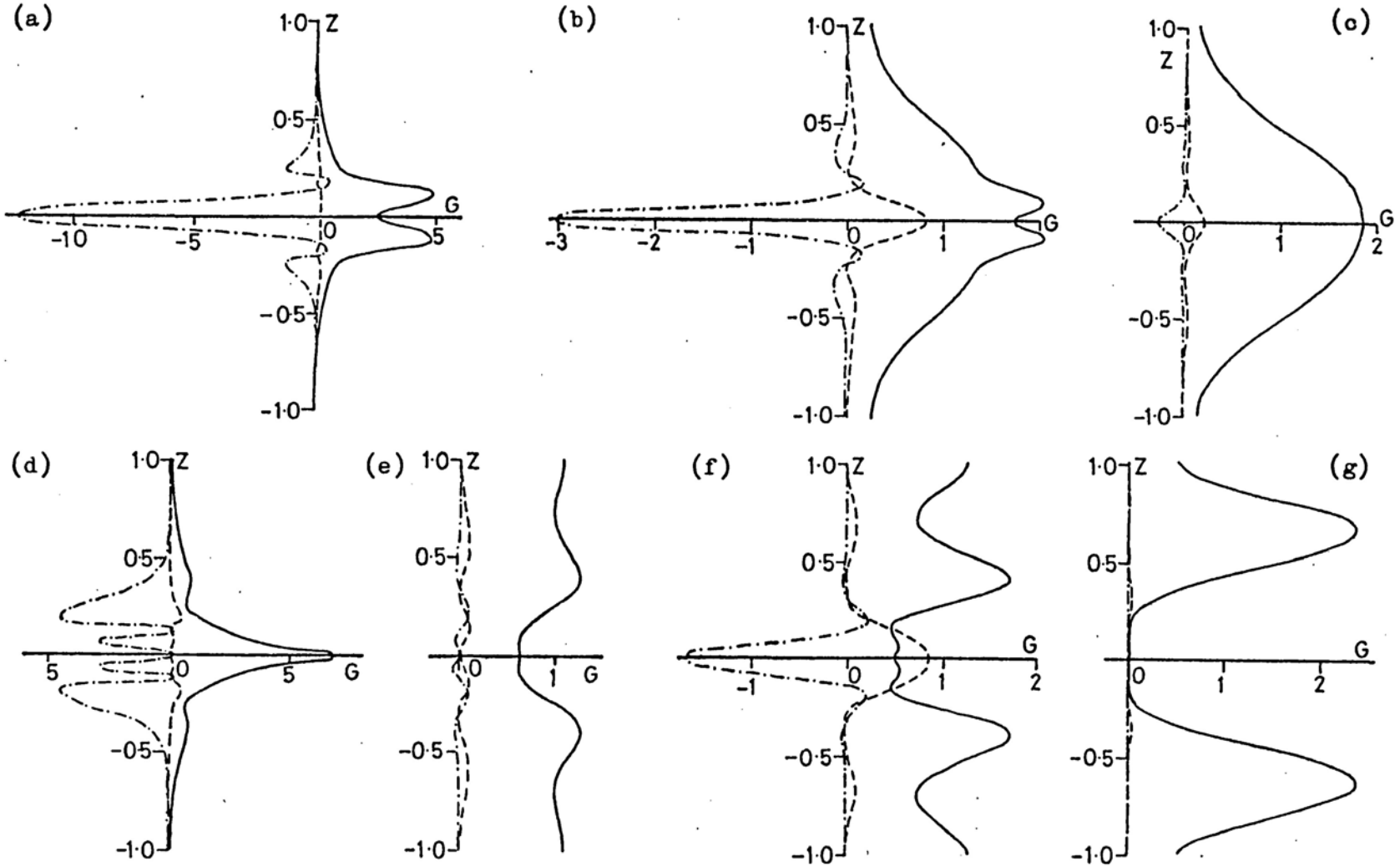


Fig 5.24. Energy transfers for th^2 profile.

- - - - - G_1: Buoyancy term

-·-·-·- G_2: Shear term

——— G_3: Total perturbation KE gain

Fig	(a)	(b)	(c)	(d)	(e)	(f)	(g)
R_θ	-0·25	-20	-240	-0.25	-20	-20	-240
log k	0·6	0·5	0·7	0·4	0·5	0·5	1
mode	S	S	S	V	(i)	(i)	(ii)

The varicose mode for $R_\theta = -0{\cdot}25$ is shown in fig 5.24d. Its net energy transfers are very similar to those of the sinuous mode (fig 5.24a), but being antisymmetric, it has $w = 0$ at the mid level, and hence G_1 and G_2 are both zero here, whereas they attain their maxima at the mid level for the sinuous mode.

The difference between symmetric and antisymmetric modes is also apparent for the first two buoyancy modes, shown for $R_\theta = -20$, $\log k = 0.5$. The symmetric mode (fig 5.24f) has large mid level values for G_1 and G_2, and since $\overline{G_1} = 0{\cdot}174$, $\overline{G_2} = -0{\cdot}102$, this represents a significant loss of KE to the mean flow. For the antisymmetric mode however (fig 5.24e), the vanishing of G_1 and G_2 at the mid level results in much smaller means: $\overline{G_1} = 0{\cdot}049$, $\overline{G_2} = -0{\cdot}001$, and hence a smaller loss of KE to the mean flow; it is thus hardly surprising that the antisymmetric mode has the larger growth rate*. For larger wavenumber, $\log k = 1$, the symmetric mode (fig 5.24g) has retained its symmetry, and not, as might have been expected, merely moved to one boundary. The transfer between eddy and mean flow KE is now negligible so, predictably, the growth rate is very nearly equal to that of the antisymmetric mode (not shown).

Finally returning to the question of modelling SQL's, here, as with the monotonic profiles, there is normally a clear distinction between buoyancy and shear driven modes. The sinuous mode for $-R_\theta \lesssim 20$ (fig 5.24 a,b) is a transverse mode in which buoyancy and shear cooperate, but for it to be the fastest growing mode for large $-R_\theta$ has been seen to be critically dependent on the sharpness of the jet, and on having a suitable large viscosity, and in any case its phase speed is nowhere near the maximum mean flow speed required. In contrast, the plane Poiseuille profile did give fastest growing buoyancy driven modes moving at nearly the maximum mean flow speed, and whilst individually these are dominated by the longitudinal mode, their significance will immediately become apparent as soon as superposition is carried out in the following section.

* A similar argument does not apply to the sinuous and varicose modes since here the perturbations obtain at least part of their energy from mean flow KE, and the extent to which their shape permits utilisation of this energy plays a large part in determination of the growth rates.

5.6 GROUP VELOCITIES.

Having ruled out the possibility of modelling a SQL as a single unstable mode, the question now turns to consideration of what happens when more than one mode is combined. The process of superposition was shown in section 4.1.3 to introduce the group velocity of the most unstable mode, and this will now be considered in order to set the scene for the study of the initial value problem in chapter 6.

5.6.1 Two Dimensions.

If only two-dimensional (i.e. transverse) modes are considered, non-dimensional group speeds (in the sense of section 4.1.2) are given simply by

$$c_g = \frac{\partial(kc_r)}{\partial k} \qquad (5.155)$$

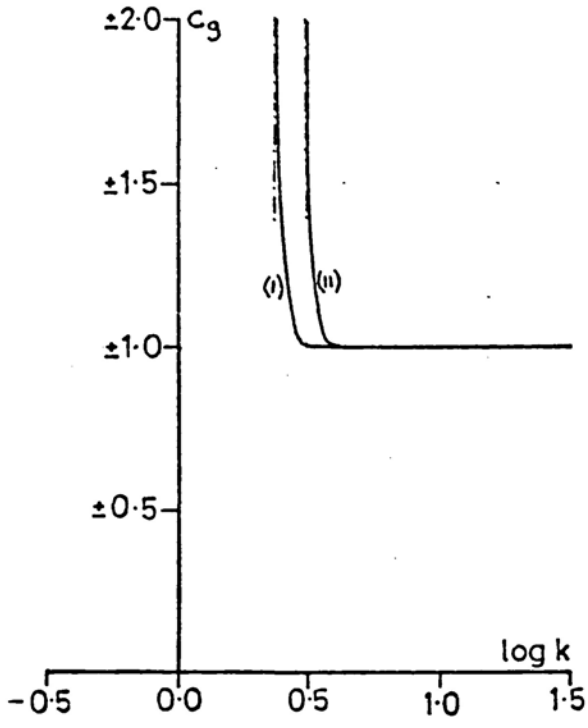
These have been computed in fig 5.25 for $R_\theta = -20$ for the four continuous profiles considered in this chapter, viz (a) $U = Z$ (b) $U = \tanh 2Z / \tanh 2$ (c) $U = 1 - Z^2$ (d) $U = 1 - \tanh^2 5Z / \tanh^2 5$, by making use of the phase speed graphs 5.3c, 5.6d, 5.19e and 5.21e respectively.

For long waves (small k), the group speed for large $-R_\theta$ may be found by differentiating (5.116) to give, for the first mode

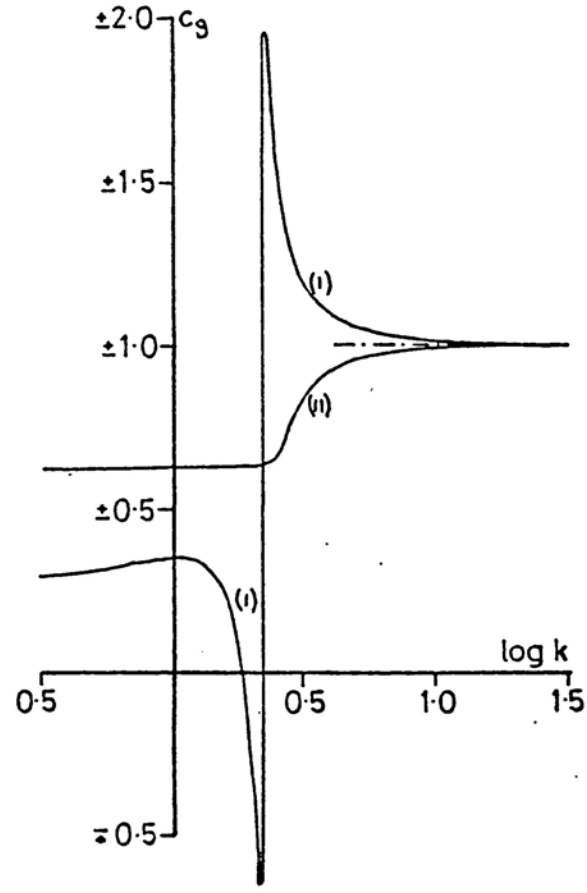
$$c_g = \int_{-1}^{1} \frac{k^2(k^2 + \frac{3}{4}\pi^2)\cos^2\frac{1}{2}\pi\zeta + \frac{1}{4}\pi^2(\frac{1}{4}\pi^2 - k^2)\sin^2\frac{1}{2}\pi\zeta}{(k^2 + \frac{1}{4}\pi^2)^2} U(\zeta)d\zeta \qquad (5.156)$$

For the antisymmetric profiles (a) and (b), this shows that group speed vanishes for long waves, as does phase speed, except for modes (i) and (ii) of the hyperbolic tangent profile (fig 5.25b) for which this expansion is not valid. For the jet profiles (c) and (d), in the long wave limit only the $\sin^2\frac{1}{2}\pi\zeta$ term remains and group speed is the same as phase speed, influenced for this first mode mainly by the mean flow at the boundary. For $k = \frac{1}{2}\pi$ however, only the $\cos^2\frac{1}{2}\pi\zeta$ term remains, and the group speed is the same as the short wave limit of the phase speed, influenced mainly by the mean flow at the velocity maximum. Furthermore, for $k > \frac{1}{2}\pi$, the $\sin^2\frac{1}{2}\pi\zeta$ term changes sign, so group speed will approach even closer to the maximum mean flow speed, and may even exceed it, though in fact for the profiles considered the expansion has broken down before this occurs, and it is therefore necessary to consider the short wave expansion.

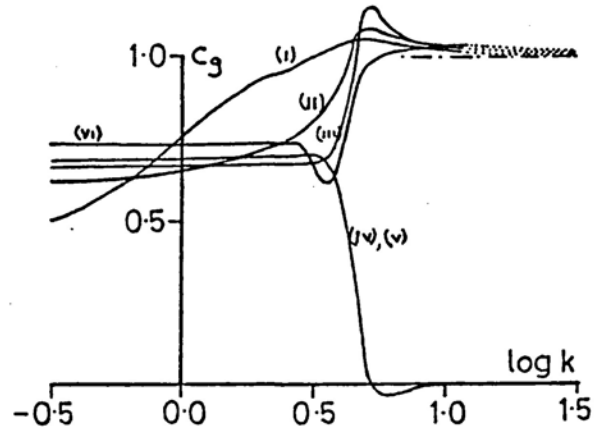
For large wavenumbers, the only modes which remain for the antisymmetric profiles (a) and (b) are ones which tend to the boundaries (i.e. with $c_g \to 1$). Modes tending to the boundaries (in this case with



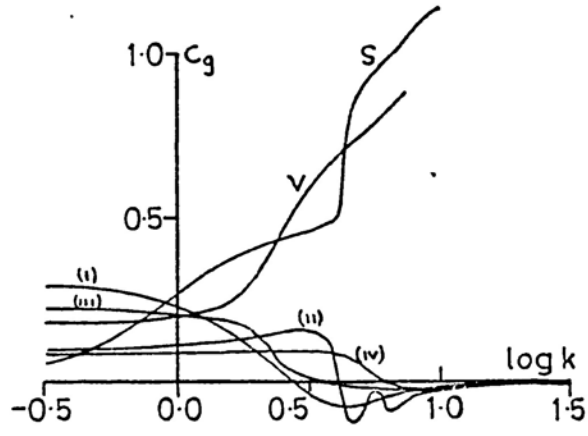
(a) Plane Couette flow



(b) Hyperbolic tangent profile



(c) Plane Poiseuille flow



(d) Th^2 jet profile

Fig 5.25. Various profiles: non-dimensional group speed c_g plotted against $\log_{10}$ of wavenumber k for transverse modes with modified Richardson number $R_\theta = -20$.

$c_g \to 0$) also exist for the jet profiles, namely modes (iv) and (v) of (c), and (i) - (iv) of (d), and it is convenient to consider all these together. Application of (5.155) to (5.137) gives (with $U(1) = 1$)

$$c_g = 1 + O\left(\frac{L'(1)}{L(1)}\frac{(-J)^{2/3}}{k^2}, \frac{U''(1)}{U'(1)}\frac{(-J)^{1/3}}{k^2}\right) \qquad (5.157)$$

where both the $1/k$ terms have disappeared, leaving all k dependence in the remaining error terms, which differ from one profile to another. In (a), c_g tends very rapidly to 1 from above whereas elsewhere it tends more slowly to 1 from above, except in (b) (ii) where it actually approaches the limit from below.

The remaining modes for (c), namely (i), (ii), (iii) and (vi), and possibly also S and V for (d) tend in the short wave limit to the velocity maximum (i.e.have $c_g \to 1$), though there is some uncertainty in (d) as it was difficult to follow the modes sufficiently far. Group speeds are given by application of (5.155) to (5.153) which, with $Z_0 = 0$, gives

$$c_g = 1 + \tfrac{1}{2}(n-\tfrac{1}{2})\frac{[-\frac{1}{2}U''(0)]^{\frac{1}{2}}}{k^{\frac{1}{2}}(-R_0)^{\frac{1}{4}}} \qquad (5.158)$$

Here there is no need to consider the error terms, the group speed for short waves being always greater than the maximum mean flow speed, a result which is borne out by the modes for (c), and at least for S in (d).

Hence in two dimensions, group speeds have been obtained greater than the mean flow speed at any level, both for antisymmetric and jet profiles. There is however an important difference. For antisymmetric profiles, group speeds greater than the maximum mean flow speed occur only for short waves at a boundary, and, reducing the wavenumber always leads to a branch point in the growth rate graph, with greatest growth rate occurring for stationary waves of even smaller wavenumber, which of course have zero group speed. The graphs for the fastest growing modes for a jet profile on the other hand do not branch; rather, growth rate increases steadily with wavenumber, while the waves move closer to the velocity maximum, with group speeds greater than the maximum mean flow speed eventually being attained; moreover, inclusion of a small amount of viscosity will tend to damp out the very shortest waves (for which group speed tends to the maximum mean flow speed) leaving as the fastest growing waves those which also have the largest group speeds.

Thus, whereas for antisymmetric profiles, one would expect an amplifying line of convection to remain stationary, for profiles with a velocity maximum, such a line would be expected to move faster than the

mean flow at any level. This result is highly significant in view of the observational evidence (section 3.2.1) that tropical SQL's only occur when there is a significant middle level jet.

5.6.2 Three Dimensions.

The above analysis does not however explain how such a two-dimensional perturbation might arise, given that apart from the th^2 profile with an unrealistically large shear and viscosity, the fastest growing buoyancy driven mode is always longitudinal. To answer this question, it is necessary to look at the full vector group velocity (4.19) which, when non-dimensionalised and expressed in polar coordinates becomes

$$\underset{\sim}{c}_g = \frac{\partial(kc_r)}{\partial k}\,\underset{\sim}{e}_k + \frac{\partial c_r}{\partial \theta}\,\underset{\sim}{e}_\theta \qquad (5.159)$$

where $\underset{\sim}{e}_k$, $\underset{\sim}{e}_\theta$ are unit vectors in the directions of increasing k, θ respectively.

Greatest growth rate occurs for the longitudinal mode $\theta = \pi/2$, so by section 4.1.3, the instability will be greatest at a point moving with group velocity obtained in the limit $\theta \to \pi/2$. This corresponds to $R_\theta \to -\infty$, so expansion (5.110) is applicable, and gives, on taking the real part

$$c_{\theta r} = \lambda_1(k) + O\left(\frac{k^2}{R_\theta}\right) . \qquad (5.160)$$

By (5.23) and (5.24)

$$c_r = \lambda_1(k)\cos\theta + O\left(\frac{k^2\cos^3\theta}{R}\right) \qquad (5.161)$$

so, by (5.159), ignoring the remainder term (the contribution from which vanishes for $\theta \to \pi/2$)

$$\underset{\sim}{c}_g \simeq \frac{\partial(kc_{\theta r})}{\partial k}\cos\theta\,\underset{\sim}{e}_k - c_{\theta r}\sin\theta\,\underset{\sim}{e}_\theta \qquad (5.162)$$

Setting $\theta = \pi/2$ thus gives for the fastest growing mode

$$\underset{\sim}{c}_g \simeq -c_{\theta r}\,\underset{\sim}{e}_\theta \qquad (5.163)$$

where $\underset{\sim}{e}_\theta$ is in the negative x direction; the group velocity is thus equal to the phase velocity of the transverse mode, or, more precisely, has magnitude equal to the large $-R_\theta$ limit of the phase speed with propagation in the positive direction of the mean flow.

This rather surprising result may be illustrated by a simple physical argument. By (5.161), ignoring the remainder term, phase velocity vectors of modes for fixed k lie on a circle of diameter λ_1 as θ varies (fig 5.26). Drawing the wavefronts of these modes (dashed lines), they are found to intersect at the forward edge of the diameter, so constructive interference of the modes will occur at a point moving

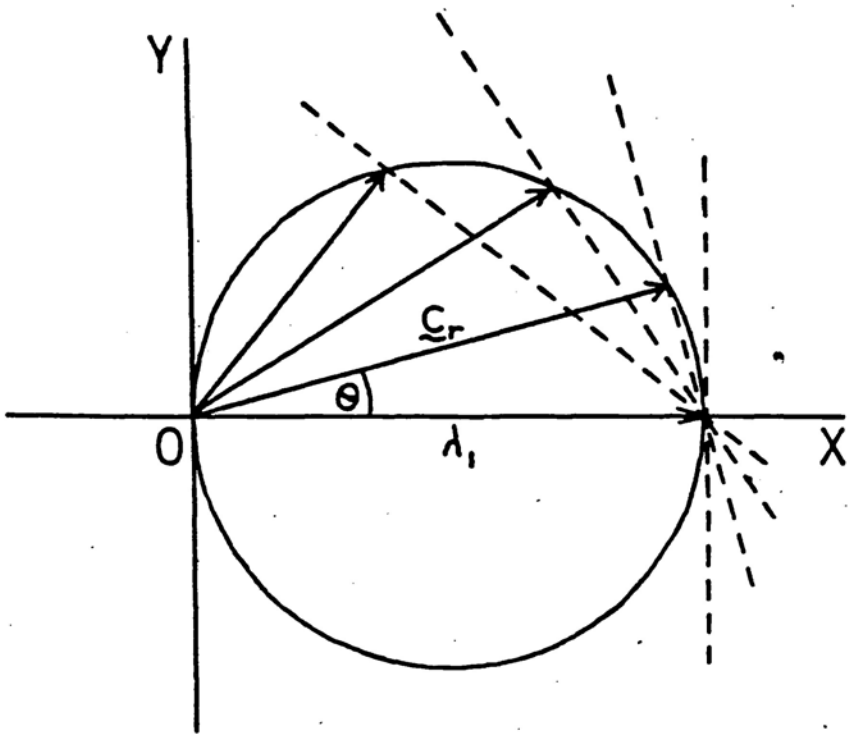


Fig 5.26. Unidirectional jet profile: phase velocity vectors (arrows) and wavefronts (dashed lines) showing constructive interference at the leading edge of the diameter of the circle.

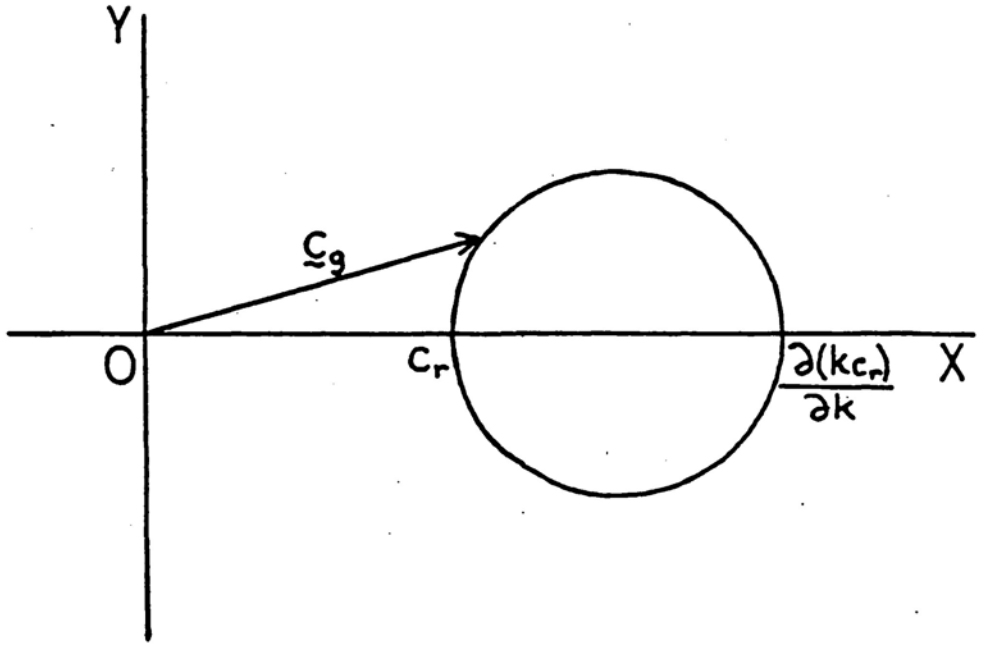


Fig 5.27. Unidirectional jet profile: circle traced out by group velocity vectors.

with the phase velocity of the transverse mode.

For antisymmetric profiles, $c_{\theta r} = 0$ for the fastest growing mode, so a disturbance will merely propagate at the mid level mean flow speed. For jet profiles however, short wave phase speeds are close to the maximum mean flow speed; a patch of convection will thus propagate, though the point of greatest instability cannot move faster than the maximum mean flow speed because of the Miles (1961) steering level constraint on $c_{\theta r}$. The actual speed of propagation depends on which k gives the greatest growth rate, and this in turn depends on the Rayleigh number which is chosen. Thus there is some uncertainty in the result, though a helpful first approximation is obtained in the limit $Ra \to \infty$, when phase and group velocity both approach the maximum mean flow velocity. This approximation, suggested observationally by Fernandez (1981) was in fact the one found in section 3.1.3 to give the best prediction of SQL velocity*.

Examining the jet profile case further, it is found that as θ varies, group velocity vectors, by (5.162), lie on a second circle (fig 5.27), the rear edge of which ($\theta = \pi/2$) moves at speed $c_{\theta r}$, while the forward edge ($\theta = 0$) moves at the two dimensional group speed $\frac{\partial(k c_{\theta r})}{\partial k}$, which can be greater than the maximum mean flow speed. A picture is thus suggested of an amplifying expanding ring of convection, the leading edge of which can in certain cases move faster than the mean flow at any level, and this at last bears a clear resemblance to the observed structure of a tropical SQL. However it should be noted that the growth rate at the forward edge is not as great as that at the rear, so that section 4.1.3, which relates only to the point of greatest amplification rate, can offer no information as to the role of the group velocity at this forward edge. A study of the initial value problem is thus needed to justify the picture suggested above, and this, together with some case studies will form the subject of the final chapter.

* In fact the above analysis only applies to unidirectional profiles, and cannot be extended to the more general profiles to which the prediction rule was applied. Caution is thus advocated when there is a significant transverse wind component.

CHAPTER 6. GROWTH OF AN INITIALLY LOCALISED PERTURBATION.

6.1 INTRODUCTION.

6.1.1 Mathematical Analysis.

In examining asymptotic behaviour of an initial perturbation, it is convenient to make use of polar coordinates. Thus, with the non-dimensionalisation of section 5.1.1, the Fourier integral (4.44) becomes

$$\omega = \int_0^\infty \int_0^{2\pi} \tilde{f}(k,\theta)\, \tilde{\omega}_{k\theta}(z)\, \exp\left\{ ik\left(X\cos\theta + Y\sin\theta\right) - i\frac{\sigma}{S}T\right\} k\, d\theta\, dk \qquad (6.1)$$

where non-dimensional time T is given by (5.12). In order to ensure that maximum growth rate does not occur in the limit $k \to \infty$, it is necessary to include viscosity, parameterised as in (4.33).

Benjamin (1961), evaluating an integral similar to (6.1) for perturbations of an unstratified flow, expanded about the fastest growing mode, which was transverse. Here however, greatest instability occurs for the first longitudinal mode (n = 1 in (5.109)), so expansions (5.110) and (5.111) will be applied, giving

$$\frac{\sigma_i}{S} = (-R)^{\frac{1}{2}}\left\{ i\sigma_0(k) + \frac{k}{(-R)^{\frac{1}{2}}} c_0(k)\cos\theta - i\frac{k^2}{(-R)}\lambda_2(k)\cos^2\theta + \cdots \right\} \qquad (6.2)$$

and

$$\tilde{\omega}_{k\theta}(z) = \cos\tfrac{1}{2}\pi z - i\frac{k}{(-R)^{\frac{1}{2}}}\omega_1(k,z)\cos\theta - \frac{k^2}{(-R)}\omega_2(k,z)\cos^2\theta \cdots \qquad (6.3)$$

In this, $$\sigma_0(k) = \lambda_0(k) - \frac{4k^2}{Ra^{\frac{1}{2}}} \qquad (6.4)$$

and $$c_0(k) \triangleq \lambda_1(k) \qquad (6.5)$$

are the first approximations to the growth rate and phase speed respectively, while R is the Richardson number for the flow as a whole which, for the expansion to be valid must satisfy

$$\frac{k}{(-R)^{\frac{1}{2}}}\cos\theta \ll 1 \qquad (6.6)$$

Remembering from section 5.6.2 that the point of maximum instability moves with the phase velocity (6.5) of the fastest growing longitudinal mode, it is convenient to set

$$\frac{X}{T} - c_0(k) = U\cos\phi \qquad (6.7)$$

$$\frac{Y}{T} = U\sin\phi \qquad (6.8)$$

where U (which should not be confused with the non-dimensional mean flow velocity) is a measure of the distance of (X,Y) from the point moving with speed c_0, and is given by

$$U = \left\{ \left[\frac{X}{T} - c_0(k)\right]^2 + \left[\frac{Y}{T}\right]^2 \right\}^{\frac{1}{2}} \qquad (6.9)$$

Thus (6.1) becomes

$$w = \int_0^\infty \int_0^{2\pi} \tilde{f}(k,\theta)\left[\cos\tfrac{1}{2}\pi Z - i\frac{k}{(-R)^{\frac{1}{2}}} w_1(k,Z)\cos\theta \ldots\right] \exp\left\{\left[(-R)^{\frac{1}{2}}\sigma_0(k) + ikU\cos(\theta-\phi) - \frac{k^2\lambda_2(k)}{(-R)^{\frac{1}{2}}}\cos^2\theta\right]T\right\} k\,d\theta\,dk \tag{6.10}$$

where use has been made of (6.2) and (6.3). The initial perturbation will be assumed to have no θ variation, so that $\tilde{f}(k,\theta) \equiv \hat{f}(k)$, and integration will first be carried out with respect to θ , so consider

$$I = \int_0^{2\pi} \left[\cos\tfrac{1}{2}\pi Z - i\frac{k}{(-R)^{\frac{1}{2}}} w_1(k,Z)\cos\theta \ldots\right] \exp\left\{\left[ikU\cos(\theta-\phi) - \frac{k^2\lambda_2(k)}{(-R)^{\frac{1}{2}}}\cos^2\theta\right]T\right\} d\theta \tag{6.11}$$

By (6.6), a first approximation to the exponent is

$$q = ikU\cos(\theta-\phi) \tag{6.12}$$

the saddle points $\frac{dq}{d\theta} = 0$ being given by

$$\theta = \phi + m\pi \qquad , \ m \text{ an integer.} \tag{6.13}$$

Here a complication arises: the greatest instability is for the longitudinal mode $\theta = \pi/2$ and in the neighbourhood of this mode, (6.6) is readily satisfied for arbitrary k, R; however the location of the saddle point means that asymptotic behaviour for a given ϕ depends on modes in the neighbourhood of $\theta = \phi$, so that, except near $\phi = \pm\pi/2$, in order to satisfy (6.6) it is necessary that

$$\frac{k}{(-R)^{\frac{1}{2}}} \ll 1 \tag{6.14}$$

which is a large Richardson number long wave condition.

With this condition, write

$$\theta = \theta_r + i\theta_i \tag{6.15}$$

so that (6.12) becomes

$$q = kU\left[\sin(\theta_r - \phi)\,\mathrm{sh}\,\theta_i + i\cos(\theta_r - \phi)\,\mathrm{ch}\,\theta_i\right] \tag{6.16}$$

A contour map of Re(q) in the complex θ plane is shown in fig 6.1, the 'high ground' being hatched and the integration path of minimum height being indicated. In asymptotically evaluating the integral (6.11) the contributions from the end points of the path cancel, so only the saddle points need be considered. Integrating through these at $\pi/4$ to the axes in order to follow the paths of steepest descent thus gives

$$I \sim 2\,\mathrm{Re}\left[\left(\frac{2\pi}{kU}\right)^{\frac{1}{2}} \cos\tfrac{1}{2}\pi Z \exp\left\{\left[ikU - \frac{k^2\lambda_2(k)}{(-R)^{\frac{1}{2}}}\cos^2\phi\right]T - i\pi/4\right\}\right] \tag{6.17}$$

where it may be shown that, provided (6.14) holds, the correction to the saddle points made by the inclusion of the term $\frac{k^2\lambda_2(k)}{(-R)^{\frac{1}{2}}}\cos^2\theta$ in

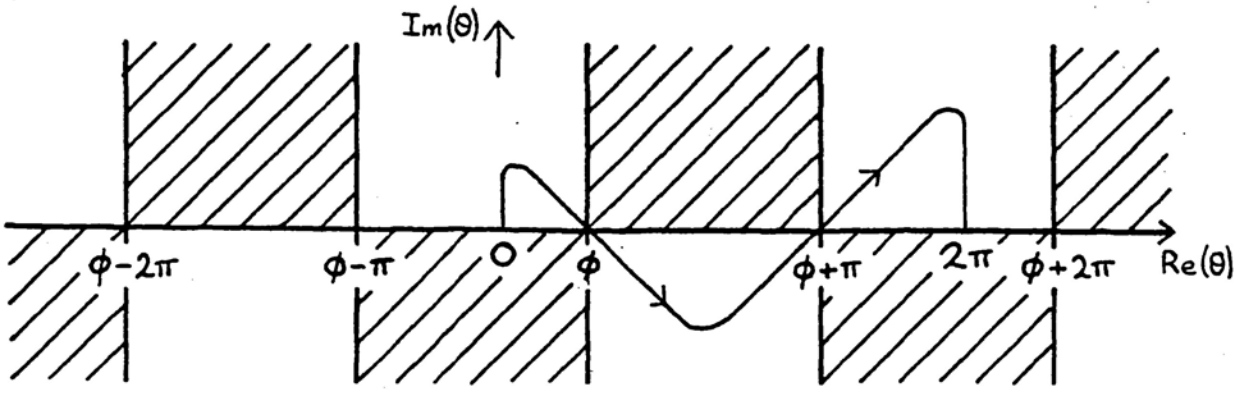


Fig 6.1. Contour map of Re(q), as in (6.16), in the complex θ plane. Areas where $Re(q) > 0$ are hatched, and the integration path of minimum height is drawn.

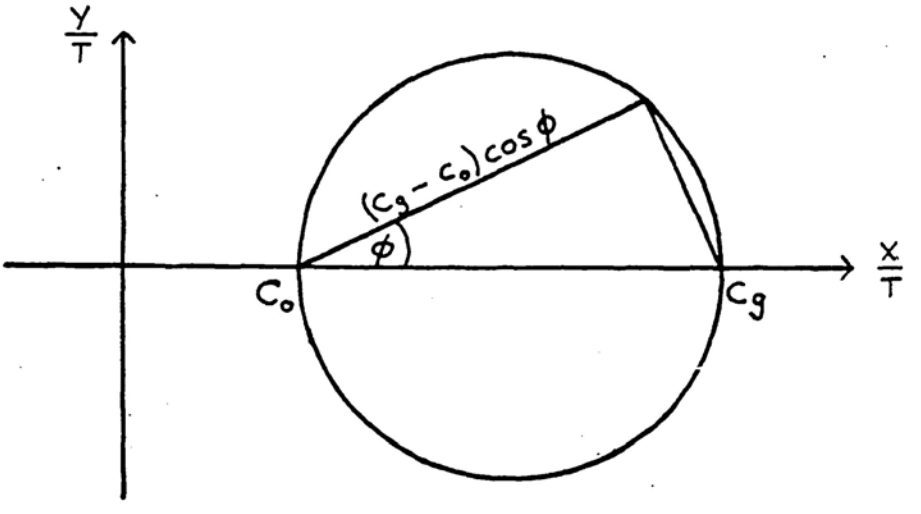


Fig 6.2. Circle traced out by points of maximum instability as ϕ varies.

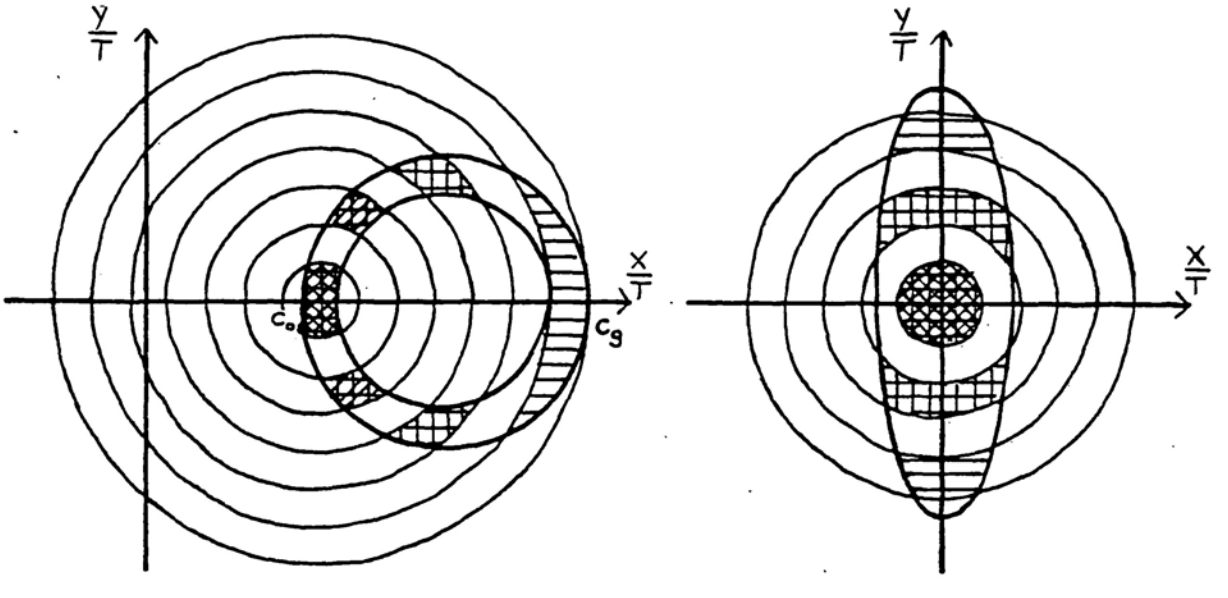


Fig 6.3. Asymptotic form of perturbation in case (a) $c_o \neq c_g$ (b) $c_o = c_g$ (taken to be both zero). Concentric circles are phase lines, and hatching (heavier for larger amplitude) denotes positive w values.

the exponent of (6.11) does not affect the answer to the degree of approximation used.

Hence substituting (6.17) in (6.10),

$$w \sim 2\,\mathrm{Re}\int_0^\infty \tilde{w}(k)\left(\frac{2\pi}{kU}\right)^{\frac{1}{2}}\cos\tfrac{1}{2}\pi Z\ \exp\left\{\left[(-R)^{\frac{1}{2}}\sigma_0(k)+ikU-\frac{k^2\lambda_2(k)}{(-R)^{\frac{1}{2}}}\cos^2\phi\right]T-i\frac{\pi}{4}\right\}k\,dk \tag{6.18}$$

Assuming (6.14) to hold, it is necessary to retain the first two terms in the exponential in determining the saddle point. A first approximation is thus k_0, where

$$\sigma_0'(k_0) = 0 \tag{6.19}$$

and a second approximation is

$$k_1 = k_0 - i\,\frac{\left[\frac{\partial}{\partial k}(kU)\right]_{k_0}}{\sigma_0''(k_0)\,(-R)^{\frac{1}{2}}} \tag{6.20}$$

In this, by (6.9)

$$\left[\frac{\partial}{\partial k}(kU)\right]_{k_0} = -\frac{\left[\frac{X}{T}-c_0(k_0)\right]\left[\frac{X}{T}-c_g(k_0)\right]+\left[\frac{Y}{T}\right]^2}{\left\{\left[\frac{X}{T}-c_0(k_0)\right]^2+\left[\frac{Y}{T}\right]^2\right\}^{\frac{1}{2}}}$$

$$= -U + (c_g - c_0)\cos\phi \tag{6.21}$$

where $$c_g = \frac{\partial(kc_0)}{\partial k} \tag{6.22}$$

Applying the method of steepest descent to (6.18) and making use of (6.19) - (6.22) thus finally gives

$$w \sim \frac{4\pi\tilde{f}(k_0)\cos\tfrac{1}{2}\pi Z}{\left[U\sigma_0''(k_0)T\right]^{\frac{1}{2}}}\cos\left(k_0U-\tfrac{\pi}{4}\right)\exp\left\{\left[(-R)^{\frac{1}{2}}\sigma_0(k_0)+\frac{\left[-U+(c_g-c_0)\cos\phi\right]^2}{2(-R)^{\frac{1}{2}}\sigma_0''(k_0)}-\frac{k_0\lambda_2(k_0)}{(-R)^{\frac{1}{2}}}\cos^2\phi\right]T\right\} \tag{6.23}$$

where U and ϕ are evaluated at k_0, the result being valid under the condition (6.14).

The cos term, by (6.9), shows that the phase lines are circles centred on the point moving with speed c_0. Assuming $c_g \neq c_0$, the exponential term is greatest for fixed ϕ when

$$U = (c_g - c_0)\cos\phi \tag{6.24}$$

(remembering $\sigma_0''(k_0) < 0$). So, bearing in mind that (U,ϕ) are measured from the point moving with speed c_0, it follows that, as ϕ varies, the points of maximum instability lie on an expanding circle with points moving at speeds c_0 and c_g as opposite ends of the diameter (fig 6.2), thus confirming the result suggested in section 5.6.2. Drawing in phase lines also, the circle is split up, with the rear divided into cells,

but with an unbroken arc at the front (fig 6.3a). Though the cells have the larger growth rate, the arc is also amplifying; it will be the first part of the ring of convection to arrive at an observer, and may even move faster than the mean flow at any level. This picture bears a strong resemblance to a tropical SQL with its arc-shaped leading edge (roll cloud) arriving first, followed by distinct cumulonimbus cells.

If $c_s = c_o$ (as for antisymmetric profiles), the condition (6.24) for maximising the exponential term reduces to $U = 0$: i.e. the previous circle of convection has collapsed to a point moving with speed c_o. Moving away from this point, the lines of equal amplification are ellipses elongated in the Y direction so, with the phase lines, the picture which now emerges is fig 6.3b. The arc-shaped leading edge has disappeared, but the line of cells transverse to the mean flow, moving at some mid level mean flow speed now has an obvious resemblance to the middle latitude SQL.

6.1.2 Numerical Method.

In presenting numerical results, it was found convenient, except for atmospheric profiles, to subtract off the average mean flow velocity, so that the non-dimensional velocities have $\overline{U} = \overline{V} = 0$. Then, if the maximum non-dimensional velocity component in the X direction is U_m, definition (5.12) for non-dimensional time was replaced by

$$T = \frac{St}{U_m} \tag{6.25}$$

The effect of these adjustments is to simplify interpretation of speeds of perturbations in the results. A point moving at the average mean flow speed will now remain at $X = 0$, while a point moving at the maximum mean flow speed will be at $X = T$ at non-dimensional time T. These conditions are in fact already satisfied for the non-dimensional antisymmetric profiles (for which $U_m = 1$), so the adjustments are only necessary for the jet profiles.

As attention will no longer be restricted to unidirectional profiles, it is not now possible to write all the equations in terms of the non-dimensional mean flow X component U; instead, use must be made of the component W along the propagation vector, given by (5.14). Equations (4.12) and (4.13) thus yield on non-dimensionalisation

$$\frac{1}{U_m k}\frac{\partial}{\partial T}\left(\frac{\partial^2}{\partial Z^2} - k^2 - \tfrac{1}{4}r^2\right)\tilde{\omega} = -\left\{iW(Z) + 4k\left(\frac{-R}{Ra}\right)^{\frac{1}{2}}\right\}\left(\frac{\partial^2}{\partial Z^2} - k^2 - \tfrac{1}{4}r^2\right)\tilde{\omega} + i\left(\frac{dW}{dZ}r + \frac{d^2W}{dZ^2}\right)\tilde{\omega} + iRL(Z)\tilde{q} \tag{6.26}$$

$$\frac{1}{U_m k}\frac{\partial \tilde{q}}{\partial T} = -\left\{iW(Z) + 4k\left(\frac{-R}{Ra}\right)^{\frac{1}{2}}\right\}\tilde{q} - i\tilde{\omega} \tag{6.27}$$

where $\tilde{q} = -ik\tilde{S}\tilde{h}$ as defined in (5.44) for the matrix methods (section 5.1.3a). Proceeding as in the Galerkin method, expand

$$\begin{Bmatrix} \tilde{w} \\ \tilde{q} \end{Bmatrix} = \sum_{n=1}^{M} \begin{Bmatrix} w_n \\ q_n \end{Bmatrix} \sin \tfrac{1}{2}n\pi(z+1) \tag{6.28}$$

Substituting in (6.26) and (6.27), multiplying by $\sin\frac{1}{2}m\pi(z+1)$ and integrating from -1 to 1 then gives

$$\begin{aligned} &\frac{1}{U_m k}\frac{\partial}{\partial T}(k^2 + \tfrac{1}{4}r^2 + \tfrac{1}{4}m^2\pi^2)w_m \\ &= -\tfrac{1}{2}i\sum_{n=1}^{M}\left\{\left[k^2+\tfrac{1}{4}r^2+\tfrac{1}{4}m(2n-m)\pi^2\right]C_{|n-m|} - \left[k^2+\tfrac{1}{4}r^2-\tfrac{1}{4}m(2n+m)\pi^2\right]C_{n+m} + \tfrac{1}{2}\pi r\left[|n-m|S_{|n-m|} - (n+m)S_{n+m}\right]\right\}w_n \\ &\quad - 4k\left(\frac{-R}{Ra}\right)^{\frac{1}{2}}(k^2+\tfrac{1}{4}r^2+\tfrac{1}{4}m^2\pi^2)w_m - \tfrac{1}{2}iR\sum_{n=1}^{M}\left\{H_{|n-m|} - H_{n+m}\right\}q_n \end{aligned} \tag{6.29}$$

$$\frac{1}{U_m k}\frac{\partial}{\partial T}q_m = -\tfrac{1}{2}i\sum_{n=1}^{M}\left\{C_{|n-m|} - C_{n+m}\right\}q_n - 4k\left(\frac{-R}{Ra}\right)^{\frac{1}{2}}q_m - i\omega_m \tag{6.30}$$

$$m = 1, 2, \ldots M,$$

where C_n and S_n are the Fourier cosine and sine coefficients of $W(Z)$, and H_n are the cosine coefficients of $L(Z)$, given respectively by

$$W(Z) = \sum_{n=0}^{M} C_n \cos\tfrac{1}{2}n\pi(Z+1) = \sum_{n=1}^{M} S_n \sin\tfrac{1}{2}n\pi(Z+1) \tag{6.31}$$

$$L(Z) = \sum_{n=0}^{M} H_n \cos\tfrac{1}{2}n\pi(Z+1) \tag{6.32}$$

Equations (6.29) and (6.30) may be compared with the Galerkin equations (5.48) and (5.49), in which the terms involving r and Ra are omitted and the time dependence is contained in the eigenvalue c_0. They form a set of first order linear ordinary differential equations of the form

$$\frac{d}{dt}\underline{\Psi} = \underline{\underline{A}}\,\underline{\Psi} \tag{6.33}$$

where $\underline{\Psi}$ is the vector $(\omega_1, \ldots, \omega_M, q_1, \ldots, q_M)$, and $\underline{\underline{A}}$ is a matrix which is independent of time. The solution may thus be found, as in Froberg (1969) from

$$\underline{\Psi}(T + \Delta T) = \underline{\underline{C}}\,\underline{\Psi}(T) \tag{6.34}$$

where

$$\underline{\underline{C}} = e^{\underline{\underline{A}}\Delta t} = \underline{\underline{I}} + \underline{\underline{A}}\Delta t + \tfrac{1}{2}(\underline{\underline{A}}\Delta t)^2 + \tfrac{1}{6}(\underline{\underline{A}}\Delta t)^3 + \ldots \tag{6.35}$$

Thus, for a pre-determined time step Δt, the matrix $\underline{\underline{C}}$ may be evaluated initially, and then each time step merely consists of multiplying the vector $\underline{\Psi}$ by the matrix $\underline{\underline{C}}$.

Now $\tilde{\omega}$ and $\tilde{q}$ are Fourier transforms, and may be evaluated as outlined above for any given k and θ (the k dependence is evident in equations (6.26) and (6.27), while the θ dependence arises from the

θ dependence of $W = U\cos\theta + V\sin\theta$), The actual vertical velocity is then given by the double Fourier transform

$$w = \int_0^\infty \int_0^{2\pi} \sum_{n=1}^{M} w_n(k,\theta)\sin\tfrac{1}{2}n\pi(z+1)\exp\left\{ik(x\cos\theta + y\sin\theta)\right\} k\,d\theta\,dk \tag{6.36}$$

with a similar expression holding for q.

The horizontal velocity components may be found by making use of (5.100) which, when non-dimensionalised becomes

$$(\tilde{\delta u}, \tilde{\delta v}) = (-\sin\theta, \cos\theta)\frac{i}{k}\frac{dQ}{dz}\tilde{q} + (\cos\theta, \sin\theta)\frac{i}{k}\left(\frac{\partial \tilde{w}}{\partial z} - \tfrac{1}{2}r\tilde{w}\right) \tag{6.37}$$

where Q is the transverse mean flow component given by (5.15). The last term on the right, though straightforward, does mean that both cosine and sine terms are required in the Fourier expansion of $(\tilde{\delta u}, \tilde{\delta v})$. For the first term, noting that $\tilde{q}$ is given by a Fourier sine series, it was found preferable to arrange that the contribution to $(\tilde{\delta u}, \tilde{\delta v})$ is also given by a sine series, which requires expanding Q in a sine series

$$Q(z) = \sum_{n=1}^{M} Q_n \sin\tfrac{1}{2}n\pi(z+1) \tag{6.38}$$

Hence, multiplying (6.37) in turn by $\sin\frac{1}{2}m\pi(z+1)$ and $\cos\frac{1}{2}m\pi(z+1)$ and integrating from -1 to 1 finally gives $(\tilde{\delta u}, \tilde{\delta v})$ in the form

$$(\tilde{\delta u}, \tilde{\delta v}) = \sum_{n=0}^{M} \left\{a_n \sin\tfrac{1}{2}n\pi(z+1) + b_n \cos\tfrac{1}{2}n\pi(z+1)\right\} \tag{6.39}$$

where $$a_m = (-\sin\theta, \cos\theta)\, i\frac{\pi}{4k}\sum_{n=1}^{M}\left\{|n-m|Q_{|n-m|} - (n+m)Q_{n+m}\right\}q_n - (\cos\theta, \sin\theta)\, i\frac{r}{2k}w_m \tag{6.40}$$

and $$b_m = (\cos\theta, \sin\theta)\, i\frac{m\pi}{2k}w_m \tag{6.41}$$

An integral similar to (6.36) may now be used to find δu and δv.

In the examples which will be presented in this chapter (other than two dimensional cases), the initial conditions were chosen to correspond to the circularly symmetric updraught

$$w \propto \exp\left\{-\tfrac{1}{2}k_0^2(x^2+y^2)\right\}\sin\tfrac{1}{2}\pi(z+1)$$
$$q = 0 \tag{6.42}$$

with k_0 taking the value 3 except where otherwise stated. The initial coefficients w_n and q_n were thus

$$w_1 \propto \exp\left\{-\tfrac{1}{2}\frac{k^2}{k_0^2}\right\}$$
$$w_n = 0 \qquad n > 1 \tag{6.43}$$
$$q_n = 0 \qquad \text{all } n$$

These clearly satisfy $w(\theta+\pi) = w(\theta)$ and so, since by (5.14), $W(\theta+\pi) = -W(\theta)$,

it can be seen from (6.26) and (6.27) that subsequent development is such that $w(\theta+\pi)$ is always the complex conjugate of $w(\theta)$, and (6.36) may be reduced to

$$w = 2\,\mathrm{Im}\int_0^\infty\int_0^\pi \sum_{n=1}^{M} w_n(k,\theta)\sin\tfrac{1}{2}n\pi(z+1)\exp\{ik(X\cos\theta+Y\sin\theta)\}\,k\,d\theta\,dk \tag{6.44}$$

corresponding simplification being possible for q, δu and δv.

In the results with idealised profiles, Richardson number R was usually taken to be -1, and the variation of mean density with height was neglected. (r = 0 in (5.2)); in the atmospheric simulations, R was determined by the sounding, while r was taken to be 0·75, corresponding to a density scale height H_o two thirds of the depth z_2-z_1 of the convective layer. For the Rayleigh number (5.9), the values $B \simeq -10^{-5}\,m^{-1}$, $z_2-z_1 \simeq 10$ km, $K \simeq 3\times10^3\,m^2s^{-1}$ were assumed, giving $Ra = 10^5$, this being the smallest realistic value (corresponding to eddies with mixing length of order 1 km, speed 3 m/s). Referring to (4.35), it can be seen that, for the longitudinal mode, even this smallest realistic Rayleigh number of 10^5 gives wavenumber k_m of maximum amplification to be as large as 3, which, by (5.3) gives a spacing $\frac{2\pi}{\gamma}$ of adjacent cells approximately equal to the depth of the convective layer. Recent observations, e.g. those of Houze (1977) suggest a rather greater spacing, a discrepancy which may be due to the exclusion of nonlinear effects from the model.

With Ra = 10^5, it is to be expected from (4.34) that short waves will be damped for wavenumber k greater than a critical value $k_c \simeq 9$. In integrating with respect to k in (6.44), it is only therefore necessary to consider a finite range of k values, and Simpson's rule may be applied; since the asymptotic behaviour is determined by values of k close to 3, greater resolution was used in this neighbourhood, so that the formula which was adopted was

$$\int_0^\infty f(k)\,dk \simeq \tfrac{1}{6}\{f(0)+4f(0{\cdot}5)+2f(1)+4f(1{\cdot}5)+1{\cdot}5f(2)+2f(2{\cdot}25)+f(2{\cdot}5)+2f(2{\cdot}75)$$
$$+f(3)+2f(3{\cdot}25)+f(3{\cdot}5)+2f(3{\cdot}75)+1{\cdot}5f(4)+4f(4{\cdot}5)+3f(5)+8f(6)+2f(7)\} \tag{6.45}$$

For the θ integration, the integrand is periodic, so in this case a 16 interval formula with equal weights was used

$$\int_0^\pi g(\theta)\,d\theta \simeq \frac{\pi}{16}\sum_{j=1}^{16} g\left(\frac{j\pi}{16}\right) \tag{6.46}$$

In contrast to the large number of points which had to be taken here, it was only found necessary to sum to M = 5 in the Fourier series (6.28) and (6.39).

The results which will be presented are all of perturbation quantities. Since the model is linear, the amplitudes are arbitrary, so the results have in all cases been scaled so that the initial vertical velocity is unity. Because of the exponential growth in time, subsequent values had to be divided by some suitable scale factor before plotting contours of results; the scale factor was usually chosen as the value which gave the clearest contours, rather than basing it, say on the maximum vertical velocity, so diagrams in which the scale factor was taken to be small will have a relatively large number of contours. In interpreting the results, it should be remembered that non-linear terms will ultimately become important, and the model will break down; however, the time at which this breakdown occurs will depend on the actual value of the initial amplitudes; this question will be taken up in the final section.

The coordinates in the plotted results are all non-dimensional and given by (5.1), with time T as in (6.25). Two types of cross-section are shown

(a) Horizontal sections, usually in the plane Z = 0. These show contours of vertical velocity plotted at values equal to $\frac{1}{4}$, 1, 2 and 4 times the scale factor, values in excess of the scale factor being hatched. Thicker lines are used for positive values, thinner lines for negative values.

(b) Vertical sections in the X-Z and Y-Z planes, through the plane of symmetry if one exists. Contours here show potential temperature excess, plotting at $\frac{1}{4}$, 1 (thicker line), 2 and 4 times the scale factor. Arrows show perturbation velocities in the plane of the section, scaled so that the maximum vertical velocity is equal to the grid length; actual velocities can be deduced by referring to the horizontal section.

6.2 CASE STUDIES WITH PLANE POISEUILLE FLOW.

6.2.1 Introduction.

The adjustments at the beginning of section 6.1.2 required to cause perturbations moving at the average and maximum mean flow speeds to be at X = 0, T respectively at time T give the non-dimensional plane Poiseuille flow to be

$$U = \tfrac{1}{3} - Z^2 \qquad (6.47)$$

with

$$T = 3\,St \qquad (6.48)$$

As there is no Y-Z plane of symmetry, vertical sections, except at time 0, are usually taken through the centre of the downdraught immediately to the right of the initial updraught.

6.2.2 Two-Dimensional Study.

As very few two-dimensional studies were made, they were carried out merely by using a two-dimensional initiallisation in the three-dimensional model. Ideally this would have taken the form

$$w \propto \exp\{-\tfrac{1}{2}kX^2\} \sin \tfrac{1}{2}\pi(Z+1) \qquad (6.49)$$

but a problem arose: in (6.37) the transformed horizontal velocity reduces to

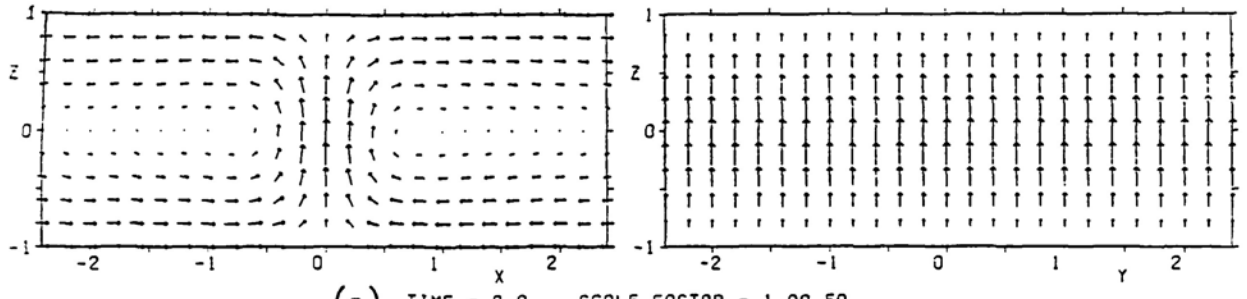
$$\delta\tilde{u} = \frac{i}{k}\frac{\partial \tilde{w}}{\partial Z} \qquad (6.50)$$

and here, unlike in three dimensions, the factor k^{-1} renders the integral for δu singular. To overcome this, w_1 in (6.43) was set equal to zero for $k = 0$, the effect of this being to impose a small compensating subsidence away from the initial updraught.

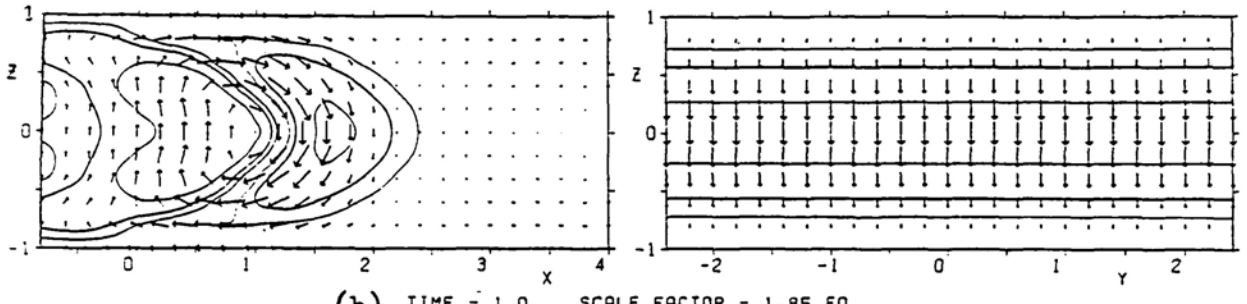
Results are shown in fig 6.4, the left-hand side giving vertical sections in the plane $Y = 0$ (while the right-hand side gives sections in the X plane in which the largest vertical velocity occurs). At time 0, no contours for potential temperature excess appear since the initial perturbation was of vertical velocity only; the compensating subsidence can be seen on careful examination. At other times, new updraughts and downdraughts are alternately generated to the right of the existing cells and rapidly grow, while to the left (bearing in mind the scale factors), the initial updraught continues to grow, though less rapidly. At each time, the greatest vertical velocity is found for X slightly greater than T, corresponding to a point which has moved faster than the mean flow at any level. This is to be expected since maximum amplification occurs for k approximately equal to 3, for which the two-dimensional group speed, computed from fig 5.19b, is 1·06, i.e. slightly faster than the maximum mean flow speed of 1. Thus the conclusion of section 5.6.1 is confirmed that, if flow could be constrained to be two-dimensional, a perturbation has been found which, like the tropical SQL moves faster than the mean flow at any level.

6.2.3 Three-Dimensional Study.

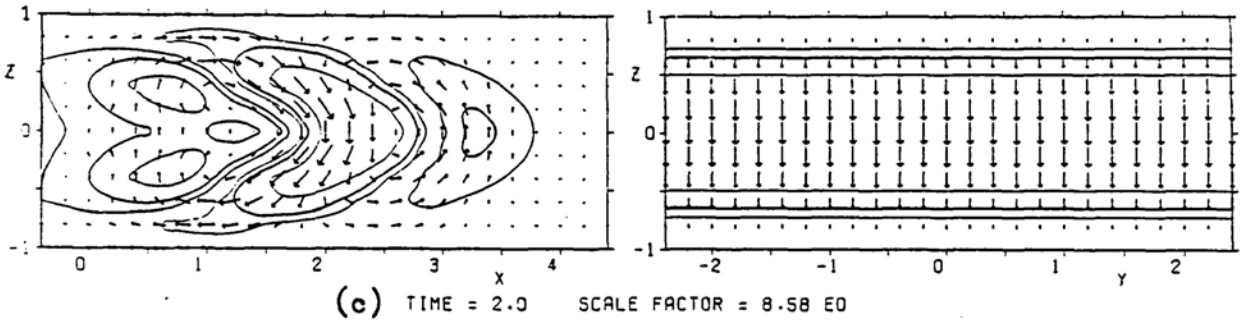
As anticipated from sections 5.6.2 and 6.1.1, the development of a three-dimensional initial perturbation does not however give a two-dimensional roll as required above, a ring of convection being formed instead.



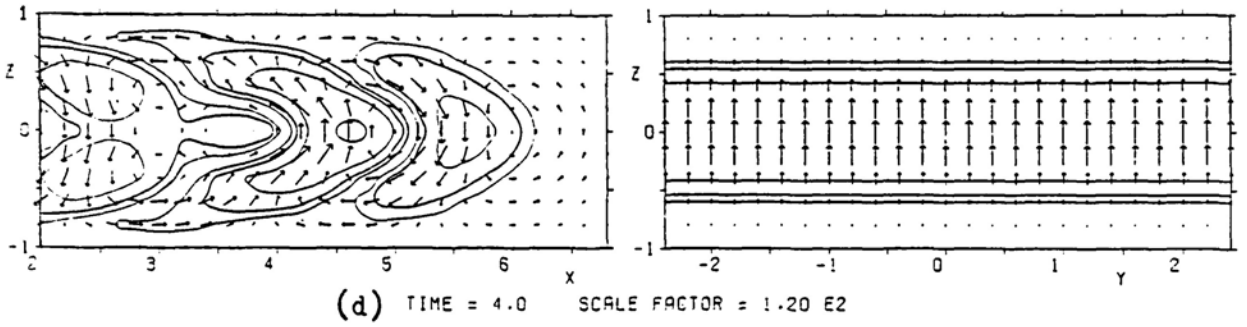
(a) TIME = 0.0 SCALE FACTOR = 1.00 E0



(b) TIME = 1.0 SCALE FACTOR = 1.85 E0



(c) TIME = 2.0 SCALE FACTOR = 8.58 E0



(d) TIME = 4.0 SCALE FACTOR = 1.20 E2

Fig 6.4. Two-dimensional perturbation of plane Poiseuille flow, $U = \frac{1}{3} - Z^2$, $R = -1$, showing vertical sections of perturbation velocity (arrows) and potential temperature excess (contours) in the planes

(a) $Y = 0$ and $X = 0$ (b) $Y = 0$ and $X = 1{\cdot}6$

(c) $Y = 0$ and $X = 2$ (d) $Y = 0$ and $X = 4{\cdot}4$

For explanation see section 6.1.2.

The plan sections, fig 6.5, show development of successive 'arc front' updraughts and downdraughts to the right of the main convection area; these are formed at X slightly greater than T for a given time T, so that the position of the successive arc fronts moves faster than the mean flow at any level. As new arc fronts form, the old ones amplify mainly to the sides, thus giving rise to the convective ring. Unlike the two-dimensional study however, greatest amplitude is always at the original updraught, and this does not move as fast as the maximum mean flow velocity. These results suggest that the picture (fig 6.3a) obtained in section 6.1.1 for large Richardson number can be extended to arbitrary Richardson number.

At T = 8, it was no longer possible to distinguish the arc front from the background noise, and motion has approximated to the longitudinal rolls which would be expected as having the greatest amplification rate. Note that in this case, and to some extent at T = 4, contours are open to the left since vertical velocities were only calculated over a restricted range of X values in the neighbourhood of the maximum amplitude, the results then being plotted on the extended grid to show more clearly the motion.

Turning now to the vertical sections, fig 6.6, those in the Y-Z plane are similar to the corresponding sections for two-dimensional motion, except that new draughts are not formed so rapidly, and maximum amplitude always remains with the initial updraught. The transverse sections show that the descent in the first downdraught extends for the whole depth of the convective layer, but that the region of maximum velocities tends to move from the centre line to the sides.

A discussion of the application of these results to the modelling of SQL's will be deferred until actual atmospheric profiles have been considered.

6.2.4 Effect of Changing Various Parameters.

(a) Width of Initial Updraught.

In fig 6.7, the parameter k_o which determines the width of the initial updraught has been taken as 1 rather than the usual 3. Development is similar to that of fig 6.5; the initial length scale reflects the lower value of k_o, but as time proceeds and wavenumber k = 3 becomes dominant, the spacing of the cells approaches that of fig 6.5.

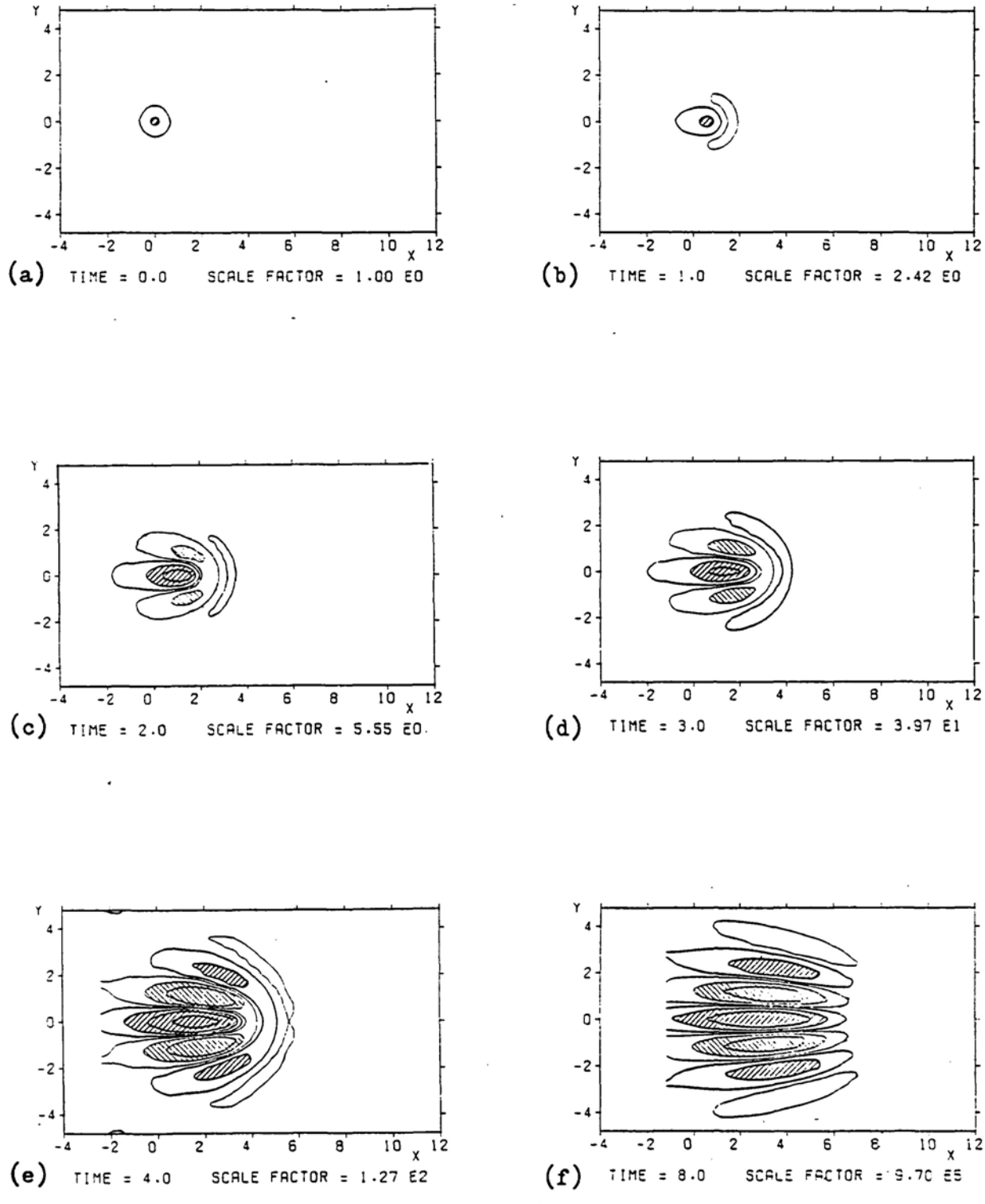
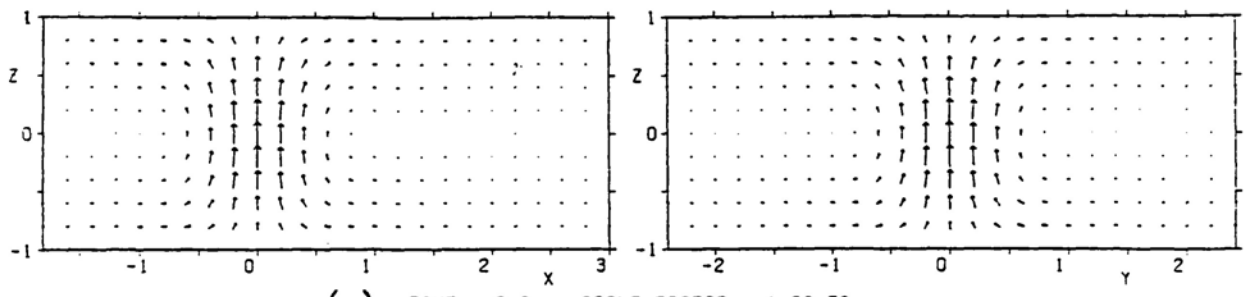


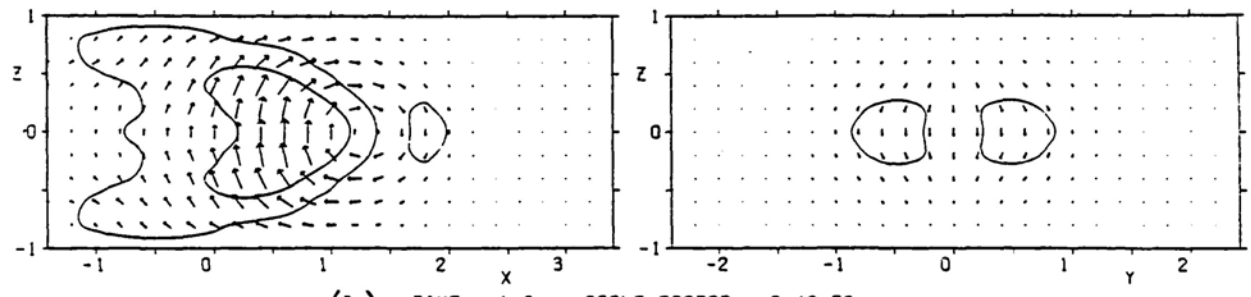
Fig 6.5. Three-dimensional perturbation of plane Poiseuille flow, $U = \frac{1}{3} - Z^2$, $R = -1$, showing horizontal sections of vertical velocity through $Z = 0$.

Upward motion } with vertical velocity in
Downward motion } excess of scale factor.

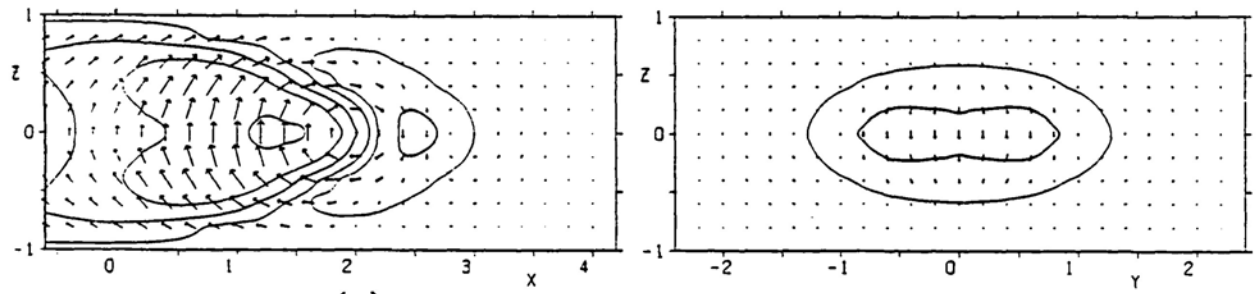
For a full explanation see section 6.1.2.



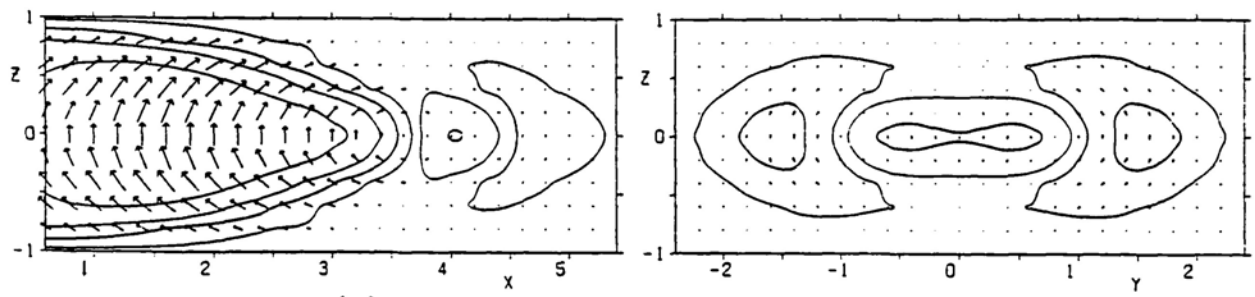
(a) TIME = 0.0 SCALE FACTOR = 1.00 E0



(b) TIME = 1.0 SCALE FACTOR = 2.42 E0



(c) TIME = 2.0 SCALE FACTOR = 5.55 E0



(d) TIME = 4.0 SCALE FACTOR = 1.27 E2

Fig 6.6. Three-dimensional perturbation of plane Poiseuille flow, $U = \frac{1}{3} - Z^2$, $R = -1$, showing vertical sections of perturbation velocity (arrows) and potential temperature excess (contours) in the planes

(a) $Y = 0$ and $X = 0$ (b) $Y = 0$ and $X = 1{\cdot}6$

(c) $Y = 0$ and $X = 2{\cdot}4$ (d) $Y = 0$ and $X = 4$

For explanation see section 6.1.2.

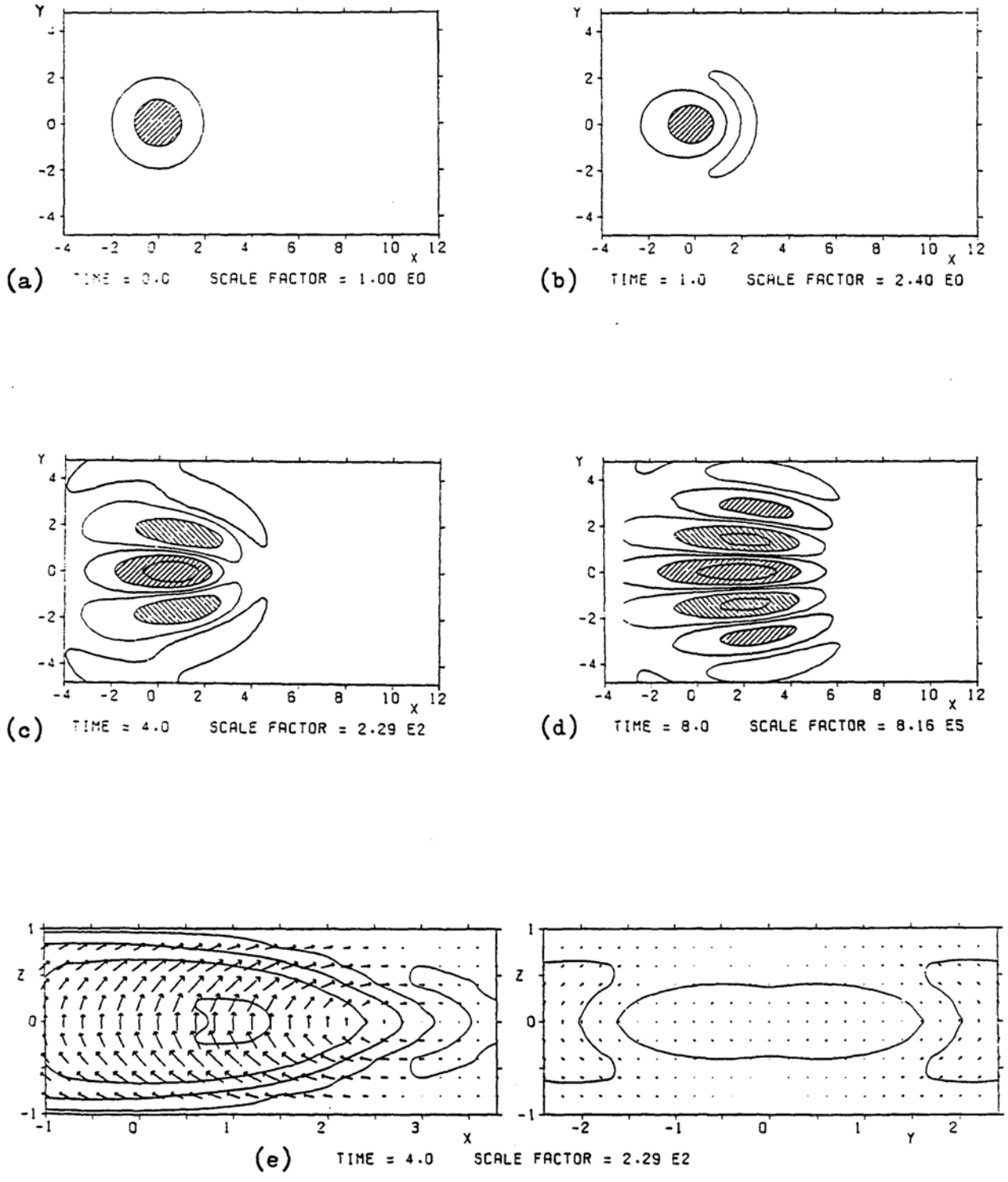


Fig 6.7. Three-dimensional perturbation of plane Poiseuille flow, $U = \frac{1}{3} - Z^2$, $R = -1$, with parameter k_o which determines width of initial updraught changed from 3 to 1.

(a) - (d) Horizontal sections of vertical velocity in the plane $Z = 0$

(e) Vertical sections of perturbation velocity (arrows) and potential temperature excess (contours) in the planes $Y = 0$ and $X = 3{\cdot}6$.

(b) Value of Rayleigh Number.

The effect of reduced viscosity is seen in fig 6.8, where Ra has been changed from its usual value of 10^5 to 10^7, the wavenumber of maximum amplification for longitudinal rolls being now, by (4.35), $k_m = 6$. With the same initial updraught as in fig 6.6a, the effect of the shorter dominant wavelength soon becomes apparent in the closer spacing of the cells, though again the form of the motion is similar to that of fig 6.5. The more rapid horizontal variation has meant that the computation was subject to greater errors, and these are manifested in the large number of spurious contours which encircle the actual area of convection.

(c) Variation of Richardson Number.

With R = -5 instead of -1 (not shown), it was found that amplification was very much more rapid than in fig 6.5 (scale factor $\simeq 2 \times 10^3$ at T = 2); this is to be expected because the effect of increasing -R may be regarded as increasing the buoyancy while holding constant the shear which determines the non-dimensional time T in (6.48). The form of the perturbation was however very similar to that of fig 6.5, which is in contrast to results obtained with plane Couette flow (section 6.3.3) where significant changes are evident.

If variable lapse rate is allowed, the situation may change considerably. Figs 6.9 and 6.10 show the results for R = -1 with lapse rate

$$L = -2Z \qquad (6.51)$$

a profile which is statically unstable only in the lower half of the flow region. The vertical sections (fig 6.10) show that the greatest amplitudes of vertical velocity are displaced from the middle towards the lower boundary; for this reason the horizontal sections (fig 6.9) are taken through Z = -0·5 rather than the usual Z = 0. An even more important difference from the case of constant lapse rate is that, apart from a weak downdraught arc formed initially to the right, the perturbation now moves to the left, the arc fronts in this direction being too weak to show in the plotted contours. The tendency to form longitudinal rolls at large T is again evident; it is not clear whether the secondary perturbations to the left of the main convection area are in fact spurious.

The reason for the movement to the left rather than to the right can be deduced from consideration of linear modes. At the level of the maximum mean flow, the fluid is now neutrally buoyant, so the short wave mode there (if any) will no longer amplify rapidly. Instead, greatest

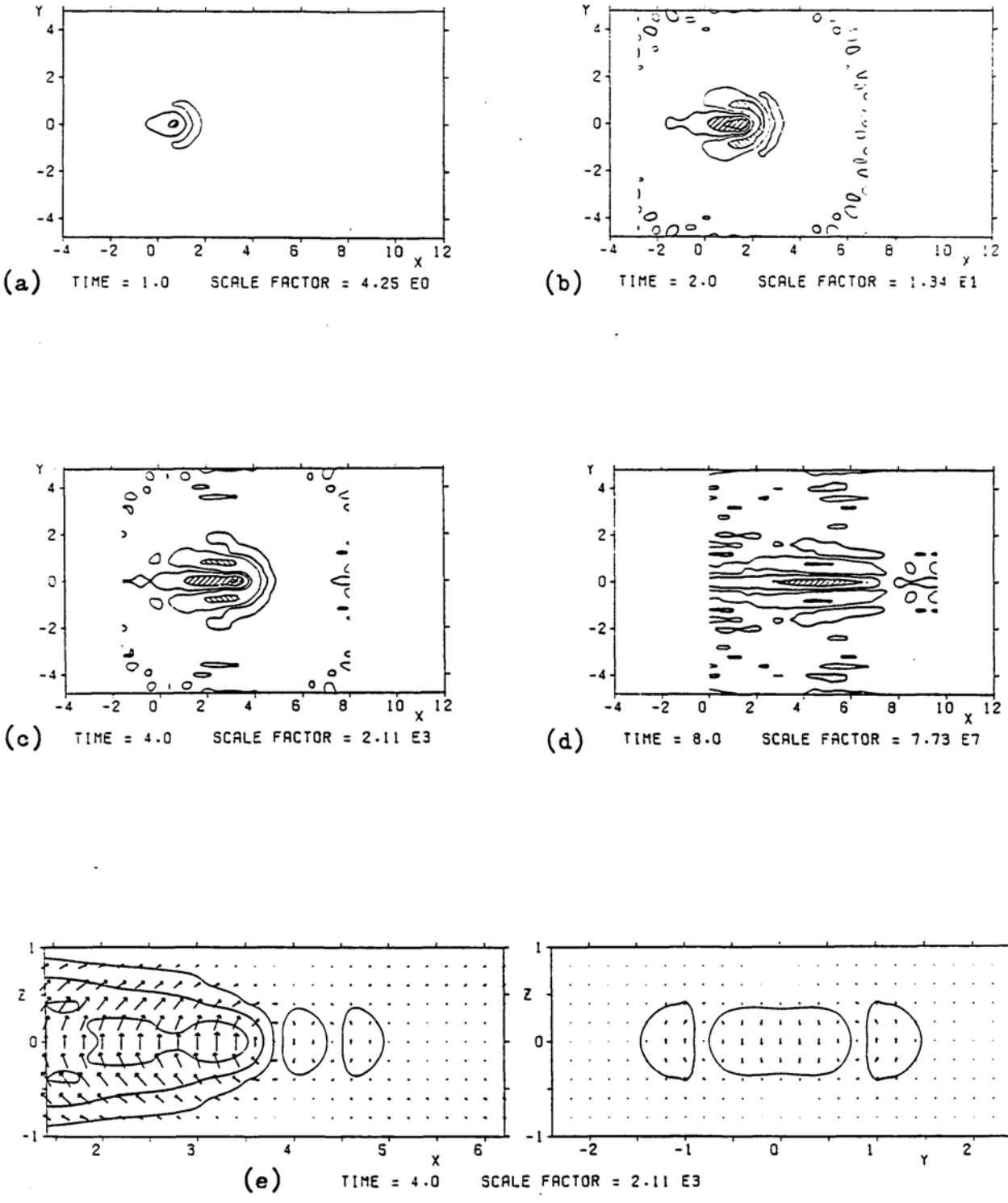


Fig 6.8. Three-dimensional perturbation of plane Poiseuille flow, $U = \frac{1}{3} - Z^2$, $R = -1$, with Rayleigh number Ra changed from 10^5 to 10^7.

(a) - (d) Horizontal sections of vertical velocity through $Z = 0$

(e) Vertical sections of perturbation velocity (arrows) and potential temperature excess (contours) in the planes $Y = 0$ and $X = 4$.

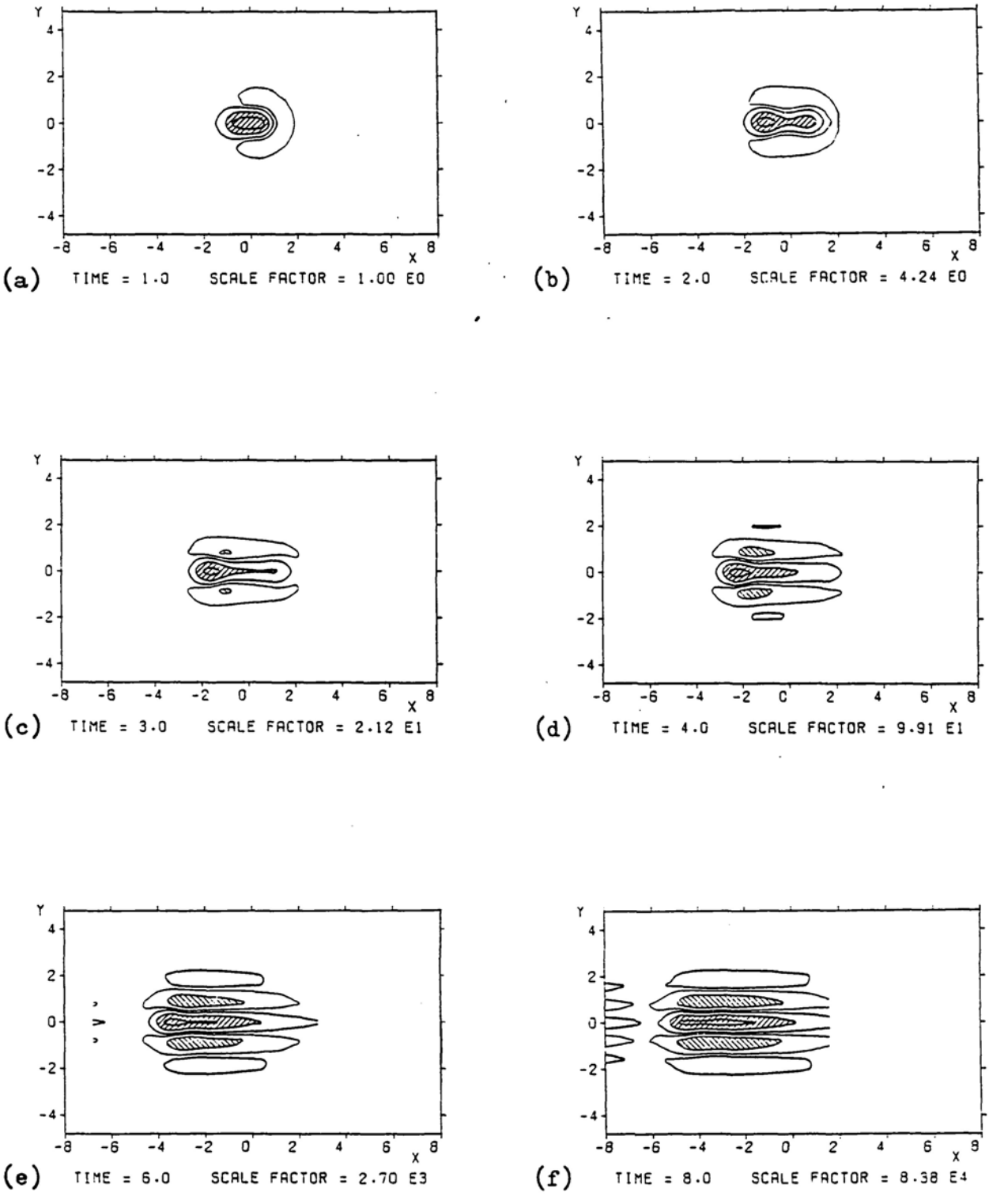


Fig 6.9. Three-dimensional perturbation of plane Poiseuille flow $U = \frac{1}{3} - Z^2$, $R = -1$, with variable lapse rate $L = -2Z$, showing horizontal sections of vertical velocity through $Z = -0.5$.

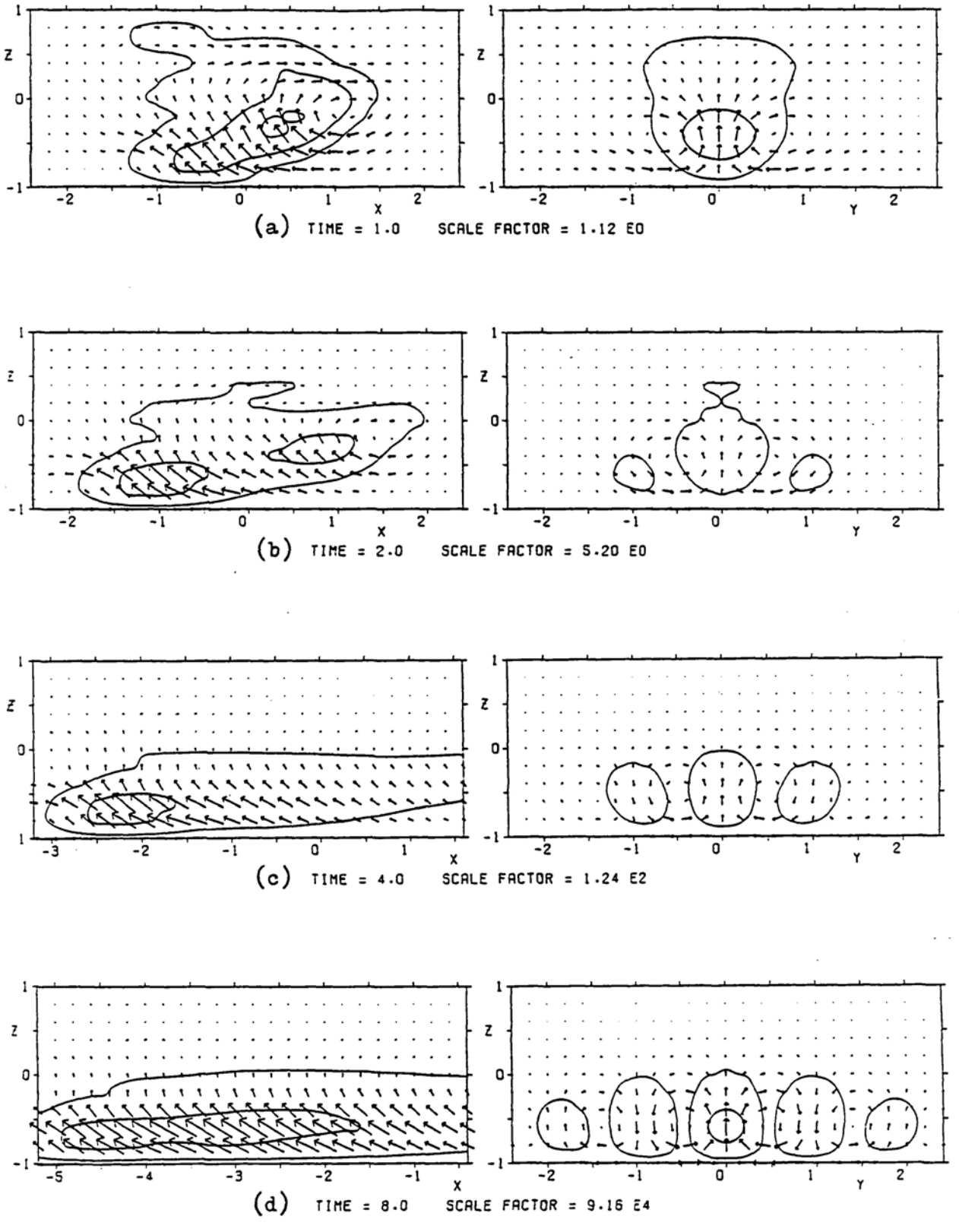


Fig 6.10. Three-dimensional perturbation of plane Poiseuille flow, $U = \frac{1}{3} - Z^2$, R = -1, with variable lapse rate L = -2Z, showing vertical sections of perturbation velocity (arrows) and potential temperature excess (contours) in the planes

(a) Y = 0 and X = 0 (b) Y = 0 and X = 0

(c) Y = 0 and X = -0·8 (d) Y = 0 and X = -2·8.

amplification rates for short waves are likely to occur for modes travelling near the lower boundary, where the buoyancy is greatest and, with the form of the mean flow adopted in (6.47), these modes will indeed propagate to the left. Thus, in order to obtain a perturbation travelling faster than the mean flow at any level it is not only necessary to have a mean flow maximum, but that there should be appreciable buoyancy at this level. This would explain the result of section 3.3.1 that it is the lower AEJ which is important in SQL formation and not the upper level TEJ, which is too high for there to be adequate buoyancy.

(d) Variable Mean Density.

With r taking the value 0·75 appropriate to the cumulonimbus layer in the atmosphere, it was found that growth of the perturbation (not shown) was very similar to that which was obtained for r = 0 (fig 6.5), as anticipated in section 5.1.1b. Amplitudes however were larger at upper levels, since it is the Fourier transforms of $\rho_o^{\frac{1}{2}}$ times the velocities which occur in the perturbation equations (4.12) onwards, so that on transforming back a factor $\rho_o^{-\frac{1}{2}}$ is introduced; this means that kinetic energies at upper and lower levels are then comparable.

6.3 CASE STUDIES WITH OTHER VELOCITY PROFILES.

6.3.1 Unsheared Flow.

For unsheared flow, S = 0, so it is necessary to define non-dimensional time to be Nt as in (5.11), the equations (6.26) etc. being correspondingly altered. Fig 6.11 shows results for R = -1. Round the initial symmetric updraught are formed successively a circular downdraught and updraught. Thus the perturbation approaches the symmetric 'Bessel function' form appropriate as the single wavenumber of maximum amplification becomes increasingly dominant.

6.3.2 Statically Neutral Hyperbolic Tangent Profiles.

The case of statically neutral plane Couette flow, U = Z, R = 0 has already been examined in section 4.1.3, where it was concluded that vertical velocity would remain bounded, but that horizontal velocity would grow with time owing to advection of initial vorticity with the mean flow. Numerical results in figs 6.12 and 6.13 confirm these conclusions. The initial perturbation is progressively stretched in the direction of the mean flow, and (fig 6.13) horizontal velocities steadily increase, while vertical velocities alter relatively little,

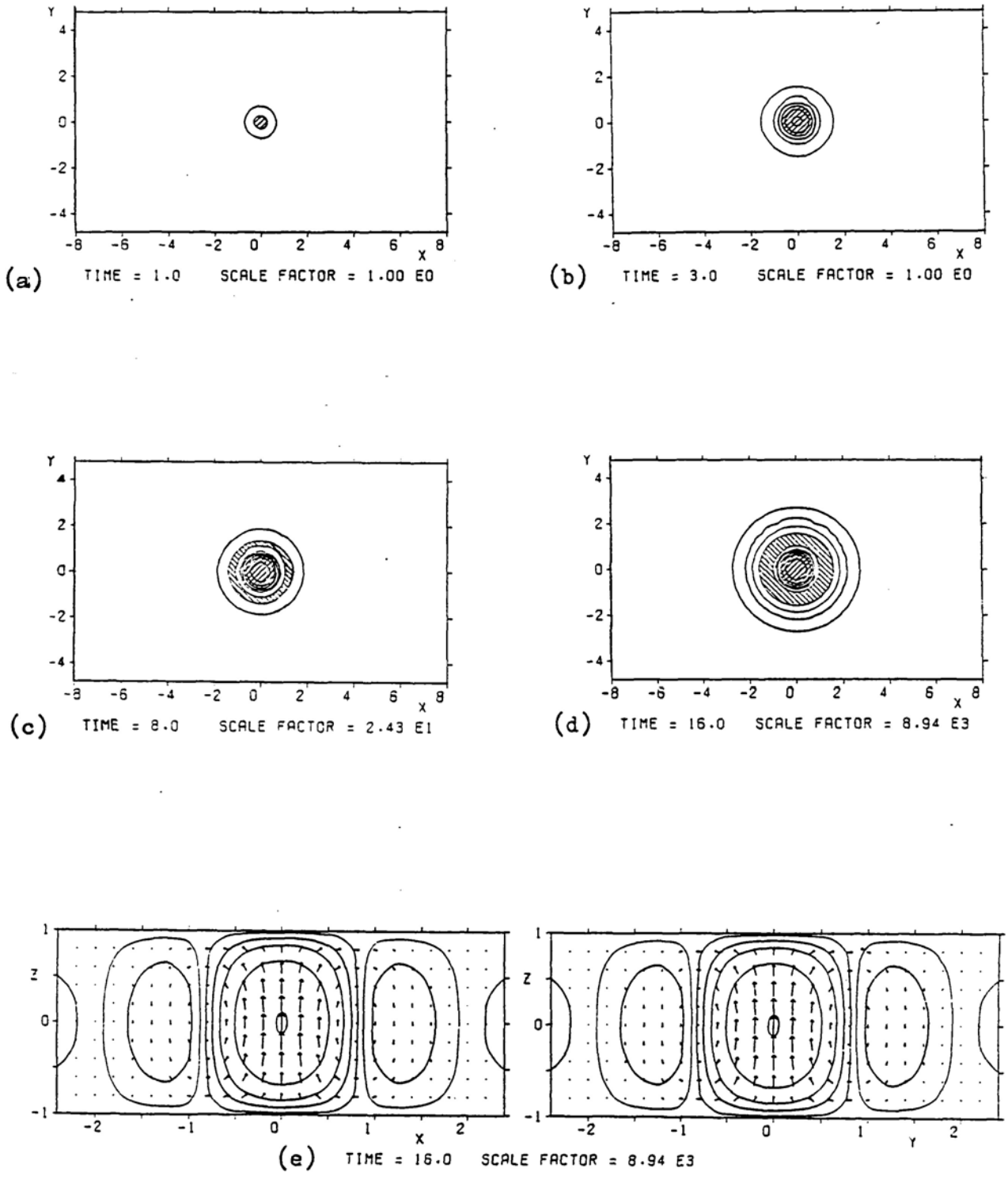


Fig 6.11. Unsheared flow, U = 0, R = -1

(a) - (d) Horizontal sections of vertical velocity through Z = 0

(e) Vertical sections of perturbation velocity (arrows) and potential temperature excess (contours) in the planes Y = 0 and X = 0.

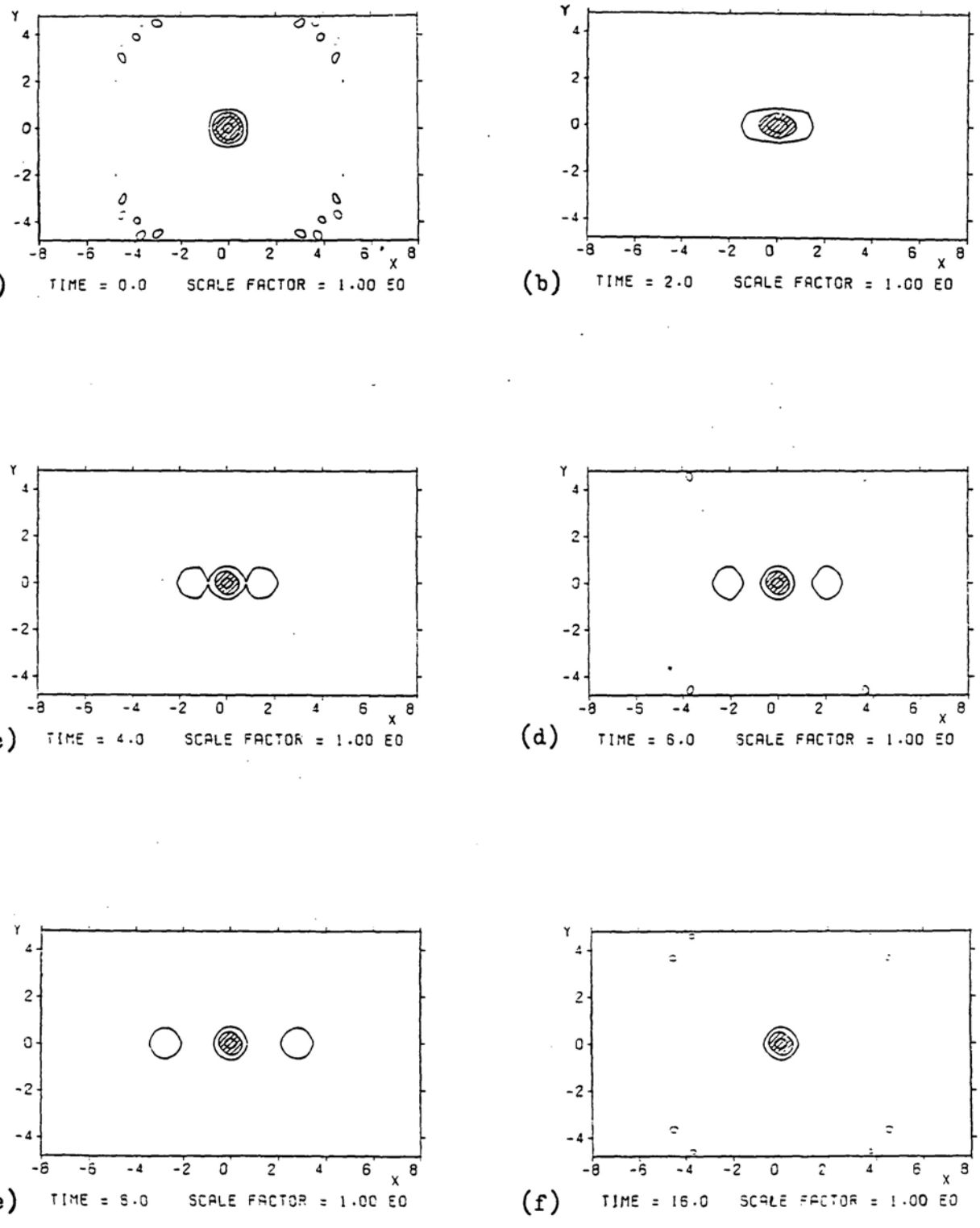
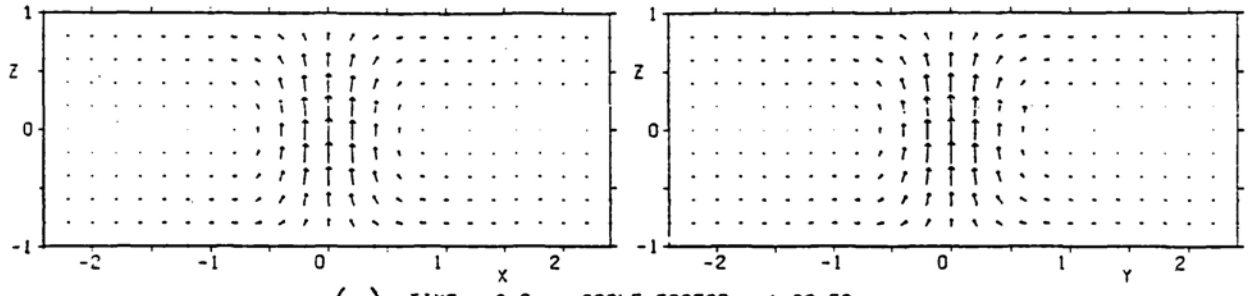
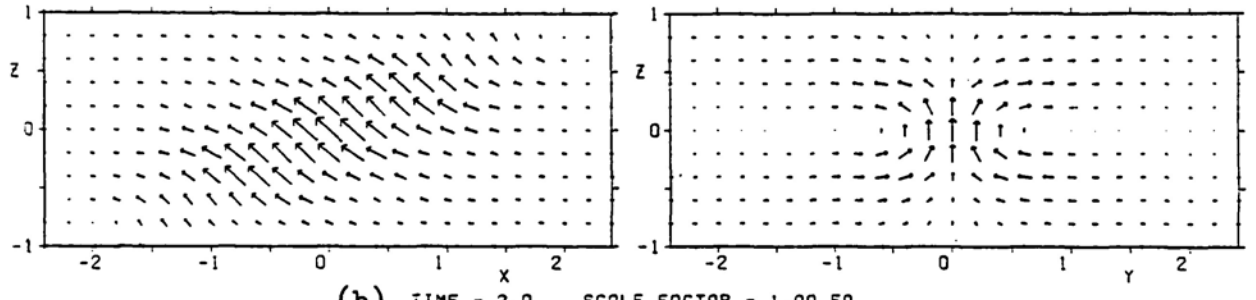


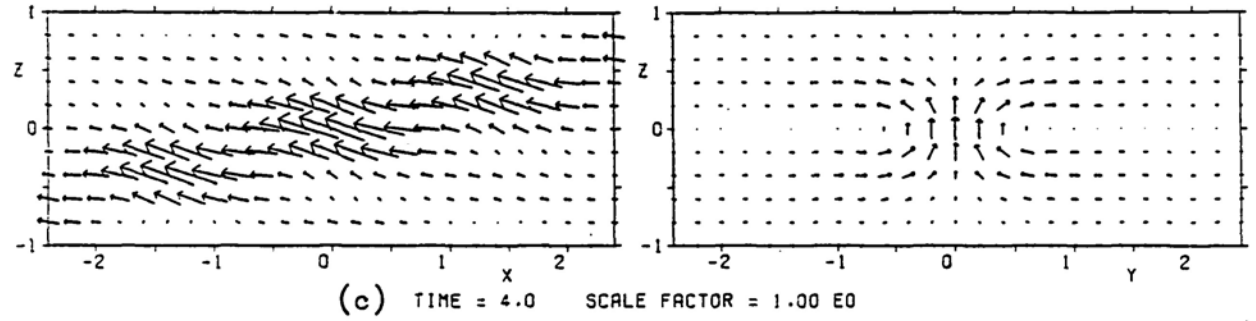
Fig 6.12. Statically neutral plane Couette flow $U = Z$, $R = 0$.
Horizontal sections of vertical velocity through $Z = 0$.



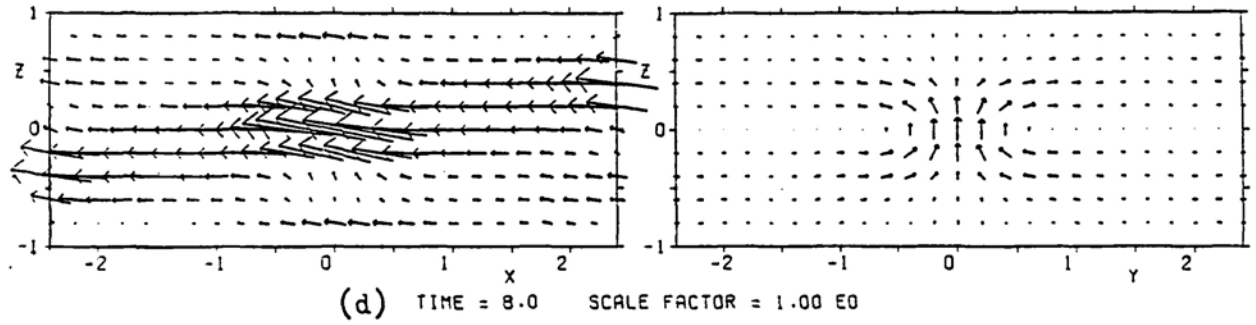
(a) TIME = 0.0 SCALE FACTOR = 1.00 E0



(b) TIME = 2.0 SCALE FACTOR = 1.00 E0



(c) TIME = 4.0 SCALE FACTOR = 1.00 E0



(d) TIME = 8.0 SCALE FACTOR = 1.00 E0

Fig 6.13. Statically neutral plane Couette flow U = Z, R = 0. Vertical sections of perturbation velocity in the planes Y = 0 and X = 0.

and maximum vertical velocity is in fact slightly reduced. One feature of the results not anticipated from the analysis in section 4.1.3 is the development of three separate regions of greatest instability - a low level region moving to the right, a high level region moving to the left, and a middle level region remaining stationary; no obvious reason can be suggested for this. Note that no contours for potential temperature are obtained since the fluid is statically neutral.

For the profile $U = \text{th}\,2Z / \text{th}\,2$ (fig 6.14), it was found that initial development up to $T = 2$ was very similar to that of plane Couette flow (figs 6.12 a,b; 6.13 a,b), with growth of horizontal velocity, and a slight reduction of maximum vertical velocity. Thereafter, horizontal velocity continues to grow much as before, except that the separate upper and lower regions of greatest instability were less obvious; but now, after its initial slight reduction, vertical velocity starts to grow also, though never approaching the magnitude of the horizontal velocity.

Thus, though the effect of the unstable normal mode associated with the inflexion point in the hyperbolic tangent profile is evident in the increasing vertical velocity, the dominant instability is the algebraic one, manifested for both plane Couette and hyperbolic tangent flows in the perturbation horizontal velocity. This emphasises the importance of the analysis of section 4.1.3 for profiles lacking significant buoyancy. One somewhat curious feature should here be mentioned: the equations (6.33) which were used in computing the numerical solution have only exponential, and not algebraic solutions, so it may seem surprising that the algebraic instability is able to emerge. Several of these exponential solutions will however be 'spurious', in the sense that the corresponding eigenvalues of the Galerkin equations (5.48) and (5.49) do not correspond to normal modes, and these spurious exponential solutions will be the ones which approximate the algebraic instability.

6.3.3 Unstably Stratified Plane Couette Flow.

Results for unstably stratified plane Couette flow are shown for two different Richardson numbers, $R = -5$ and -1. For $R = -5$, the horizontal sections (fig 6.15) show development of an elliptical patch of convection, as predicted in section 6.1.1, with formation of successive cells in a line transverse to the mean flow, and gradual elongation of the cells into longitudinal rolls. The vertical sections (fig 6.16) show the tilting of the cells in the direction of the mean flow.

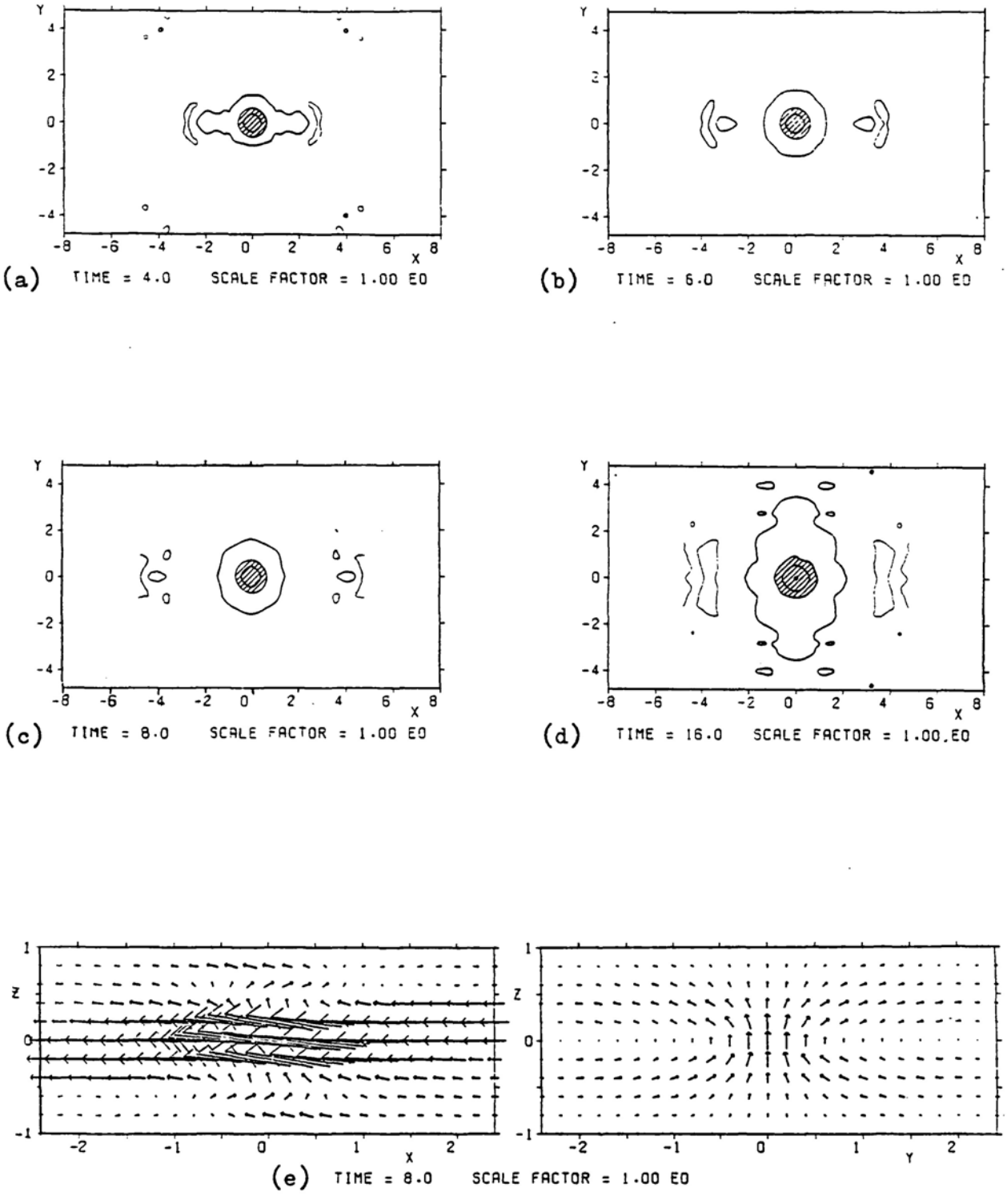


Fig 6.14. Statically neutral hyperbolic tangent profile
U = th 2Z / th 2, R = 0

(a) - (d) Horizontal sections of vertical velocity through Z = 0

(e) Vertical sections of perturbation velocity in the planes Y = 0 and X = 0.

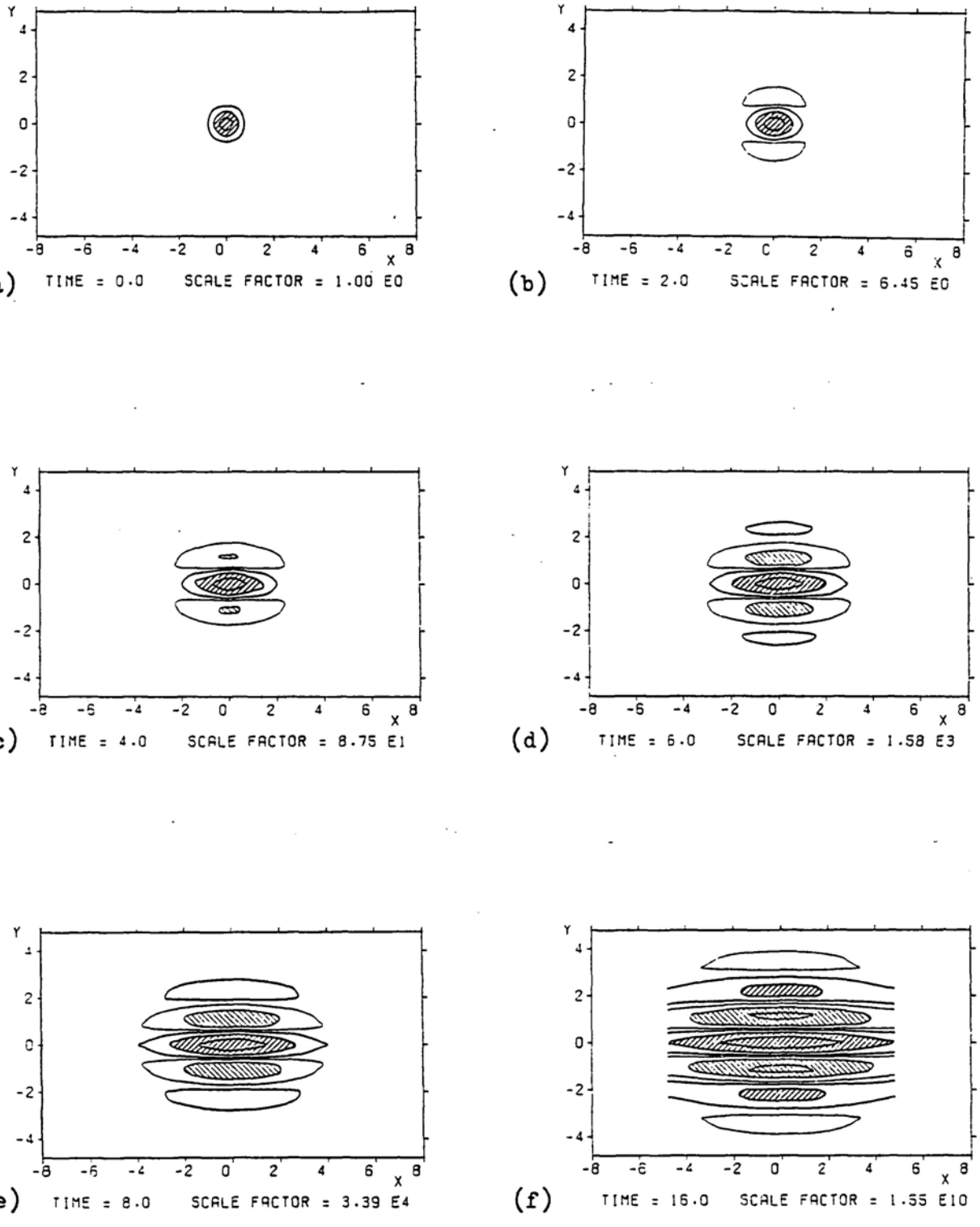
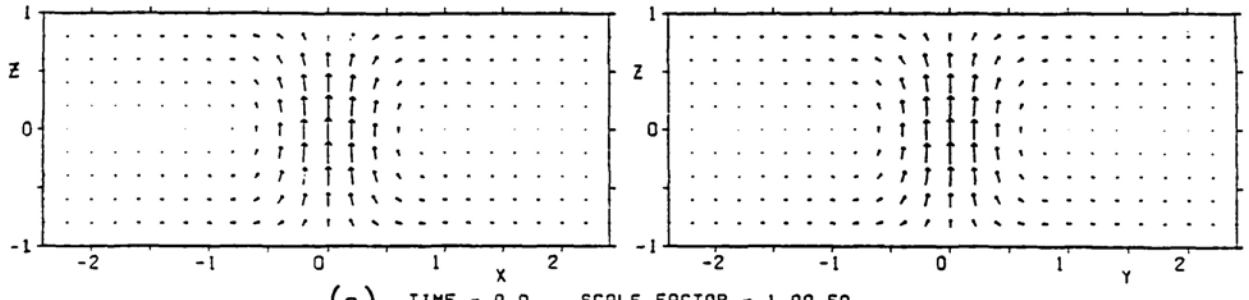
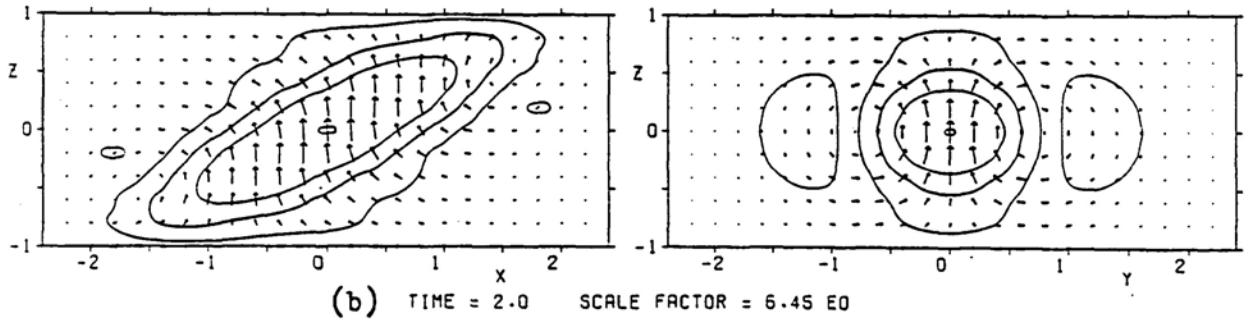


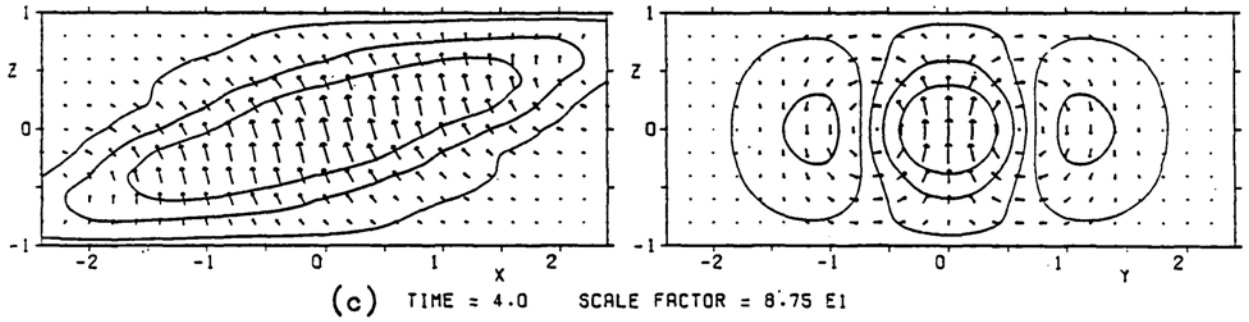
Fig 6.15. Unstably stratified plane Couette flow $U = Z$, $R = -5$. Horizontal sections of vertical velocity through $Z = 0$.



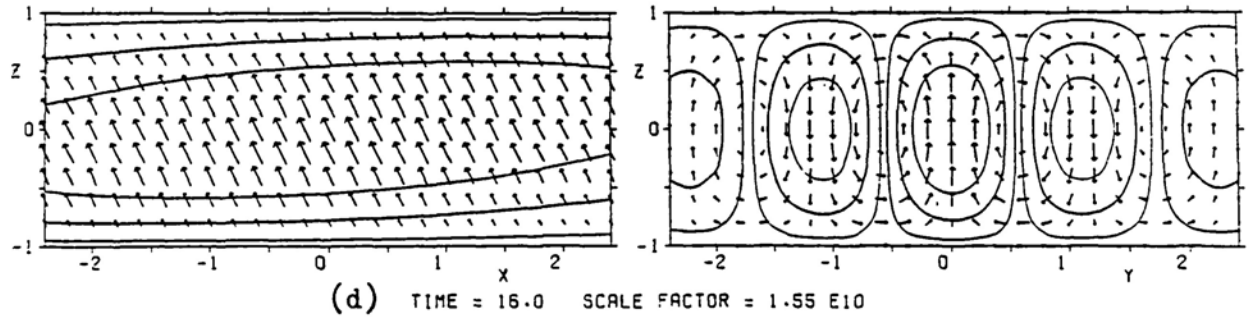
(a) TIME = 0.0 SCALE FACTOR = 1.00 E0



(b) TIME = 2.0 SCALE FACTOR = 6.45 E0



(c) TIME = 4.0 SCALE FACTOR = 8.75 E1



(d) TIME = 16.0 SCALE FACTOR = 1.55 E10

Fig 6.16. Unstably stratified plane Couette flow $U = Z$, $R = -5$. Vertical sections of perturbation velocity (arrows) and potential excess (contours) in the planes $Y = 0$ and $X = 0$.

For R = -1 (fig 6.17), growth is slower, as expected from the smaller buoyancy available for a given shear (see section 6.2.4c). Also, development of new cells in a line transverse to the mean flow is very much inhibited while, in addition to the middle level region of greatest instability, separate upper and lower regions develop, reminiscent of those in the statically neutral case, fig 6.13.

Consideration of linear modes for plane Couette flow in figs 5.2 and 5.3 shows that in addition to the stationary long wave modes, propagating short wave modes exist for $-R_\theta > 2$. For the case R = -1, modified Richardson numbers satisfying $-R_\theta > 2$ do occur for modes sufficiently inclined to the X axis, and it would be attractive to explain the upper and lower regions of instability as being due to these modes. The absence of distinct upper and lower regions for R = -5 could be explained as arising from the increasing number of modes existing as -R increases, so that it is no longer possible to distinguish individual modes. However this explanation does not account for the distinct upper and lower regions for R = 0, where there are no normal modes, so it seems likely the explanation should be sought in the algebraic instability, and not in normal modes.

6.3.4 Mixed Poiseuille and Couette Flow.

Considering the flow

$$U = a\left(\tfrac{1}{3} - Z^2\right) \qquad V = bZ \tag{6.52}$$

the component in a direction making angle θ with the X axis is

$$\begin{aligned} W &= a\left(\tfrac{1}{3} - Z^2\right)\cos\theta + bZ\sin\theta \\ &= -a\cos\theta\left[\left(Z - \frac{b}{2a}\tan\theta\right)^2 - \frac{b^2}{4a^2}\tan^2\theta - \tfrac{1}{3}\right] \end{aligned} \tag{6.53}$$

The component in the X direction, $\theta = 0$, is a symmetric parabolic profile; as θ is increased, the parabola becomes asymmetric until for $\tan\theta = \pm\frac{2a}{b}$, the velocity maximum has moved to one or other boundary; increasing θ still further, the profile no longer has a maximum, but tends to the constant shear obtained with $\theta = \frac{\pi}{2}$.

The short wave analysis of section 5.4.2 suggests that the greatest growth rate will occur for the short wave mode at a velocity maximum for which $|U''|$ is smallest, and here this occurs for modes with $\tan\theta = \pm\frac{2a}{b}$, for which the velocity maximum is at a boundary. Two cases will be considered below (a) a = 1, b = $\frac{1}{3}$ (b) a = $\frac{1}{2}$, b = 1; the respective values of θ for the fastest growing modes are $\pm 81^\circ$ and $\pm 45^\circ$.

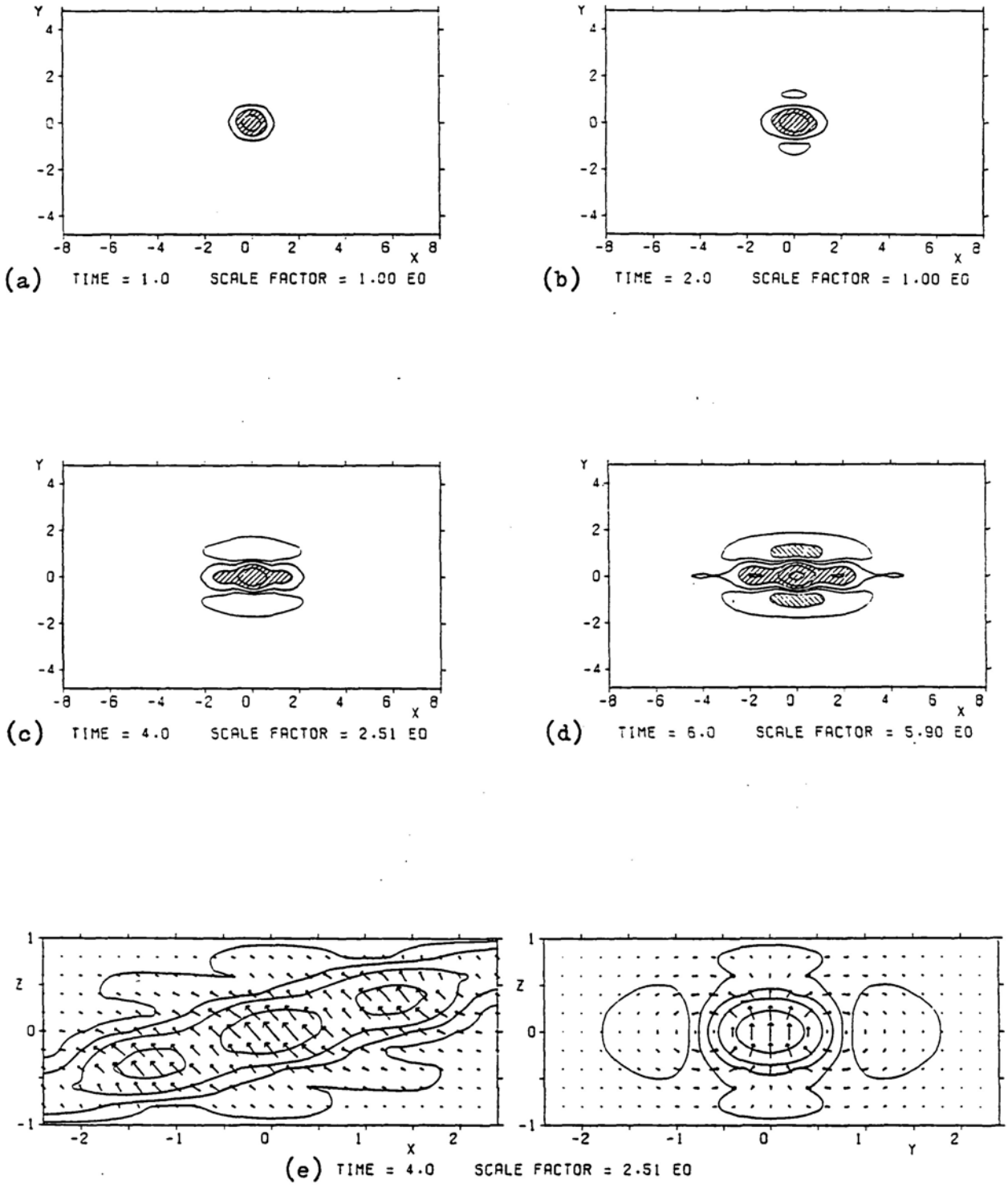


Fig 6.17. Unstably stratified plane Couette flow $U = Z$, $R = -1$.

(a) - (d) Horizontal sections of vertical velocity through $Z = 0$

(e) Vertical sections of perturbation velocity (arrows) and potential temperature excess (contours) through $Y = 0$ and $X = 0$.

(a) $U = \frac{1}{3} - Z^2$, $V = \frac{1}{3}Z$, $R = -1$.

Here the greatest shear is in the X direction, so the definition (6.48) of non-dimensional time appropriate to the parabolic profile was used. Results (fig 6.18) show initial development of updraught and downdraught arc fronts at points moving faster than the maximum mean flow. These fronts display a tilt (fig 6.18e) in the Y-Z section owing to the influence of the two fastest growing short wave modes for $\theta = \pm 81^\circ$, which propagate near the upper and lower boundaries. After a further time, the two modes become distinct, and there is eventual separation into upper and lower level perturbations propagating in different directions (though admittedly not inclined to the X axis by as much as the predicted $\pm 81^\circ$)

(b) $U = \frac{1}{2}(\frac{1}{3} - Z^2)$, $V = Z$, $R = -5$.

Here the greatest shear is in the Y direction, so time was non-dimensionalised as for the constant shear profile, (5.11); the larger Richardson number was used to avoid the algebraic instability which dominates the results for this profile with $R = -1$. Here again (fig 6.19) successive downdraught and updraught fronts were formed at points moving faster than the mean wind (in this case $U_{max} = \frac{1}{6}$, so a point moving at the greatest U velocity component would only be at $X = \frac{8}{6}$ at time 8). The fronts are tilted as before, but now the two fastest growing short wave modes for $\theta = \pm 45^\circ$ are propagating in a sufficiently similar direction that no separation is apparent even at $T = 8$, rolls transverse to the constant shear component having formed instead.

The splitting obtained with (a) could have relevance to the formation of severe right and left moving storms in mid latitudes. The right moving perturbation, having its maximum amplitude at a lower level, where in the atmosphere there is a greater energy supply, would tend to be the more intense, as is commonly observed (section 2.1.3a). Raymond (1976), using an actual atmospheric sounding, obtained a similar splitting (see section 4.2.2), and he likewise attributed this to a double maximum in the growth rate/direction graph (fig 4.4b); his profile however bore more resemblance to (b) than to (a) above, and his results do not show any evidence of a distinction between upper and lower level perturbations.

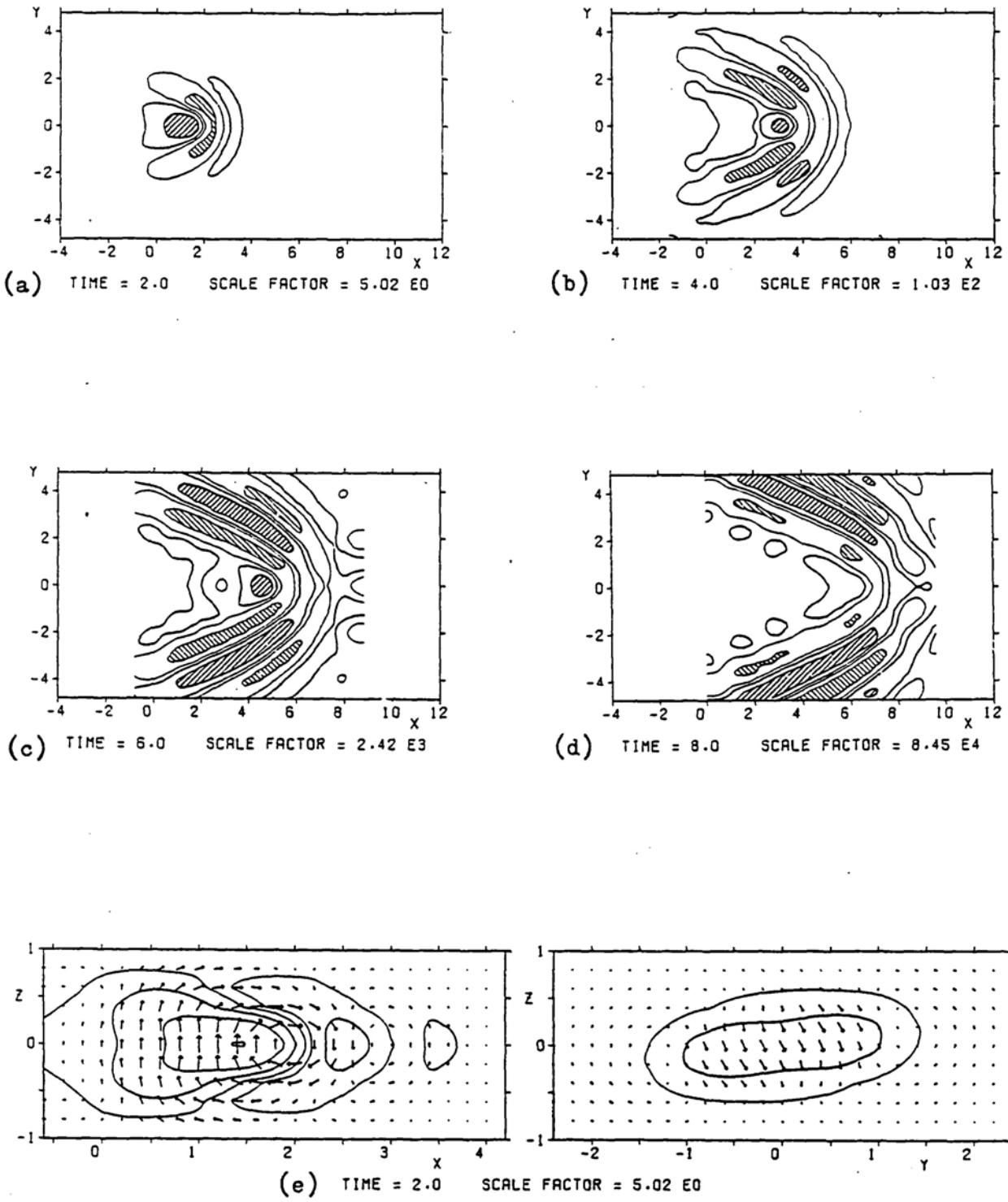


Fig 6.18. Mixed Couette-Poiseuille flow, $U = \frac{1}{3} - Z^2$, $V = \frac{1}{3}Z$, $R = -1$

(a))- (d) Horizontal sections of vertical velocity through $Z = 0$

(e) Vertical sections of perturbation velocity (arrows) and potential temperature excess (contours) through $Y = 0$ and $X = 2{\cdot}4$.

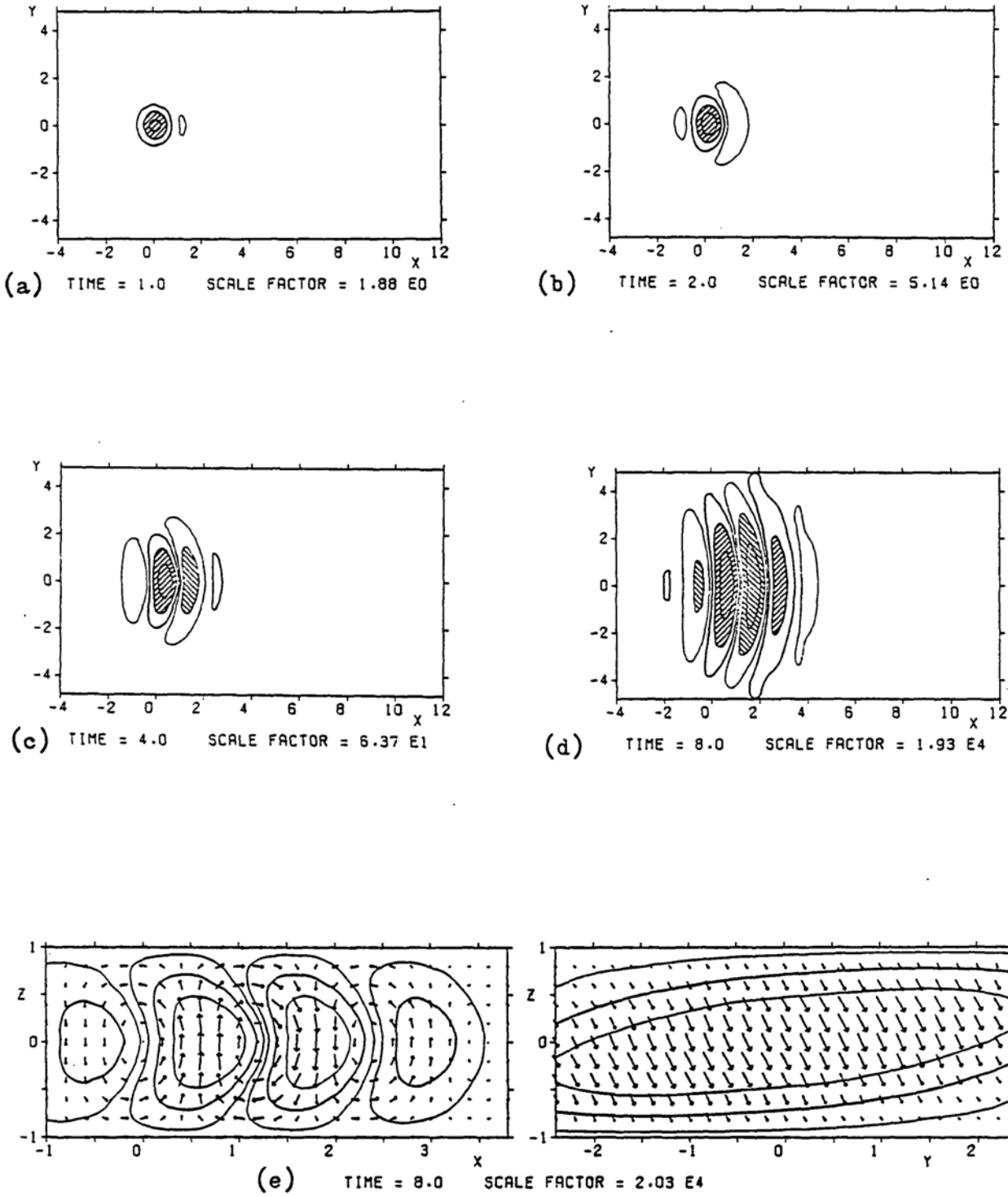


Fig 6.19. Mixed Couette-Poiseuille flow $U = \frac{1}{2}(\frac{1}{3} - Z^2)$, $V = Z$, $R = -1$

(a) - (d) Horizontal sections of vertical velocity through $Z = 0$

(e) Vertical sections of perturbation velocity (arrows) and potential temperature excess (contours) through $X = 0$ and $Y = 1{\cdot}6$.

6.4 CASE STUDIES WITH ATMOSPHERIC DATA.

6.4.1 Analysis of Data.

In dealing with atmospheric data, variables were non-dimensionalised as in section 5.1.1, and it was found more convenient not to subtract off average mean flow velocities, so that actual progress of the patch of convection could be followed. Non-dimensional time was defined as in (5.12), and as the AEJ is roughly easterly it was arranged that a point moving at the maximum jet speed would be at X = -T at time T.

The Fourier coefficients in (6.31), (6.32) and (6.38) were found from the non-dimensionalised mean flow variables by minimisation of an error integral, which for the C_n takes the form

$$E = \int_{p_1}^{p_2} \left[W(Z) - \sum_{n=0}^{M} C_n \cos \tfrac{1}{2} n\pi (Z+1) \right]^2 dp \,. \qquad (6.54)$$

Here p_1 and p_2 are taken to be the pressures at the surface and tropopause respectively, integration being carried out with respect to p rather than Z so as not to give undue weight to the values at upper levels. Differentiation with respect to each C_n in turn gives a set of linear equations

$$\sum_{n=0}^{M} C_n \int_{p_1}^{p_2} \cos \tfrac{1}{2} n\pi (Z+1) \cos \tfrac{1}{2} m\pi (Z+1) dp = \int_{p_1}^{p_2} W(Z) \cos \tfrac{1}{2} m\pi (Z+1) dp \qquad (6.55)$$

$$m = 0, 1, \ldots, M.$$

The integrals here were readily approximated by the trapezoidal rule applied between the standard pressure levels at which the soundings were given, and the C_n could thus be found. Determination of the S_n and Q_n followed similar lines, while for the H_n excess potential temperature (3.3) was non-dimensionalised making use of B as in (5.5), and a Fourier sine series with an added linear term was fitted,

$$\frac{1}{B} \delta\phi_p(Z) = \phi_0(Z) + \sum_{n=1}^{M} \phi_n \sin \tfrac{1}{2} n\pi (Z+1) \qquad (6.56)$$

differentiation then giving coefficients for the cosine expansion of

$$L(Z) = \frac{d}{dZ} \left(\frac{1}{B} \delta\phi_p \right) \qquad (6.57)$$

It was found that summing to M = 9 gave best results in that the data values were reasonably accurately approximated without introduction of a lot of spurious fluctuations between the data points; the Fourier series in (6.28), (6.39) are in fact only summed to M = 5, but the higher Fourier coefficients are needed for instance in (6.29).

A comment should be made here about the form of lapse rate adopted in (6.57). In a linear model, the only possible parameterisations of

latent heat release are via a modified static stability, as in section 4.3.1, or via a forcing term, as in section 4.2.2. The latter has been shown to be unsatisfactory in that it introduces an arbitrary phase shift, and has in any case been extensively studied by Raymond (1975, 1976). So here, the parameterisation used is that of a modified static stability. Since this can only be a function of height Z, all air, whatever its origin is assumed to have the same thermodynamic properties, namely those of a parcel rising from 950 mb (this being the level used in the computation of excess potential temperature); this is not entirely satisfactory in the updraught, but a far more serious problem occurs for the downdraught, where air is automatically negatively buoyant whenever the updraught air is buoyant. Thus the downdraught is a priori prescribed to be cold (whereas the mesoscale downdraught is in fact warm), and will originate from a level near the tropopause, rather than from the middle troposphere as observed (section 2.2.3a), this latter point also being a limitation of the Moncrieff models (section 4.3.2). Other shortcomings of the model can also be traced in part to the unrealistic thermodynamics, but a discussion of these points will be deferred until after the numerical results have been presented.

Studies were made for three atmospheric profiles, each of which had the tropopause at about 100 mb (16 km) with $B \simeq -3 \times 10^{-6}$ m^{-1}, $S \simeq 5 \times 10^{-3}$ s^{-1} so that the Richardson number was about -1. The non-dimensional time and space components were such that

T = 1 corresponded to a time of approximately 8 minutes

X = 1 corresponded to a distance of approximately 8 km.

Results are shown in figs 6.21 - 6.23 and 6.25. The horizontal sections, taken at Z = -0·6 corresponding approximately to 700 mb, show development of successive downdraught and updraught arcs. With the exception of fig 6.21, where development is somewhat slower, the first updraught arc at T = 2 corresponds to a time of 15 minutes. By T = 8, corresponding to 1 hour, this arc has split into two cells, with formation of a new updraught arc at the front. The vertical sections, which show the structure of the cells, are in the W-E and S-N directions through the initial cell, which is always the most rapidly amplifying.

6.4.2 Squall Lines at Minna.

The Minna sounding for 1200 on 22 September 1974 is shown in fig 6.20. The wind shows an easterly jet at 700 mb, and a considerable southerly component, except near 600 and 300 mb. In the thermodynamic sounding, an inversion between 850 and 800 mb resulted in negative

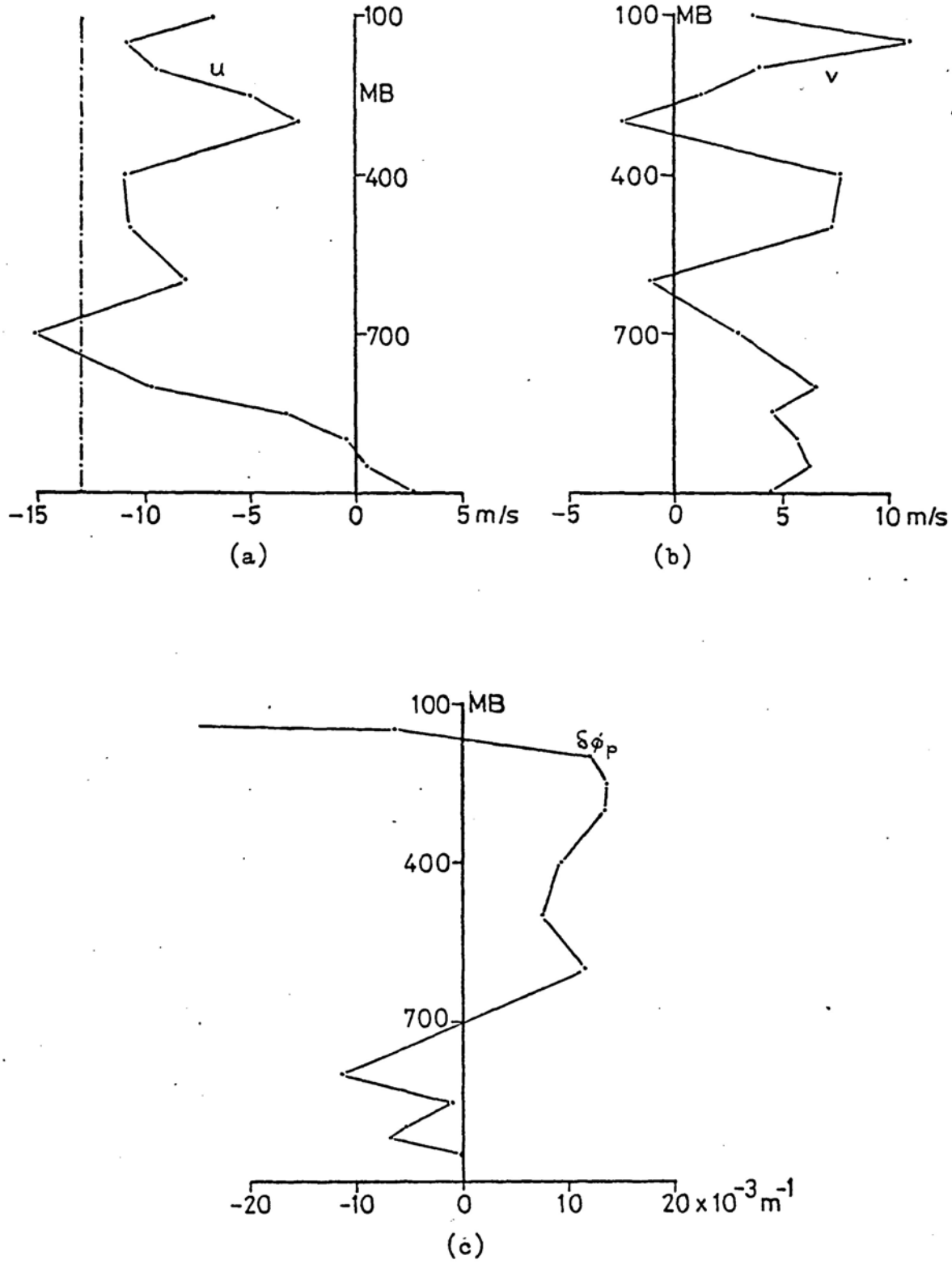


Fig 6.20. Minna sounding at 1200 on 22 September 1974 for

(a) Easterly wind component u (b) Southerly wind component v

(c) Parcel log potential temperature excess $\delta\phi_p$

Dash-dot line: speed of squall line.

buoyancy right up to 700 mb, so that conditions were ideal for build-up of potential energy in the surface layer until the SQL arrived at 1545. The storm velocity, from 090° at 13 m/s is close to the actual wind at 650 mb, and suggests influence not only from the easterly jet, but also from the drop in southerly wind component at 600 mb. The satellite images (fig 3.3, storm 2) show that while the cloud mass as a whole moved roughly from the east, the front of the SQL moved from significantly north of east, say 070°, the arc front being roughly at right angles to this, 160 - 340°.

Numerical results (figs 6.21, 6.22) show a similar distinction between motion of the disturbance as a whole and of the arc front. As a whole, the disturbance moves from slightly south of east, but the arc front is on its southern flank, moving in a direction very similar to that of the observed arc front, though its orientation 120 - 300° was no longer perpendicular to this motion. Agreement obtained over the storm speed was however less satisfactory. In fig 6.21d, the front of the disturbance is at $X \simeq -2{\cdot}2$, while a point moving at the maximum environmental wind speed would have reached $X = -4$, implying that the front of the disturbance moved at approximately 8 m/s, as opposed to the observed storm speed of 13 m/s. This may be due in part to an underestimation of the maximum environmental wind by the Fourier series of section 6.4.1 (maximum wind as given by the Fourier series is about 14 m/s, 1 m/s less than the observed 700 mb wind, which might not in any case be the maximum if soundings at intermediate levels were available). But in any case, the error in the estimated storm velocity is no greater than typical errors in fig 3.8 obtained with other estimates. The excess potential temperature contours here (fig 6.22) and also for the other case studies do, as anticipated in the previous section, show a warm updraught, cold downdraught everywhere, with the downdraught originating from an unrealistically high level.

The SQL of 22 September 1974 was the only one for which both clear satellite images and a full sounding were available. As it was not entirely typical of SQL's at Minna, with its anomalous motion of the arc front as compared with the cloud mass, a second simulation was carried out (fig 6.23) using the 24 hour 'before' mean sounding of fig 3.12. In the results this time, both arc front and disturbance as a whole moved from approximately 085°, with the arc front oriented perpendicular to the motion. The speed of the system, determined at $T = 4$, was 12 m/s, so that agreement with the observed propagation velocity, 16 m/s from 079° was quite good, though it must be noted that

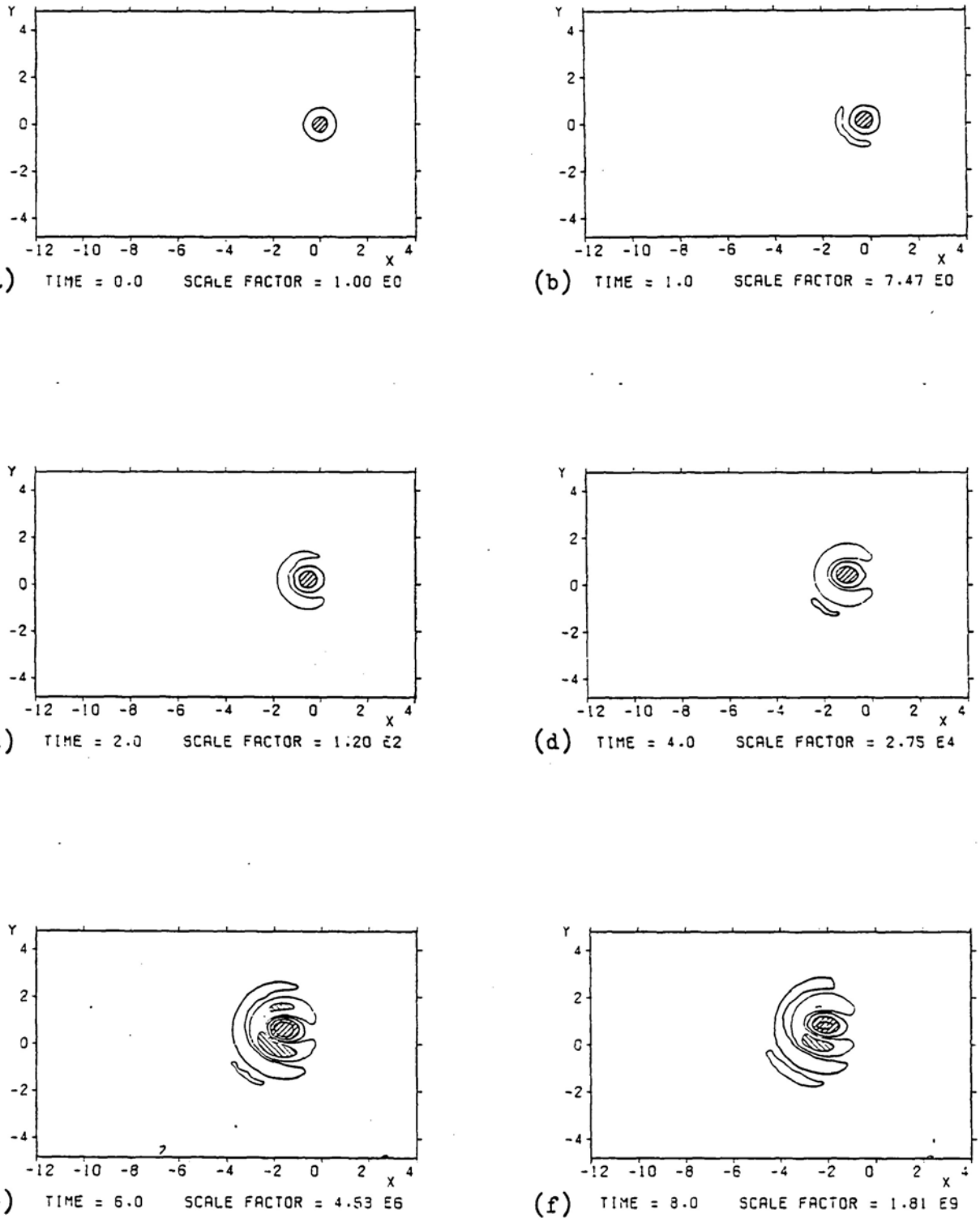


Fig 6.21. Simulation of Minna squall line of 22 September 1974. Horizontal sections of vertical velocity through Z = -0·6. For explanation see sections 6.1.2, 6.4.1.

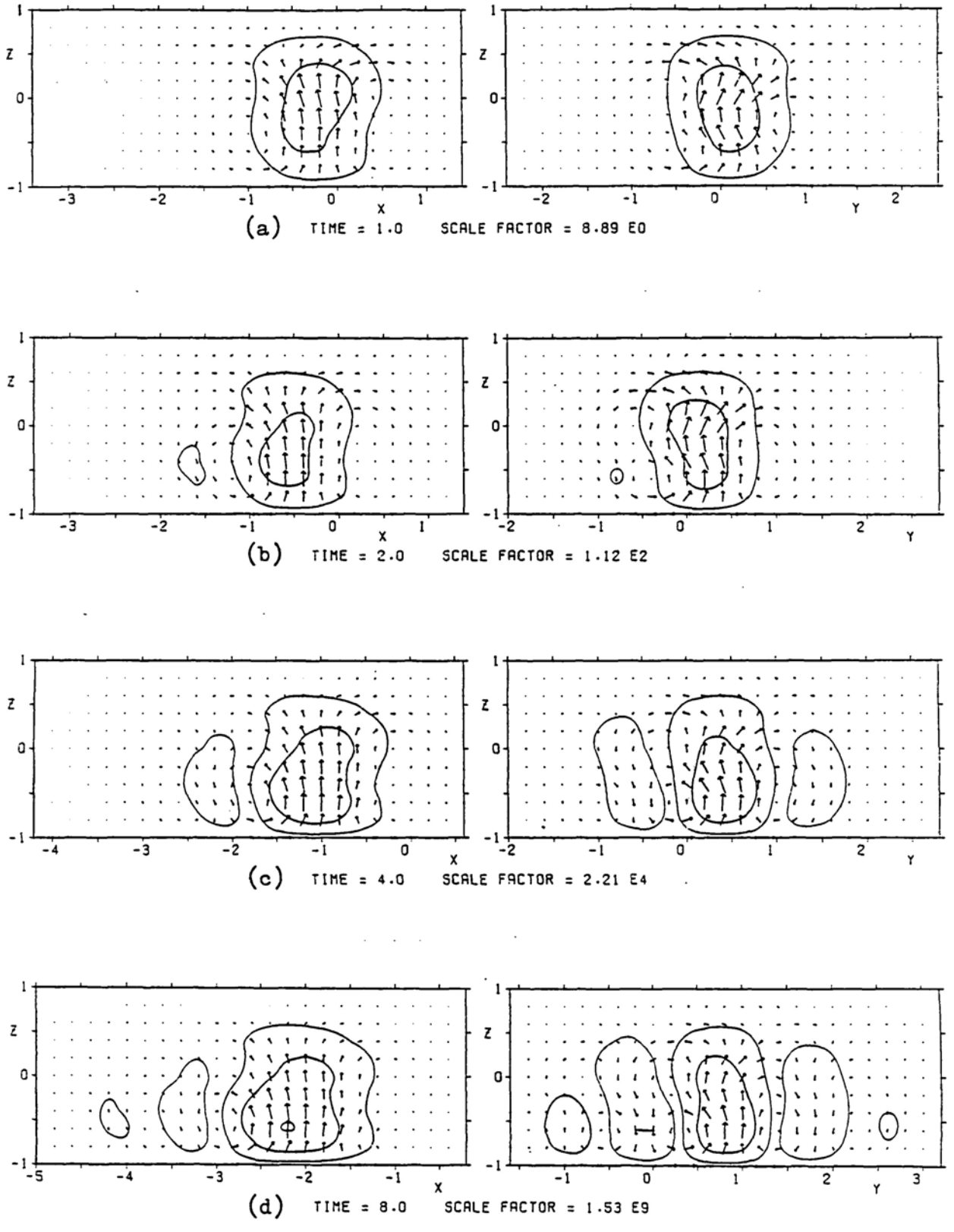


Fig 6.22. Simulation of Minna squall line of 22 September 1974. Vertical sections of perturbation velocity (arrows) and potential temperature excess (contours) in the planes

(a) Y = 0 and X = −0·4 (b) Y = 0·4 and X = −0·4

(c) Y = 0·4 and X = −1·2 (d) Y = 0·8 and X = −2·0.

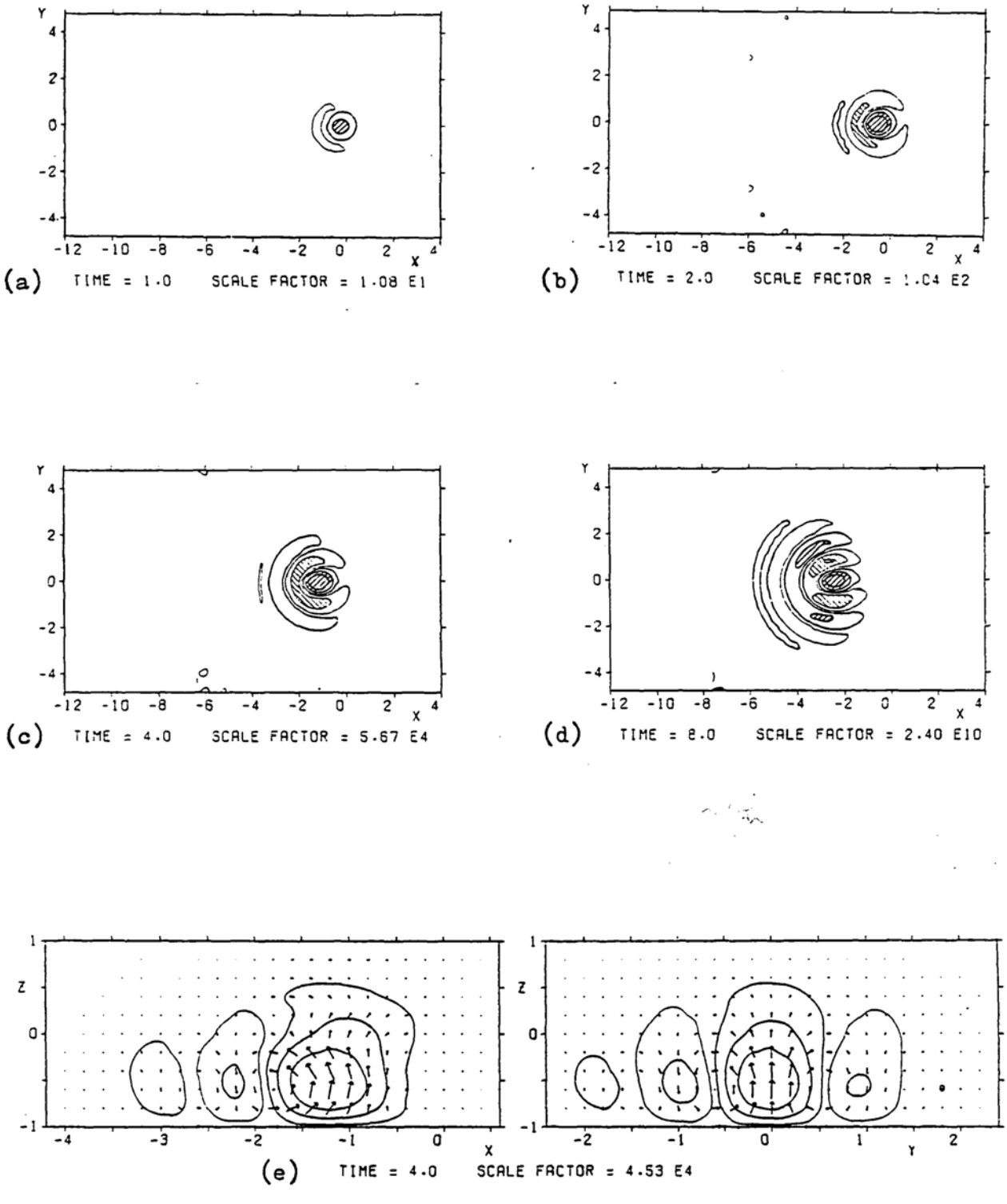


Fig 6.23. Simulation based on Minna mean sounding.
(a) - (d) Horizontal sections of vertical velocity through Z = -0·6
(e) Vertical sections of perturbation velocity (arrows) and potential temperature excess (contours) in the planes Y = 0 and X = -1·2.

whereas the observed speed was greater than the wind at any level, the model speed was slightly less than the maximum wind. This again may be due in part to the underestimation of the maximum wind by the Fourier series, particularly since the maximum average wind in fig 3.12a is likely to be significantly less than the average maximum wind. But it is also interesting to note that Thorpe (personal communication - see section 4.4.3) was unable to generate a SQL with the model of Miller and Pearce (1974) using a West African profile, apparently because the storm speed, as determined by the location of successive cells, did not match the speed of the downdraught outflow.

6.4.3 VIMHEX Squall Line.

The final simulation which will be presented is of the Venezuelan SQL of 24 July 1972 (disturbance no. 47 of VIMHEX), modelled in Moncrieff and Miller (1976) and in Marroquin and Raymond (1979) - see sections 4.4.3 and 4.1.2 respectively. The sounding, fig 6.24, differs from West African soundings in the complete absence of an upper level easterly jet, upper winds instead being north westerly. The thermodynamic profile shows no low level inversion, so surface air has only to be lifted to 800 mb before becoming buoyant; this greater buoyancy, as compared with the West African soundings is to be expected since the SQL arrived at 1800, only three quarters of an hour after the sounding was taken.

Results of the simulation (fig 6.25) show a disturbance speed of 18 m/s (as found at T = 6), which is in this case slightly greater than the maximum environmental wind speed, though the observed storm speed, 15·3 m/s was rather less. The model storm moved from 115°, well to the north of the observed motion from 065°, the orientation of the arc front, 040 - 220° correspondingly differing from the observed 155 - 335°. This is not however surprising since the strongest wind in fig 6.24, that at 700 mb, was 16·5 m/s from 108°, and did therefore have a significant southerly component. Perhaps therefore in this case the motion of the observed SQL was determined by some synoptic scale feature such as a trough, as suggested by Moncrieff and Miller (1976).

6.4.4 Comparison with other Models.

A direct comparison of all the various models is difficult in that there is no single storm to which they have all been applied. Most widely studied was the Venezuelan SQL of the previous section, though even for this, Raymond has published no results for the initial value problem; furthermore, nearly all the model predictions for the velocity

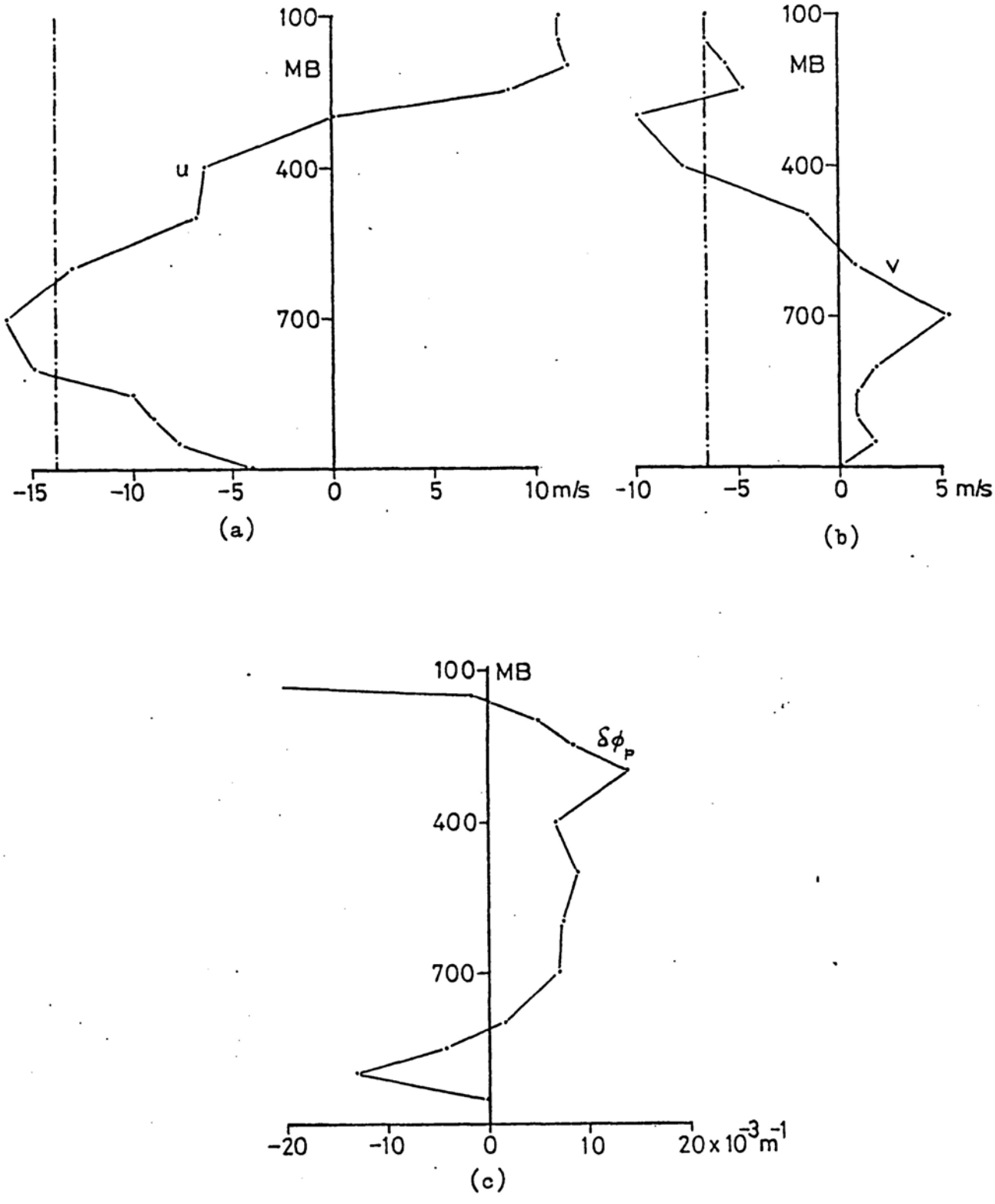


Fig 6.24. Venezuelan sounding at 1713 on 24 July 1972 for
(a) Easterly wind component u (b) Southerly wind component v
(c). Parcel log potential temperature excess $\delta\phi_p$

Dash-dot line shows motion of squall line.

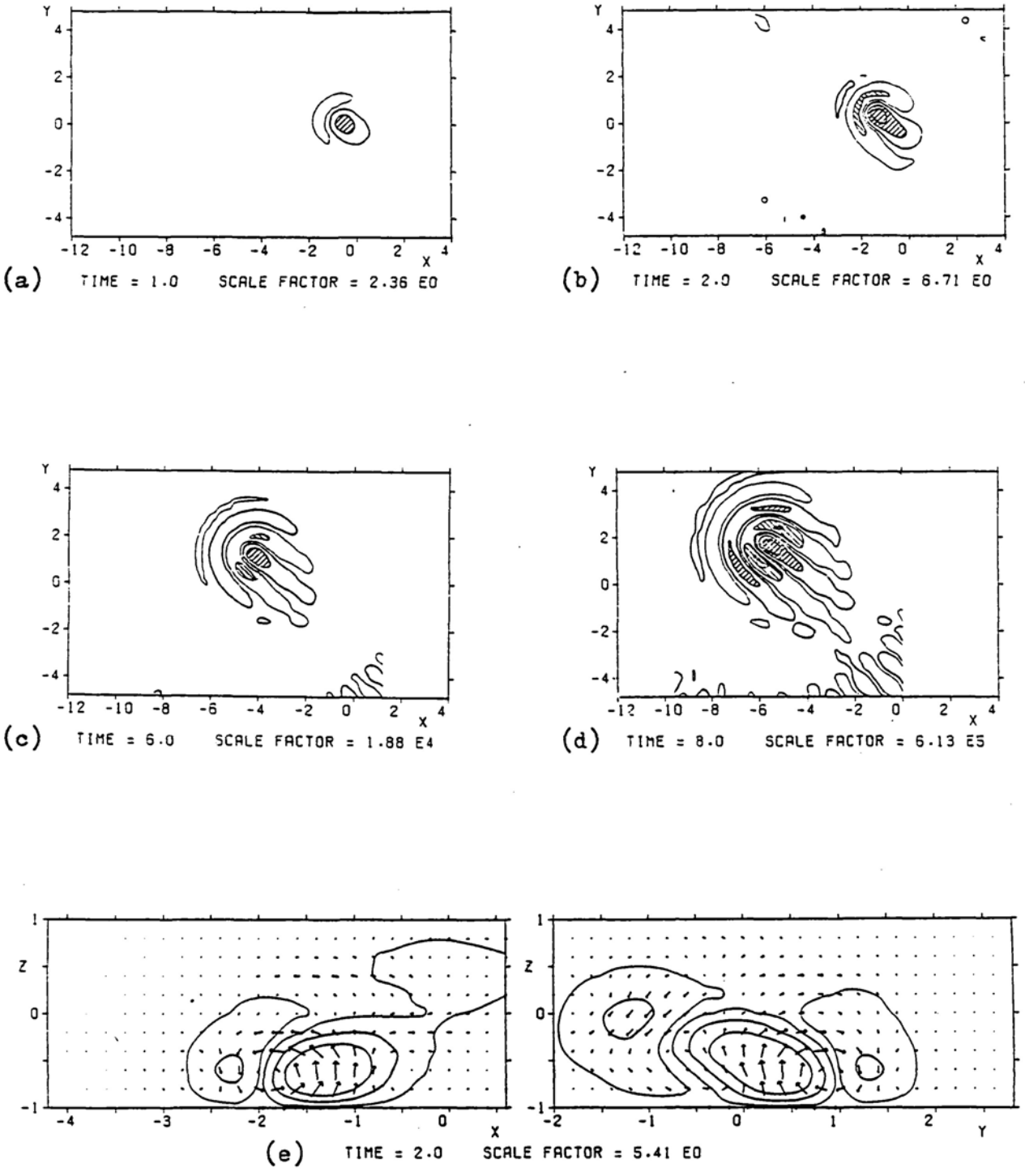


Fig 6.25. Simulation of Venezuelan squall line of 24 July 1972.

(a) - (d) Horizontal sections of vertical velocity through Z = -0·6

(e) Vertical sections of perturbation velocity (arrows) and potential temperature excess (contours) in the planes Y = 0·4 and X = -1·2.

of this storm differed significantly from what was observed, possibly because of the trough suggested above, so that this may not be altogether a representative storm to study. It will however be used as the basis of comparison, supplemented by the other results where appropriate.

(a) Storm Velocity.

Marroquin and Raymond (1979) noted that for this storm their group velocity vector varied considerably with wavenumber, and their model badly underestimated the storm speed (by 5 m/s) though giving a reasonable prediction of direction (fig 4.2); the variation of group velocity may be related to the fact that group velocities lie on a circle, as shown in section 5.6.2, and the underestimate of the speed could have arisen from using the rear rather than the forward edge of that circle for prediction. It is not however then clear why the previous section with a similar model should have estimated storm speed reasonably well, but be considerably in error on direction (by 50°), though it may be noted that Fernandez' estimate using the maximum environmental wind (section 3.1.3) is similarly in error. Raymond's (1975) wave CISK model gave a very poor estimate of storm velocity (in error by nearly 15 m/s - see fig 4.2), though in fairness it must be noted that for other SQL's the observed storm speed usually lay close to the computed propagation velocity curve, even though not near to the point of maximum amplification.

The Moncrieff-Miller speed (3.5) was 17 m/s which, like the speed obtained above is a slight over-estimate (by 2 m/s); if the direction is assumed to be that of the mean wind (as suggested in section 3.1.3), say 070° (though this depends significantly on the depth of the layer considered), then in contrast to the poor showing in fig 3.8, a very fair estimate has here been obtained. This is even rather better than was achieved by the Moncrieff and Miller (1976) simulation (section 4.4.3) where the estimated speed of 13 m/s was slightly small, but the estimated direction was well to the north of the observed motion, though not as seriously in error as the present model; also it should be noted that Moncrieff and Miller (1976) did give a reasonable orientation, 155 - 335° for the line.

(b) Storm Structure.

Though Raymond has not actually published any initial value problem results for SQL's, his (1976) simulations of other storms (section 4.2.2) suggest certain shortcomings in common with the

simulations above, namely growth to unrealistically large amplitudes, failure of the initial cell to dissipate, cold downdraughts, rising again of downdraught air, and origin of the downdraught near the tropopause. These problems of linear systems will be taken up in the closing section, and are clearly avoided by a fully non-linear numerical model such as that of Moncrieff and Miller (1976), which was able to give a much better picture of storm structure, particularly as regards the downdraught. One aspect in which the present model is superior however is the formation of the arc front (presumably made possible by the greater resolution achieved with the Fourier transform method), and of course various other deductions, especially on the role of the jet, have also arisen from the linear analysis.

6.5 CONCLUDING REMARKS.

Certain limitations of the linear system are evident in the case studies presented, notably

(a) Even assuming initial perturbation speeds to be only those appropriate to a cumulus, of order a few centimetres per second, the large scale factors which were obtained by the time the second updraught arc has appeared (in excess of 10^9 for the simulations at Minna) imply quite unrealistic perturbation speeds. This over-rapid growth must be due partly to the omission of non-linear terms, partly to the simplified thermodynamics which are likely to overestimate the buoyancy, especially in the downdraught.

(b) The initial cell did not eventually dissipate, but instead always had the greatest amplitude. Again omission of non-linear terms may be partly to blame, but the main cause must be thermodynamic, in that air is treated as buoyant no matter what its past history, so that for example, air rising in the arc front is then available to rise again in the main updraught.

(c) Also as a result of the unrealistic thermodynamics, the downdraught was always cold and originated near the tropopause, as anticipated in section 6.4.1.

(d) As remarked in section 6.1.2, the spacing obtained for the cells is less than that normally observed even when Rayleigh number is given its smallest realistic value. Here it is likely that the main reason is omission of the non-linear terms.

In spite of these limitations however, the straightforward unforced linear model can give considerable insight into some aspects of SQL generation, in particular

(a) In the tropics, the need for a jet to generate disturbances moving as fast as, or faster than the maximum environmental wind speed is explained (section 5.6.1) and a reason is given (section 6.2.4c) why this jet should be at the mid level rather than at an upper level; also a justification is provided (section 5.6.2) for the Fernandez (1981) forecasting rule that the storm velocity should be close to the maximum mid level environmental wind velocity. In addition, the nature of a tropical SQL is seen (section 6.1.1) as an expanding ring of convection in which an arc front is followed by individual cells, rather than as a two-dimensional line, and this picture corresponds well with satellite images (e.g. fig 2.4).

(b) In middle latitudes on the other hand where there is no jet, insight is provided (section 6.1.1) as to why SQL's should take the form of transverse lines of cells moving at some mid level environmental wind speed. Furthermore, the influence of a transverse velocity component in which there is a maximum is suggested (section 6.3.4) as a cause of storm splitting.

REFERENCES.

Abramowitz, M. and Stegun, I.A. 1964: Handbook of mathematical functions. Publ. U.S. Nat. Bur. Standards.

Acton, F.S. 1970: Numerical methods that work. Publ. Harper and Row.

Adejokun, J.A. 1964: The three-dimensional structure of the inter-tropical discontinuity over Nigeria. Nigerian Met. Dept. Tech. Note no. 39.

Arnason, G., Greenfield, R.S. and Newburg, E.A. 1968: A numerical experiment in dry and moist convection including the rain stage. J. Atmos. Sci. 25, 404-415.

Asai, T. 1964: Cumulus convection in the atmosphere with vertical wind shear: numerical experiment. J. Met. Soc. Japan 42, 245-259.

Asai, T. 1970a: Three-dimensional features of thermal convection in a plane Couette flow. J. Met. Soc. Japan 48, 18-29.

Asai, T. 1970b: Stability of a plane parallel flow with variable vertical shear and unstable stratification. J. Met. Soc. Japan 48, 129-138.

Asai, T. 1972: Thermal instability of a shear flow turning the direction with height. J. Met. Soc. Japan 50, 525-532.

ASECNA 1974: Operation pre-GATE ASECNA, tome 1, 1-10 Août 1973. Bureau d'Etudes, ASECNA.

ASECNA 1975: Operation pre-GATE ASECNA, tome 2: Complements d' analyse, 1-10 Août 1973. Bureau d'Etudes, ASECNA.

Aspliden, C.I., Tourre, Y. and Sabine, J.B. 1976. Some climatological aspects of West African disturbance lines during GATE. Mon. Wea. Rev. 104, 1029-1035.

Banks, W.H.H., Drazin, P.G. and Zaturska, M.B. 1976: On the normal modes of parallel flow of inviscid stratified fluid. J. Fluid Mech. 75, 149-171.

Barrefors, B.B. 1965: Disturbances in West Africa as gravity waves in the inter-tropical discontinuity surface. Nigerian Met. Dept. Tech. Note no. 29.

Beebe, R.G. and Bates, F.C. 1955: A mechanism for assisting in the release of convective instability. Mon. Wea. Rev. 83, 1-10.

Benjamin, T.B. 1961: The development of three-dimensional disturbances in an unstable film of liquid flowing down an inclined plane. J. Fluid Mech. 10, 401-419.

Benjamin, T.B. 1968: Gravity currents and related phenomena. J. Fluid Mech. 31, 209-248.

Bers, A. 1975: Linear waves and instabilities. Physique de plasmas, ed. de Witt, C. and Peyraud, J., publ Gordon and Breach.

Betchov, R. and Criminale, W.O. 1967: Stability of parallel flows. Publ. Academic Press.

Betts, A.K. 1978: Convection in the tropics. Meteorology over the tropical oceans, ed. Shaw, D.B., R. Met. Soc., 105-132.

Betts, A.K., Grover, R.W. and Moncrieff, M.W. 1976: Structure and motion of tropical squall lines over Venezuela. Q.J.R. Met. Soc. 102, 395-404.

Blackburn, M. 1979: A comparison of formulations concerning available potential energy. M.Sc. Thesis, Imperial College, London.

Bolton, D. 1980a: The computation of equivalent potential temperature. Mon. Wea. Rev. 108, 1046-1053. See Appendix C.

Bolton, D. 1980b: Application of the Miles theorem to forced linear perturbations. J. Atmos. Sci. 37, 1639-1642.

Boussinesq, J. 1903: Théorie analytique de la chaleur, 2. Publ. Gauthier Villars, Paris.

Brown, J.M. 1979: Mesoscale unsaturated downdraughts driven by rainfall evaporation: a numerical study. J.Atmos. Sci. 36, 313-338.

Browning, K.A. 1962: Cellular structure of convective storms. Met. Mag. 91, 341-350.

Browning, K.A. 1964: Airflow and precipation trajectories within severe local storms which travel to the right of the winds. J. Atmos. Sci. 21, 634-639.

Browning, K.A. 1968: The organization of severe local storms. Weather 23, 429-434.

Browning, K.A. 1977: The structure and mechanism of hailstorms. Hail: a review of hail science and hail suppression, Met. Monog. no. 38, ed Foote, G.B. and Knight, C.A., Am. Met. Soc., 1-43.

Burpee, R.W. 1972: The origin and structure of easterly waves in the lower troposphere of North Africa. J. Atmos. Sci. 29, 77-90.

Burpee, R.W. 1974: Characteristics of North African easterly waves during the summers of 1968 and 1969. J. Atmos. Sci. 31, 1556-1570.

Burpee, R.W. 1975: Some features of synoptic-scale waves based on a compositing analysis of GATE data. Mon. Wea. Rev. 103, 921-925.

Byers, H.R. and Battan, L.J. 1949: Some effects of vertical wind shear on thunderstorm structure. Bull. Am. Met. Soc. 30, 168-175.

Byers, H.R. and Braham, R.R. 1949: The thunderstorm: report of the Thunderstorm Project. U.S. Wea. Bur.

Carlson, T.N. 1969a: Synoptic histories of three African disturbances that developed into Atlantic hurricanes. Mon. Wea. Rev. 97, 256-276.

Carlson, T.N. 1969b: Some remarks on African disturbances and their progress over the tropical Atlantic. Mon. Wea. Rev. 97, 716-726.

Carlson, T.N. and Ludlam, F.H. 1968: Conditions for the occurrence of severe local storms. Tellus 20, 203-226.

Case, K.M. 1960a: Stability of inviscid plane Couette flow. Phys. Fluids 3, 143-148.

Case, K.M. 1960b: Stability of an idealized atmosphere. I. Discussion of results. Phys. Fluids 3, 149-154.

Charba, J. 1974: Application of gravity current model to analysis of squall-line gust front. Mon. Wea. Rev. 102, 140-156.

Chimonas, G. 1979: Algebraic disturbances in stratified sheared flows. J. Fluid Mech. 90, 1-19.

Chisholm, A.J. and Renick, J.H. 1972: The kinematics of multicell and supercell Alberta hailstorms, Alberta Hail Studies, 1972. Res. Council of Alberta, Hail Studies Rep. no 72-2, 24-31.

Clark, T.L. 1973: Numerical modelling of the dynamics and microphysics of warm cumulus convection. J. Atmos. Sci. 30, 857-878.

Connor, J.J. and Brebbia, C.A. 1976: Finite element techniques for fluid flows. Publ. Newnes-Butterworths.

Criminale, W.O. and Kovasznay, L.S.G. 1962: The growth of localized disturbances in a laminar boundary layer. J. Fluid Mech. 14, 59-80.

Dhonneur, G. 1974: Les lignes de grains. Ch. 9, Nouvelle approche des realités meteorologiques de l'Afrique Occidentale et Centrale. Ph.D. Thesis, Univ. of Dakar, 377-414.

Drazin, P.G. 1958: The stability of a shear layer in an unbounded heterogeneous inviscid fluid. J. Fluid Mech. 4, 214-224.

Drazin, P.G. 1961: On the steady flow of a fluid of variable density past an obstacle. Tellus 13, 239-251.

Drazin, P.G. and Howard, L.N. 1962: The instability to long waves of unbounded parallel inviscid flow. J. Fluid Mech. 14, 257-283.

Drazin, P.G. and Howard, L.N. 1966: Hydrodynamic stability of parallel flow of inviscid fluid. Adv. Appl. Mech. 9, 1-89, publ. Academic Press.

Dubreil-Jacotin, M.L. 1935: Complément à une note antérieure sur les ondes de type permanent dans les liquides héterogènes. Atti Accad. Lincei, Rend. Cl. Sci. Fis. Mat. Nat. (6), 21, 344-346.

Einaudi, F. and Lalas, D.P. 1976: The effect of boundaries on the stability of inviscid stratified shear flows. J. Appl. Mech. 43, 243-248.

Eisler, T.J. 1965: Stability of shear flow in an unstable layer. Phys. Fluids 8, 1635-1640.

Eldridge, R.H. 1957: A synoptic study of West African disturbance lines. Q.J.R. Met. Soc. 83, 303-314.

Eliassen, A., Høiland, E. and Riis, E. 1953: Two-dimensional perturbation of a flow with constant shear of a stratified fluid. Publ. 1, Inst. for Weather and Climate Res., Norwegian Acad. Sci. Letters.

Fankhauser, J.C. 1971: Thunderstorm-environment interactions determined from aircraft and radar observations. Mon. Wea. Rev. 99, 171-192.

Fernandez, W. 1981: Environmental conditions and structure of the West African and Eastern Tropical Atlantic squall lines. To appear in Arch. Met. Geoph. Biokl., Ser. A.

Fernandez, W. and Thorpe, A.J. 1979: An evaluation of theories of storm motion using observations of tropical convective systems. Mon. Wea. Rev. 107, 1306-1319.

Fjørtoft, R. 1950: Application of integral theorems in deriving criteria of stability of laminar flow and for the baroclinic circular vortex. Geofys. Publ. 17, 1-52.

Fortune, M.A. 1977: The West African squall line: a satellite perspective of a tropical tempest. M.Sc. Thesis, Univ. Wisconsin.

Fortune, M.A. 1980: Properties of African squall lines inferred from time-lapse satellite imagery. Mon. Wea. Rev. 108, 153-168.

Frank, W.M. 1978: The life cycles of GATE convective systems. J. Atmos. Sci. 35, 1256-1264.

Froberg, C.E. 1969: Introduction to numerical analysis. Publ. Addison-Wesley.

Fulks, J.R. 1951: The instability line. Compendium of Meteorology, ed. Malone, T.F., Am. Met. Soc., 647-652.

Fujita, T. 1965: Formation and steering mechanisms of tornado cyclones and associated hook echoes. Mon. Wea. Rev. 93, 67-78.

Fujita, T. and Grandoso, H. 1968: Split of a thunderstorm into anticyclonic and cyclonic storms and their motion as determined from numerical model experiments. J. Atmos. Sci. 25, 416-439.

Gage, K.S. and Reid, W.H. 1968: The stability of thermally stratified plane Poiseuille flow. J Fluid Mech. 33, 21-32.

Garcia, R.V. 1956: Barotropic waves in straight parallel flow with curved velocity profile. Tellus 8, 82-93.

Gaster, M. 1968: The development of three-dimensional wave packets in a boundary layer. J. Fluid Mech. 32, 173-184.

Gaster, M. and Davey, A. 1968: The development of three-dimensional wave packets in unbounded parallel flows. J. Fluid Mech. 32, 801-808.

Gokhale, N.R. 1975: Hailstorms and hailstone growth. State Univ. of New York Press.

Gossard, E.E. and Hooke, W.H. 1975: Waves in the atmosphere. Publ. Elsevier.

Green, J.S.A. 1970: Transfer properties of large-scale eddies and the general circulation of the atmosphere. Q.J.R. Met. Soc. 96, 157-185.

Green, J.S.A. and Pearce, R.P. 1962: Cumulonimbus convection in shear. Tech. note no. 12, Dept. Met., Imperial College, London.

Grover, R.W. 1974: Characteristics of tropical squall lines over Venezuela. Atmos. Sci. paper no. 228, Colorado State University.

Gurka, J.J. 1976: Satellite and surface observations of strong wind zones accompanying thunderstorms. Mon. Wea. Rev. 104, 1484-1493.

Hamilton, R.A. and Archbold, J.W. 1945: Meteorology of Nigeria and adjacent territory. Q.J.R. Met. Soc. 71, 231-262.

Hane, C.E. 1973: The squall line thunderstorm: numerical experimentation. J.Atmos. Sci. 30, 1672-1690.

Hazel, P. 1972: Numerical studies of the stability of inviscid stratified shear flows. J. Fluid. Mech. 51, 39-61.

Houze, R.A. 1977: Structure and dynamics of a tropical squall-line system. Mon. Wea. Rev. 105, 1540-1567.

Howard, L.N. 1964: The number of unstable modes in hydrodynamic stability problems. J. de Mech. 3, 433-443.

Huschke, R.E., ed. 1959: Glossary of Meteorology. Am. Met. Soc.

Kelly, R.E. 1978: The onset and development of Rayleigh-Benard convection in shear flows: a review. Proc. Int. Conf. Phys. Chem. and Hydrodynamics, publ Hemisphere Publ. Corp.

Klemp, J.B. and Wilhemson, R.B. 1978a: The simulation of three-dimensional convective storm dynamics. J. Atmos. Sci. 35, 1070-1096.

Klemp, J.B. and Wilhemson, R.B. 1978b: Simulations of right and left moving storms produced through storm splitting. J. Atmos. Sci. 35, 1097-1110.

Kuo, H.L. 1963: Perturbations of plane Couette flow in stratified fluid and origin of cloud streets. Phys. Fluids 6, 195-211.

Lalas, D.P. and Einaudi, F. 1976: On the characteristics of gravity waves generated by atmospheric shear layers. J. Atmos. Sci. 33, 1248-1259.

Lamb, H. 1932: Hydrodynamics. Publ. C.U.P.

Latrasse, J. 1972: Photographies prises par satellites - elements d' application à la météorologie tropicale. Direction de l'Exploitation Météorologique, ASECNA, publ. no. 22.

Le Roux, M. 1971: La dynamique des precipitations en Afrique Occidentale. Ph.D. Thesis, Univ. of Dakar, 1970. Direction de l'Exploitation Météorologique, ASECNA, publ. no. 39.

Lilly, D.K. 1962: On the numerical simulation of buoyant convection. Tellus 14, 148-172.

Lilly, D.K. 1975: Severe storms and storm systems: scientific background, methods and critical questions. Pure Appl. Geophys. 113, 713-734.

Lilly, D.K. 1979: The dynamical structure and evolution of thunder-storms and squall lines. Ann. Rev. Earth Planet. Sci. 7, 117-161.

Lin, C.C. 1955: The theory of hydrodynamic stability. Publ. C.U.P.

Lindzen, R.S. 1974: Wave-CISK in the tropics. J. Atmos. Sci. 31, 156-179.

Long, R.R. 1953: Some aspects of the flow of stratified fluids. 1. A theoretical investigation. Tellus 5, 42-58.

Long, R.R. 1965: On the Boussinesq approximation and its role in the theory of internal waves. Tellus 17, 46-52.

Ludlam, F.H. 1963: Severe local storms: a review. Met. Monog. no.27, ed. Atlas, D., Am. Met. Soc., 1-30.

Ludlam, F.H. 1980: Cumulonimbus convection. Ch. 8, Clouds and Storms, publ. Penn. State Univ. Press.

McBride, J.L. and Gray, W.M. 1980: Mass divergence in tropical weather systems. Paper I: Diurnal variation. Q.J.R. Met Soc. 106, 501-516.

McIntyre, M.E. 1978: Absolute instabilities, convective instabilities and the instability cone. Unpublished manuscript.

Malkus, J.S. and Witt, G. 1959: The evolution of a convective element: a numerical calculation. The atmosphere and the sea in motion, ed. Bolin, B., Rockefeller Inst. Press, 425-439.

Mansfield, D.A. 1977: Squall lines observed in GATE. Q.J.R. Met. Soc. 103, 569-574.

Marroquin, A. and Raymond, D.J. 1979: Predictions of thunderstorm movement by a linearized convective overturning model. Presented at 11th Conf. on Severe Local Storms, Oct. 2-5 1979, Kansas City, Missouri. Unpublished manuscript.

Marwitz, J.D. 1972: The structure and motion of severe hailstorms. Parts I, II and III. J. Appl. Met. 11, 166-201.

Michalke, A. 1964: On the inviscid instability of the hyperbolic tangent velocity profile. J. Fluid Mech. 19, 543-556.

Miles, J.W. 1961: On the stability of heterogeneous shear flows. J. Fluid Mech. 10, 496-508.

Miles, J.W. 1963: On the stability of heterogeneous shear flows. Part 2. J. Fluid Mech. 16, 209-227.

Miles, J.W. 1968: Lee waves in a stratified flow.
a: Part 1. Thin barrier. J. Fluid Mech. 32, 549-567.
b: Part 2. Semi-circular obstacle. J. Fluid Mech. 33, 803-814.

Miller, M.J. 1978: The Hampstead storm: a numerical simulation of a quasi-stationary cumulonimbus system. Q.J.R. Met. Soc. 104, 413-427.

Miller, M.J. and Betts, A.K. 1977: Travelling convective storms over Venezuela. Mon. Wea. Rev. 105, 833-848.

Miller, M.J. and Pearce, R.P. 1974: A three-dimensional primitive equation model of cumulonimbus convection. Q.J.R. Met. Soc. 100, 133-154.

Moncrieff, M.W. 1978: The dynamical structure of two-dimensional steady convection in constant vertical shear. Q.J.R. Met. Soc. 104, 543-567.

Moncrieff, M.W. and Green, J.S.A. 1972: The propagation and transfer properties of steady convective overturning in shear. Q.J.R. Met. Soc. 98, 336-352.

Moncrieff, M.W. and Miller, M.J. 1976: The dynamics and simulation of tropical cumulonimbus and squall lines. Q.J.R. Met. Soc. 102, 373-394.

Newton, C.W. 1950: Structure and mechanism of the prefrontal squall line. J. Met. 7, 210-222.

Newton, C.W. 1963: Dynamics of severe convective storms. Met. Monog. no. 27, ed. Atlas, D., Am. Met. Soc., 33-58.

Newton, C.W. 1966: Circulations in large sheared cumulonimbus. Tellus 18, 699-712.

Newton, C.W. and Newton, H.R. 1959: Dynamical interactions between large convective clouds and environment with vertical shear. J. Met. 16, 483-496.

Norquist, D.C., Recker, E.E. and Reed, R.J. 1977: The energetics of African wave disturbances as observed during phase III of GATE. Mon. Wea. Rev. 105, 334-342.

Obasi, G.O.P. 1976: Some statistics concerning the disturbance lines of West Africa. Unpublished manuscript.

Ogura, Y. and Charney, J.G. 1960: A numerical study of thermal convection in the atmosphere. Proc. Internat. Symposium on Num. Wea. Prediction, Tokyo, Met. Soc. Japan, 431-452.

Okulaja, F.O. 1970: Synoptic flow perturbations over West Africa. Tellus 22, 663-680.

Olver, F.W.J. 1974: Asymptotics and special functions. Publ. Academic Press.

Omotosho, J.A. 1976: A survey of the temperature and wind fields over tropical West Africa and their relation to the line squall. B.Sc. project report, Geophys. Dept., Reading Univ.

Orville, H.D. and Sloan, L.J. 1970: A numerical simulation of the life history of a rainstorm. J. Atmos. Sci. 27, 1148-1159.

Pastushkov, R.S. 1975: The effects of vertical wind shear on the evolution of convective clouds. Q.J.R. Met. Soc. 101, 281-291.

Payne, S.W. and McGarry, M.M. 1977: The relationship of satellite-inferred convective activity to easterly waves over West Africa and the adjacent ocean during phase III of GATE. Mon. Wea. Rev. 105, 413-420.

Pedlosky, J. 1964: An initial value problem in the theory of baroclinic instability. Tellus 16, 12-17.

Porter, J.M., Means, L.L., Hovde, J.E. and Chappell, W.B. 1955: A synoptic study on the formation of squall lines in the North Central United States. Bull. Am. Met. Soc. 36, 390-396.

Priestley, C.H.B. 1959: Turbulent transfer in the lower atmosphere. Publ. Univ. Chicago Press.

Rayleigh, Lord, 1880: On the stability or instability of certain fluid motions. 'Scientific papers', vol. 1, publ. C.U.P., 474-487.

Raymond, D.J. 1975: A model for predicting the movement of continuously propagating convective storms. J. Atmos. Sci. 32, 1308-1317.

Raymond, D.J. 1976: Wave-CISK and convective mesosystems. J. Atmos. Sci. 33, 2392-2398.

Reed, R.J., Norquist, D.C. and Recker, E.E. 1977: The structure and properties of North African wave disturbances as observed during phase III of GATE. Mon. Wea. Rev. 105, 317-333.

Reiter, E.R. 1963: Jet stream meteorology. Publ. Univ. Chicago Press.

Rennick, M.A. 1976: The generation of African waves. J. Atmos. Sci. 33, 1955-1969.

Riehl, H. 1954: Tropical meteorology. Publ. McGraw-Hill.

Riehl, H., Rossignol, D. and Lückefedt, W. 1974: On the structure and maintenance of West African squall lines. Direction de l'Exploitation Météorologique, ASECNA.

Rosenbluth, M.N. and Simon, A.S. 1964: Necessary and sufficient conditions for stability of plane parallel inviscid flow. Phys. Fluids 7, 557-558.

Sasaki, Y. 1959: A numerical experiment of squall line formation. J. Met. 16, 347-353.

Savic, P. 1941: On accoustically effective vortex motion in gaseous jets. Phil. Mag. 32, 245-252.

Savic, P. and Murphy, J.W. 1943: The symmetrical vortex street in sound sensitive plane jets. Phil. Mag. 34, 139-144.

Schlesinger, R.E. 1973: A numerical model of deep moist convection. Part I. Comparative experiments for variable ambient moisture and wind shear. J. Atmos. Sci. 30, 835-856.

Schlesinger, R.E. 1975: A three-dimensional model of an isolated deep convective cloud: preliminary results. J. Atmos. Sci. 32, 934-957.

Schlesinger, R.E. 1978: A three-dimensional model of an isolated thunderstorm. Part I. Comparative experiments for variable ambient wind shear. J. Atmos. Sci. 35, 690-713.

Schove, D.J. 1946: A further contribution to the meteorology of Nigeria. Q.J.R. Met. Soc. 72, 105-110.

Simmons, A.J. 1977: A note on the instability of the African easterly jet. J. Atmos. Sci. 34, 1670-1674.

Simmons, A.J. and Hoskins, B.J. 1979: The downstream and upstream development of unstable baroclinic waves. J. Atmos. Sci. 36, 1239-1254.

Simpson, J.E. 1969: A comparison between laboratory and atmospheric density currents. Q.J.R. Met. Soc. 95, 758-765.

Simpson, J.E. and Britter, R.E. 1980: A laboratory model of an atmospheric mesofront. Q.J.R. Met. Soc. 106, 485-500.

Soong, S.-T. and Ogura, Y. 1973: A comparison between axisymmetric and slab-symmetric cumulus cloud models. J. Atmos. Sci. 30, 879-893.

Spiegel, M.R. 1972: Statistics. Schaum outline series, publ. Mcgraw Hill.

Squire, H.B. 1933: On the stability for three-dimensional disturbances of viscous fluid flow between parallel walls. Proc. Roy. Soc. A 142, 621-628.

Steiner, J.T. 1973: A three dimensional model of cumulus cloud development. J. Atmos. Sci. 30, 414-435.

Sulakvelidze, G.K., Gleishkova N.I. and Fedchenko, L.M. 1970: Forecasting of hail, thunderstorms and showers. Translated from Russian, 1977, by Israel Prog. for Sci. Translations.

Takeda, T. 1965: The downdraught in convective shower-cloud under the vertical wind shear and its significance for the maintenance of convective system. J. Met. Soc. Japan 43, 302-309.

Takeda, T. 1966: Effects of the prevailing wind with vertical shear on the convective cloud accompanied with heavy rainfall. J. Met. Soc. Japan 44, 129-144.

Takeda, T. 1971: Numerical simulation of a precipitating convective cloud: the formation of a 'long-lasting' cloud. J. Atmos. Sci. 28, 350-376.

Tanaka, H. 1975: Quasi-linear and non-linear interactions of finite amplitude perturbations in a stably stratified fluid with hyperbolic tangent shear. J. Met. Soc. Japan 53, 1-31.

Taylor, G.I. 1931: Effect of variation of density on the stability of superposed streams of fluid. Proc. Roy. Soc. A 132, 499-523.

Tepper, M. 1950: A proposed mechanism of squall lines: the pressure-jump line. J. Met 7, 21-29.

Thorpe, A.J. and Guymer, T.H. 1977: The nocturnal jet. Q.J.R. Met. Soc. 103, 633-653.

Thorpe, A.J. and Miller, M.J. 1978: Numerical simulations showing the role of the downdraught in cumulonimbus motion and splitting. Q.J.R. Met. Soc. 104, 873-893.

Thorpe, A.J., Miller, M.J. and Moncrieff, M.W. 1980: Dynamical models of two-dimensional downdraughts. Q.J.R. Met. Soc. 106, 463-485.

Thorpe, S.A. 1969: Neutral eigensolutions of the stability equation for stratified shear flow. J. Fluid Mech. 36, 673-684.

Tollmien, W. 1935: Ein allgemeines Kriterium der Instabilitat Laminarer Geschwindigkeitsverteilungen, Nachr. Ges. Wiss. Göttingen, Math.-Phys. Klasse 50, 79-114.

Turner, J.S. 1973: Buoyancy effects in fluids. Publ. C.U.P.

Uccelini, L.W. 1975: A case study of apparent gravity wave initiation of severe convective storms. Mon. Wea. Rev. 103, 497-513.

Warner, C. 1972: Calculations of updraught shapes in storms. J. Atmos. Sci. 29, 1516-1519.

Whitham, G.B. 1974: Linear and nonlinear waves. Publ. Wiley.

Wilhemson, R. 1974: The life cycle of a thuderstorm in three dimensions. J. Atmos. Sci. 31, 1629-1651.

Wilhemson, R.B. and Klemp, J.B. 1978: A numerical study of storm splitting that leads to long-lived storms. J. Atmos. Sci. 35, 1974-1986.

Winston, J.S., ed. 1956: Forecasting tornadoes and severe thunderstorms. Forecasting guide no. 1, U.S. Wea. Bureau.

Yih, C.S. 1960a: A transformation for non-homentropic flows, with an application to large-amplitude motion in the atmosphere. J. Fluid Mech. 9, 68-80.

Yih, C.S. 1960b: Exact solutions for steady two-dimensional flows of a stratified fluid. J. Fluid Mech. 9, 161-174.

Yih, C.S. 1965: Dynamics of nonhomogeneous fluid flows. Publ. MacMillan.

Yih, C.S. 1967: Equations governing steady three-dimensional large-amplitude motion of a stratified fluid. J. Fluid Mech. 29, 539-544.

Yih, C.S. 1969: Fluid mechanics. Publ. McGraw-Hill.

Zipser, E.J. 1969: The role of organized unsaturated convective downdraughts in the structure and rapid decay of an equatorial disturbance. J. Appl. Met. 8, 799-814.

Zipser, E.J. 1977: Mesoscale and convective-scale downdraughts as distinct components of squall-line structure. Mon. Wea. Rev. 105, 1568-1589.

APPENDIX A. ESTIMATION OF STORM VELOCITIES FROM SURFACE REPORTS OF SQUALLS.

Suppose a SQL is reported at Minna at time T_o, and at N other stations with coordinates (x_i, y_i) relative to Minna at times T_i. Let the squall front be approximated by a parabola passing through Minna at time T_o, and defined by the following parameters.

(q_1, q_2) = storm velocity

q_3 = distance of Minna from axis of parabola

q_4 = radius of curvature of centre of parabolic front.

Then if $v = (q_1^2 + q_2^2)^{\frac{1}{2}}$ = storm speed (A.1)

and $\phi = \tan^{-1}(q_1 / q_2)$ = storm direction (A.2)

coordinates of the i^{th} station relative to Minna along and perpendicular to the storm motion are

$$x_i' = x_i \sin\phi + y_i \cos\phi \quad (A.3)$$

$$y_i' = y_i \cos\phi - x_i \sin\phi \quad (A.4)$$

(see fig A.1 below).

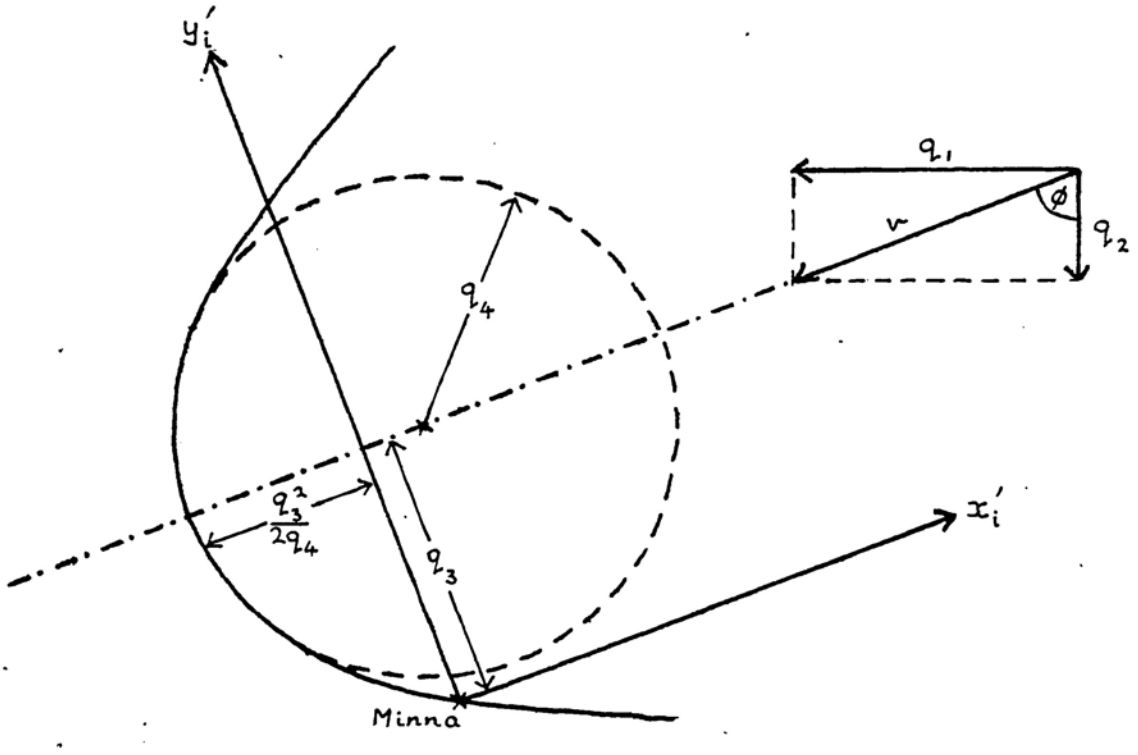


Fig A.1. Parabolic squall front passing through Minna.
Dash-dot line represents axis of parabola; for explanation of symbols see text.

If τ_i is the estimated time of arrival at the i^{th} station,

$$x_i' + \frac{q_3^2}{2q_4} + v_i(\tau_i - T_0) = \frac{(y_i' - q_3)^2}{2q_4} \qquad (A.5)$$

(from the equation of a parabola). The difference between the actual and estimated time is thus

$$\tau_i - T_i = T_0 - T_i + \frac{1}{v_i}\left\{ \frac{(y_i' - q_3)^2 - q_3^2}{2q_4} - x_i' \right\} \qquad (A.6)$$

and an error sum of squares may be formed:

$$E(q_1, q_2, q_3, q_4) = \sum_{i=1}^{N} \frac{(\tau_i - T_i)^2}{w_i} \qquad (A.7)$$

where w_i is a weighting function of the form

$$w_i = x_i^2 + y_i^2 + \text{constant} \qquad (A.8)$$

this form being chosen to attach greater importance to reports at stations nearer to Minna.

A minimum method, adapted from Acton (1970) may now be used to choose some or all of the q_i so as to minimise E. Initial estimates Q_i for the q_i are chosen. With a very small initial step δQ_1, E is evaluated with Q_1 replaced by $Q_1 \pm \delta Q_1$; stepping is continued in the direction in which E was decreased, using an exponentially increasing step length, until E starts to increase again; interval halving is then used to find the step δq_1 which minimises E. This process is repeated in turn for q_2 and whichever (if any) of q_3, q_4 are to be optimised. The procedure may be repeated, starting again with q_1, until the minimum of E is obtained. Convergence is however improved if, after stepping each of the q_i individually, stepping is carried out in the direction $(\delta q_1, \delta q_2, \ldots)$ determined by the individual optimum steps, before returning to the individual stepping of q_1 etc.

APPENDIX B. THREE-DIMENSIONAL LAGRANGIAN VORTICITY EQUATIONS.

B.1 Lagrangian Description.

In the three-dimensional Lagrangian formulation, a fluid element is identified by its position $\underline{r}_o = (x_o, y_o, z_o)$ at some initial time t_o, its density, velocity and vorticity at this time being ρ_o, $\underline{u}_o = (u_o, v_o, w_o)$ and $\underline{\xi}_o = (\xi_o, \eta_o, \zeta_o)$ respectively. If at some subsequent time t, the position and density are $\underline{r} = (x, y, z)$ and ρ, the Jacobian of the transformation $(x, y, z, t) \to (x_o, y_o, z_o, t)$ is provided by the Lagrangian continuity equation

$$\frac{\rho}{\rho_o} \frac{\partial(x, y, z)}{\partial(x_o, y_o, z_o)} = 1 \tag{B.1}$$

This may be used in determining transformations from one set of coordinates to the other. For example, for any field variable ψ,

$$\frac{\partial \psi}{\partial x} \equiv \left(\frac{\partial \psi}{\partial x}\right)_{y,z,t} = \frac{\partial(\psi, y, z)}{\partial(x, y, z)} = \frac{\rho}{\rho_o} \frac{\partial(\psi, y, z)}{\partial(x_o, y_o, z_o)} \tag{B.2}$$

with similar expressions for $\frac{\partial \psi}{\partial y}$, $\frac{\partial \psi}{\partial z}$; conversely

$$\frac{\partial \psi}{\partial x_o} \equiv \left(\frac{\partial \psi}{\partial x_o}\right)_{y_o,z_o,t} = \frac{\rho_o}{\rho} \frac{\partial(\psi, y_o, z_o)}{\partial(x, y, z)} \tag{B.3}$$

In particular

$$\frac{\partial \underline{r}}{\partial x_o} = \frac{\rho_o}{\rho} \frac{\partial(\underline{r}, y_o, z_o)}{\partial(x, y, z)} = \frac{\rho_o}{\rho} \nabla y_o \times \nabla z_o \tag{B.4}$$

and therefore $\frac{\partial \underline{r}}{\partial x_o} \cdot \nabla x_o = 1$, $\frac{\partial \underline{r}}{\partial x_o} \cdot \nabla y_o = \frac{\partial \underline{r}}{\partial x_o} \cdot \nabla z_o = 0$, with similar results for $\frac{\partial \underline{r}}{\partial y_o}$, $\frac{\partial \underline{r}}{\partial z_o}$, so that $\left\{\frac{\partial \underline{r}}{\partial x_o}, \frac{\partial \underline{r}}{\partial y_o}, \frac{\partial \underline{r}}{\partial z_o}\right\}$ and $\left\{\nabla x_o, \nabla y_o, \nabla z_o\right\}$ are reciprocal sets of vectors.

For the time derivatives, the following notation will be adopted

$$\frac{\partial}{\partial t} \equiv \left(\frac{\partial}{\partial t}\right)_{x,y,z} \qquad \frac{D}{Dt} \equiv \left(\frac{\partial}{\partial t}\right)_{x_o,y_o,z_o}$$

Now

$$\frac{\partial \psi}{\partial t} = \frac{D\psi}{Dt} + \frac{\partial \psi}{\partial x_o}\frac{\partial x_o}{\partial t} + \frac{\partial \psi}{\partial y_o}\frac{\partial y_o}{\partial t} + \frac{\partial \psi}{\partial z_o}\frac{\partial z_o}{\partial t}$$

so the derivative following the motion is

$$\frac{D}{Dt} = \frac{\partial}{\partial t} - \frac{\partial x_o}{\partial t}\frac{\partial}{\partial x_o} - \frac{\partial y_o}{\partial t}\frac{\partial}{\partial y_o} - \frac{\partial z_o}{\partial t}\frac{\partial}{\partial z_o} \tag{B.5}$$

B.2 Lagrangian Equations.

As in section 4.3.1, conservation of entropy implies

$$\delta\phi = \phi_o(z_o) - \phi_o(z) \tag{B.6}$$

The momentum equation may be written

$$\frac{D^2\underline{r}}{Dt^2} + \nabla\frac{\delta p}{\rho} - g\delta\phi\,\underline{k} = 0 \qquad (B.7)$$

Taking the scalar product with $\frac{\partial \underline{r}}{\partial x_0}$, and using $\frac{\partial \underline{r}}{\partial x_0}\cdot\nabla \equiv \frac{\partial}{\partial x_0}$ gives

$$\frac{D^2\underline{r}}{Dt^2}\cdot\frac{\partial \underline{r}}{\partial x_0} + \frac{\partial}{\partial x_0}\left(\frac{\delta p}{\rho}\right) - g\delta\phi\frac{\partial z}{\partial x_0} = 0 \qquad (B.8)$$

there being similar equations with y_0, z_0 replacing x_0. Now, integrating along a streamline (indicated by writing SL under the integral sign), as in Lamb (1932)

$$\int_{SL}^{t}\frac{D^2\underline{r}}{Dt^2}\cdot\frac{\partial \underline{r}}{\partial x_0}\,dt = \left[\frac{D\underline{r}}{Dt}\cdot\frac{\partial \underline{r}}{\partial x_0}\right]_0^t - \int_{SL}^{t}\frac{D\underline{r}}{Dt}\cdot\frac{D}{Dt}\left(\frac{\partial \underline{r}}{\partial x_0}\right)dt$$

$$= \frac{D\underline{r}}{Dt}\cdot\frac{\partial \underline{r}}{\partial x_0} - U_0 - \frac{1}{2}\frac{\partial}{\partial x_0}\int_{SL}^{t}\left|\frac{D\underline{r}}{Dt}\right|^2 dt$$

so that (B.8) and the other equations integrate to

$$\frac{D\underline{r}}{Dt}\cdot\frac{\partial \underline{r}}{\partial x_0} = U_0 - \frac{\partial \chi}{\partial x_0} \qquad (B.9)$$

$$\frac{D\underline{r}}{Dt}\cdot\frac{\partial \underline{r}}{\partial y_0} = V_0 - \frac{\partial \chi}{\partial y_0} \qquad (B.10)$$

$$\frac{D\underline{r}}{Dt}\cdot\frac{\partial \underline{r}}{\partial z_0} = W_0 - \frac{\partial \chi}{\partial z_0} - \int_{SL}^{t} g\beta(z_0)(z-z_0)\,dt \qquad (B.11)$$

$$\chi = \int_{SL}^{t}\left\{\frac{\delta p}{\rho} - g(z-z_0)\phi_0(z_0) + g\int_{z_0}^{z}\phi_0(z')\,dz' - \frac{1}{2}\left|\frac{D\underline{r}}{Dt}\right|^2\right\}dt \qquad (B.12)$$

Hence, remembering that $\left\{\frac{\partial \underline{r}}{\partial x_0}, \frac{\partial \underline{r}}{\partial y_0}, \frac{\partial \underline{r}}{\partial z_0}\right\}$ and $\left\{\nabla x_0, \nabla y_0, \nabla z_0\right\}$ are reciprocal sets of vectors

$$\underline{u} = \frac{D\underline{r}}{Dt}\cdot\frac{\partial \underline{r}}{\partial x_0}\nabla x_0 + \frac{D\underline{r}}{Dt}\cdot\frac{\partial \underline{r}}{\partial y_0}\nabla y_0 + \frac{D\underline{r}}{Dt}\cdot\frac{\partial \underline{r}}{\partial z_0}\nabla z_0$$

$$= U_0\nabla x_0 + V_0\nabla y_0 + \left\{W_0 - \int_{SL}^{t} g\beta_0(z_0)(z-z_0)\,dt\right\}\nabla z_0 - \nabla\chi \qquad (B.13)$$

Taking the curl of this and using (B.4) and similar equations gives

$$\frac{\underline{\xi}}{\rho} = \frac{1}{\rho_0}\left[\left\{\xi_0 - g\beta_0(z_0)\frac{\partial}{\partial y_0}\int_{SL}^{t}(z-z_0)\,dt\right\}\frac{\partial \underline{r}}{\partial x_0} + \left\{\eta_0 + g\beta_0(z_0)\frac{\partial}{\partial x_0}\int_{SL}^{t}(z-z_0)\,dt\right\}\frac{\partial \underline{r}}{\partial y_0} + \zeta_0\frac{\partial \underline{r}}{\partial z_0}\right] \qquad (B.14)$$

which is a generalisation of the Lagrangian vorticity equation. Forming the scalar product in turn with $\nabla x_0, \nabla y_0, \nabla z_0$ and expressing vorticity in Lagrangian form:

$$\frac{\underline{\xi}}{\rho}\cdot\nabla x_0 \equiv \frac{1}{\rho_0}\left\{\frac{\partial(x,\frac{Dx}{Dt})}{\partial(y_0,z_0)} + \frac{\partial(y,\frac{Dy}{Dt})}{\partial(y_0,z_0)} + \frac{\partial(z,\frac{Dz}{Dt})}{\partial(y_0,z_0)}\right\} = \frac{1}{\rho_0}\left\{\xi_0 - g\beta_0(z_0)\frac{\partial}{\partial y_0}\int_{SL}^{t}(z-z_0)\,dt\right\} \qquad (B.15)$$

$$\frac{\underline{\xi}}{\rho}\cdot\nabla y_0 \equiv \frac{1}{\rho_0}\left\{\frac{\partial(x,\frac{Dx}{Dt})}{\partial(z_0,x_0)} + \frac{\partial(y,\frac{Dy}{Dt})}{\partial(z_0,x_0)} + \frac{\partial(z,\frac{Dz}{Dt})}{\partial(z_0,x_0)}\right\} = \frac{1}{\rho_0}\left\{\eta_0 + g\beta_0(z_0)\frac{\partial}{\partial x_0}\int_{SL}^{t}(z-z_0)\,dt\right\} \qquad (B.16)$$

$$\frac{\underline{\xi}}{\rho}\cdot\nabla z_0 \equiv \frac{1}{\rho_0}\left\{\frac{\partial(x,\frac{Dx}{Dt})}{\partial(x_0,y_0)} + \frac{\partial(y,\frac{Dy}{Dt})}{\partial(x_0,y_0)} + \frac{\partial(z,\frac{Dz}{Dt})}{\partial(x_0,y_0)}\right\} = 0 \qquad (B.17)$$

These and the continuity equation (B.1) may in principle be solved for (x, y, z) , but are highly non-linear in the derivatives, which renders solution very difficult. (B.17) incidentally is equivalent to the potential vorticity equation.

B.3 Special Cases.

(a) Horizontal Inflow. If inflow is horizontal and takes the form

$$\underline{U}_0 = (U_0(z_0), V_0(z_0), 0) \quad , \tag{B.18}$$

(B.13) reduces to a Clebsh transformation (Lamb 1932)

$$\underline{u} = \left\{ y_0 \xi_0 - x_0 \eta_0 - g\beta_0(z_0) \int_0^t (z - z_0)\, dt \right\} \nabla z_0 + \nabla(U_0 x_0 + V_0 y_0 - \chi) \tag{B.19}$$

where the first term vanishes if there is no inflow vorticity and no buoyancy, leaving the second as a scalar potential.

(b) Steady Flow. If in addition flow is steady, $\frac{\partial x_0}{\partial t} = -U_0$, $\frac{\partial y_0}{\partial t} = -V_0$, and (B.5) reduces to

$$\frac{D}{Dt} = U_0 \frac{\partial}{\partial x_0} + V_0 \frac{\partial}{\partial y_0} \tag{B.20}$$

so that fluid velocity is

$$\underline{u} = \frac{D\underline{r}}{Dt} = U_0 \frac{\partial \underline{r}}{\partial x_0} + V_0 \frac{\partial \underline{r}}{\partial y_0} \tag{B.21}$$

Forming the scalar product with (B.14) and using $\frac{\partial \underline{r}}{\partial x_0} \times \frac{\partial \underline{r}}{\partial y_0} = \frac{\rho_0}{\rho} \nabla z_0$ and similar equations

$$\underline{u} \times \underline{\xi} = \left\{ U_0 \eta_0 - V_0 \xi_0 + g\beta_0(z_0) \left(U_0 \frac{\partial}{\partial x_0} + V_0 \frac{\partial}{\partial y_0} \right) \int_0^t (z - z_0)\, dt \right\} \nabla z_0$$

$$- \left\{ \frac{d}{dz_0} \tfrac{1}{2}(U_0^2 + V_0^2) + g\beta_0(z_0)(z - z_0) \right\} \nabla z_0$$

which, for $V_0 = 0$, is the result of Drazin (1961). The scalar product of this with $\frac{1}{\rho_0} \frac{\partial \underline{r}}{\partial z_0}$ gives on using (B.21)

$$\frac{\underline{\xi}}{\rho} \cdot (U_0 \nabla y_0 - V_0 \nabla x_0) = \frac{1}{\rho_0} \left\{ \frac{d}{dz_0} \tfrac{1}{2}(U_0^2 + V_0^2) + g\beta(z_0)(z - z_0) \right\} \tag{B.23}$$

which is a generalisation of (4.75) (and may be derived from (B.14) directly), while the scalar products with $\frac{1}{\rho_0} \frac{\partial \underline{r}}{\partial x_0}$, $\frac{1}{\rho_0} \frac{\partial \underline{r}}{\partial y_0}$ each reduce to

$$\frac{\underline{\xi}}{\rho} \cdot \nabla z_0 = 0 \tag{B.24}$$

as in (B.17). These two equations, with vorticity expressed in the form

$$\underline{\xi} = \nabla \times \frac{\rho_0}{\rho} (U_0 \nabla y_0 \times \nabla z_0 + V_0 \nabla z_0 \times \nabla x_0) \tag{B.25}$$

were derived using a different method by Yih (1967) for $V_0 = 0$, in which case they can in principle be solved for y_0 and z_0 . They are however still non-linear in the derivatives except in the special case of two-dimensional motion, when $\nabla y_0 = (0, 1, 0)$ and the system reduces to that of section 4.3.1.

APPENDIX C.

The Computation of Equivalent Potential Temperature

DAVID BOLTON

Atmospheric Physics Group, Imperial College, London, England

(Manuscript received 1 August 1979, in final form 18 March 1980)

ABSTRACT

A simplified procedure is described for computation of equivalent potential temperature which remains valid in situations such as in the tropics where a term which is omitted in the derivation of the conventional formula can lead to an error of several degrees absolute. The procedure involves new empirical formulas which are introduced for the saturated vapor pressure of water, the lifting condensation level temperature and the equivalent potential temperature. Errors are estimated for each of these, and results are compared with those obtained by the similar, but more complicated procedures of Betts and Dugan (1973) and Simpson (1978).

1. Introduction

The equivalent potential temperature (also known as pseudo-equivalent potential temperature) will be taken, as in Holton (1972), to be the final temperature θ_E which a parcel of air attains when it is lifted dry adiabatically to its lifting condensation level, then pseudo-wet adiabatically (with respect to water saturation) to a great height (dropping out condensed water as it is formed), then finally brought down dry adiabatically to 1000 mb.

The first two processes are examined by Simpson (1978), the first by Betts and Miller (1975) and the second by Betts and Dugan (1973), hereafter referred to as SS, BM and BD, respectively. SS shows that a term normally neglected in the pseudo-adiabatic ascent can lead to errors of up to 3 K in the computed value of θ_E which would, for instance, result in a significant underestimate of the height to which penetrative convection can reach. Both SS and BD give approximate empirical formulas for correcting this error.

In this paper the formulas of SS and BD are examined and compared with simpler empirical formulas which are proposed, and which are found to permit a better fit to values computed by numerical integration. Estimates are made of the errors introduced at each of the stages for attaining the equivalent potential temperature, including the final dry adiabatic descent.

It should be noted that the definition of equivalent potential temperature given above is not the only possible one, since account could have been taken of heat retained by condensed water, and of latent heat of ice formation, which can affect the value by several degrees, as shown in Saunders (1957). Inclusion of these effects, however, would require a detailed study of cloud microphysics, which is beyond the scope of this paper and, therefore, they have been omitted in keeping with common practice.

2. Constants and empirical formulas

Based on List (1951), using the conversion 1 IT cal = 4.18684 J where necessary to convert to SI units, the following constants and empirical formulas will be used as giving best values for the temperature range $-35°C \leq T \leq 35°C$, and pressure range $200 \text{ mb} \leq p \leq 1000$ mb. For some constants, the error over this range is negligible; for the specific heats, however, there is an appreciable variation with temperature and pressure, and maximum errors are estimated.

a. Temperature

Absolute temperature: $T_K = T + 273.15$, (1)

where T is the temperature in degrees Celsius. For all temperatures apart from the above, a capital subscript will be used to denote absolute, a small subscript Celsius; e.g., for the lifting condensation level temperature, $T_L = T_l + 273.15$.

b. Dry air

Gas constant:

$$R_d = 287.04 \text{ J kg}^{-1} \text{ K}^{-1}.$$

Specific heat at constant pressure:

$$c_{pd} = 1005.7 \pm 2.5 \text{ J kg}^{-1} \text{ K}^{-1}.$$

$$\kappa_d = \frac{R_d}{c_{pd}} = 0.2854 \pm 0.0007.$$

0027-0644/80/071046-08506.00
© 1980 American Meteorological Society

c. Water

Specific heat:

$$c_w = 4190 \pm 30 \text{ J kg}^{-1} \text{ K}^{-1} \quad (\text{for } T \geq 0°\text{C only}).$$

Latent heat of vaporization:

$$L_w = (2.501 - 0.00237\,T) \times 10^6 \text{ J kg}^{-1}. \quad (2)$$

d. Water vapor

Gas constant:

$$R_v = 461.50 \text{ J kg}^{-1} \text{ K}^{-1}.$$

Specific heat at constant pressure:

$$c_{pv} = 1875 \pm 25 \text{ J kg}^{-1} \text{ K}^{-1}.$$

$$\epsilon = \frac{R_d}{R_v} = 0.6220.$$

e. Potential temperature for moist air

An unsaturated parcel moving adiabatically satisfies

$$c_{pm} \frac{dT_K}{T_K} + R_m \frac{dp}{p} = 0, \quad (3)$$

where

$$R_m \approx R_d(1 + 0.608 \times 10^{-3}\, r), \quad (4)$$

$$c_{pm} \approx c_{pd}(p, T_K)[1 + 0.887 \times 10^{-3}\, r], \quad (5)$$

the latter being obtained as the best fit to the tabulated data of List (1951); r here is the mixing ratio (expressed in g kg^{-1}).

Potential temperature θ is defined as the temperature an unsaturated parcel would attain if taken adiabatically to 1000 mb. Taking account of the variation of c_{pd} with pressure and temperature, θ may be found approximately by the iterative formula

$$\theta = T_K \left(\frac{1000}{p}\right)^{[R_d/c_{pd}(\bar{p},\bar{T}_K)](1-0.28\times10^{-3}r)} \quad (6)$$

where c_{pd} is evaluated at $\bar{p} = \frac{1}{2}(1000 + p)$, $\bar{T}_K = \frac{1}{2}(\theta + T_K)$ in order to minimize error. Setting c_{pd} to its value at 1000 mb, 0°C gives

$$\theta = T_K \left(\frac{1000}{p}\right)^{0.2854(1-0.28\times10^{-3}r)}, \quad (7)$$

with an error of up to 0.2 K from neglecting variation of c_{pd}.

f. Saturated vapor pressure of water

BM and SS both make use of the formula of Tetens (1930) in which the saturated vapor pressure (mb) of water is given by

$$e_s(T) = 6.11 \times 10^{7.5T/(T+237.3)}. \quad (8)$$

As remarked by Murray (1967), this is acceptable for most meteorological purposes, except when extreme accuracy is required at low temperatures where, for example, there is a 2% error at $T = -30$°C, as compared with the value obtained using the formulation of Goff and Gratch (1946). In what follows, unfortunately, an accuracy of better than 0.5% is necessary at low temperatures in order that the lifting condensation level temperature, found by inverting the formula for $e_s(T)$, may be sufficiently accurately determined. A modified formula has therefore been derived, based on values obtained using the more recent formula of Wexler (1976).

According to Wexler, the saturated vapor pressure (mb) of water for 0°C $\leq T \leq$ 100°C is given to better than 0.005% by

$$\ln e_s = \sum_{i=0}^{6} g_i T_K^{i-2} + g_7 \ln T_K, \quad (9)$$

where the coefficients g_i take the following values:

$g_0 = -2.9912729 \times 10^3$, $g_4 = 1.7838301 \times 10^{-5}$

$g_1 = -6.0170128 \times 10^3$, $g_5 = -8.4150417 \times 10^{-10}$

$g_2 = 1.887643854 \times 10^1$, $g_6 = 4.4412543 \times 10^{-13}$

$g_3 = -2.8354721 \times 10^{-2}$, $g_7 = 2.858487 \times 10^0$.

The following formula was fitted to Wexler's results, extrapolated for $T <$ 0°C, to an accuracy of 0.1% for -30°C $\leq T \leq$ 35°C:

$$e_s(T) = 6.112 \exp\left(\frac{17.67\,T}{T + 243.5}\right). \quad (10)$$

For $T <$ 0°C, owing to the lack of accurate experimental data, there is some uncertainty about the validity of extrapolating Wexler's formula. The values of List (1951), obtained by extrapolating the formula of Goff and Gratch (1946) were therefore also taken into account, and the formula fits both sets of data to 0.3% for -35°C $\leq T \leq$ 35°C.

Inverting (10) gives

$$T = \frac{243.5 \ln e_s - 440.8}{19.48 - \ln e_s}, \quad (11)$$

which gives temperatures accurate to 0.03°C for this range.

A similar empirical formula is required for $T_K^{-1/\kappa_d} e_s(T)$. Taking $1/\kappa_d = 3.504$, the following formula fits Wexler's data to 0.2% for -30°C $\leq T \leq$ 35°C, and fits both Wexler's and List's data to 0.4% for -35°C $\leq T \leq$ 35°C:

$$\frac{e_s(T)}{T_K^{1/\kappa_d}} = 1.7743 \times 10^{-8} \exp\left(\frac{12.992\,T}{T + 217.8}\right). \quad (12)$$

Inverting this gives temperatures accurate to 0.05°C.

TABLE 1. Saturated vapor pressure of water calculated from Wexler's formula (9), and percentage errors δ_1, δ_2 and δ_3 in Tetens' formula (8), and in (10) and (12), respectively.

T°C	$e_s(T)$ (mb)	δ_1	δ_2	δ_3
−40	0.1905	−3.2	−0.47	−0.91
−30	0.5106	−1.7	−0.05	−0.07
−20	1.2563	−0.77	0.09	0.20
−10	2.8657	−0.26	0.07	0.15
0	6.1121	−0.03	−0.00	−0.00
10	12.279	0.04	−0.06	−0.14
20	23.385	0.02	−0.07	−0.16
30	42.452	−0.02	0.01	−0.01
40	73.813	−0.05	0.18	0.34

Table 1 gives values of saturated vapor pressure obtained using Wexler's formula (9), and the percentage errors obtained when Tetens' (1930) formula (8) and the new formulas (10) and (12) are compared with Wexler's values. The superiority of (10) over Tetens' formula for $T < 0$°C can be clearly seen, while for $T > 0$°C, the loss in accuracy is unimportant.

3. The lifting condensation level

The first stage in computing the equivalent potential temperature of a parcel of air is to find the temperature T_L which it would attain if lifted adiabatically to its condensation level.

By eliminating z from the equations

$$\frac{dT_D}{dz} = \frac{-gT_D^2}{\epsilon L_w(T_D)T_K} \quad \text{and} \quad \frac{dT_K}{dz} = \frac{-g}{c_{pd}} \tag{13}$$

for the lapse rate of dew point and the dry adiabatic lapse rate, respectively, and integrating making use of (2), it can be shown that T_L is given by

$$\frac{1}{T_L} - \frac{1}{T_D} + 1.266 \times 10^{-3} \ln\left(\frac{T_L}{T_D}\right) = 0.514 \times 10^{-3} \ln\left(\frac{T_K}{T_D}\right). \tag{14}$$

This, however, can only be solved iteratively for T_L. By approximating the T_L and T_D dependence by rational functions, a direct formula may be obtained

$$T_L = \frac{1}{\dfrac{1}{T_D - 56} + \dfrac{\ln(T_K/T_D)}{800}} + 56, \tag{15}$$

where temperatures are all absolute. This gives agreement with (14) to within a tenth of a degree and is therefore adequate.

However, since subsequent work makes use of the mixing ratio r, it is more convenient (rather than working in terms of the dew point) to derive a formula directly which uses mixing ratio, or rather, water vapor pressure e, related to it by

$$e = \frac{pr}{\epsilon + r} = \frac{pr}{622 + r}. \tag{16}$$

The starting point in deriving such a formula is the relationship

$$\frac{T_L}{T_K} = \left[\frac{e_s(T_L)}{e}\right]^{\kappa_d(1-0.28\times10^{-3}r)}, \tag{17}$$

which follows from conservation of potential temperature. SS uses this relationship to derive an implicit formula for T_L which, making use of (10) instead of Tetens' formula and taking natural logs rather than logs to base 10 as in SS, gives

$$\ln\left(\frac{6.112}{e}\right) + \frac{\ln(T_K/T_L)}{0.2854(1 - 0.28 \times 10^{-3} r)} + \frac{17.67(T_L - 273.15)}{T_L - 29.65} = 0. \tag{18}$$

Such a formula involves the inconvenience of solving iteratively for T_L, so a direct formula will be derived instead, and will be shown to be equally accurate.

Eq. (17) may be rewritten

$$\frac{e_s(T_L)}{T_L^{1/\kappa_d}} = \frac{e}{T_K^{1/\kappa_d}}\left(\frac{T_K}{T_L}\right)^{0.28\times10^{-3}r/\kappa_d}. \tag{19}$$

Making use of (12) and taking logarithms gives

$$\ln(1.7743 \times 10^{-8}) + \frac{12.992\, T_l}{T_l + 217.8} = \ln e - 3.504 \ln T_K + 0.981 \times 10^{-3} r \ln\left(\frac{T_K}{T_L}\right) \tag{20}$$

(writing T_l on the left since temperature here is in °C). Now, since r is never greater than 40 g kg^{-1}, the last term on the right is considerably smaller than $\ln e$, and will be neglected (whereas SS includes it). Hence, with slight adjustment of the coefficients,

$$T_L = \frac{2840}{3.5 \ln T_K - \ln e - 4.805} + 55. \tag{21}$$

An equally straightforward formula, which makes use of percentage relative humidity U can be derived in a similar way:

$$T_L = \frac{1}{\dfrac{1}{T_K - 55} - \dfrac{\ln(U/100)}{2840}} + 55. \tag{22}$$

The main errors in (21) and (22) are those which arise from the empirical formula (12), and those from neglecting r and the variation of c_{pd} (and hence κ_d) in

TABLE. 2. Lifting condensation level temperature T_l found using the modified Simpson formula (18), and errors ϵ_1, ϵ_2, ϵ_3 and ϵ_4 in the original Simpson formula, and in the approximate formulas (15), (21) and (22), respectively.

T (°C)	U (%)	p (mb)	T_l (°C)	ϵ_1	ϵ_2	ϵ_3	ϵ_4
20	75	1000	14.383	−0.003	0.000	−0.006	0.008
20	75	700	14.381	−0.003	0.001	−0.004	0.009
−20	75	1000 & 500	−23.903	0.037	−0.001	−0.027	0.004
20	25	1000	−4.797	0.039	−0.015	−0.016	−0.004
20	25	700	−4.799	0.039	−0.013	−0.013	−0.002
−20	25	1000 & 500	−37.522	0.188	0.008	0.020	0.047

(17); these are less than 0.05 K, 0.03 K and 0.03 K, respectively, so it can be concluded that (21) and (22) determine T_L correct to 0.1 K.

Table 2 gives values (°C) of T_l as calculated by the modified version (18) of the formula of SS. The errors for the original formula of SS and for (15), (21) and (22) are also given, the dew-point temperature for (15) being found using (11). In Eqs. (15), (21) and (22), T_l does not vary with pressure, whereas it does in (18) because of inclusion of the term involving r; such variation, however, can be seen to be negligible, and all three formulas agree with (18) to within 0.05°C in all realistic cases. The error in the original formula of SS is significantly larger for low temperatures owing to the error in Tetens' formula.

For the parcel of air at its lifting condensation level, in addition to the temperature, two potential temperatures will be required. The (moist) potential temperature θ is conserved in the lifting, so is given simply by (7). The potential temperature θ_D of dry air, given by

$$\theta_D = T_K\left(\frac{1000}{p-e}\right)^{\kappa_d}, \tag{23}$$

is not conserved, however. Making use of conservation of θ, it can be shown that the value θ_{DL} of θ_D at the lifting condensation level is given by

$$\theta_{DL} = T_K\left(\frac{1000}{p-e}\right)^{0.2854}\left(\frac{T_K}{T_L}\right)^{0.28\times10^{-3}r}, \tag{24}$$

where T_K, p and e are evaluated at the initial level. The extra term $(T_K/T_L)^{0.28\times10^{-3}r}$ can make a difference of up to 0.2 K in θ_{DL}.

4. Equivalent potential temperature

Having brought the air to its lifting condensation level, it is now necessary to raise it to a great height along a water-saturation pseudo-adiabat, i.e., dropping out condensed water as soon as it is formed. Such a process satisfies the equation [derived, for example, in Holton (1972)]

$$c_{pd}\frac{d\theta_D}{\theta_D} + c_w r_s \frac{dT_K}{T_K} + d\left(\frac{r_s L_w}{T_K}\right) = 0, \tag{25}$$

where

$$r_s = \frac{\epsilon e_s(T)}{p - e_s(T)}, \tag{26}$$

$$\theta_D = T_K\left(\frac{1000}{p-e_s(T)}\right)^{\kappa_d}. \tag{27}$$

The equivalent potential temperature θ_E is given as the value obtained for θ_D when (25) is integrated from the lifting condensation level to a great height. As a simplification, the middle term of (25) has commonly been neglected, giving the following approximation for θ_E:

$$\theta'_E = \theta_{DL}\exp\left[\frac{r_s(T_L)L_w(T_L)}{c_{pd}T_L}\right]. \tag{28}$$

TABLE 3. Values of θ_E obtained by numerical integration of (25), together with errors η_1, η_2, η_3, η_4, η_5 and η_6 from the conventional formula (28), from Simpson's original formula, and from (33), (35), (38) and (39), respectively, assuming a parcel initially saturated at pressure p_l (mb), temperature T_l (°C).

p_l (mb)	T_l (°C)	θ_E (K)	η_1	η_2	η_3	η_4	η_5	η_6
1000	30	386.28	−3.90	−0.33	0.08	0.39	0.01	−0.018
1000	20	335.61	−1.56	0.04	−0.08	0.18	−0.02	−0.005
1000	0	283.60	−0.27	0.09	0.02	−0.02	0.04	−0.003
1000	−30	244.01	−0.02	0.02	0.02	−0.01	0.01	−0.001
700	20	394.71	−2.83	−0.39	−0.04	−0.10	−0.04	0.015
700	0	319.13	−0.45	0.05	0.02	−0.09	0.03	−0.002
700	−30	270.57	−0.02	0.02	0.03	−0.03	0.02	−0.001
200	−30	391.82	−0.13	−0.06	0.09	−0.19	0.03	−0.006
200	−50	354.11	−0.01	0.01	0.03	−0.03	0.01	−0.002
Maximum error			−4	−0.4	0.1	0.4	0.05	0.02

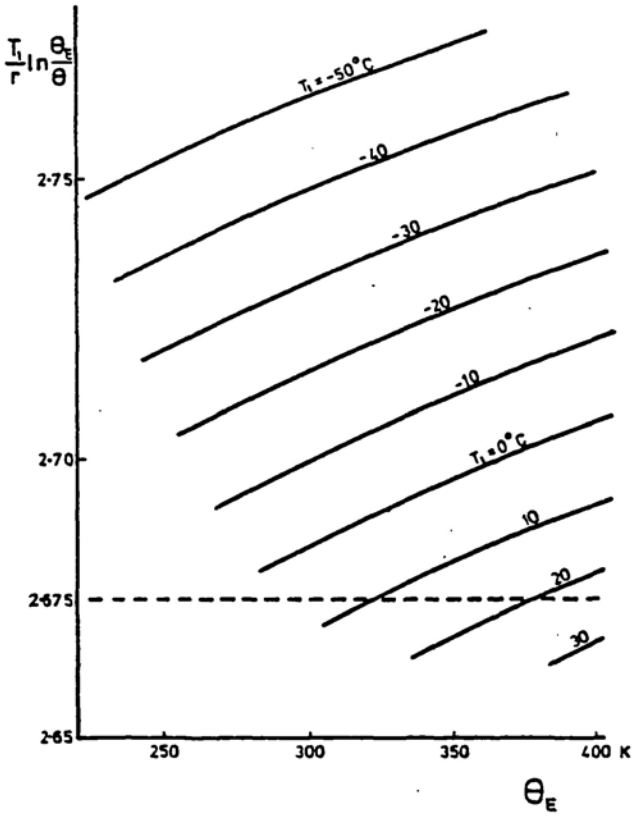


FIG. 1. Plot of $(T_L/r)\ln(\theta_E/\theta)$ against θ_E for various values of T_l; the best fit for θ_E is shown dashed.

For a more accurate integration of (25) it is necessary to state rather carefully the process by which the water is condensed out; were this carried out maintaining the parcel at a constant temperature, the middle term would vanish and (28) would be exactly the potential temperature attained. However, for a pseudo-adiabatic process as defined earlier, no such simplification exists, and it is necessary to integrate (25) numerically. For this purpose, the following variables will be introduced.

$$\chi = \frac{L_w(T)r_s(T)}{c_{pd}T_K}, \tag{29}$$

$$\theta_x = \theta_D \exp(\chi). \tag{30}$$

Thus (25) becomes

$$\frac{d\theta_x}{\theta_x} + \frac{c_w}{L_w(T)}\chi dT = 0. \tag{31}$$

Eliminating p and r_s from (26)–(30) gives

$$\chi \exp(\chi/\kappa_d) = \frac{\epsilon}{1000c_{pd}}\theta_x^{1/\kappa_d}\frac{L_w(T)e_s(T)}{T_K^{1/\kappa d+1}}. \tag{32}$$

This may be used to solve for χ, and hence to integrate (31) from the lifting condensation level, where θ_x takes the value θ'_E [given by (28)] to a great height, where θ_E is now the value obtained for θ_x. Results are given in Table 3, where they are compared with those obtained from the various approximate formulas; η_1, the error in θ'_E, can be seen to be as large as 4 K, thus confirming the results of SS.

SS derived a correction to (28) by making a linear approximation in the integration of (25). The errors as compared with the numerical results, given as η_2 in Table 3, can be seen to be significant at lower levels for large values of θ_E. For consistency in comparison, the errors here and in subsequent formulas were adjusted to give minimax best fits to the numerical results for the range 200 mb $\leq p \leq$ 1000 mb, $\theta_E \leq$ 400 K. The formula of SS thus becomes

$$\theta_E = \theta'_E \exp[\exp(3.0\ln\theta'_E + 13.5\ln T_L - 99.55)], \tag{33}$$

where θ'_E is given by (28). The errors, η_3 in Table 3, are now everywhere less than 0.1 K. However, it should be noted that SS overlooks an additional error of up to 0.2 K in assuming that θ_D is conserved when bringing air to its lifting condensation level; this extra error can be avoided by making use of (24), but the procedure by this stage is becoming rather cumbersome.

The formula of BD makes use of θ not θ_D and hence avoids this additional source of error. They fit numerically computed values to a formula of the form

$$\theta_E = \theta \exp\left[\frac{A(\theta_E)\,r}{T_L}\right], \tag{34}$$

where $A(\theta_E)$ is a linear function of θ_E; the occurrence of θ_E on the right-hand side means that the formula is iterative. However, plotting $(T_L/r)\ln(\theta_E/\theta)$ against θ_E for different T_l (Fig. 1), using results of the numerical integration, it can be clearly seen that the inclusion of θ_E dependence in A makes negligible improvement to the formula. A best fit to the numerical results is thus given simply by

$$\theta_E = \theta \exp\left[\frac{2.675\,r}{T_L}\right] \tag{35}$$

(dashed line in Fig. 1), with errors (η_4 in Table 3) which can be as large as 0.4 K.

As neither of the formulas of SS and BD was entirely satisfactory, even when modified, new formulas were fitted to the numerical results, which gave negligible error for 200 mb $\leq p \leq$ 1000 mb, $\theta_E \leq$ 400 K. The formula of BD was used as a starting point as it has the advantage of using θ, not θ_D. A graph was plotted of $(C_{pd}T_L/L_w \times 10^{-3}\,r)\ln(\theta_E/\theta)$

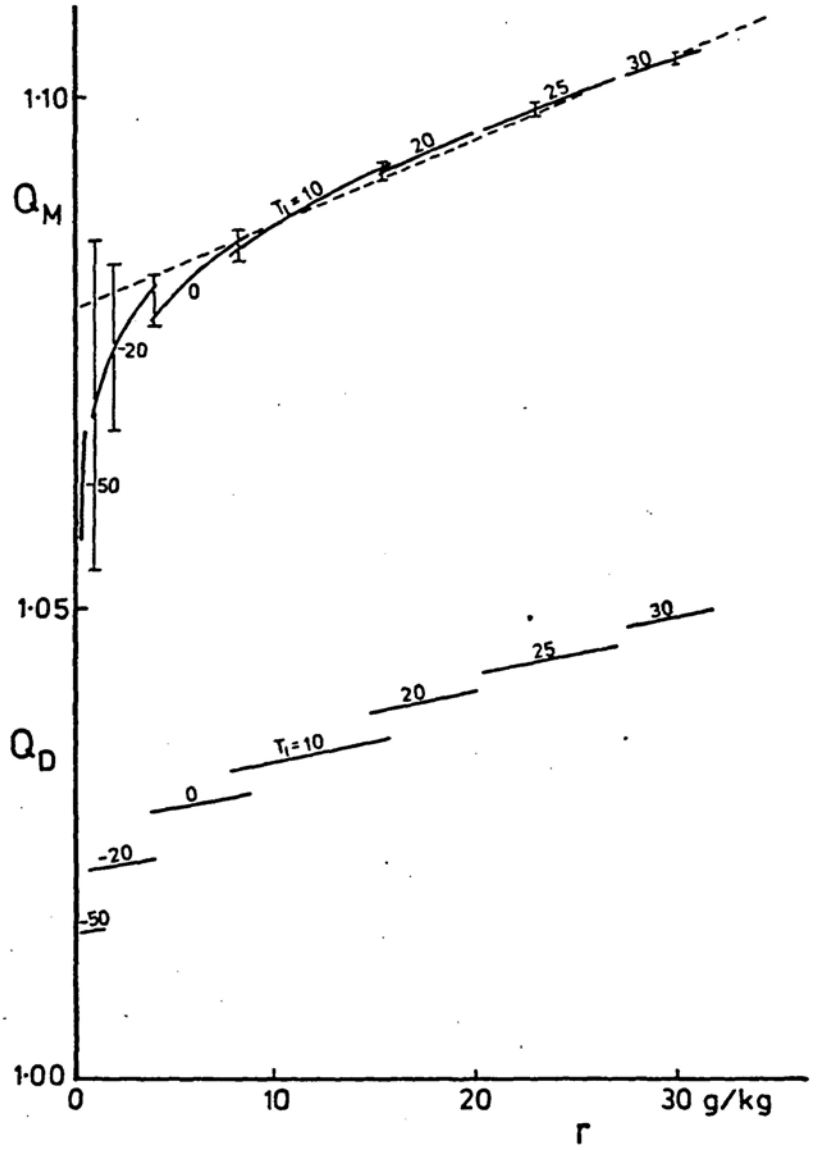


FIG. 2. Plots of $Q_M = (c_{pd}T_L/L_w \times 10^{-3}\, r)\ln(\theta_E/\theta)$ (upper graph), and $Q_D = (c_{pd}T_L/L_w \times 10^{-3}\, r)\ln(\theta_E/\theta_{DL})$ (lower graph) against r for various values of T_l; the error bars and best fit for θ_E (dashed) are shown for the upper graph.

against r for different T_l (Fig. 2); it showed very little dependence on T_l, so a formula of the type

$$\frac{c_{pd}T_L}{L_w \times 10^{-3}\, r}\ln(\theta_E/\theta) = f(r) \tag{36}$$

could be fitted. Error bars are drawn for an error of ± 0.05 K in θ_E; they vary in length because $f(r)$ is multiplied by r in computing θ_E. Hence, although $f(r)$ shows a rapid fall near $r = 0$, a linear fit to $f(r)$ (dashed) was found to be sufficient to determine θ_E to an accuracy of 0.05 K. The best fit thus obtained was

$$f(r) = 1.0784(1 + 0.810 \times 10^{-3}\, r), \tag{37}$$

giving

$$\theta_E = \theta \exp\left[1.0723 \times 10^{-6}\frac{L_w(T_L)}{T_L} \times r(1 + 0.810 \times 10^{-3}\, r)\right]$$
$$= \theta \exp\left[\left(\frac{3.376}{T_L} - 0.00254\right) \times r(1 + 0.81 \times 10^{-3}\, r)\right], \tag{38}$$

where the coefficients in the last line have been adjusted so as to minimize rounding errors. Errors in the computed θ_E are given as η_5 in Table 3.

Fig. 2 also shows a plot of $(c_{pd}T_L/L_w \times 10^{-3}\, r) \times \ln(\theta_E/\theta_{DL})$, with θ_{DL} now replacing θ, against r. There is now a dependence on T_l, but this and the dependence on r are both very nearly linear. Hence with a formula similar to (38) but with $L_w(T_L)$ replaced by another linear function of T_L, it is possible to evaluate θ_E to an accuracy better than 0.02 K, the appropriate formula being

$$\theta_E = \theta_{DL} \exp\left[\left(\frac{3.036}{T_L} - 0.00178\right) \times r(1 + 0.448 \times 10^{-3}\, r)\right]. \quad (39)$$

The errors are given as η_θ in Table 3.

For most purposes, Eq. (38) is probably to be preferred, since it makes use of θ. As a basis for very accurate work, however, Eq. (39) with θ_{DL} given by (24) is suggested. Either is simpler and more accurate than the formulas of SS and BD.

Eq. (38), as it makes use of θ, also provides a relationship between θ_E and the wet-bulb potential temperature θ_W which is attained when a parcel is brought down to 1000 mb from its lifting condensation level along a pseudo-adiabat. This is due to the fact that a saturated parcel at $T_K = \theta = \theta_W$ at 1000 mb, when taken pseudo-adiabatically to a great height and then returned adiabatically to 1000 mb, will attain a temperature θ_E, so that

$$\theta_E = \theta_W \exp\left[\left(\frac{3.376}{\theta_W} - 0.00254\right) \times r_s(1 + 0.81 \times 10^{-3}\, r_s)\right], \quad (40)$$

where

$$r_s = \frac{622 \times e_s(\theta_w)}{1000 - e_s(\theta_w)}, \quad (41)$$

and $e_s(\theta_w)$ is given by (10).

Apart from the errors arising in the fit to the numerically computed results (i.e., those listed in Table 3), all the approximate formulas are subject to the following errors:

- The most serious computational error is from neglect of the variation of c_{pd} with temperature and pressure. This affects not only taking a parcel from its lifting condensation level to a great height, but also raising it initially to its lifting condensation level and, most importantly, returning it from a great height to the surface, processes for which the potential temperatures which are conserved should be defined by formulas similar to (6). The cumulative effect of these errors is that the assumed value 1005.7 of c_{pd} should be replaced wherever it occurs by $c_{pd}(\bar{p},\bar{T}_K)$, where now $\bar{p} = \frac{1}{2}(1000 + p)$, $\bar{T}_K = \frac{1}{2}(\theta_E + T_K)$ so that, for instance, Eq. (38) would be replaced by

$$\theta_E = T_K \left(\frac{1000}{p}\right)^{(R_d/c_{pd}(\bar{p},\bar{T}_K))(1-0.28\times10^{-3}r)} \times \exp\left[\frac{1.0784 \times 10^{-3} L_w(T_L)}{c_{pd}(\bar{p},\bar{T}_K)T_L \times r(1 + 0.81 \times 10^{-3}\, r)}\right]. \quad (42)$$

The error in assuming a fixed value of c_{pd} can be as large as 0.2 K.

- The error from assuming a fixed value of c_w in (25) is by contrast small: less than 0.02 K.
- It was shown in Section 3 that the value of T_L may be in error by 0.1 K, leading to a possible error of 0.03 K in θ_E.

Apart from these errors listed above, it must be remembered that a water saturation pseudo-adiabatic process has been assumed throughout this paper. As mentioned in the Introduction, the answer would be altered by several degrees were heat retained by condensed water or latent heat of ice formation included.

5. Conclusion

The following formula is recommended for computation of equivalent potential temperature for a water-saturation pseudo-adiabatic process:

$$\theta_E = T_K \left(\frac{1000}{p}\right)^{0.2854(1-0.28\times10^{-3}r)} \times \exp\left[\left(\frac{3.376}{T_L} - 0.00254\right) \times r(1 + 0.81 \times 10^{-3}\, r)\right], \quad (43)$$

where T_K, p, and r are the absolute temperature, pressure and mixing ratio at the initial level, and T_L is the absolute temperature at the lifting condensation level, given by any of (15), (21) or (22). The maximum error in values thus obtained is 0.3 K, the main contribution to the error arising from neglect of variation of the specific heat of dry air with temperature and pressure, an error which also affects the value of the potential temperature θ.

Acknowledgments. I would like to thank Dr. A. K. Betts, Dr. K. J. Bignell, Mr. G. Dugdale and Mr. J. R. Probert-Jones for their helpful comments on this work.

REFERENCES

Betts, A. K., and F. J. Dugan, 1973: Empirical formula for saturation pseudo-adiabats and saturation equivalent potential temperature. *J. Appl. Meteor.*, 12, 731–732.

——, and R. D. Miller, 1975: VIMHEX 1972 rawinsonde data. Dept. of Atmospheric Science, Colorado State University, 178 pp.

Goff, J. A., and S. Gratch, 1946: Low pressure properties of water from −160 to 212 F. *Trans. ASHVE*, **52**, 95–121.

Holton, J. R., 1972: *An Introduction to Dynamical Meteorology*. Academic Press, 319 pp.

Iribarne, J. V., and W. L. Godson, 1973: Atmospheric thermodynamics. *Geophys. Astrophys. Monogr.*, No. 6, Reidel, 222 pp.

List, R. J., 1951: *Smithsonian Meteorological Tables*, 6th rev. ed. Smithsonian Institute Press, 527 pp.

Murray, F. W., 1967: On the computation of saturation vapor pressure. *J. Appl. Meteor.*, **6**, 203–204.

Saunders, P. M., 1957: The thermodynamics of saturated air: a contribution to the classical theory. *Quart. J. Roy. Meteor. Soc.*, **83**, 342–350.

Simpson, R. H., 1978: On the computation of equivalent potential temperature. *Mon. Wea. Rev.*, **106**, 124–130.

Tetens, O., 1930: Über einige meteorologische Begriffe. *Z. Geophys.*, **6**, 297–309.

Wexler, A., 1976: Vapor pressure formulation for water in range 0 to 100°C. A revision. *J. Res. Nat. Bur. Stand.*, **80A**, 775–785.

ACKNOWLEDGEMENTS.

I would like to thank all those who have helped and encouraged me in the preparation of this thesis both practically and in innumerable discussions. Particular thanks are due to my parents for their continual support, to Dr. J.S.A. Green who has patiently supervised me for the seven years which it has taken to complete this project, and to Dr. F.B.A. Giwa and Mr. G. Dugdale who first interested me in the theoretical and observational studies respectively. Mr. A. Seaton advised me in the use of the computer, Dr's D.A. Mansfield and A.J. Thorpe have read and commented on drafts of the various chapters, and Dr. K.J. Bignell, Miss I. Matthews and Mr. G. Moore have helped in the actual preparation of the thesis, and their help is gratefully acknowledged.

Thanks are also due to the Nigerian Meteorological Services for their kind provision of the surface and upper air data, and to University of Ibadan, Nigeria, and to Atmospheric Physics Group, Imperial College, London for extensive use of computing and other facilities, and for making it possible for me to pursue these studies whilst I was working for them, especially during my 1976 Study Leave from Ibadan and during my 1978-79 Research Assistantship at Imperial College.

Finally, I must express my profound thanks to God who, through Christ, has inspired and upheld me in a very real way throughout.